Diploma Thesis

Study on electrospinning of self-reinforcing thermoplastic polyurethane(urea) elastomers

performed at

Institute of Applied Synthetic Chemistry

TU Wien

under the supervision of

Assistant Prof. Dipl.-Ing. Dr.techn. Stefan Baudis

and

Univ.Prof. Dipl.-Ing. Dr.techn. Robert Liska

by

Philip Sgarz, BSc

11771123

Vienna 2025

Danksagung

Bei **Prof. Dr. Stefan Baudis** möchte ich mich für die ausgezeichnete Betreuung bedanken. Bereits während meiner Bachelorarbeit unter dir habe ich tolle Einblicke in die Welt der Polymerchemie bekommen und es freut mich, dass ich diese im Zuge meiner Diplomarbeit weiter vertiefen konnte. Deine aktive Unterstützung, aber auch der Freiraum zum selbstständigen Arbeiten, den du mir geboten hast, hat diese Arbeit für mich zu einem würdigen Abschluss meines Studiums gemacht.

Danke auch **Prof. Dr. Robert Liska** für die guten Ratschläge und die Möglichkeit diese Arbeit innerhalb einer so tollen Arbeitsgruppe abzuschließen. Das Arbeitsklima, dass du hier geschaffen hast, ist selten und motiviert einen nicht nur selbst sein Bestes zu geben, sondern auch die Zusammenarbeit mit Kollegen nicht zu scheuen.

Besonderer Dank gilt auch **Dr. Thomas Koch** und dem Institut für Werkstoffwissenschaft und Werkstofftechnologie, für die Hilfe bei allen thermischen und mechanischen Messungen sowie bei der Elektronenmikroskopie der elektroversponnenen Materialien. Ohne deine stete Hilfsbereitschaft, aber auch die spannenden Gespräche zwischendurch, wäre meine Arbeit in dieser Form nicht möglich gewesen.

Bei **Katharina Rauchenwald** vom Institut für Chemische Technologien und Analytik möchte ich mich dafür bedanken, dass ich das digitale Lichtmikroskop mitbenutzen durfte. Im Praktikum bei dir habe ich viele Sachen für meine Arbeit mitnehmen können und eines davon war ebendieses Gerät.

Simon Seisenbacher gilt mein persönlicher Dank für die Einführung in den Umgang mit dem Elektrospinn-Gerät und die rasche Rückmeldung bei allerlei Fragen und Unsicherheiten. Als Chemiker betrachtet man Maschinen oft mit gewisser Skepsis, aber mit deiner Unterstützung konnte ich diese schnell abschütteln.

Vielen Dank auch **Dr. Katharina Ehrmann, Markus Fitzka, Klaus Ableidinger** und **Philip Schwarzl**, die ihr Wissen und ihre Erfahrungen über thermoplastische Polyurethane mit mir geteilt haben. Ohne eure hätte ich so manches Mal nicht weitergewusst und mir sicher einiges an Extraarbeit angeschafft. Den „reverse funnel" würde ich wahrscheinlich heute noch suchen.

Ich bedanke mich auch beim gesamten H21, bei **Selina, Jelena, Thomas** (du gehörst ja praktisch genauso dazu) **und** insbesondere meiner Bench-Nachbarin **Kaja,** für die stets heitere Stimmung im Labor, die einen selbst in angespannten Zeiten schnell wieder auf bessere Gedanken gebracht hat.

Weiters hat es mich sehr gefreut mit meinen Diplomanden-Kollegen **Theresa, Björn, Edma, Kristina, Selina und Olja** zusammenzuarbeiten, mit euch konnte man sich immer austauschen und es war schön gemeinsam in einem Boot sitzen zu dürfen. Auch an alle Seniors **Michi, Chrissie, Flo M., Flo. P, Toni, Dani, Carola, Tina und Miri**, und Post-Docs **Davide und Patrick** meinen herzlichen Dank für die immer freundliche Unterstützung und dass ihr mich mit so offenen Armen in eure Gruppe aufgenommen habt. **Dagmar, Jürgen und Walter**, euch ebenfalls vielen lieben Dank, ihr wart die beste Hilfe bei allen administrativen, logistischen und technischen Belangen, die man sich wünschen kann.

Außerhalb der Arbeitsgruppe, möchte ich mich auch bei meinen Studienkollegen **Till, Nicole, Martin, Theresa, Christoph, Kathi und Anna** bedanken, die mich durch die besten und stressigsten Zeiten der letzten Jahre begleitet haben. Danke auch an meine Freunde **Tobi, Michi, Alex, Jasmina, Maxi R., Lucas, Lili, Sayuri, Maxi W., Beni und Luisa,** die mich regelmäßig daran erinnert haben, dass es auch eine Welt außerhalb des Studiums gibt. Ein ganz liebes Dankeschön auch an dich **Christina**, dass du mich in all dieser Zeit unterstützt, also quasi diesen Tanz mit mir durchgestanden hast (^^). Du motivierst mich immer mein Bestes zu geben und schaffst es wie keine andere mir in stressigen Zeiten die Anspannung zu nehmen.

Mein größter Dank gilt zum Schluss noch meiner Familie, deren Unterstützung mir zu jeder Zeit den nötigen Rückhalt gegeben hat. Ich bedanke mich bei meinem Bruder **Stephan,** dafür dass er mir immer zur Seite steht und trotzdem den nötigen Ehrgeiz in mir weckt weiter zu nach vorn zu sehen. Genauso bedanke ich mich bei meinen Eltern **Albin und Isabella,** die mich zeit meines Lebens gefördert haben und mir trotz der schwierigen familiären Umstände im letzten Jahr immer mit voller Kraft zur Seite gestanden sind.

Table of Content

Introduction

Appendix

Abstract

Atherosclerosis and other cardiovascular diseases are major health concern worldwide. While preventative measures can be taken through the reduction of risk factors regarding diet and exercise, acute treatment often requires surgical intervention in the form of stents and especially vascular bypasses. For the latter, donatable human vascular tissue would be ideal but this is often in short supply. An alternative here are synthetic vascular grafts, which can be mass-produced and do not require a donor. While such grafts are already in use for larger blood vessels, the materials used are so far unviable for small-diameter vascular grafts (< 6 mm), which provides the impetus for further research.

In this regard, thermoplastic poly(urethane(urea)) elastomers (TPU(U)s) are promising by combining the desired mechanical properties provided by thermosets with the necessary processibility of thermoplastics. However, increasing the strength of TPU(U)s generally coincides with poorer processing, which so far has been a limiting factor. To reconcile this issue, previous research done by our research group introduced dynamic hindered urea or oxime urethane bonds into the backbone of TPU(U)s. Through these dynamic bonds, the mechanical strength of TPU(U)s can be increased after processing *via* formation of urea bond *in situ* in the presence of moisture (i.e., macromolecular metamorphism). Additionally, this process can be used to introduce cleavable moieties into TPU(U)s through careful monomer design for potential applications in targeted drug delivery.

In this thesis, it could be demonstrated that it is possible to introduce different dynamic bond motifs i.e., hindered urea and oxime urethane bonds, into TPU(U)s together, for greater versatility and better modifiability of TPU(U)s. This coincides with the successful synthesis of TPU(U)s following a prepolymer approach with a chain extender system of up to three different species. These TPU(U)s were further characterized regarding their monomer composition and molecular weight as well as their thermal and mechanical properties. Thermal properties of these new TPU(U)s are similar to established references, while the inclusion of a third chain extender species resulted in an increased elasticity and reduced mechanical stiffness of the material. Subsequent conditioning studies in deionized water further showed a significant increase in ultimate tensile strength and therefore self-reinforcement in these new TPU(U)s.

Lastly, to process the synthesized TPU(U)s into vascular grafts, a working procedure was established, based on existing literature, for electrospinning of these materials into fibrous, tubular structures on the in-house electrospinning device. Additional methods were established to further characterize the thickness of these electrospun structures and to determine their tensile properties using ring tensile tests.

Kurzfassung

Atherosklerose und andere Herz-Kreislauf-Erkrankungen stellen ein weltweites Gesundheitsproblem dar. Während vorbeugende Maßnahmen zur Verringerung von Risikofaktoren beispielsweise durch eine ausgewogene Ernährung getroffen werden können, erfordern akute Behandlungen häufig einen chirurgischen Eingriff in Form von Stents und häufig auch Bypässen. Für solche Bypässe wäre menschliches Gewebe von einem geeigneten Spender ideal, doch dieses ist nicht immer vorhanden. Eine Alternative bieten hier synthetische Implantate, die in großen Mengen und ohne die Notwendigkeit eines Spenders hergestellt werden können. Solche Implantate sind für größere Blutgefäße bereits in Verwendung. Die derzeit verwendeten Materialien sind allerdings noch ungeeignet für Gefäße mit kleineren Durchmessern (< 6 mm), was einen Anstoß für weitere Forschung bietet.

In dieser Hinsicht sind thermoplastische Elastomere basierend auf Poly(urethan(harnstoffen)) (TPU(U)s) vielversprechend, da sie die gewünschten mechanischen Eigenschaften von Elastomeren mit der notwendigen Verarbeitbarkeit von Thermoplasten kombinieren. Allerdings führt die Erhöhung der mechanischen Festigkeit von TPU(U)s in der Regel zu einer schlechteren Verarbeitbarkeit, was sich bisher als ein limitierender Faktor erwiesen hat. Um dieses Problem zu lösen, wurden in früheren Forschungsarbeiten unserer Arbeitsgruppe dynamische gehinderte Harnstoff- oder Oxim-Urethan-Bindungen in die Polymerketten von TPU(U)s eingebaut. Durch diese dynamischen Bindungen konnte die mechanische Festigkeit von TPU(U)s nach der Verarbeitung durch die Bildung von Harnstoffverbindungen in nasser Umgebung deutlich erhöht werden. Darüber hinaus kann dieser Prozess genutzt werden, um abspaltbare Molekülgruppen in TPU(U)s einzubringen, die beispielsweise bei der gezielten Verabreichung von Medikamenten eingesetzt werden können.

In dieser Arbeit konnte gezeigt werden, dass es möglich ist, verschiedene dynamische Bindungsmotive, d.h. gehinderte Harnstoff- und Oxim-Urethan-Bindungen, gemeinsam in TPU(U)s einzuführen, um eine größere Kontrolle im Design von TPU(U)s zu erreichen. Des Weiteren gelang hiermit die erfolgreiche Synthese eines TPU(U)s mit bis zu drei verschiedenen Kettenverlängerungsmonomeren. Die so hergestellten TPU(U)s wurden hinsichtlich ihrer molekularen sowie ihrer thermischen und mechanischen Eigenschaften charakterisiert. Anschließende Konditionierungsstudien in deionisiertem Wasser zeigten außerdem eine signifikante Erhöhung der Zugfestigkeit und damit die gewünschte Selbstverstärkung dieser neuen TPU(U)s.

Um die so hergestellten TPU(U)s weiterzuverarbeiten, wurde zuletzt basierend auf der vorhandenen Literatur ein Arbeitsverfahren für das Elektrospinnen dieser Materialien zu faserigen, röhrenförmigen Strukturen entwickelt. Des Weiteren wurden Methoden zur Charakterisierung der Dicke dieser elektroversponnenen Strukturen und zur Bestimmung ihrer mechanischen Zugeigenschaften mit Hilfe von Ringzugtests entwickelt.

Introduction

1. Cardiovascular system

The cardiovascular system (CVS) is one of the ten major systems of the human body next to the nervous, reproductive and digestive system among others. It is comprised of the heart muscle and a closed set of blood vessels (arteries, veins, capillaries), which ensure blood circulation throughout the body, providing nutrients and oxygen to surrounding tissue and removing waste products and CO_2. The heart keeps the blood in constant motion, while blood vessels distribute it throughout the body, controlling blood amount and destination. Arteries transport blood away from the heart, while veins return it. Capillaries act as small intermediaries and permeate every part of the body to exchange gases and fluids with surrounding tissue. The structure and interconnection of the blood vessels is depicted in Figure 1.[1-3]

Within the context of this work, the focus will be on arteries and veins i.e., the vascular part of the CVS. These blood vessels are multilayered structures as depicted in Figure 1. The innermost layer, the *tunica intima*, is in direct contact with blood and consists of a squamous epithelium, which prevents blood clotting and can facilitate vasodilation. Blood pressure is maintained by the smooth muscle cells of the *tunica media* through contraction and dilatation. The outermost layer, *tunica adventitia*, connects blood vessels to surrounding tissue and prevents rupture. It mainly consists of fibroblasts, elastin and collagen. Further structural stability is provided by an internal and external membrane in between layers, consisting of porous elastin sheets, which ensures a sufficient elasticity of blood vessels and overall excellent mechanical properties for their function.[2-4]

Conditions, which impair the function of the CVS are referred to as circulatory disease or cardiovascular diseases (CVDs) e.g., ischemic heart disease and strokes. Given the essential role of the CVS in the human body and its strong interconnection with other systems, failure of the CVS by such diseases can be lethal. As such, CVDs are leading causes of death within the EU (see Figure 2) but also worldwide with a global death toll of 18 million people in 2019 representing 32 % of all global deaths in that year.[5-7]

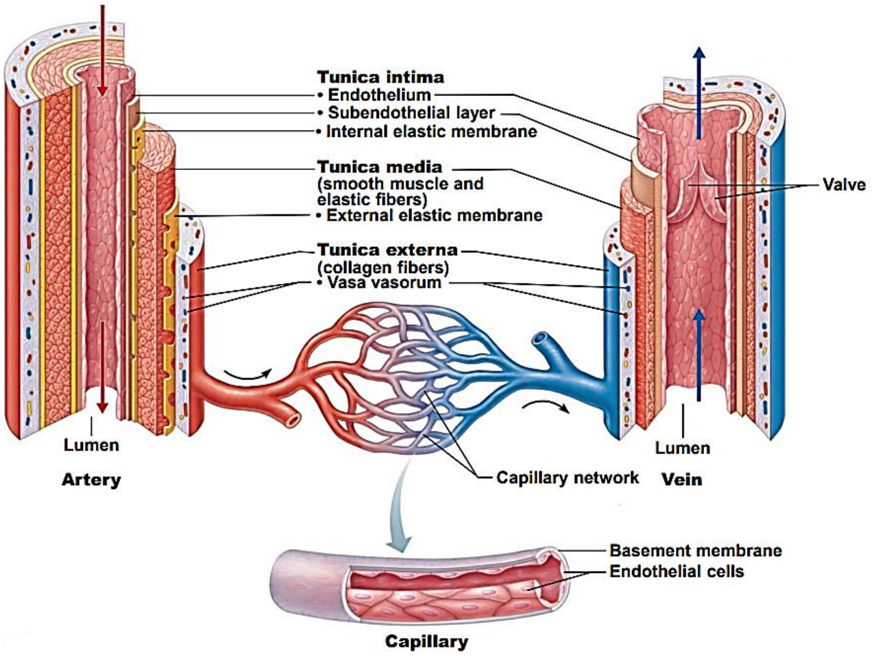

Figure 1: Structure of arteries, veins, and capillaries and their interconnection regarding blood flow: Fresh blood flows from the heart through the arteries (red arrows). Parts of the blood flow are diverted into capillary networks (black arrows) to distribute it within a given tissue and facilitate gas and liquid exchange with adjacent cells. Depleted blood then exits the capillary network and is directed back to the heart through veins (blue arrows). Image reproduced from Hoehn et al.[4]

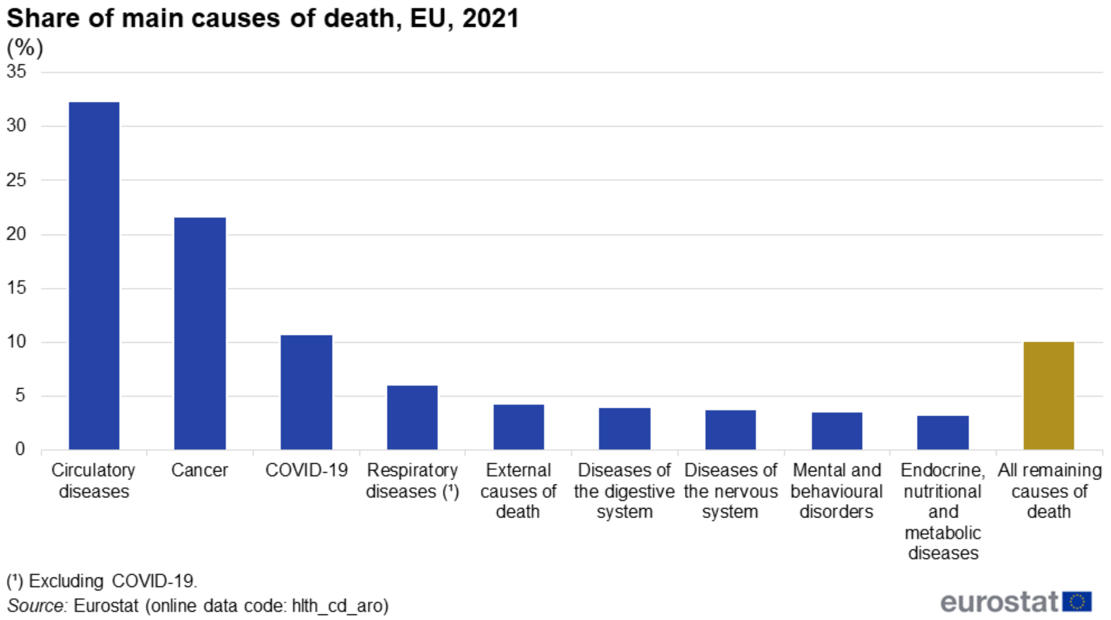

(¹) Excluding COVID-19.
Source: Eurostat (online data code: hlth_cd_aro)

Figure 2: Share of main causes of death within the EU in 2021. Image reproduced from Eurostat.[5]

Common CVDs can be localized blood vessel dilatation (aneurysms), contraction (stenosis), and occlusion by accumulation of atherosclerotic plaque (atherosclerosis), which impede or prevent blood flow and subsequently reduce the supply to tissues. This results in tissue ischemia and thrombosis, and potentially tissue necrosis and cardiac arrest.[3, 6, 8, 9] A schematic of these CVDs, treatment methods, and their challenges are depicted in Figure 3.

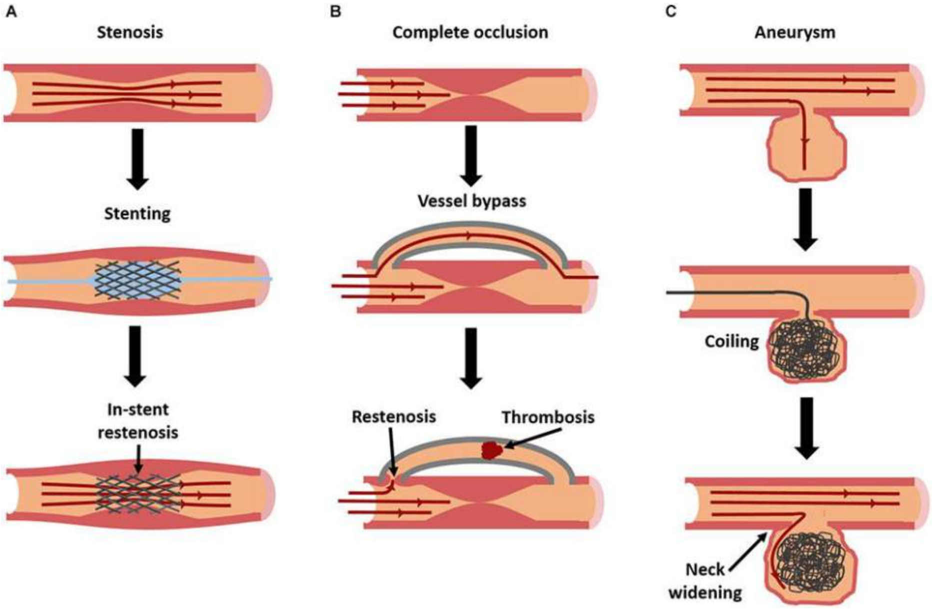

Figure 3: Summary of vascular diseases, their treatments and modes of failure: Stenosis (A) is frequently treated via stents but can suffer from in-stent restenosis. Occlusion (B) necessitates a vessel bypass, which can suffer from restenosis or thrombosis. Aneurysms (C) may be treated by filling the cavity with an aneurysm coil, but these can leak and let fluid back in, leading to an enlargement of the aneurysm. Images reproduced from Strobel et al.[10]

Addressing CVDs is difficult: They are noncommunicable diseases that are often triggered by endogenous sources. As a result, conventional containment strategies and immunotherapy prove ineffective. Preventative measures involve the reduction of risk factors for patients regarding lifestyle (e.g. stress, sedentariness, smoking) and pre-existing conditions (e.g. obesity, hypertension, diabetes) through healthier diets, regular exercise, and the use of lipid-lowering medication among others.[6, 11] In severe cases, surgical intervention can become necessary, e.g. vascular bypass grafts for circumvention of occluded blood vessels (see Figure 3, B).[12, 13]

These vascular grafts, can be transplants harvested from the patient's own body (autologous) e.g., from the saphenous vein, or artificial implants: Autologous grafts are ideal regarding graft compatibility but require harvestable tissue and an invasive harvesting procedure, which must be close in time to the surgical procedure to avoid tissue decomposition. Artificial grafts circumvent these issues through production in bulk and higher shelf-lives, but currently demonstrate poorer performance particularly as substitutes for narrow blood vessels with inner diameters below 6 mm. There, formation of thrombosis and hyperplasia can be observed leading to short patency rates. As such, research is ongoing to further improve the functionality of vascular grafts.[14-16]

2. Tissue engineering

To prepare artificial grafts, which mimic native tissue and assume its functions, a range of chemical, physical, and biological aspects have to be considered. The research field, that deals with this interdisciplinary problem, is tissue engineering (TE), which tries to restore, replace, maintain or augment bodily functions, tissues, and organs.[17] The term was coined in the 1980s and 1990s in the USA and can be attributed to the bioengineering pioneers *Yuan-Cheng Fung*, as well as *Joseph P. Vacanti* and *Robert Langer*.[18, 19] However, applications of artificial skin grafts in the treatment of burn injuries were already published in 1962 by *Chardack et al*.[20, 21]

Tissue engineering is complementary to regenerative medicine but focuses more on the construction of tissue. The construction of tissue is thereby achieved through the combination of appropriate cells with scaffolds mimicking the extracellular matrix, in the presence of growth-stimulating signals. These three pillars, cells, biomaterials, and signals, are referred to as the “triad of tissue engineering” (see Figure 4) and are essential for successful tissue construction.[22]

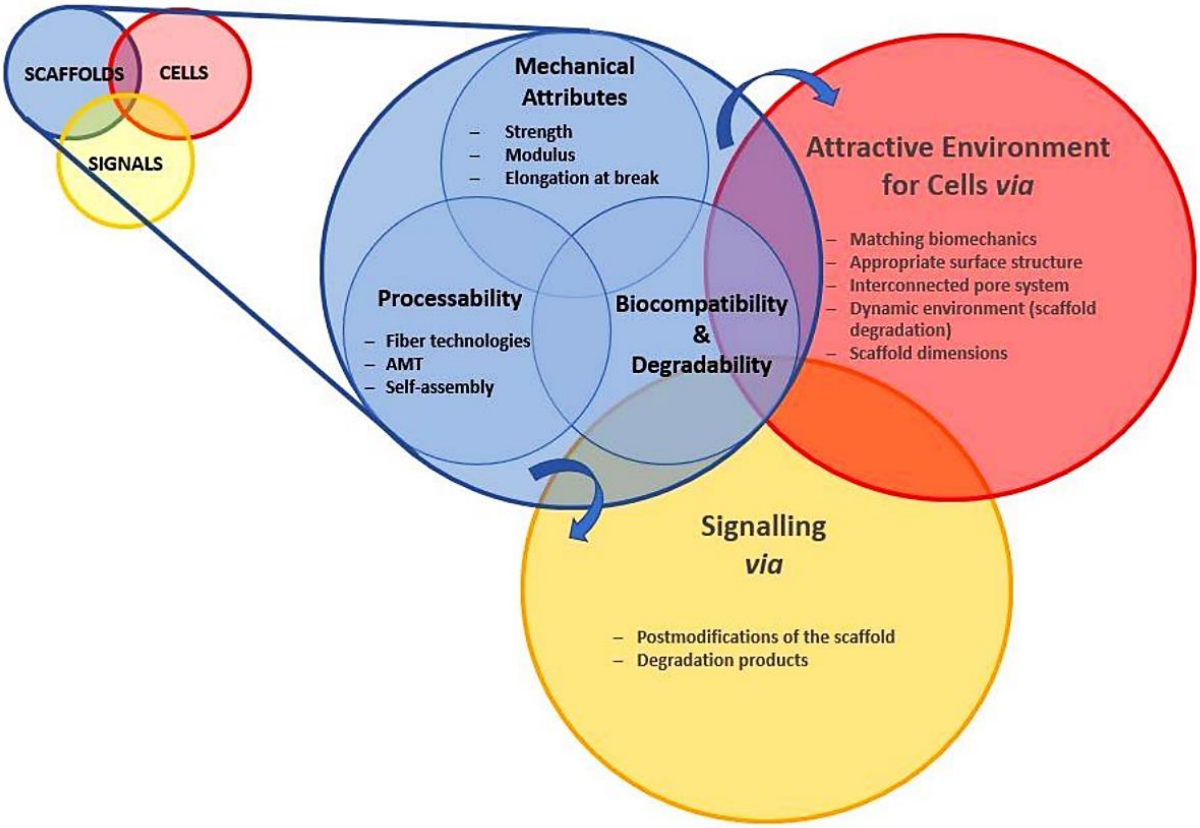

Figure 4: The triad of tissue engineering essential for the reconstruction and mimicking of native tissue, which relies on the combination of appropriate scaffolds (blue), cells (red), and signals (yellow). Image reproduced from Katharina Ehrmann.[23]

Tissue construction can take place *ex vivo*, where a scaffold is seeded with isolated cells outside the body e.g., in a bioreactor, and the formed tissue is subsequently implanted. This allows control over cell differentiation and tissue growth, and leads to grafts with good mechanical properties.[24] However, *ex vivo* tissue engineering is time-consuming, difficult to reproduce, and suitable cell isolation is not always possible. Alternatively, cell seeding and tissue formation can occur *in vivo* onto a pre-prepared scaffold, which is implanted into target tissue and attracts surrounding cells. As a result, the procedure becomes more convenient, and issues related to immunogenicity or implant rejection are more easily avoided. However, such methods are limited to self-regenerating tissue and, therefore, unsuitable for certain applications related to e.g., cardiac or neural tissue.[17, 25, 26]

Regardless of strategy, the material used for scaffolding significantly influences treatment success. These materials must interact appropriately with the biological host system as biomaterials[27], fulfill the functions of substituted tissue, and be bioactive (i.e. stimulate desired biological activity).[28] To introduce these features, both artificial and naturally occurring materials are considered, ranging from metals[29] and polymers[30] to ceramics, glass, and minerals[31].[32]

To ensure sufficient integration of the scaffold into the biological host system, the used biomaterial must be nontoxic and biocompatible i.e., produce a positive response from host tissue and avoid immunogenicity.[33, 34] It must further mimic the behavior and structure of the substituted tissue regarding biomechanics, porosity, and surface topography, and facilitate cell adhesion.[25] Additionally, the biodegradability of the material need to be considered: To what extent and at which rate the implanted material decays over time and whether its degradation products impact the human body.[35]

For vascular grafts, polymer materials are well suited as scaffold materials, due to similarities with the extracellular matrix.[36] For this, not only natural polymers are considered like proteins elastin and collagen, which are already components of native blood vessels as established in chapter 1, but also synthetic polymers. The latter of which have the important advantage of being more customizable and more easily obtained: Since scaffold materials need to be put into their desired shape prior to implantation, the chosen material must not only meet the demands of the implant but also withstand the often times demanding processing conditions. By varying their building blocks, synthetic polymers can simply be modified to meet these requirements, whereas with natural polymers there is less leeway. Due to their artificial nature, synthetic polymers can also be prepared in bulk compared to the complex and expensive isolation and purification procedures necessary for natural polymers.[37]

As such, large-diameter vascular grafts with an inner diameter above 6 mm prepared from synthetic poly(ethylene terephthalate) (PET, *Dacron*®) or expanded poly(1,1,2,2-tetrafluoroethylene) (PTFE, *Gore-Tex*®) have already been made.[15] However, as already mentioned in chapter 1, such materials demonstrate poor patency rates in small diameter vascular grafts caused by thrombosis and hyperplasia.[16] In these cases, new materials are required, which meet not only the mechanical demands of vascular grafts but also overcome the biocompatibility issue. Here, one promising class of materials, are poly(urethane(urea))s, which are non-toxic, hemocompatible, and demonstrate good mechanical properties and wear resistance.[38-40]

Depending on the choice of material, different processing techniques have to be deployed to give the graft its desired shape and microstructure i.e., roughness and porosity. On the one hand, there are conventional molding techniques, where a material is cast, and the desired porosity is introduced through gases (gas foaming)[41], leachable particulate[42] or thermally induced phase separation with an extractable liquid[43] among others.[44] However, the requirement of a custom mold as well as the introduction and removal of a porogen makes such techniques generally less versatile. Therefore, the use of additive manufacturing becomes increasingly relevant ranging from conventional 3D-printing[45] to electrospinning[46]. For vascular grafts in particular, the latter is of interest, given that the resulting fibrous, nonwoven structures are porous in the micro to nanometer scale with a large surface area, which resembles the vascular extracellular matrix and is ideal for cell infiltration and tissue regeneration.[15]

3. Nonwoven fabrics

In case of artificial vascular grafts, fibrous materials (i.e. fabrics) demonstrate suitable properties for substituting blood vessels.[47] Fabrics are arrangements of multiple fibers into ordered or randomly oriented webs. Depending on how the individual fibers are held together, these fabrics can be either woven, knitted or nonwoven fabrics (see Figure 5). In case of woven and knitted fabrics, the fibers are held together structurally *via* weaving[48] or knitting[49]. In case of nonwoven fabrics (**NWFs**), they are held together mainly through friction, cohesion or adhesion induced by thermal, chemical, or mechanical consolidation methods.[50-52]

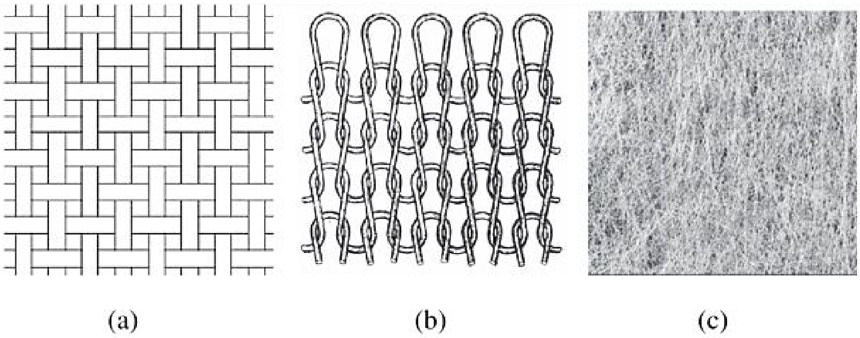

Figure 5: Comparison of woven fabrics (a), knitted fabrics (b), and non-woven fabrics (c). Image adopted from Misnon et al.[53]

Particularly the field of NWFs became subject of renewed interest in recent years with an average annual growth in production of 5.4 % between 2013 and 2023 according to the European Disposables and Nonwovens Association.[54, 55] This is partially due to their potential recyclability by simple detachment of the fibers from one another, as well as the wide range of available materials and fabrication techniques, which can be used to prepare NWFs. Therefore, common applications range from everyday dry wipes and wound dressings over thermal and sound insulations to respiratory filters and oil sorption.[50] Due to their randomly-oriented fibrous microstructure, which mimics natural tissue, NWFs also show increasing potential as scaffold material in tissue engineering.[56]

Given the multitude of different methods and materials available for NWFs, a good characterization of the fabric regarding their chemical, physical, and structural properties is essential. For this, standardized testing methods are available in a series of standards summarized under DIN EN ISO 9073.[57] Due to the anisotropic nature of the present fibers, especially the mechanical properties of NWFs vary significantly from those of corresponding bulk materials comprised of similar substances. This anisotropy is caused by the large length-to-width ratio, which gives fibers a higher tensile strength in fiber direction and higher flexibility in radial direction.[58, 59] In fiber arrangements like NWFs, these properties of the individual fibers overlap, thereby significantly altering deformation and fracture behavior of the overall material.

Upon exposure to mechanical stress, energy dissipation in NWFs not only involves deformation of the individual fibers but also deformation of the fiber arrangement, primarily through in-plane tension and through-thickness compaction. Additionally, the mechanical stress is distributed between the individual fibers, which are mostly independent from one another. Consequently, failure of one fiber through fracture or unwinding does not immediately result in a total failure of the material leading to often ductile rupture.[60-62] All these aspects influence strain behavior of NWFs under stress and are the reason why mechanical properties of NWFs deviate significantly from those of bulk materials.

Fabrication of NWFs can be divided into drylaid, wetlaid and polymer-laid methods corresponding to the state of the fibers during their deposition for fabric formation. In drylaid NWFs, the fibers are processed in a dry state without the use of a solvent, whereas in wetlaid NWFs, fibers are initially suspended in a liquid. In contrast, polymer-laid NWFs start initially with polymer melts or solutions rather than fibers, which are then spun into fibers and directly processed into fabrics.[63-65] While typically requiring a more sophisticated processing setup, such polymer-laid methods have the advantage of preparing fibers and fabrics in a single procedure. This is especially of interest in case of tissue engineering, where polymer-laid methods like electrospinning can be used to prepare microstructured NWFs for the substitution of cardiovascular tissue for example.[47]

4. Electrospinning

Given the high structural demands for scaffolds in tissue engineering, processing techniques that allow a high degree of control over the products microstructure are of interest. One such technique is electrospinning (**ES**), a fiber spinning process, that produces filaments with diameters in the micrometer to nanometer range and allows construction of nonwoven fabrics. The procedure was introduced in a patent by *Anton Formhals* in 1934[66] and became subject of renewed focus starting in the 1990s.[67]

ES is based around electrokinetic or rather electrohydrodynamic principles involving the motion of a liquid in an electric field between two electrodes. Aside from polarization effects, this motion mainly results from Coulomb interactions of the electric field with the charged particles (e.g., ions) contained in the liquid. The charged particles migrate towards their respective electrodes and accumulate at the liquid surface, where they are held back by surface tension. With the accumulation of similarly charged particles, their electrostatic repulsion of one another increases, which creates a growing force counteracting the surface tension of the liquid, causing motion and deformation of the liquid shape. As the strength of the electric field increases, the density of charged particles at the liquid surface increases as well.[68, 69] Past a certain charge density at the liquid surface (Rayleigh limit), the electrostatic repulsions start to exceed the liquid's surface tension, leading to a rapid emission of charged material through fine jets (Rayleigh jets) as depicted in Figure 6.[70]

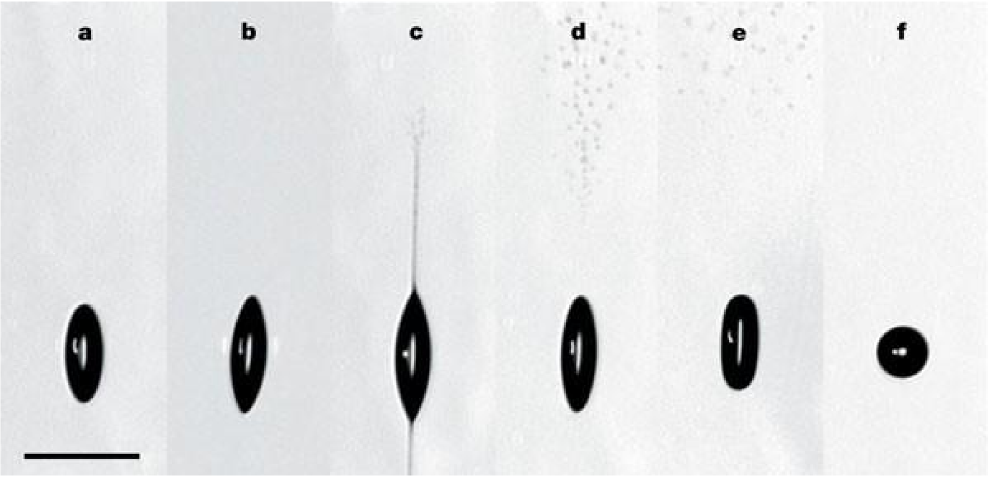

Figure 6: High-speed imaging of the deformation and disintegration of a charged levitated droplet of ethylene glycol in an electric field: Through evaporation of neutral molecules, the volume of the droplet decreases and the charge density of the droplet increases. As a result, the droplet starts to deform into an ellipsoid (a) with increasingly pointy poles (b). Once the electrostatic repulsion of the charges in the droplet supersedes the surface tension of the droplet, fine jets (Rayleigh jets) form at these poles (c) and eject charged liquid from droplet, until stability is reestablished. Whereupon, the jets disintegrate and the droplet returns to its spherical shape (d-f).Scale bar in the bottom left corner measures 100 µm.[70]

This electrohydrodynamic emission through fine jets is responsible for the small diameters of electrospun fibers, and is not only the basis for ES[68], but also electrospraying[71] and electrohydrodynamic jet printing[72]. The schematic of an ES process is depicted in Figure 7, A. For ES, a strong electric field is applied between two electrodes using a high-voltage power supply. These electrodes are separated by a dielectric, usually air, to prevent direct contact and short circuiting. From one electrode, the emitter electrode, the liquid fiber precursor, usually a polymer melt[73, 74] or polymer solution[75], is continuously fed into the electric field. Free ions present in the precursor are drawn towards the counter electrode, the collector electrode, and lead to a deformation of the liquid into a conical shape (Taylor cone). Once the applied electric field is high enough, aforementioned Rayleigh jets form at the tip of the cone, and the precursor is accelerated towards the collector electrode (see Figure 7, B).[68]

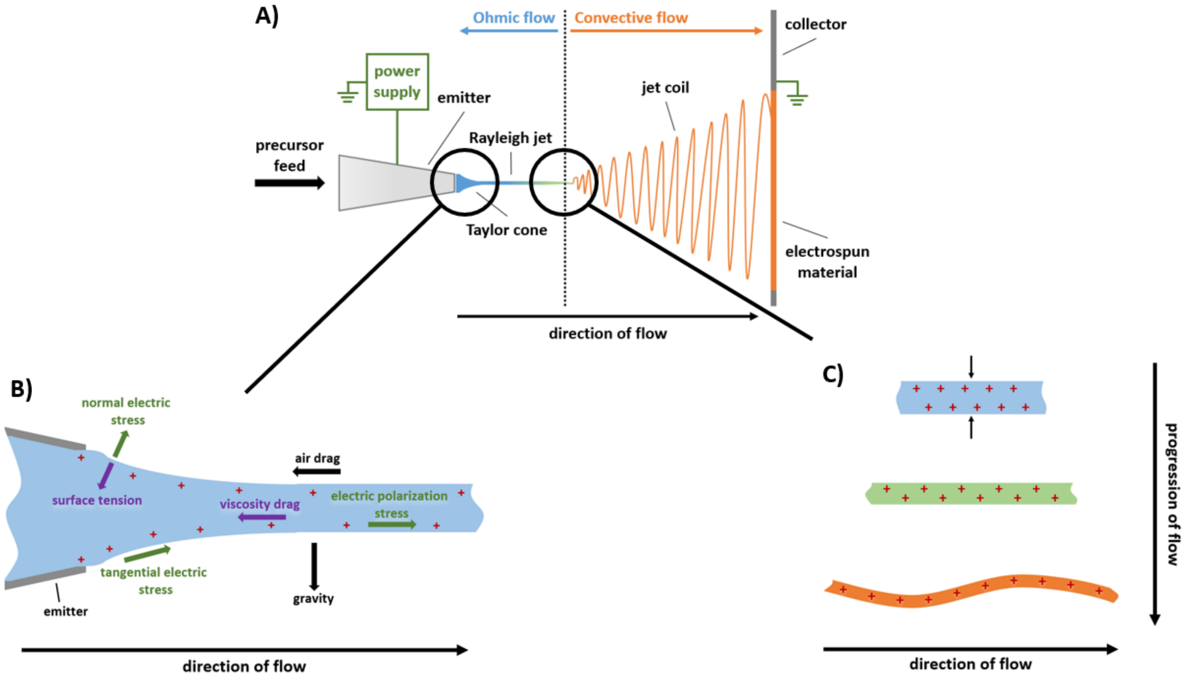

Figure 7: A) Schematic of the electrospinning process: A liquid fiber precursor is fed into a strong electric field generated by a high-voltage power supply between an emitter and a collector electrode. In the electric field, the fiber precursor feed adopts a conical shape (Taylor cone) and a thin jet of fiber precursor (Rayleigh jet) is ejected from its tip towards the collector electrode. This movement from emitter to collector is the product of different forces and drags (B) stemming from the environment (black), the applied electric field (green), and the properties of the liquid (violet, "+" symbolizes charged particles in the liquid precursor). During its way to the collector, the diameter of the jet decreases (C), which leads to a concentration of charged particles in radial direction. The increasing electrostatic repulsion further decreases the jet diameter and leads to bending and coiling of the jet, which also prolongs the jets travel towards the collector. The continuous decrease in diameter leads to an increase in the surface to volume ratio of the jet, which facilitates fiber formation by cooling of the melt or evaporation of the solvent. The solid fibers are ultimately collected on the collector. Motion in the Taylor cone and the straight jet segment (blue) can be described through Ohmic flow, while the coiling of the jet close to the collector (orange) follows a convective flow pattern.[76] Images A, B, and C are adapted from Joanna Gatford[77], Iranshahi et al.[68] and Reneker et al.[78] respectively.

In ES, unlike Figure 6, this jet does not disintegrate into smaller droplets but remains in an elongated shape due to viscoelastic properties of the precursor. This is caused among others by the entanglement of polymer chains on a molecular level.[79] As a result, the precursor jet is continuously stretched and decreases in diameter towards the collector electrode.[69]

The narrowing of the jet increasingly impedes the redistribution of contained charges, and leads to the formation of electrical bending instabilities due to electrostatic repulsion. These bending instabilities lead to increased coiling of the jet, creating a whipping motion as depicted in Figure 8, which further elongates the precursor jet and decreases its diameter.[78, 80] Meanwhile, the precursor jet also starts to solidify, either through the evaporation of solvent or cooling down of the melt and the formed fibers are ultimately collected on the collector electrode.[69]

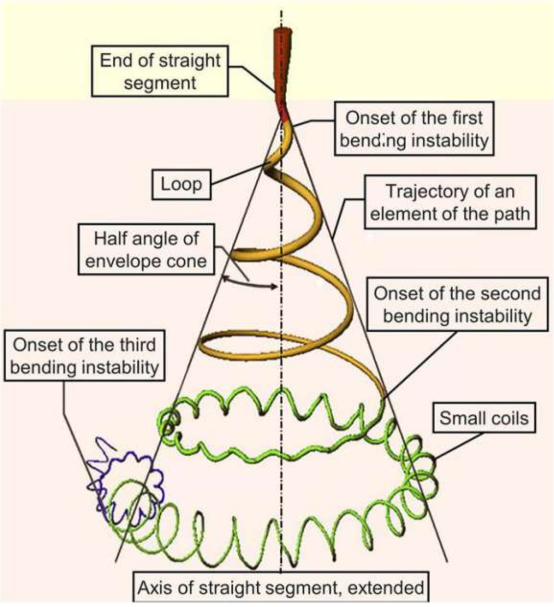

Figure 8: Path of the electrospun jet past the Taylor cone towards the target: The initially straight jet segment of fiber precursor becomes subject to elongation and bending instabilities caused by electrostatic repulsion of adjacent surface charges.[69]

The success of ES relies on the careful optimization of multiple parameters, which can be broadly divided into ambient, precursor, and process-related parameters. For polymer solution-based ES, relevant parameters are depicted in Table 1. [69, 75, 81, 82]

Table 1: Summarized parameters for polymer solution-based electrospinning[69, 75, 81-83]

solution parameters	process parameters	ambient parameters
solvent type (surface tension, conductivity, volatility)	applied voltage and electric current	temperature
polymer type	solution feed rate	relative humidity
molecular weight of the polymer	distance between emitter and collector electrode	
polymer concentration (viscosity)	shape and material of emitter and collector electrode	
	movement and movement speed of emitter and collector electrode relative to one another	

These parameters not only influence, whether fiber formation takes place (see Figure 9), but also control fiber diameters and fiber morphology, leading potentially to beading, branching and porosity on the fiber surface among other things.[80, 83] Self-assembly approaches and special collector setups further allow the construction of complex microstructures with these fibers, like honeycomb meshes[84] or Lotus-Leaf-like superhydrophobic surfaces[85]. It is this versatility, which makes ES a promising method for the fabrication of microstructured scaffolds for biomedical applications, as long as suitable materials are available.[81]

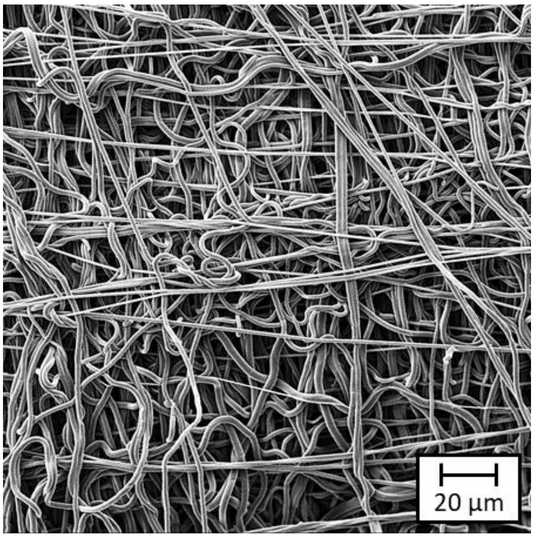

Figure 9: Scanning electron microscopy image of electrospun Pellethane® 2363-80A, a commercial thermoplastic poly(urethane) elastomer, spun from a 5 wt.% solution in 1,1,1,3,3,3-hexafluoro-2-propanol.

5. Thermoplastic poly(urethane(urea)) elastomers

5.1. General aspects

For tissue-engineered vascular grafts, the mechanical properties of the scaffold material are crucial for withstanding the high and periodically changing blood pressure (in healthy adults between 10.7 kPa and 16.0 kPa or 80 mmHg and 120 mmHg respectively).[86] At the same time, the used material also needs to have an appropriate processibility, so it can be easily formed into its desired shape. For this, thermoplastics are desired, given that they can be soluble and meltable. However, thermoplastics show a comparatively low tensile strength. This can be improved through crosslinking of polymer chains.[87] Conventionally, crosslinking is achieved by formation of covalent bonds between chains creating thermoset elastomers like rubber. But the resulting polymer networks are insoluble and infusible, and therefore difficult to process. An alternative here are thermoplastic elastomers, where crosslinking occurs through non-covalent, physical interactions between polymer chains like hydrogen bonding. These physical interactions result in microphase separation of chain segments creating a network of soft block chains with little to no physical crosslinking connected through hard block nodes with strong physical crosslinking (see Figure 10, center). These physical crosslinkages give the material the mechanical properties of an elastomer but can also be reversibly disrupted for processing in solution or as melt. Prime examples here are thermoplastic poly(urethane(urea)) elastomers, which are of particular interest given their great biocompatibility as mentioned in chapter 2.[88-90]

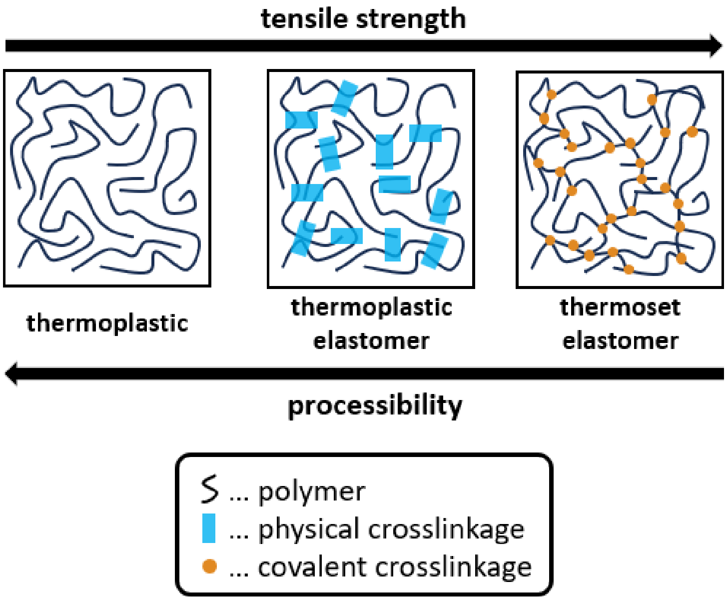

Figure 10: Schematic comparison of thermoplastics, thermoplastic elastomers, and elastomers, regarding their tensile strength, processibility, and crosslinking

Initially developed by *Otto Bayer* at *I.G. Farben* in 1937[91], poly(urethane(urea))s (PU(U)s) are polymers produced *via* polyaddition of multifunctional isocyanates with multifunctional alcohols, oximes, or amines *via* nucleophilic attack on the isocyanate carbon. Thereby, the addition reactions of alcohols with isocyanates, leads to formation of urethanes[92], which produce poly(urethane)s, while the addition of amines leads to urea formation and produces poly(urea)[93] (see Scheme 1).

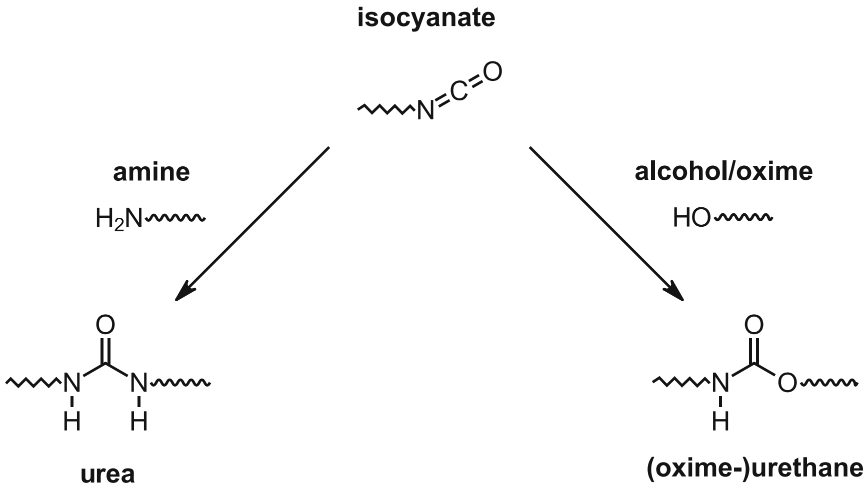

Scheme 1: Urea (left) and (oxime-)urethane (right) formation through addition reactions amines, alcohols or oximes with isocyanates.

Since one isocyanate group reacts with one hydroxy or amine group, the selective synthesis of both linear and crosslinked PU(U)s is possible and can be set *via* the number of functional groups within the used monomers. In case of linear, and therefore thermoplastic, poly(urethane/urea) chains, these monomers are difunctional, while polymer networks require at least one trifunctional monomer species for covalent crosslinking.[94] The presence of these urethane and urea groups in the backbone enables strong hydrogen bonding within and between polymer chains (see Figure 11). As a result, thermoplastic poly(urethane(urea)) elastomers (TPU(U)s) can be prepared, which consist of linear PU(U) chains, that are physically crosslinked through hydrogen bonding at the urethane or urea segments. This provides TPU(U)s, on the one hand, with the desirable mechanical properties of an elastomeric network, while also maintaining the thermoplastic properties of linear polymer chains, namely solubility and meltability.[94,95] This was first discovered in 1955 by *Charles Schollenberger* at *Goodrich Corporation*.[91, 96]

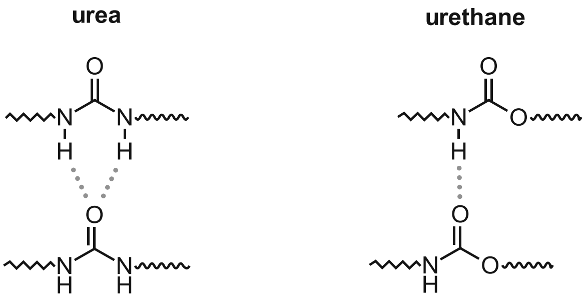

Figure 11: Hydrogen bonding (dotted lines) between two urea segments of two poly(urethane(urea)) chains[95]

TPU(U) chains typically follow a block copolymer structure, where long, flexible, often aliphatic soft-chain segments with low glass transition temperatures and no physical crosslinking, alternate with, often short and aromatic hard-chain blocks responsible for hydrogen bonding (see Figure 12). By varying the sizes of these blocks, and the amount of crosslinking between hard-chain blocks during synthesis, the prepared TPUUs can have a range of different mechanical properties, making them customizable for different applications.[95, 97, 98]

Figure 12: Schematic of polyurethane soft-block (thin lines) and hard-block (black bars) morphology[99]

5.2. Synthesis

TPU(U) synthesis usually involves at least two to three monomer species depending on the chosen method: A long-chain diol (macrodiol) responsible for the soft-block segments, a diisocyanate necessary for urethane or urea formation, and a chain-extender species, which connects the different soft-block segments and produces the intermediate hard-block segments together with the diisocyanates. Typically used macrodiols are aliphatic polyesters, polyethers, and poly(carbonate)s with hydroxy endgroups. Chain extenders can be diols, diamines, or dioximes among others and can be aromatic or sterically demanding to improve rigidity of the hard block segment.[98, 100, 101]

For synthesis, two approaches can be considered: First, all monomers can be mixed together at once, in a *one-shot method*. This approach is simple and time-efficient, but presents limited control over the resulting monomer sequence. A greater degree of control is gained by following the *prepolymer method* depicted in Figure 13. Here, the different monomers are added stepwise to the reaction, leading initially to the formation of prepolymers, usually by addition reaction of a macrodiol with diisocyanates, which are subsequently linked together after addition of the chain extenders. As a result, repetitive monomer sequences can be prepared leading to the formation of uniform soft and hard-block segments.[102]

As a polyaddition, TPU(U) synthesis is a step-growth polymerization and follows Carothers' Law (see Eq. 1): To achieve a high degree of polymerization and thus high molecular weights, not only a high reaction conversion ($p \rightarrow 1$) is necessary but also precise stoichiometric ratios ($q \rightarrow 1$) between the number of isocyanate groups and the number of functional groups with active hydrogen (i.e., alcohols, amines, oximes).[102, 103]

$$\overline{X_n} = \frac{1+q}{1+q-2qp} \qquad \text{Eq. 1}$$

$\overline{X_n}$ … mean degree of polymerization
p … reaction conversion
q … ratio between the number of reacting functional groups

As a result, successful TPU(U) synthesis requires precise weighing and pure monomers. Additionally, moisture in the environment and the water content in reactants must be kept to a minimum to avoid hydrolysis of isocyanates (see Scheme 2). There, through decarboxylation, hydrolyzed isocyanates are converted into amines, which can react with other isocyanates *via* urea formation.[104] As a consequence, one water molecule leads to conversion of two isocyanate groups, effectively reducing the amount of available isocyanate groups for polyaddition.

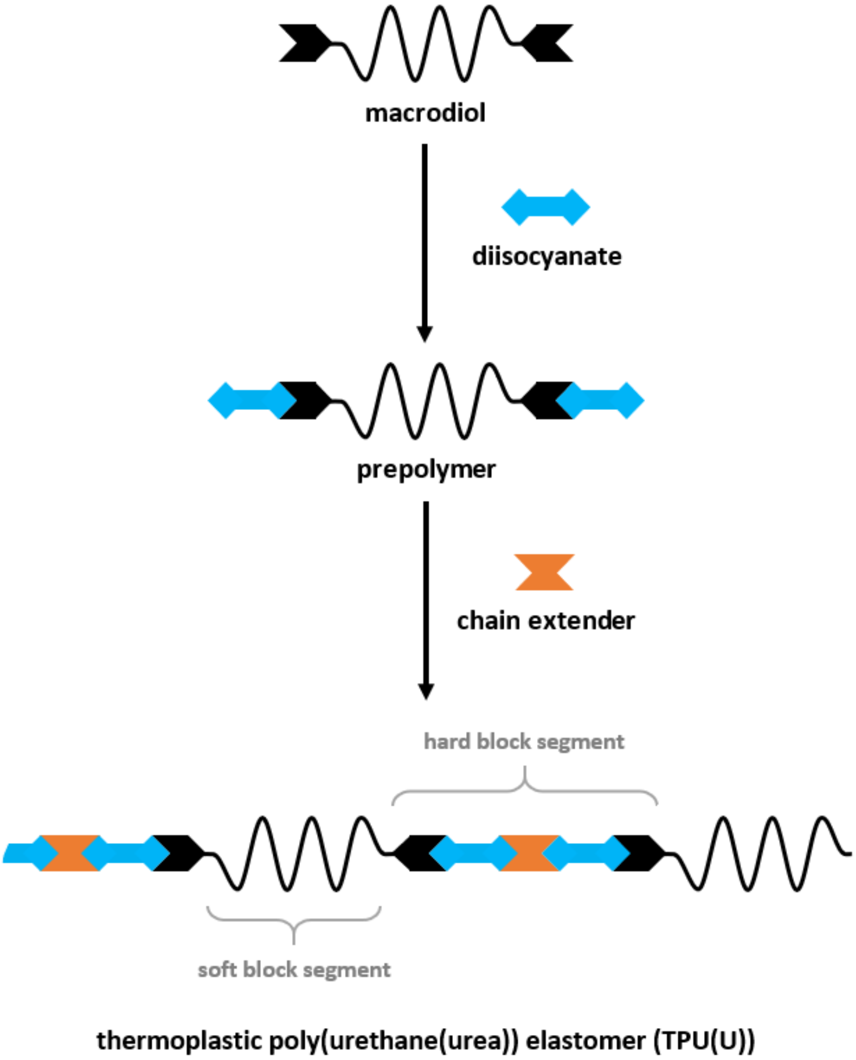

Figure 13: Reaction scheme of the prepolymer method for synthesis of thermoplastic poly(urethane(urea) elastomers: A macrodiol reacts with diisocyanates to prepolymers, which are ultimately linked together into polymers using chain extenders.

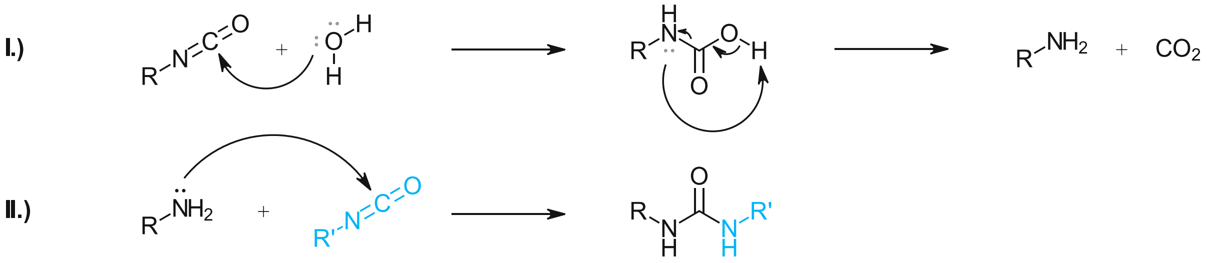

Scheme 2: Result of moisture next to isocyanates: Hydrolysis and decarboxylation (I) and urea formation (II) with a second isocyanate group (blue)

5.3. Structural dynamics

As already mentioned, TPU(U)s are highly versatile and can be tailored to different applications through their modular synthesis and variety of available monomers. This also provides a simple way to introduce dynamic covalent bonds (**DCBs**) into TPU(U)s, which can reversibly break and reform depending on environmental factors like temperature, pH, moisture, or the presence of light at specific wavelengths.[105]

While conventional urethane bonds already show minor dynamic properties through transcarbamoylation (e.g. in poly(urethane) vitrimers),[106, 107] they are generally slow and require high temperatures, making conventional urethane bonds less suitable for functional applications.[108] Consequently, more efficient DCB motifs can be introduced through hindered urea bonds (**HUBs**),[109, 110] oxime urethane bonds (**OUBs**),[111, 112] and thiourethane bonds (**TUBs**),[108, 113] which are summarized in Scheme 3. HUBs use amines with sterically demanding substituents to destabilize the urea bonds formed with them, making them more dynamic. The dynamic nature of OUBs is mediated by the nitrone tautomer of the oxime, which enables a favorable transition state. TUBs engage primarily in dynamic thiol exchange reactions, but can also reversibly dissociate at elevated temperatures. Apart from dynamic urethane and urea bonds, which are typically formed during polymerization, dynamic moieties like aromatic pinacols[114] or disulfides[115] can also be introduced as components in the used monomers. This provides additional options for customization, but may complicate synthesis as dissociation of these already existing DCBs needs to be suppressed.[108]

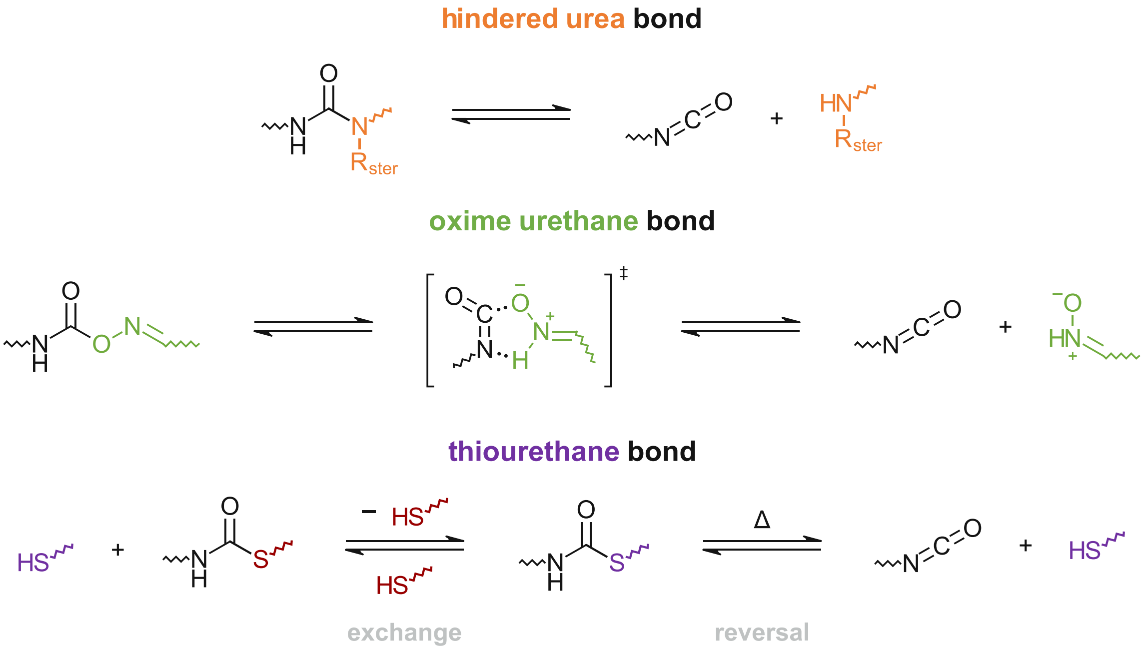

Scheme 3: Dynamic equilibrium of hindered urea bonds with a sterically demanding substituent R_{ster} (orange), oxime urethane bonds with a stabilized transition state ‡ (green), and thiourethane bonds (purple), which can engage in associative thiol exchange or, at elevated temperatures Δ, in dissociative bond reversal.

Through incorporation of DCBs into poly(urethane(urea))s, structurally dynamic polymers[116] can be produced. Such polymers respond to the environmental factors influencing the incorporated DCBs, which can result in macroscopic changes to their macromolecular architecture and composition. Such changes in the structure of polymers can also be referred to as macromolecular metamorphosis[117] since already established macromolecular architectures can be retroactively transformed into completely different ones e.g., segmented hyperbranched polymers into comb polymers. In covalent adaptable networks (CANs)[118] i.e., structurally dynamic thermosets, such dynamic features can further be used to enable otherwise unfeasible reprocessing, recycling or even self-healing.[108]

Structurally dynamic polymers can be used to prepare dynamic and reconfigurable materials,[119] which show great potential as functional materials[120, 121] e.g., for sensors and actuators,[116] due to their high responsiveness to specific physical and chemical stimuli. For structural materials[122], structurally dynamic polymers can further improve processing or introduce self-healing properties as already mentioned with CANs. Also, the degradation behavior of materials can be influenced[123] or mechanical properties such as material strength can be enhanced as *Ehrmann*[23] was able to demonstrate for TPU(U)s in a process termed self-reinforcement. By converting one of the binding partners of DCBs in their disassociated state and breaking the DCB, it is also possible to cleave off smaller moieties from structurally dynamic polymers, which has potential uses in targeted drug delivery.[124]

Objective

Thermoplastic poly(urethane(urea)) elastomers are a versatile class of polymers, which are used in various applications ranging from commodities to high-tech components. Their excellent mechanical properties mixed with a good processibility makes them particularly promising in the field of tissue engineering, where they can be used to substitute tissue in vascular grafts.

To withstand the high internal blood pressure as well as the periodic pressure change of such applications, tough materials are required. In case of poly(urethane(urea))s, the mechanical properties of the material can be simply improved by incorporating more urea bonds into the polymer chain. This, however, worsens processibility. Previous findings in our research were able to relieve that issue by introducing dynamic bonds into the polymer chain like hindered urea bonds or oxime urethane bonds. The dynamic nature of these bonds can then be used to form urea bonds after processing to achieve self-reinforcement of the material prior or during application. Furthermore, as part of this self-reinforcement, small molecules are released, which can be potentially used for targeted release of small-molecule drugs at application site.

Aim of this thesis is to find out, whether incorporation of multiple different dynamic bond species into thermoplastic poly(urethane(urea)) elastomer chains is possible and what consequences this has on the properties and the self-reinforcement of the final material. To evaluate the suitability of these polymers for applications such as vascular grafts, it is further necessary to establish working procedures for electrospinning of the synthesized thermoplastic poly(urethane(urea)) elastomers into their desired shape and introduce characterization methods for the electrospun materials regarding structure and mechanical properties. The goals of this thesis can consequently be summarized accordingly:

- reproduce previous findings regarding self-reinforcing thermoplastic poly(urethane(urea)) elastomers using either hindered urea bonds or oxime urethane bonds for direct comparison of the different systems and as reference material
- establish a synthetic procedure of new thermoplastic poly(urethane(urea)) elastomers containing both hindered urea bonds and oxime urethane bonds
- molecular and material characterization of these new thermoplastic poly(urethane(urea)) elastomers and comparison with the previous findings
- establish a working procedure for electrospinning of thermoplastic poly(urethane(urea)) elastomers on the available electrospinning
- establish characterization methods for electrospun thermoplastic poly(urethane(urea)) elastomers regarding structure, dimensions, and mechanical properties in tubular shape

State of the art

The cardiovascular system, responsible for blood circulation, is one of the most important systems in the human body. As such, cardiovascular diseases (CVD)s can be particularly dangerous and are consequently one of the leading causes of death worldwide.[6] One such CVD, atherosclerosis, results from the accumulation of material like lipids and fibrous elements in blood vessels. This causes stenosis and occlusion of the blood vessel, which impedes blood flow and may result in tissue ischemia and strokes.[125] While preventative measures against atherosclerosis can be taken, such as the minimization of risk factors (e.g., diet or sedentariness) or lipid-lowering medication (statins),[6, 11] severe cases require surgical intervention using stents or bypasses.

Stents have the advantage of not requiring a complex surgery, instead stents are inserted percutaneously from an arterial entry site and transferred to their destination from there.[126] However, risks of restenosis and acute thrombosis often necessitate a bypass (i.e. vascular graft), which requires a more rigorous surgical intervention, but demonstrates a higher efficacy over time without the need for additional revascularization procedures.[127] In case of bypasses, it is important that the bypass material is able to assume the functions of the blood vessel it is replacing without being rejected by the body. Consequently, autografts or allografts of suitable blood vessels would be ideal. Unfortunately, donatable tissue is often not available, which creates a need for synthetic substitutes.[128]

Given the flexibility of blood vessels, polymer materials are an obvious choice for such synthetic substitutes with materials such as *Dacron*© (poly(ethylene terephthalate)) and *Gore-Tex*© (poly(1,1,2,2-tetrafluoroethylene)) being already in use for large-diameter vascular grafts.[15] Their chemical structures are depicted in Figure 14. However, these materials are so far unsuitable for vascular grafts of smaller diameter (< 6 mm) due to insufficient biocompatibility.[16] Also mechanically, synthetic vascular grafts do not match native tissue, particularly regarding compliance, which further contributes to graft failure.[129] Ongoing research tries to address this issue by looking into alternative polymer classes such as poly(urethane(urea))s, which are biocompatible and demonstrate suitable mechanical properties.[130]

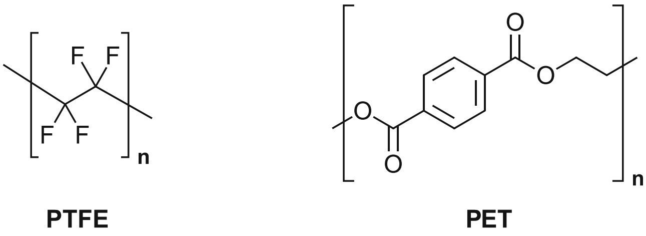

Figure 14: Chemical structures of poly(1,1,2,2-tetrafluoroethylene) (PTFE) and poly(ethylene terephthalate) (PET).

Poly(urethane(urea))s are polymers prepared *via* polyaddition of multifunctional isocyanates with monomers containing multiple functional groups with active hydrogens like alcohols or amines. These polymers can occur as networks but also as chains, depending whether only difunctional monomers are present. In case of polymer chains, poly(urethane(urea)) materials become thermoplastic elastomers (TPU(U)s) due to physical crosslinking of the urethane and urea bonds *via* hydrogen bonding. This gives TPU(U)s rubbery properties, while still allowing dissolution and melting of the material for processing, making them an attractive material class for various applications ranging from shoe soles and cable jackets over industrial tubing to various medical applications.[102, 131]

Synthesis of TPU(U)s often follows a prepolymer approach, where different monomer species are added stepwise to the reaction forming increasingly larger prepolymer chains that are subsequently linked together in the final addition step.[102] This enables the synthesis of structurally segmented TPU(U)s: Soft segments, which add flexibility to TPU(U)s are introduced through telechelic polyols like polyethers, polyesters, and polycarbonates (see Figure 15).[99, 132] The introduction of ester groups can thereby be used to improve degradability through ester hydrolysis or multiblock copolymer formation, while polyethers are more hydrolytically stable.

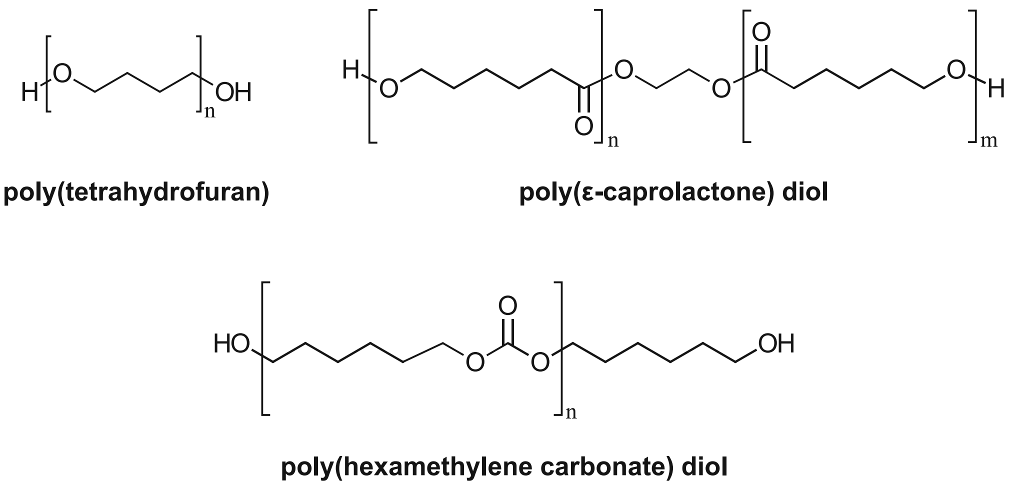

Figure 15: Chemical structures of common macrodiols used in synthesis of thermoplastic poly(urethane(urea)) elastomers.

Hard segments, responsible for physical crosslinking between the poly(urethane(urea)) chains, are formed by low molecular weight diisocyanates and difunctional chain extenders (CE) based on amines or alcohols. Regarding diisocyanates, aromatic species like methylene diphenyl diisocyanates are commonly used, which provide excellent mechanical properties. However, for biomedical applications, their potentially carcinogenic degradation products[133, 134] make aromatic diisocyanates less viable. In such cases, aliphatic diisocyanates like hexamethylene diisocyanate are more commonly used.[99] Chemical structures of common aliphatic and aromatic diisocyanates are depicted in Figure 16.

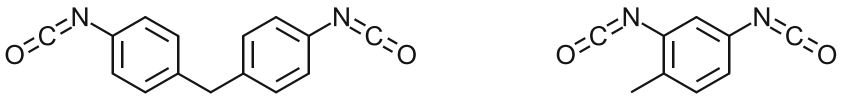

4,4′-methylene diphenyl diisocyanate **toluene diisocyanate**

hexamethylene diisocyanate **4,4′-diisocyanato dicyclohexylmethane**

Figure 16: Chemical structures of common aromatic and aliphatic diisocyanates used in synthesis of thermoplastic poly(urethane(urea)) elastomers.

CEs are used to set the length of hard segments and the strength of physical crosslinking. While aliphatic diols like ethylene glycol and their resulting urethane bonds can be used to improve elasticity, the urea bonds formed by aliphatic diamines like putrescine improve tensile strength through strong crosslinkages due to bidentate hydrogen bonding.[99] Through the presence of ester[100] or carbonate[101] functionalities e.g., *via* bis(2-hydroxyethyl) terephthalate or bis(3-hydroxypropyl) carbonate, CEs can also be used to introduce cleavable bonds into TPU(U)s. Chemical structures of common diol, diamine, and degradable CEs are depicted in Figure 17.

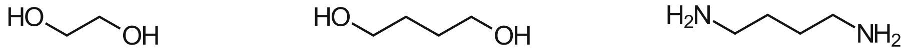

ethylene glycol **1,4-butanediol** **1,4-butanediamine (putrescine)**

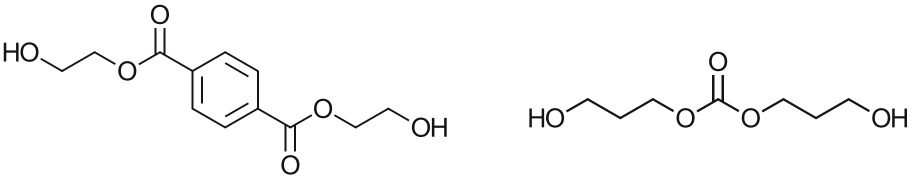

bis(2-hydroxyethyl) terephthalate **bis(3-hydroxypropyl) carbonate**

Figure 17: Chemical structures of common alcohol or amine based difunctional chain extenders used in synthesis of thermoplastic poly(urethane(urea)) elastomers.

Given the variety of available monomers, the material properties of TPU(U)s can be easily modified by variation of monomers and their ratios. It further allows the introduction of additional functionalities. As already mentioned, the incorporation of ester and carbonate bonds through macrodiols or CEs can be used to influence degradability. The inclusion of aromatic moieties and urea bonds can improve tensile strength, aliphatic moieties improve elasticity and processibility, and the use of ethers can influence hydrophilicity.

Due to this customizability, it is also possible to incorporate dynamic covalent bonds (DCBs) into TPU(U)s to prepare structurally dynamic polymers and materials. These DCBs can thereby be introduced as components of the monomer, such as disulfide bonds[135] and boronic acid esters,[123] or formed during synthesis, such as dynamic hindered urea bonds[109] and oxime urethane bonds.[111] The resulting structurally dynamic polymers can enable self-healing,[110, 136] or improve heat resistance.[137]

Through the conscious incorporation of different DCB species and exploitation of the chemistries of neighboring functional groups, it is further possible to significantly alter the structure of TPU(U)s *in situ* through macromolecular metamorphosis.[117] This was recently demonstrated within our research group by *Schwarzl et al.*[123], who were able to demonstrate that a thermoplastic poly((thio)urethane) can be transformed into a crosslinked network under hydrolytic conditions through deliberate combination of a dynamic boronic acid ester and thiourethane bond together with thioglycerol (see Scheme 4). By introducing this crosslinking mechanism subsequently into hydrolytically degradable materials, the loss in mechanical properties during degradation can be offset.

A similar process termed self-reinforcement was also developed within our research group by *Ehrmann*[23] to improve the mechanical strength of TPU(U)s without compromising on the processibility of the material: Given that higher strengths in TPU(U)s are achieved by increasing physical crosslinking,[104] but stronger physical crosslinking impedes melting or dissolution of the material,[138] the achievable mechanical properties for a given application are limited by the required processibility. To circumvent this, weakly crosslinking dynamic urethane and urea bonds are initially incorporated into the polymer chain during synthesis. After processing, these bonds are then converted into strongly crosslinking urea bonds, which engage in bidentate hydrogen bonding[104, 139] and lead to a significant increase in the mechanical strength of the material.

The DCBs initially used to demonstrate this self-reinforcement phenomenon were hindered urea bonds (HUBs) with a sterically demanding N-substituent, which destabilizes the urea bond and causes its dynamic nature.[110] In their disassociated state, HUBs form free isocyanates, which can react with moisture in the environment under elimination of CO_2 to form an amine. If a second free isocyanate is then in close proximity to this amine, a urea bond between the two can be established resulting in the aforementioned self-reinforcement. However, this process is not just limited to HUBs and *Ableidinger*[140] could make similar observations with dynamic oxime urethanes (OUBs), which derive their dynamic nature from a favorable transition state.[111] The reaction schemes responsible for self-reinforcement involving either HUBs or OUBs is depicted in Scheme 5.

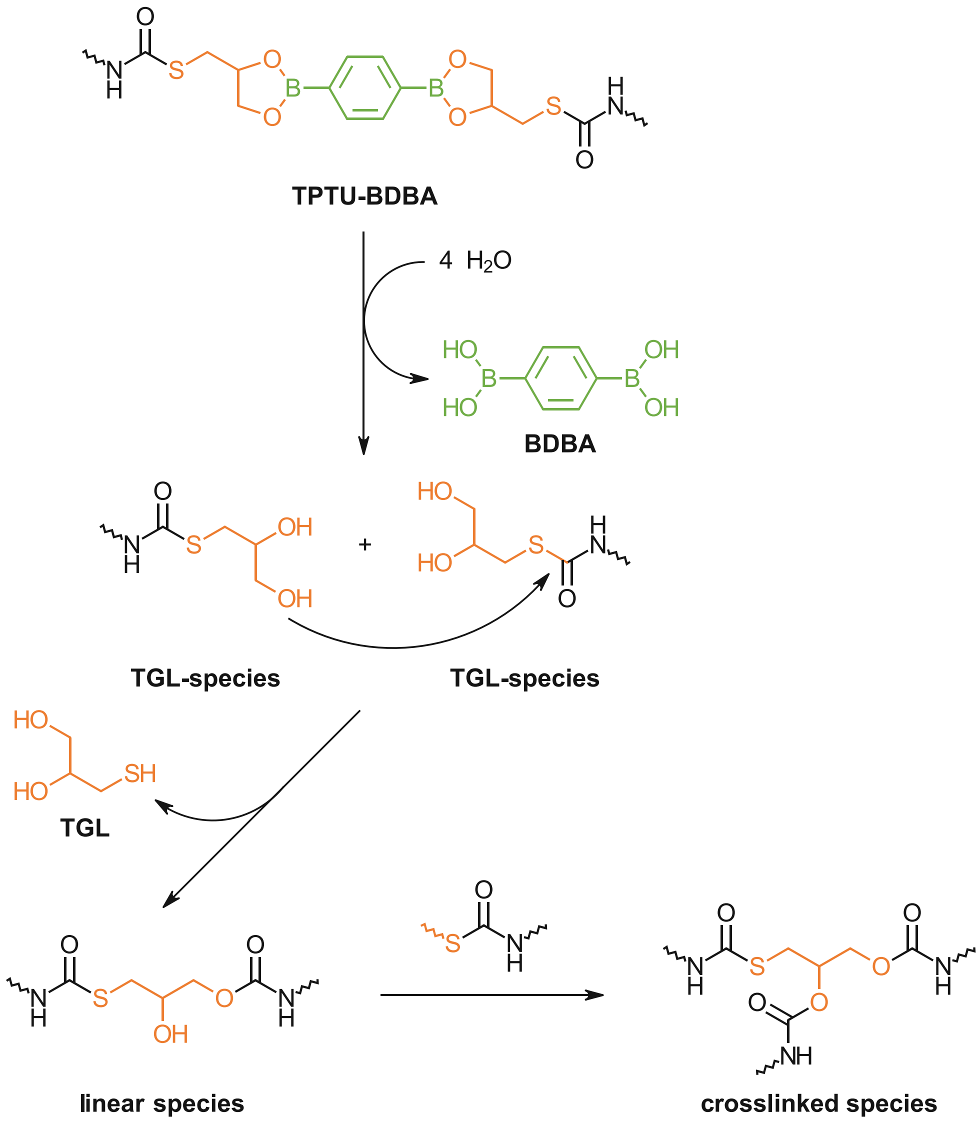

Scheme 4: Macromolecular metamorphosis of a thermoplastic poly((thio)urethane) (TPTU-BDBA) into a crosslinked network by hydrolytic cleavage of benzene-1,4-diboronic acid (BDBA) and dynamic thiol exchange through thioglycerol (TGA). Scheme reproduced from Schwarzl et al.[123]

Since hydrolysis of the dissociated isocyanate breaks the corresponding dynamic urethane or urea bond, this process may also be used to introduce cleavable moieties into the polymer chain, which can be released as a byproduct of *in situ* urea formation (see Figure 18). This also offers potential uses in targeted drug delivery by loading the polymer with bioactive substances, adding to the growing field of polymer-drug conjugates.[124, 141] For such applications OUBs are of particular interest given the prominent role of oximes in different pharmaceuticals e.g., as cholinesterase reactivators.[142, 143]

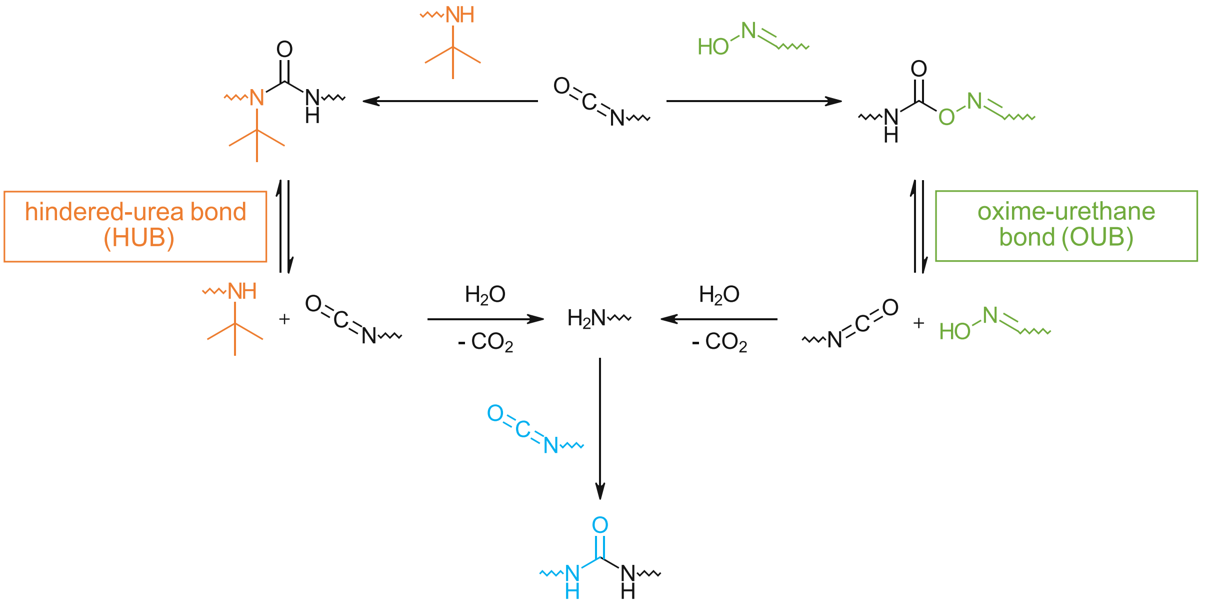

Scheme 5: Self-reinforcement effect via dynamic hindered-urea bond (orange) or aldoxime-urethane bond (orange) via formation of a urea bond through hydrolysis of the free isocyanate (black) with water from the environment followed by an addition reaction with a second free isocyanate (blue).

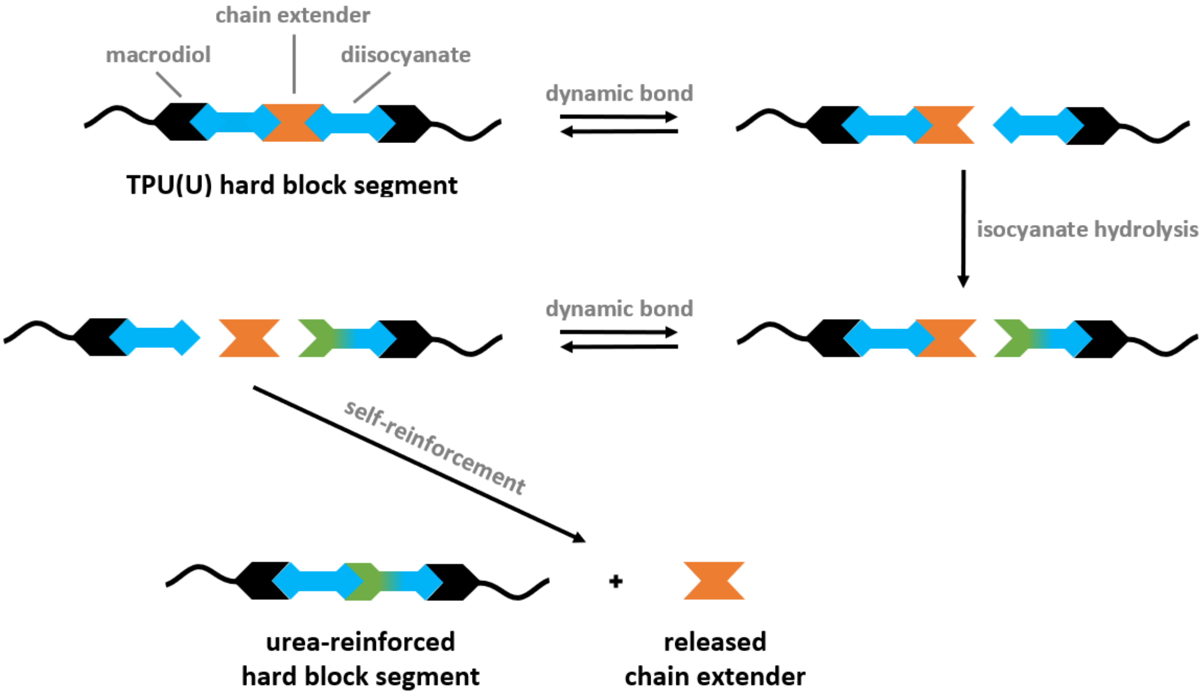

Figure 18: Functional principle of the self-reinforcement in TPU(U) hard block segments and the targeted release of dynamically incorporated chain extenders (orange) through moisture in the environment.

Apart from the molecular composition of the material, its physical structure is also important to consider. To mimic the extracellular matrix of blood vessels, microfibrous graft structures have proven effective. The most common method to prepare such fibrous scaffolds is electrospinning, where a feed of liquid fiber precursor, typically a solution, is distorted into a very thin jet using a strong electric field, which subsequently solidifies by physical means.[144-146]

Due to a difficult setup, low production rates, and a large number of influencing factors – viscosity of the fiber precursor, precursor feed rate, applied electric field strength, … – electrospinning remained less viable in the past. However, recent advances in solvent-free melt-electrospinning,[73, 74] core-shell-structured coaxial electrospinning[147] and especially the emergence of scalable needleless electrospinning,[148] led to an increasing interest in this method not only for special applications but potentially also the fabrication of more common industrial and consumer goods. This also coincides with a growing market for industrial nonwoven fabrics[54], which represents an increasing number of potential customers for electrospun products.

Applications of electrospun products are onot just limited to tissue engineering and vascular grafts.[69] *Wu et al.* recently produced a self-cooling textile using electrospinning, which is able to emit heat *via* radiative cooling, to tackle issues concerning increasing global temperatures.[149] Given the large surface to volume ratio of fibers in the micrometer to nanometer range as well as a high porosity, electrospun materials also find use in air filtration[150], fuel cell membranes[151], sensors (e.g. for glucose),[152] and fast stimuli-responsive materials (e.g. for biofabrication)[153]. Electrospinning is also useful to prepare inorganic fibers[154] as demonstrated by *Wang et al.,*[155] which were able to prepare porous TiO_2-SiO_2 fibers with high photocatalytic activity for the degradation of organic pollutants. Such inorganic electrospun fibers can further be used as catalyst supports[156] or electrodes.[157]

In case of vascular grafts, electrospinning is already well established with both synthetic (e.g., poly(esters) and poly(urethanes)) and natural materials (e.g., collagen, fibroin, silk, and elastin) as well as their blends.[158, 159] With TPU(U)s in particular, even successful animal testing on rats has already been performed by *Bergmeister et al.*[160] using commercially available *Pellethane 2363-80A* with a patency rates above 95 % and visible cell ingrowth within 7 days. However, adequate biomechanical properties in combination with sufficient graft healing remain an issue: Using an auxiliary electrical field *Grasl et al.*[161] were recently able to further improve compliance of electrospun grafts prepared from TPU(U) and poly(lactic acid) by introducing a preferential fiber orientation. In a recent collaboration with our research group, *Rohringer et al.*[162] prepared bioresorbable small-diameter synthetic vascular grafts using aforementioned self-reinforcing TPU(U)s. These grafts intend to facilitate the growth of natural tissue, which slowly replaces the degrading synthetic scaffold. Meanwhile, self-reinforcement of the material ensures sufficient biomechanical properties for the vascular graft until the newly formed tissue supports itself.

Results and Discussion

1. Polymer synthesis and characterization

1.1. Preparation of the reagents

1.1.1. Substance overview

As discussed in the Introduction in chapter 5.2, the primary components for the synthesis of thermoplastic poly(urethane(urea)) elastomers (**TPU(U)**) are macrodiols, diisocyanates, and chain extenders (**CE**). In the context of this work, poly(tetrahydrofuran) (**pTHF**) served as a macrodiol, and hexamethylene diisocyanate (**HMDI**) as diisocyanate for all synthesized TPU(U)s. As chain extenders, the diol bis(2-hydroxyethyl) terephthalate (**BHET**), the diamine *N,N′*-di-*tert*-butylethylenediamine (**TBEDA**), and the dioximes, bis(4-hydroxybenzaldehyde oxime)fumarate (**HBOF**) and bis(4-hydroxybenzaldehyde oxime)succinate (**HBOS**) were used in different ratios for the different TPU(U)s. The polyaddition of these reagents is performed in solution with *N,N'*-dimethylformamide (**DMF**) as a solvent in the presence of stannous octoate (**$Sn(Oct)_2$**). The chemical structures of all substances are depicted in Figure 20. pTHF, HMDI, BHET, TBEDA, DMF, and $Sn(Oct)_2$ were thereby obtained commercially, while HBOF and HBOS were adopted from Klaus Ableidinger, who synthesized them during his diploma thesis.[140]

As a commercial reference TPU(U) *Pellethane® 2363-80A* (**Pell**) was chosen, which is comprised of the following monomers: The macrodiol pTHF, the aromatic diisocyanate 4,4'-methylene diphenyl diisocyanate and the aliphatic chain extender 1,4-butanediol. The chemical structures of these monomers are depicted in Figure 19.

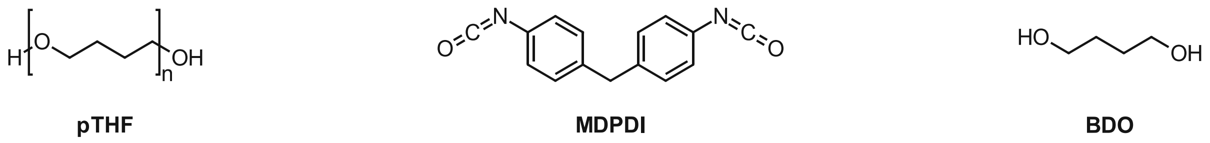

Figure 19: Chemical structures of the monomers poly(tetrahydrofuran) (pTHF), 4,4'-methylene diphenyl diisocyanate (MDPDI) and 1,4-butanediol (BDO) comprising the commercial TPU(U) Pellethane® 2363-80A

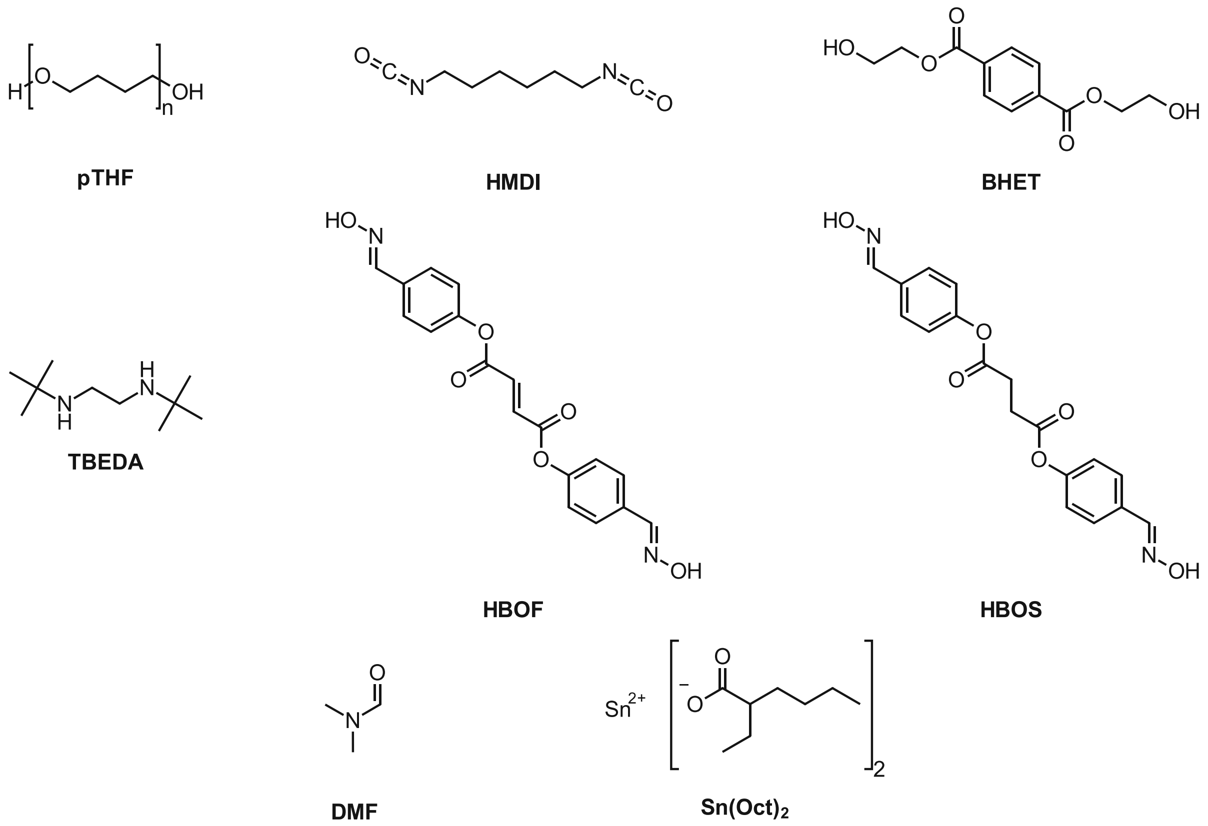

Figure 20: Chemical structures of the substances used during thermoplastic poly(urethane(urea) elastomer synthesis: poly(tetrahydrofuran) (pTHF), hexamethylene diisocyanate (HMDI), bis(2-hydroxyethyl) terephthalate (BHET), N,N'-di-tert-butylethylenediamine (TBEDA), bis(4-hydroxybenzaldehyde oxime)fumarate (HBOF), bis(4-hydroxy-benzaldehyde oxime)succinate (HBOS), N,N'-dimethylformamide (DMF), stannous octoate ($Sn(Oct)_2$).

1.1.2. Purification and water content of reagents

Given the importance of an exact stoichiometry for a successful TPU(U) synthesis, the used reagents and solvents must be of high purity. For this, it was necessary to recrystallize BHET in deionized water, and HMDI and TBEDA were distilled under reduced pressure shortly before use. All other substances were deemed to be of sufficient purity based on ^{1}H-NMR measurements.

Among impurities, moisture is also especially important to consider, given that isocyanates react with water in their environment as established in Introduction chapter 5.2. While this reaction is desired later for self-reinforcement of the synthesized TPU(U)s (see Introduction chapter 5.3), it is fatal during their synthesis due to the decrease in free isocyanate groups available for polyaddition. Therefore, it is essential to minimize residual moisture in the reagents, especially in case of the macrodiol pTHF due to their high molecular weight, and the solvent DMF because of the comparatively large amounts used in the reaction.

Drying of pTHF, and the solid chain extenders BHET, HBOF, and HBOS were performed under high vacuum. HMDI, and TBEDA were distilled prior to use under reduced pressure, and stored under N_2 atmosphere. DMF was used in the quality it was obtained. To measure the water content, coulometric Karl Fischer titration was performed using an *Enviortech CA-21* moisture meter. Liquid substances were measured directly, while solid substances were measured in solution with dry DMF. As an upper threshold, a water content of 50 ppm (w/w) was targeted in accordance with prior work done by Markus Fitzka.[163]

1.1.3. Molecular weight determination of poly(tetrahydrofuran)

To ensure an exact stoichiometry and by extent a successful TPU(U) synthesis, precise weighing of the monomers is essential. This requires an accurate molecular weight, to establish a correct conversion between the mass and the amount of substance.

For smaller molecules, with a known and discrete molecular formular like HMDI or BHET, the molecular weight can be determined by adding the average atomic masses of the individual atoms together. In the case of macromolecules, however, substances do not have a singular molecular formula, since the contained molecules usually have a range of different sizes due to their way of synthesis. As a result, the molecular weight of macromolecular substances follows a distribution function (see Figure 21) characterized by a maximum, the number average molecular weight ($\boldsymbol{\overline{M_n}}$), and a width, represented by the weight average molecular weight ($\boldsymbol{\overline{M_w}}$), and the polydispersity index ($\boldsymbol{PDI}$), which can be defined by Eq. 2 to Eq. 4.[164, 165] Therefore, the appropriate molecular weight of a macromolecular substance for reaction approaches has to be determined by other means than simple addition and in accordance with desired characteristics.

$$\overline{M_n} = \frac{\sum_i N_i M_i}{\sum_i N_i} \qquad \textit{Eq. 2}$$

$$\overline{M_w} = \frac{\sum_i N_i M_i^2}{\sum_i N_i M_i} \qquad \textit{Eq. 3}$$

$$PDI = \frac{M_w}{M_n} \qquad \textit{Eq. 4}$$

N_i … number of molecules of size I (-)

M_i … molecular weight of molecules of size I (g mol^{-1})

$\overline{M_n}$ … number average molecular weight (g mol^{-1})

$\overline{M_w}$ … weight average molecular weight (g mol^{-1})

PDI … polydispersity (-)

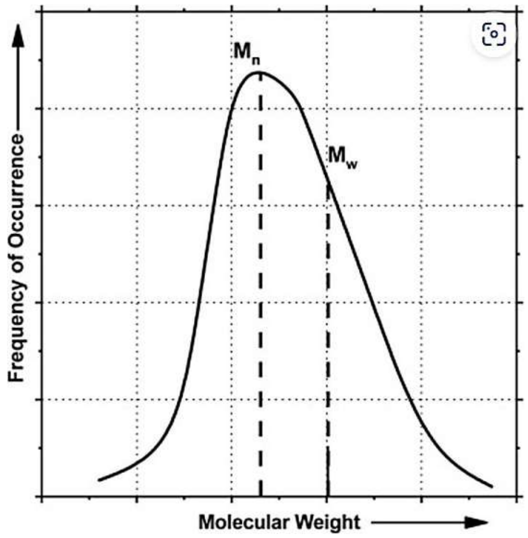

Figure 21: Diagram of a hypothetical molecular weight distribution of a macromolecular substance corresponding to their frequency of occurrence. M_n *refers to the number average molecular weight and is the distribution maximum.* M_w *is the weight average molecular weight and considers not only the number of molecules in a substance but also their size.*[164]

For TPU(U) synthesis, the molecular weight of the macrodiol is of interest to determine the number of hydroxy groups linked to it in a given amount of substance. The used macrodiol pTHF has two hydroxy groups, one at either end of the polyether chain, which allows the calculation of the molecular weight by determination of the number of present hydroxy groups. This was accomplished through quantitative ^{31}P-NMR spectroscopy, or through determination of the hydroxyl value by acid-base titration. For reference, the producer's certificate of analysis for the used pTHF (product number: *345296*, batch number: *MKCM7483*) cites a molecular number of 997 Da and a hydroxyl value of 112.5 mg KOH g^{-1} for a specification range of 950 – 1050 Da and 107.0 – 118.0 mg KOH g^{-1}.

1.1.3.1. Hydroxyl value

Determination of the molecular weight of pTHF *via* its hydroxyl value was performed according to DIN 53240-1 standard.[166] In this procedure, 1 eq. macrodiol is acetylated with excess acetic anhydride dissolved in dry pyridine following Scheme 6. After hydrolysis of the remaining acetic anhydride with deionized water, the number of acetyl units bound by pTHF was determined *via* automated back titration of the free acetic acid with 0.5 N methanolic potassium hydroxide solution (KOH). The titration measurements were performed using a *Metrohm 848 Titrino Plus*. Equivalence point detection was done *via* pH electrode. A titer of 0.963 was determined prior *via* titration of benzoic acid as primary titer substance dissolved in methanol.

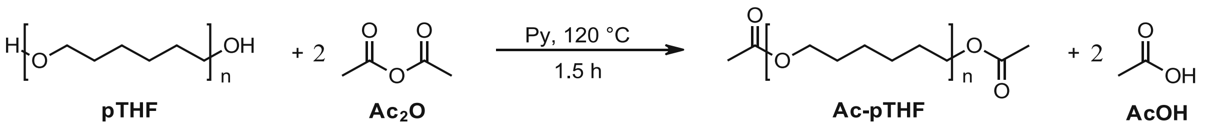

Scheme 6: Acetylation of poly(tetrahydrofuran) (pTHF) into Ac-pTHF through acetic anhydride (Ac_2O) under elimination of acetic acid (AcOH) in the presence of pyridine (Py)

In total, three measurements were taken each for titer determination, blank consumption and sample consumption. Representative titration curves of benzoic acid, pure methanol and acetic acid are depicted in Figure 22. The many smaller equivalence points seen in the plot for benzoic acid on the left were set by the software and not considered for titer determination.

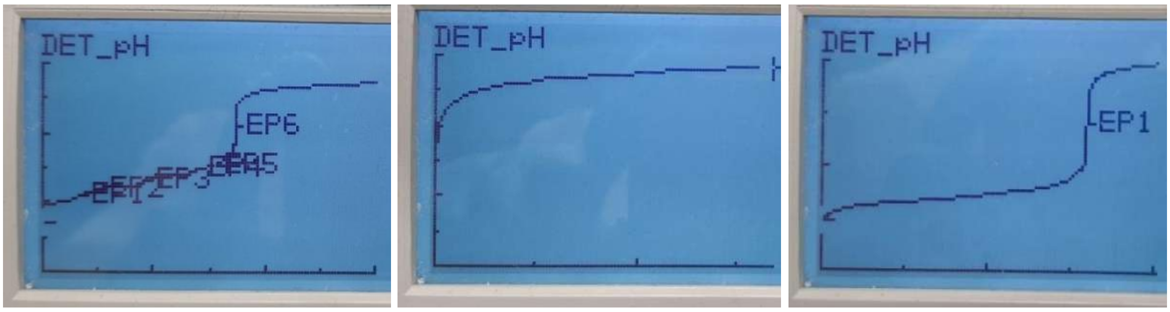

Figure 22: Titration curves regarding volume of consumed titrant 0.5 N methanolic potassium hydroxide solution plotted against measured pH for primary titer substance benzoic acid (left), pure methanol (center) and acetic acid (right). 'EP's mark detected equivalence points by the device.

Based on the weighed mass of the sample, the measured titer, and the titrant consumption of blanks as well as of samples, an average hydroxyl value (OHV) of 112.2 ± 0.6 mg g^{-1} and an average number average molecular weight ($\overline{M_n^{OHV}}$) of 1.001 ± 0.005 kDa were determined for the macrodiol pTHF.

1.1.3.2. Quantitative ^{31}P-NMR spectroscopy

The molecular weight of pTHF was also determined *via* quantitative ^{31}P-NMR spectroscopy through phosphorylation of the hydroxy groups using excess 2-chloro-4,4,5,5-tetramethyl-1,3,2-dioxaphospholane (TMDP). The formed P-substituents at the chain ends of pTHF subsequently produce sharp signals in ^{31}P-NMR, that can be quantified using an alcoholic internal standard like cyclohexanol. While this procedure is particularly useful in lignin and polysaccharide analysis[167, 168], where ^{1}H-NMR spectroscopy produces complex spectra, it is also well-suited for the characterization of macrodiols like pTHF, where it excels regarding speed and small sample consumption. A reaction overview of the phosphorylation of pTHF is depicted in Scheme 7. Possible structures and their corresponding chemical shifts in the ^{31}P-NMR spectrum are depicted in Figure 23.

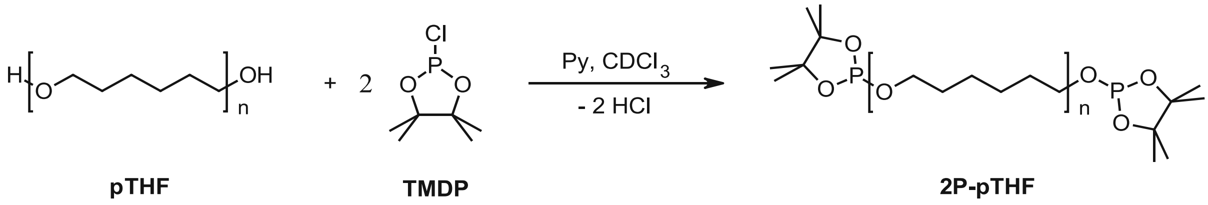

Scheme 7: Phosphorylation of poly(tetrahydrofuran) (pTHF) via 2-chloro-4,4,5,5-tetramethyl-1,3,2-dioxaphospholane (TMDP) under elimination of hydrogen chloride (HCl) in the presence of deuterated chloroform (CDCl₃) and pyridine (Py)

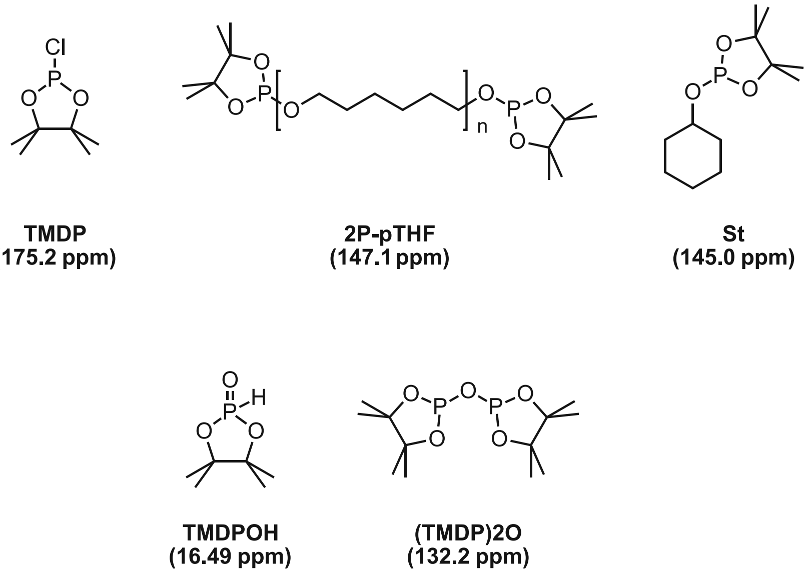

Figure 23: Chemical structures and corresponding shifts visible in the ^{31}P-NMR spectrum of the phosphorylation agent 2-chloro-4,4,5,5-tetramethyl-1,3,2-dioxaphospholane (TMDP) and its hydrolysis products (TMDPOH, (TMDP)2O), the phosphorylated poly(tetrahydrofuran) (2P-pTHF), and the phosphorylated cyclohexanol standard (St).

Sample preparation involved the mixing of dry pTHF dissolved in chloroform-d ($CDCl_3$) with a defined amount of cyclohexanol as internal standard, pyridine for HCl scavenging and an excess of the phosphorylation agent TMDP. To improve NMR resolution the relaxing agent chromium(III)acetylacetonate was also added. After a brief reaction period, the resulting mixture was measured at a 600 MHz NMR-spectrometer. The entire experiment was performed twice. Based on the weighed mass of the sample, and the measured integrals of the phosphorylated pTHF and cyclohexanol, an average molecular weight $\overline{M_n^{31P}}$ of 1.01 ± 0.01 kDa was calculated.

1.1.3.3. Summary and comparison

The $\overline{\mathrm{M_n}}$ of pTHF ultimately used for synthesis of TPU(U)s was determined *via* comparison of the available values: Table 2 summarizes the individual $\overline{\mathrm{M_n}}$ provided by the manufacturer (see chapter 1.1.3) and determined through the hydroxyl value of the available pTHF (see chapter 1.1.3.1) as well as quantitative ^{31}P-NMR (see chapter 1.1.3.2). All available molecular weights demonstrate similar values with the manufacturer citing a mean slightly below 1 kDa, while the $\overline{\mathrm{M_n}}$ determined through the hydroxyl value and ^{31}P-NMR have their mean slightly above 1 kDa. Consequently, a $\overline{\mathrm{M_n}}$ of 1 kDa was chosen for pTHF and used in the approaches of all subsequent reactions.

Table 2: Summary of the number average molecular weights ($\overline{M_n}$) provided by the manufacturer or determined either via hydroxyl value or quantitative ^{31}P-NMR.

Source	**$\overline{M_n}$ (kDa)**
manufacturer	0.997
hydroxyl value determination	1.001 ± 0.005
quantitative ^{31}P-NMR	1.01 ± 0.01

1.2. Synthesis of reference polymers

1.2.1. General procedure

As established in Introduction chapter 5.2, synthesis of thermoplastic poly(urethane(urea)) elastomers (**TPU(U)**) can follow either a one-shot approach, where all monomers are added at once, or a prepolymer approach, where the different monomer species are added step-wise to the mixture. In this thesis, a multi-shot approach was favored for greater control over reaction proceedings, given the amount of different monomer species used in synthesis.

TPU(U) synthesis follows a general procedure from literature using a prepolymer approach.[169] Prior to synthesis, all reagents and solvents are prepared according to chapter 1.1. For the approach, all weigh-ins are adjusted to the amount of used pTHF. As a reaction vessel, a dry three-necked round-bottom flask equipped with stirring bar, a stop-cock, and two glass plugs is used. It is assembled hot and set under N_2 atmosphere. To avoid moisture from the environment during transfers, conventional Schlenk techniques are employed.

As already mentioned, the synthesis takes place stepwise. First, 1 eq. of dry pTHF is mixed with 2 eq. of freshly distilled HMDI dissolved in dry DMF and 3 drops of $Sn(Oct)_2$, and stirred for 3 h at 60 °C. Afterwards, a total of 1 eq. of chain extenders (**CE**) dissolved in dry DMF are added: In case of a singular CE species this addition occurs at once. In case of multiple CE species, the different CEs are added sequentially, with breaks greater than 3 h in between. After addition of the last chain extender, the reaction is left stirring at set temperature overnight. For work-up, the reaction is cooled back down to room temperature and felled in dry diethyl ether (Et_2O), leading to precipitate formation.

A general reaction scheme for synthesis of a TPU(U) with up to 3 CEs is depicted in Scheme 8 excluding potential side products due to incomplete conversions, side reactions, or deviations from stoichiometric ratios. For systems with fewer CEs the scheme works by removing the relevant number of addition steps from the top down.

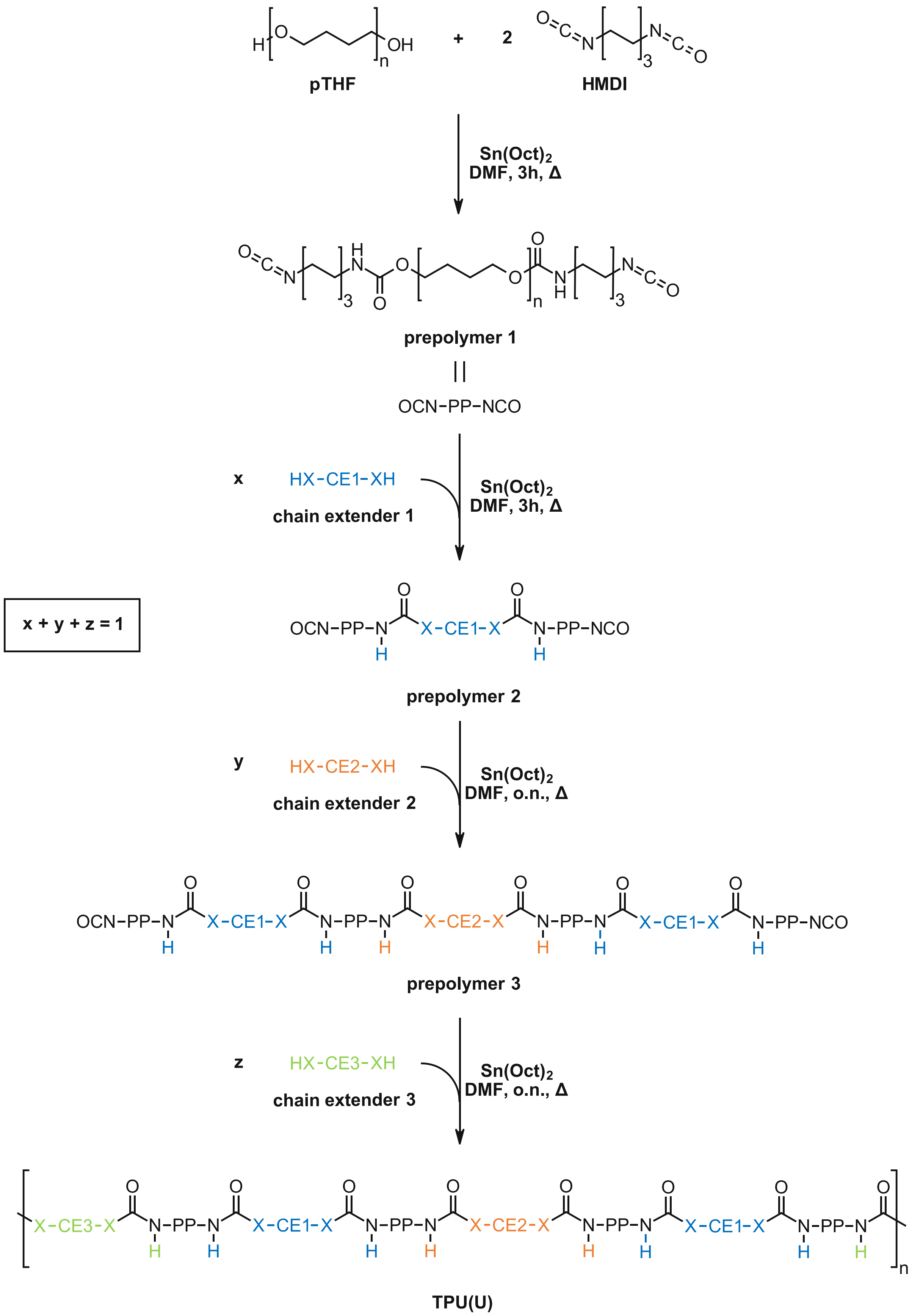

Scheme 8: General procedure for stepwise synthesis of thermoplastic poly(urethane(urea)) elastomers (TPU(U)) with 1 eq. macrodiol pTHF, 2 eq. diisocyanate HMDI, and up to three chain extenders (CE) adding up to 1 eq.

1.2.2. Synthesized polymers and yields

To characterize a TPU(U) containing three different chain extenders, references are required by which they can be compared. For that, already established TPU(U)s by Baudis[169], Ehrmann[23], and Ableidinger[140] were synthesized containing the chain extenders BHET, TBEDA, HBOS, and HBOF individually (**100BH**) or in pairs (**50TB, 25TB, 50HF, 50HS**). As benchmarks, three batches of the TPU(U) 100BH and two batches of 50TB were synthesized. 25TB, 50HF, and 50HS were synthesized once. For clarity, only batch 1 of 100BH and batch 1 of 50TB will be mentioned in this thesis, since these were used for the subsequent material characterization and for electrospinning. The TPU(U)s synthesized are summarized in Table 3 together with their yields.

Table 3: Summary of the synthesized reference thermoplastic poly(urethane(urea) elastomers (TPU(U)s) with their contained monomers (poly(tetrahydrofuran) (pTHF), hexamethylene diisocyanate (HMDI), bis(2-hydroxyethyl) terephthalate (BHET), N,N'-di-tert-butylethylenediamine (TBEDA), bis(4-hydroxybenzaldehyde oxime)fumarate (HBOF) and bis(4 hydroxy-benzaldehyde oxime)succinate (HBOS)), the ratio of these monomer in the reaction approach, and their yield after purification and drying.

TPU(U)	contained monomers	monomer ratio	yield (%)
100BH	pTHF, HMDI, BHET	1:2:1	85
50TB	pTHF, HMDI, BHET, TBEDA	1:2:0.5:0.5	73
25TB	pTHF, HMDI, BHET, TBEDA	1:2:0.75:0.25	71
50HS	pTHF, HMDI, BHET, HBOS	1:2:0.5:0.5	33
50HF	pTHF, HMDI, BHET, HBOF	1:2:0.5:0.5	38

All yields concur with literature.[23, 140, 169] However, yields of the TPU(U)s 50HS and 50HF are significantly lower than that of 100BH, 50TB, and 25TB. This may be the result of the used oxime-based CEs HBOS and HBOF, given that the yields of 50HS and 50HF are in a similar range, and could suggest an insufficient degree of polyaddition. To look into this, the molecular weight and chemical composition of the synthesized TPU(U)s need to be characterized.

1.2.3. Chemical composition

Based on the ^{1}H-NMR of the synthesized polymers, their chemical composition and degree of incorporation of the different chain extenders into the polymer chain can be determined. This is achieved by comparing sizes of integrals representing characteristic protons of the individual CEs. The shares of the different CEs present in the synthesized reference polymers are summarized in Figure 24 and compared with their theoretical shares (black bars) based on their weigh-in during synthesis.

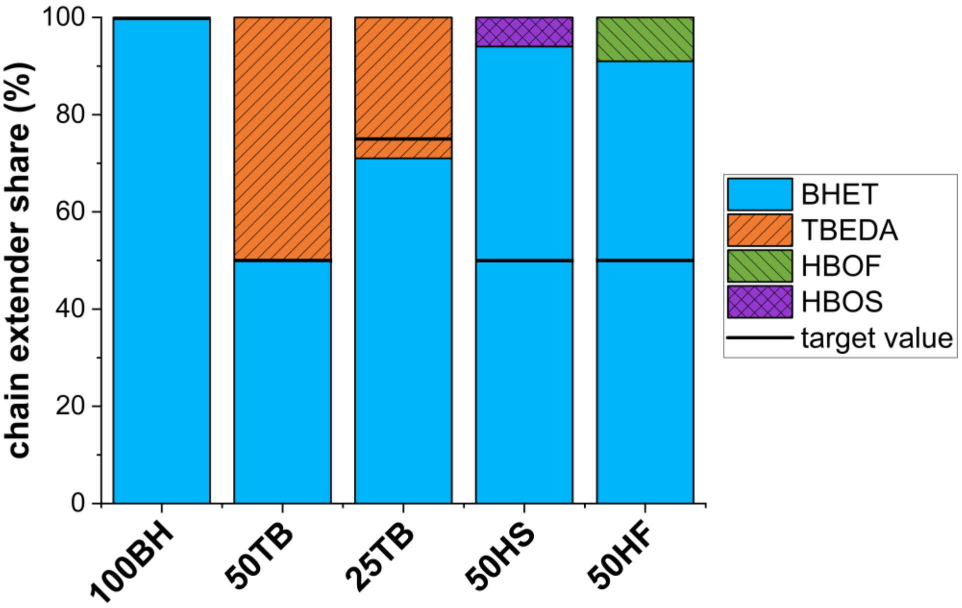

Figure 24: Share of the chain extenders bis(2-hydroxyethyl) terephthalate (BHET, blue), N,N'-di-tert-butylethylenediamine (TBEDA, orange), bis(4-hydroxybenzaldehyde oxime)fumarate (HBOF, green), and bis(4 hydroxy-benzaldehyde oxime)succinate (HBOS, purple) present in the synthesized reference TPU(U)s 100BH (batch 1), 50TB (batch 1), 25TB, 50HS, and 50HF. The black bars indicate the target values for chain extender share based on the weigh-ins of the chain extenders during synthesis.

Figure 24 shows that 100BH and 50TB match their theoretical target values. 25TB also resembles its theoretical composition. Its overrepresentation compared to the target share is likely due to the overlapping signals of the incorporated diisocyanate HMDI units. These are more intensive due to the higher prevalence of bound HMDI in the polymer chain relative to TBEDA especially in case of the TPU(U) 25TB (theoretical ratio of 8:1 between incorporated HMDI and TBEDA units).

In case of 50HS and 50HF, on the other hand, the calculated share of HBOS and HBOF is significantly lower than expected. This observation is in line with literature[140], where *Ableidinger* did not identify any signals of HBOS and HBOF in the measured ^{1}H-NMR spectrum. The lower amount of incorporated HBOS and HBOF coincides with the aforementioned lower yields of 50HS and 50HF compared to other synthesized TPU(U)s (see chapter 1.2.2) and could also suggest an insufficient degree of polyaddition.

1.2.4. Molecular weight

Apart from the chemical composition, which looks at the relative amount of the different monomer species incorporated into the polymer chain, the molecular weight of the synthesized polymers is an important factor to determine the success of a TPU(U) synthesis. As already discussed in chapter 1.1.3 in relation to the molecular weight of pTHF, determination of the molecular weight of polymeric substances requires additional considerations, since polymers within a given amount of macromolecular substance have different chain lengths. The distribution of these different chain lengths can be described through the number and weight-average molecular weight, $\overline{M_n}$ and $\overline{M_w}$ respectively.

Unlike the macrodiol pTHF, where only the number of hydroxy end groups in a given substance amount were of interest, not only the $\overline{M_n}$ but also the distribution width of the synthesized TPU(U)s are of interest. As such, a method is required, which can determine not only $\overline{M_n}$ but also $\overline{M_w}$. This was achieved *via* gel permeation chromatography (GPC) using both conventional calibration by external calibration with different polystyrene standards, and triple detection through change of the refractive index during measurement of different sample volumes. The results for both methods are depicted in Figure 25 for conventional calibration and Figure 26 for triple detection. For reference, $\overline{M_n}$ and $\overline{M_w}$ of the commercially-available TPU *Pellethane® 2363-80A* (Pell) was measured.

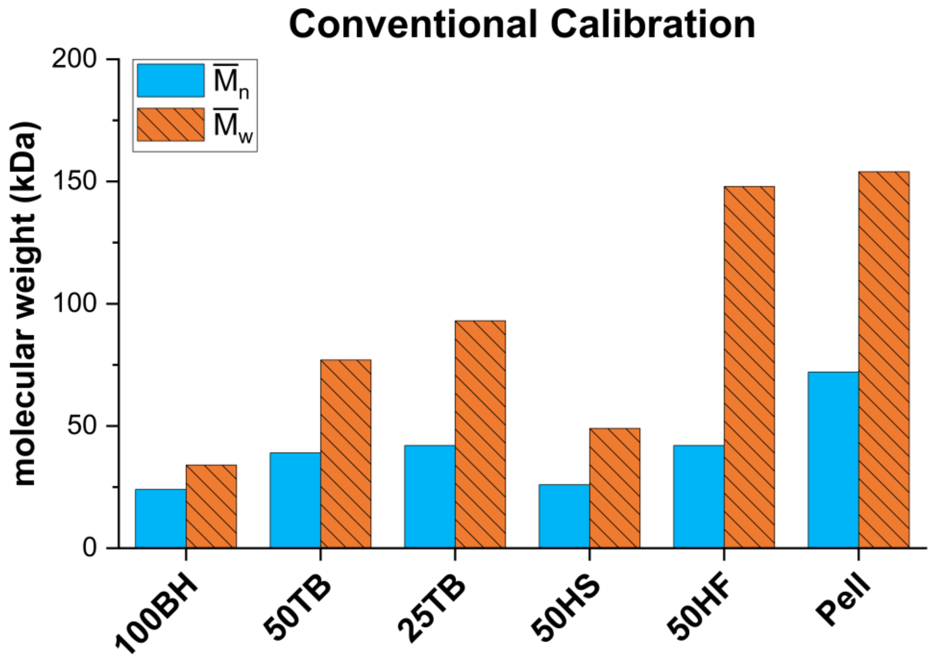

Figure 25: Number-average ($\overline{M_w}$) and weight-average ($\overline{M_w}$) molecular weights of the synthesized TPU(U)s 100BH (batch 1), 50TB (batch 1), 25TB, 50HS, 50HF, and the commercial TPU(U) Pellethane® 2363-80A (Pell) determined through gel permeation chromatography using conventional calibration.

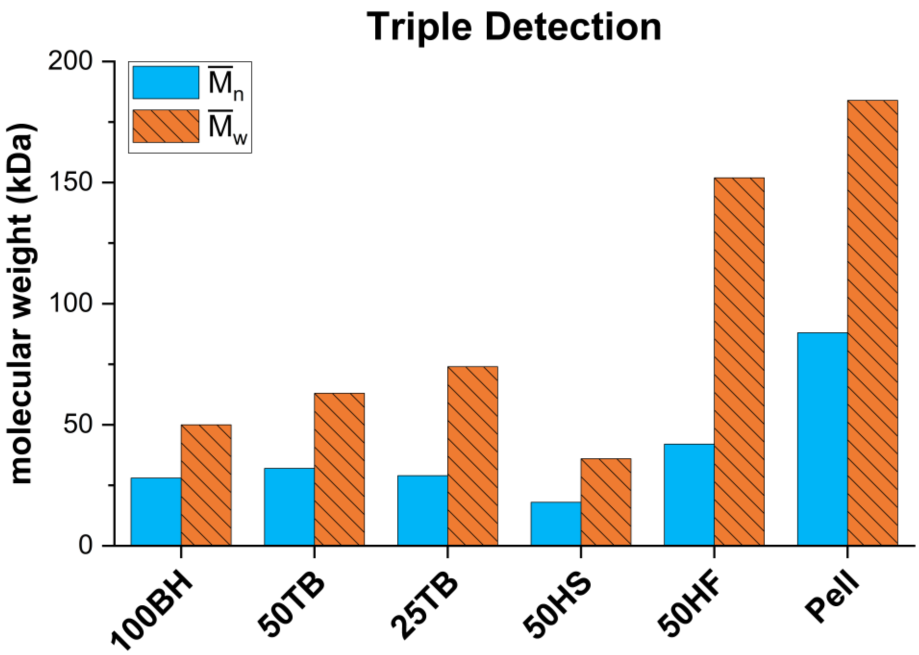

Figure 26: Number-average ($\overline{M}_n$) and weight-average ($\overline{M}_w$) molecular weights of the synthesized TPU(U)s 100BH (batch 1), 50TB (batch 1), 25TB, 50HS, 50HF, and the commercial TPU(U) Pellethane® 2363-80A (Pell) determined through gel permeation chromatography using triple detection.

The GPC results of the synthesized reference TPU(U)s depicted in Figure 25 and Figure 26 show, that all syntheses indeed produced polymers with $\overline{\mathrm{M}_\mathrm{n}}$ above 25 kDa or of 18 kDa in case of 50HS. The polydispersity index (PDI) of the synthesized TPU(U)s varies around 2.0 except for 50HF, where the PDI sits at around 3.6. Compared to the commercial reference Pell the synthesized reference TPU(U)s demonstrate a similar PDI, except for 50HF, but consistently lower molecular weights.

Overall, the measured molecular weights and PDI resemble literature values[140, 163], with exception of 50HF, which shows a significantly higher $\overline{\mathrm{M}_\mathrm{w}}$, not only to literature but also compared to the other synthesized reference TPU(U)s, regardless of method. This could be connected to its considerably poorer solubility in pure THF, and the addition of minor amounts of 1,1,1,3,3,3-hexafluoro-2-propanol (HFIP), but is otherwise unexpected, given the low yield (see chapter 1.2.2) and low incorporation of HBOF (see chapter 1.2.3), which would suggest lower molecular weights similar to 50HS. During the prolonged dissolution of 50HF, solvent may have evaporated leading to distortion of the results

1.3. Synthesis of oxime-containing polymers

1.3.1. Synthesized polymers and yields

As chapter 1.2.3 showed, the TPU(U)s of 50HF and 50HS showed very low incorporation of the dioxime chain extenders HBOF and HBOS in their chemical composition. One possible explanation could be an insufficient reaction time: A model reaction done by Ableidinger of monofunctional benzaldehyde oxime and hexylisocyanate to N-hexyl-N'-benzaldehyde oxime urethane yielded required 72 h at 40 °C to yield 20 % of product.[140]

To test this hypothesis, a second batch of 50HF was synthesized (**50HF32h**), where the reaction was left stirring for 32 h after addition of HBOF rather than just 12 h overnight. Thereby, 50HF was chosen because it demonstrated higher amounts of incorporated oxime-based CE as well as a higher molecular weight than 50HS.

Following this principle, TPU(U)s containing all three CEs – the diol BHET, the dioxime HBOF, and the diamine TBEDA – in a ratio of 2:1:1 were synthesized following general procedure (see 1.2.1). The addition sequence was first BHET, followed by HBOF to take into account its longer reaction time, and finally TBEDA. Two such TPU(U)s were prepared with reaction times of 24 h (**25HF25TB24h**) and 48 h (**25HF25TB48h**) after addition of the last CE.

Furthermore, one TPU(U) containing all three CEs was synthesized, where HBOF and TBEDA were added simultaneously in one step (**25HF25TB1st**). Here, an immediate orange discoloration (see Figure 27) of the solution could be observed, which stayed for the remainder of the synthesis and led to an orange discoloration of the otherwise white to off-white final polymer. A similar discoloration was not observed in either 25HF25TB24h or 25HF25TB48h but could be recreated by mixing just TBEDA and HBOF either dissolved in DMF or DMSO in a small screw cap vial. However, a subsequent reaction NMR proved inconclusive regarding potential side reactions.

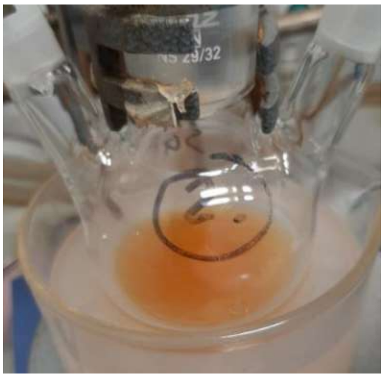

Figure 27:Orange discoloration of the reaction solution for the synthesis of 25HF25TB1st after simultaneous addition of the chain extenders bis(4-hydroxybenzaldehyde oxime)fumarate (HBOF) and N,N'-di-tert-butylethylene diamine (TBEDA).

A summary of all these synthesized oxime-containing TPU(U)s and their theoretical monomer ratios based on weighing is depicted in Table 3.

Table 4: Summary of the synthesized oxime-based thermoplastic poly(urethane(urea) elastomers (TPU(U)s) with their contained monomers (poly(tetrahydrofuran) (pTHF), hexamethylene diisocyanate (HMDI), bis(2-hydroxyethyl) terephthalate (BHET), N,N'-di-tert-butylethylenediamine (TBEDA), and bis(4-hydroxybenzaldehyde oxime)fumarate (HBOF), the ratio of these monomer in the reaction approach, and their yield after purification and drying.

TPU(U)	contained monomers	monomer ratio	yield (%)
50HF32h	pTHF, HMDI, BHET, HBOF	1:2: 0.5:0.5	62
25HF25TB24h	pTHF, HMDI, BHET, TBEDA, HBOF	1:2:0.5:0.25:0.25	87
25HF25TB48h	pTHF, HMDI, BHET, TBEDA, HBOF	1:2:0.5:0.25:0.25	77
25HF25TB1st	pTHF, HMDI, BHET, TBEDA, HBOF	1:2:0.5:0.25:0.25	82

In case of 50HF32h, the prolonging of the reaction time by 24 h led to an almost doubling of the final product yield from 38 % to 62 % compared to 50HF prepared in chapter 1.2.2. The polymers of the 25HF25TB series containing all three CEs showed comparable yields to the reference polymers. There, an increase by 24 h to 48h reaction time demonstrated rather a decrease in the final yield, though this might just be the result of the work-up.

1.3.2. Chemical composition

The degree to which the different CE were incorporated into the synthesized TPU(U) chains was determined similar to 1.2.3 using their respective integrals in the recorded ^{1}H-NMR spectra. The results are depicted in Figure 28. For comparison, the CE share of the synthesized reference TPU(U) 50HF is included as well.

Comparing the newly synthesized 50HF32h with the previously synthesized reference TPU 50HF, it is apparent, that an increase in reaction time after addition of all CEs by 24 h leads to more than a doubling in incorporated oxime-based CE HBOF. An opposite effect is visible upon extension of the reaction time by 24 h in case of 25HF25TB24h to 25HF25TB48h: There, the share of incorporated HBOF decreased by 30 %, which coincides with a lower polymer yield during synthesis of 25HF25TB48h compared to 25HF25TB24h as discussed in chapter 1.3.1. In case of 25HF25TB1st, the simultaneous addition of HBOF and amine-based CE TBEDA decreased the incorporation of HBOF further, which may be linked to the observed discoloration process. Regardless, in all three synthesized TPU(U)s of the 25HF25TB series, ^{1}H-NMR signals of all three CEs – BHET, TBEDA, and HBOF – are present.

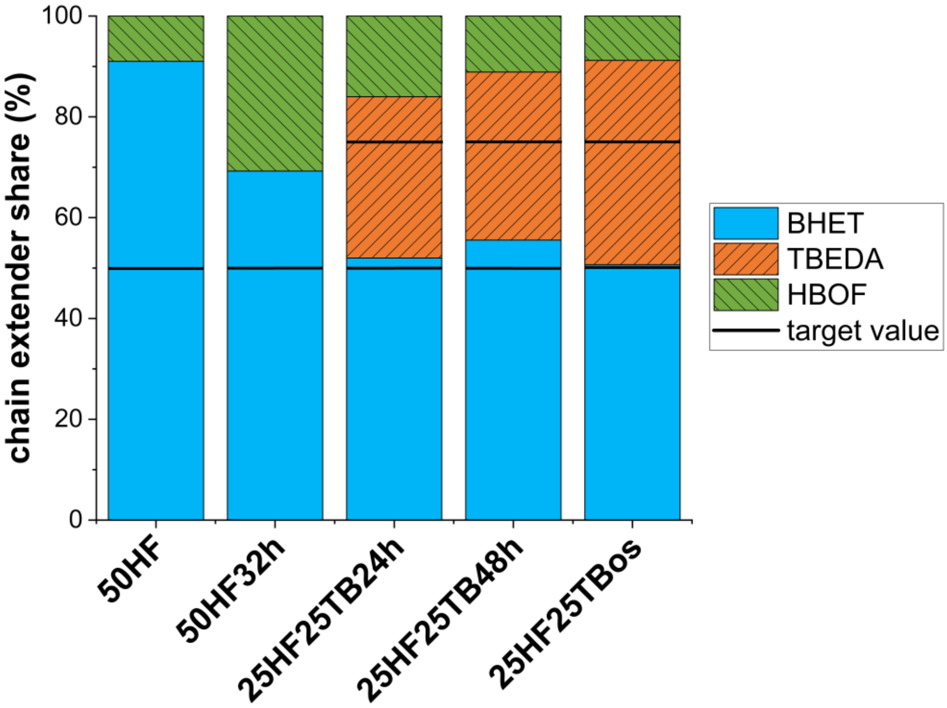

Figure 28: Share of the chain extenders bis(2-hydroxyethyl) terephthalate (BHET, blue), N,N'-di-tert-butylethylene diamine (TBEDA, orange), and bis(4-hydroxybenzaldehyde oxime)fumarate (HBOF, green) present in the synthesized oxime-containing TPU(U)s 50HF32h, 25HF25TB24h, 25HF25TB48h, and 25HF25TB1st. The black bars indicate the theoretical target values for chain extender share based on the weigh-ins of the chain extenders during synthesis.

1.3.3. Molecular weight

The molecular weight of the synthesized oxime-containing TPU(U)s were characterized *via* GPC like in chapter 1.2.4 using both conventional calibration and triple detection. The results for both methods are depicted in Figure 29 and Figure 30 respectively together with those of synthesized references 100BH and 50HF. During sample preparation, dissolution of 50HF32h proved challenging and required multiple days in small amounts of HFIP.

The synthesized oxime-containing TPU(U)s of the 25HF25TB series show comparable molecular weights to the synthesized reference 100BH but slightly higher PDI. This is likely the result of the more complex system of three chain extenders, which introduces greater variability to chain sequences. 50HF32h shows a reduced PDI compared to 50HF in a similar range to the other synthesized TPU(U)s regarding triple detection.

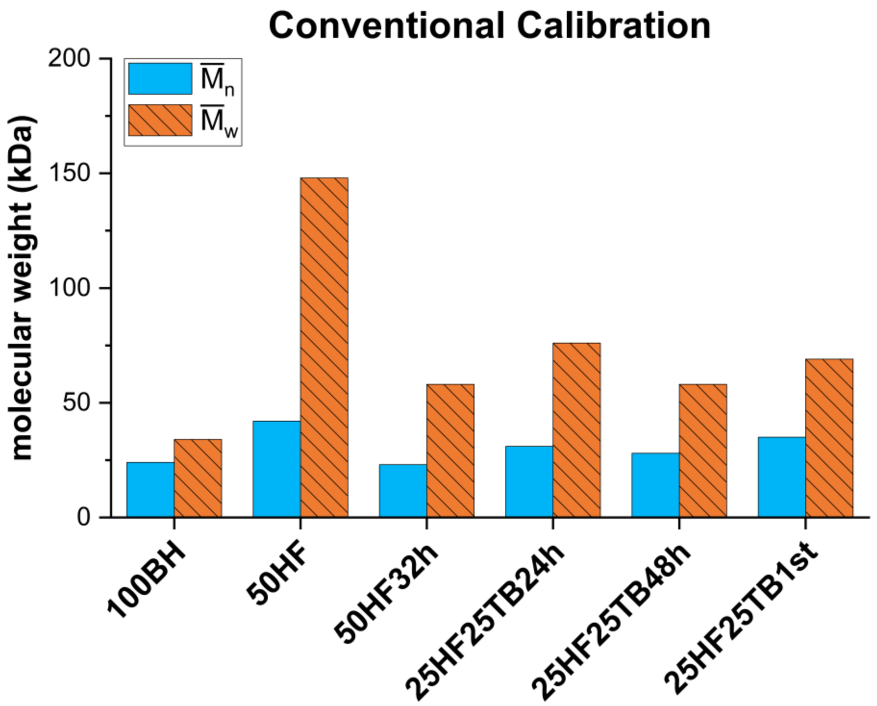

Figure 29: Number-average ($\overline{M_n}$) and weight-average ($\overline{M_w}$) molecular weights of the synthesized reference 100BH (batch 1) and the synthesized oxime-containing TPU(U)s 50HF32h, 25HF25TB24h, 25HF25TB48h, and 25HF25TB1st determined through gel permeation chromatography using conventional calibration.

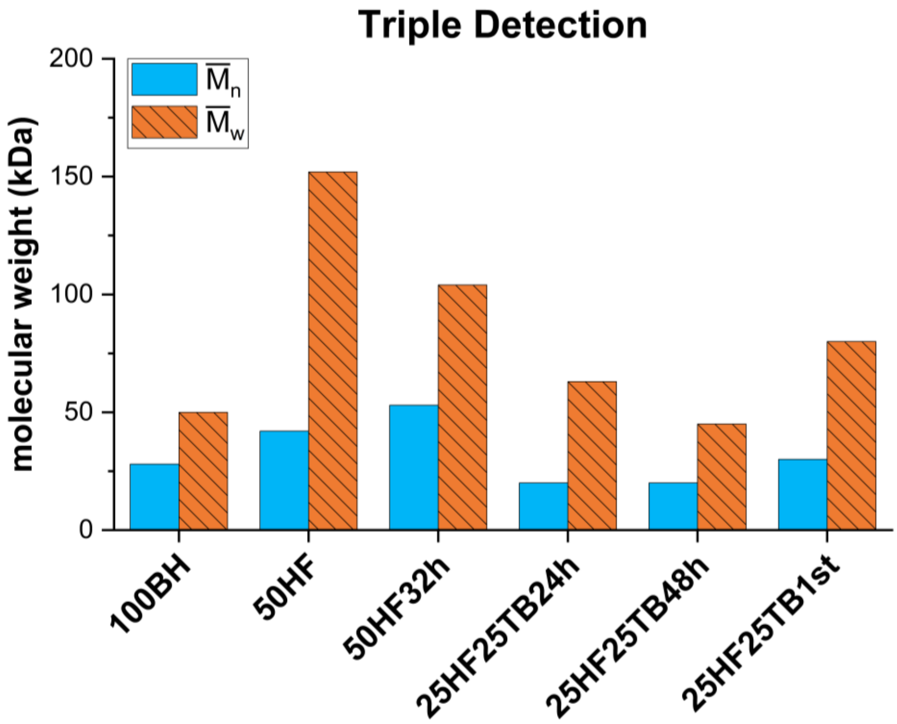

Figure 30: Number-average ($\overline{M_n}$) and weight-average ($\overline{M_w}$) molecular weights of the synthesized reference 100BH (batch 1), and the synthesized oxime-containing TPU(U)s 50HF32h, 25HF25TB24h, 25HF25TB48h, and 25HF25TB1st determined through gel permeation chromatography using triple detection.

1.4. Material characterization

For further use of the synthesized polymers, not only the molecular properties like size and chemical structure are important, but also their properties in the aggregate: Isolated macromolecules of a given composition can take a variety of different shapes (macroconformations), through rotation of substituents along the axes of the various chemical bonds. In the aggregate, these movements become constricted through an interplay of intramolecular and intermolecular interactions, which can lead to the formation of different structures ranging from random entanglements to the formation of orderly spheroids or rods. The degree to which these structures are present depends in part on the considered polymer and has great influence on the physical properties of the final material.[170, 171]

Material characterization of the synthesized TPU(U)s was performed on samples of polymer films (see Figure 31), which were cast from solution in 1,1,1,3,3,3-hexafluoropropan-2-ol. Apart from the synthesized reference TPU(U)s 100BH, 50TB, 25TB, 50HF, and 50HS from chapter 1.2, and the prepared oxime-based TPU(U)s 50HF32h, 25HF25TB24h, 25HF25TB48h, and 25HF25TB1st from chapter 1.3, films were also prepared for the commercial reference Pell as well as the polymer mixture **50HF32h+50TB**, containing the synthesized TPU(U)s 50HF32h and 50TB in a ratio of 1:1. 50HF32h+50TB was prepared to compare the properties of 25HF25TB, which incorporates both HBOF and TBEDA in one polymer, with a polymer mixture, that contains these two CEs in similar ratios but separate polymers. All prepared films were used for characterization of the thermal and mechanical properties of the polymers using differential scanning calorimetry (**DSC**), thermogravimetric analysis (**TGA**), and tensile tests.

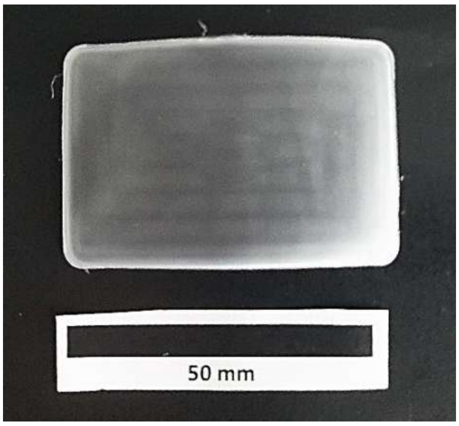

Figure 31: Solution-casted polymer film of 100BH used for material characterization

1.4.1. Differential scanning calorimetry

Thermal properties of polymer materials stand out from those comprised of smaller molecules: With increasing temperature, substances containing small molecules generally transition from a solid, (semi)crystalline state over a liquid state into a gaseous state. This is mainly caused by changes in intermolecular interactions, while intramolecular interactions play only a tangential role due to the small size of the molecules. For larger macromolecules, however, the impact of intramolecular interactions is no longer negligible, so changes in temperature lead not only to thermal transitions like melting or crystallization but also to thermal relaxations like glass transition, where increases in temperature enable the movement of molecule segments.[172]

Characterization of and differentiation between thermal transitions and relaxations is difficult and requires appropriate measurement techniques. Here, DSC was chosen, which measures such processes in a given temperature range based on their endothermic or exothermic nature through changes in the heat flow between a material sample and a reference substance like air.[172, 173]

DSC measurements were performed on a *DSC 2500* by *TA Instruments* together with *Thomas Koch* from the *Institute of Materials Science and Technology*. The measurements were performed in an N_2 atmosphere and were comprised of two heating steps with one cooling step in between. The first heating step was used for purging the thermal history of the TPU(U) sample. The DSC results of the second heating step and of the intermediary cooling step are depicted in Figure 32 for the reference TPU(U)s and in Figure 33 for the synthesized TPU(U)s containing three chain extenders BHET, TBEDA, and HBOF.

All synthesized reference TPU(U)s show glass transition temperatures ($\boldsymbol{T_g}$) around – 60 °C and start melting above 80 °C. The commercial reference Pell undergoes glass transition at around – 50°C and does not melt within the set temperature range. Depending on the prevalence of a second CE (25TB, 50HS, and 50HF), a decrease in recrystallization during cooling can be observed compared 100BH with only one CE species, BHET. In case of 50TB and 50HF32h, where shares of the second CE were highest (see chapter 1.2.3 and chapter 1.3.2), no sharp crystallization signal during cooling was visible. In contrast, these two TPU(U)s undergo a more visible exothermic transition below 50 °C, which may be attributable to cold crystallization.[172, 174] Overall the results resemble available literature.[163] At room and body temperature, all TPU(U)s synthesized or commercially obtained, are above T_g and show no significant thermal transitions or relaxations in this temperature ranges except for a potential onset of cold crystallization in 50TB and 50HF32h.

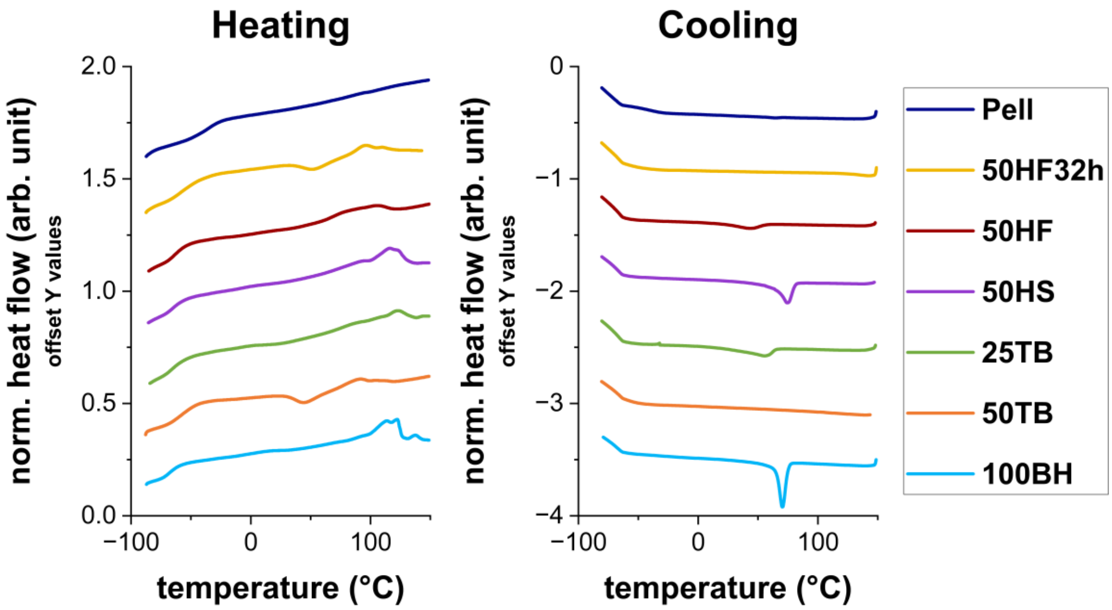

Figure 32: Differential scanning calorimetry results of the measured heat flow depending on temperature for the second heating step (left) and the cooling step (right) of the TPU(U)s 100BH, 50TB, 25TB, 50HS, 50HF, 50HF32h, and Pell.

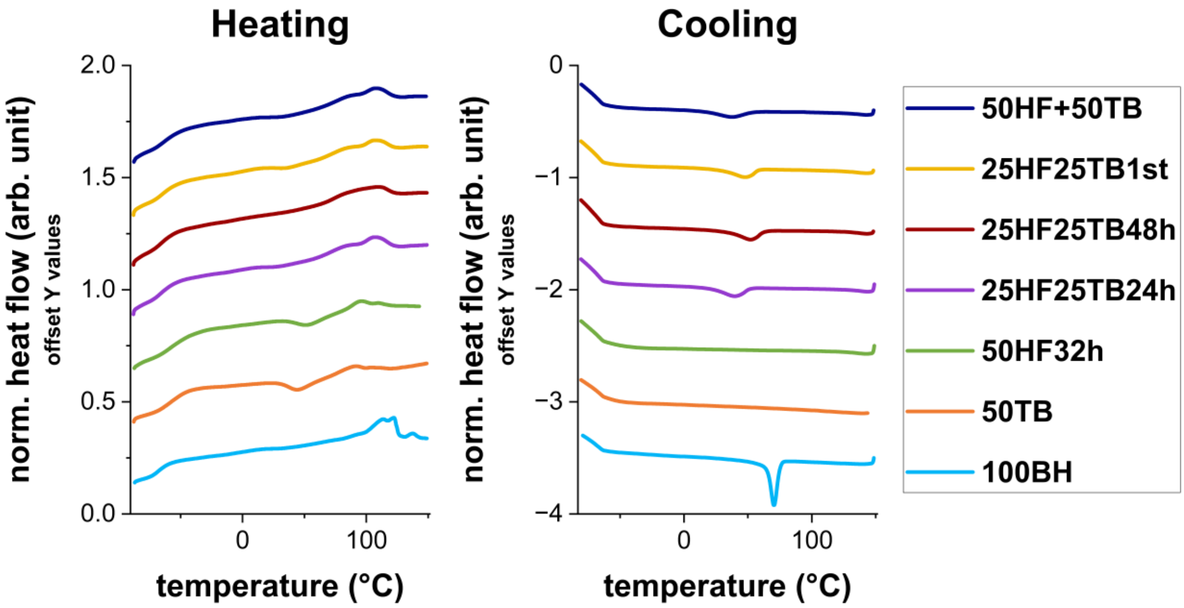

Figure 33: Differential scanning calorimetry results of the measured heat flow depending on temperature for the second heating step (left) and the cooling step (right) of the synthesized TPU(U)s 100BH, 50TB, 50HF32h, 25HF25TB24h, 25HF25TB48h, and 25HF25TB1st as well as the polymer mixture 50HF32h+50TB.

Comparing the signals of the synthesized TPU(U)s with one (100BH) or two CEs (50TB, 50HF32h) to the synthesized TPU(U)s containing all three CEs (25HF25TB) as depicted in Figure 33, T_g and the onset temperature for melting remain similar at around – 60 °C and 80 °C respectively. However, unlike 50TB and 50HF32h, despite similarly low amounts of incorporated BHET (see chapter 1.2.3 and chapter 1.3.2), crystallization can be observed during cooling below 50 °C for all polymer materials containing both HBOF and TBEDA together, and not just in a single molecule but also in mixture (50HF32h+50TB). However, also minor cold crystallization is visible for the 25HF25TB TPU(U)s and 50HF32h+50TB starting at around 25 °C during heating, similar to 50TB and 50HF32h.

1.4.2. Thermogravimetric analysis

Apart from thermal transitions and relaxations, an increase in temperature can also lead to mass loss of materials due to evaporation of smaller molecules contained within, or of formed degradation products. Such processes can be characterized using TGA, where the mass of a material sample is continuously measured over a given temperature interval.[172] Such TGA measurements were performed under N_2 atmosphere together with Thomas Koch from the *Institute of Materials Science and Technology* on samples of all prepared polymer films using a *TGA Q500* device by *TA Instruments*. The results of all TGA measurements are depicted in Figure 34 for the reference TPU(U)s and in Figure 35 for the synthesized TPU(U)s containing three CEs (25HF25TB) and the polymer mixture 50HF32h+50TB.

Regarding the results in Figure 34, all TPU(U)s show a significant mass loss starting at around 350 °C, which can be attributed to pTHF, given that it is present in all synthesized TPU(U)s as well as in the commercial reference Pell (see Figure 19). pTHF represents around 60 % of the total mass of any synthesized TPU(U) based on the chosen approach, which is covered by the total mass lost during this process. A distinct second mass loss can be seen at around 300 °C likely corresponding to the mass of the used diisocyanate HMDI representing around 20 % of the total mass of synthesized TPU(U)s.

Largely overlapping with this second mass loss, a third mass loss process probably related to BHET is discernable at slightly higher temperatures. Concerning, the other two CEs, 50TB and 25TB show minor mass loss around 200 °C, which is in the area of the boiling point of the diamine chain extender TBEDA.[175] Similarly, 50HS, 50HF and 50HF32h also show minor mass loss at around 200 °C, where the temperature exceeds the decomposition temperature of the oxime-based chain extenders HBOS[140] and HBOF[23]. In any case, no significant thermal degradation is observable around room and body temperature.

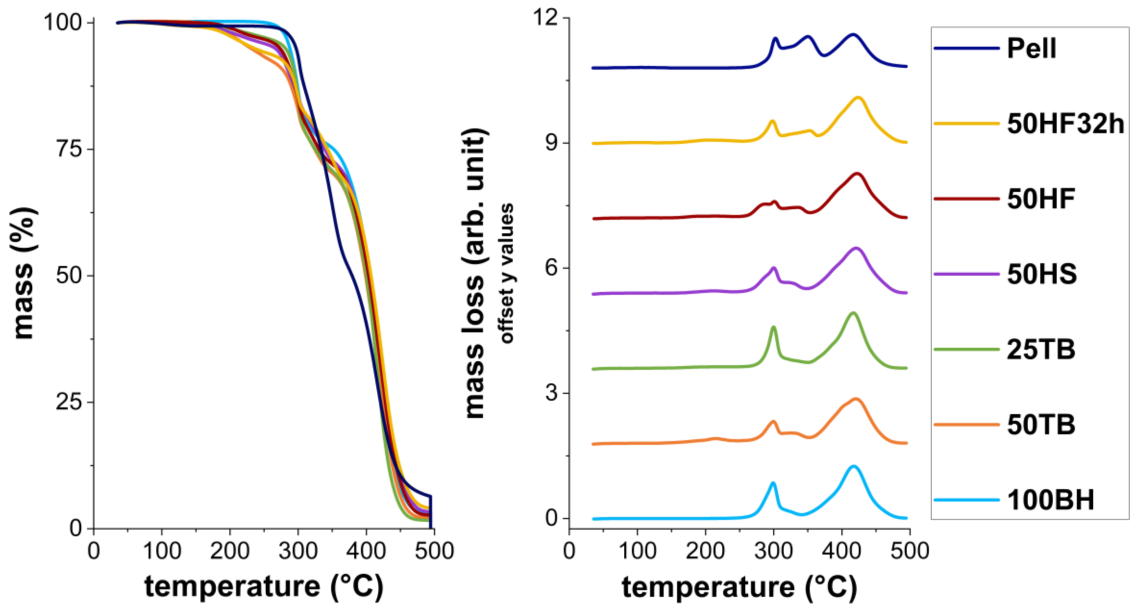

Figure 34: Thermogravimetric analysis results of the TPU(U)s Pell 100BH, 50TB, 25TB, 50HS, 50HF, and 50HF32h regarding change in mass (left), and mass loss (right) over temperature.

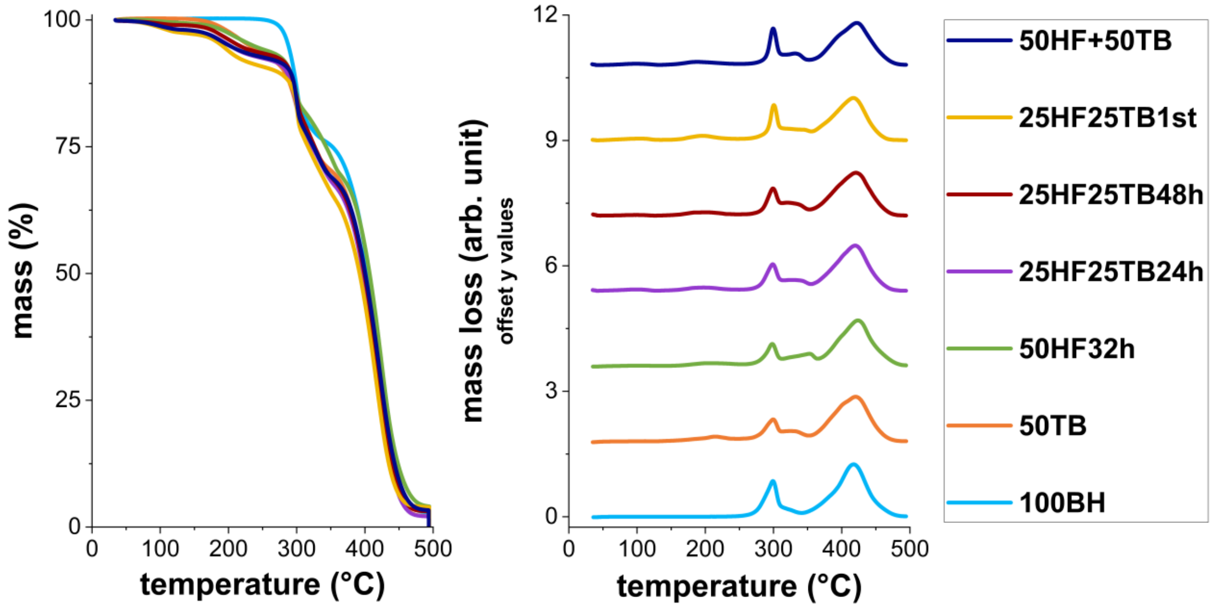

Figure 35: Thermogravimetric analysis results of the TPU(U)s 100BH, 50TB, 50HF32h, 25HF25TB24h, 25HF25TB48h, 25HF25TB1st, and the polymer mixture 50HF32h+50TB regarding change in mass (left), and mass loss (right) over temperature.

Regarding the results in Figure 35 for the TPU(U) materials incorporating three CEs, the mass loss behavior is similar across all of them and resembles the previously addressed reference TPU(U)s 50TB and 50HF32h: Minor mass loss up to 250 °C attributable to TBEDA and HBOF, a distinct mass loss at 300 °C related to HMDI, which transitions into a mass loss ascribable to BHET followed by a large mass loss starting at 350 °C related to pTHF. Again, no significant mass loss is observable around room and body temperature.

1.4.3. Tensile tests

To be suitable for future applications, the synthesized TPU(U)s must also be able to withstand the present mechanical forces, especially in the case of vascular grafts, where the material is continuously exposed to a considerable blood pressure. Such forces lead to deformation, which can be reversible (i.e., elastic deformation) or irreversible (i.e., viscous deformation) depending on the mechanical properties of the material under working conditions. As viscoelastic materials, polymer materials generally demonstrate both types of deformation to different degrees: While thermoplastic polymer materials below T_g are for example more rigid and show little elasticity, elastomers above T_g are more flexible.[176]

As a result, mechanical characterization of the polymer materials is important. For this, tensile tests at room temperature were performed on test specimens punched out of the prepared polymer films. Of interest here, are the initial material stiffness represented by the size of Young's Modulus (***YM***), the ultimate tensile strength (***UTS***), and the elongation at break (***EAB***), which are obtainable from the measured stress-strain curve. An example of such a stress-strain curve typical for the measured TPU(U) test specimens are depicted in Figure 36.

The measurements were carried out on a *Zwick Z050* by *Zwick* under supervision of *Thomas Koch* from the *Institute of Materials Science and Technology*. Tensile test measurements were done in triplicates for individual films. The results are depicted in Figure 37 for the reference TPU(U)s and in Figure 38 for the synthesized TPU(U)s containing three CEs (**25HF25TB**) and the polymer mixture 50HF32h+50TB.

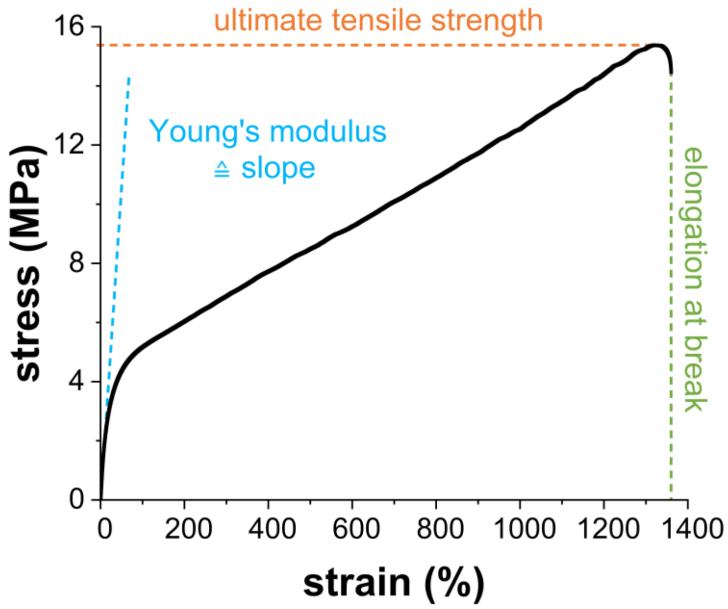

Figure 36: Tensile test stress-strain curve of a measured test specimen of the synthesized TPU(U) 25HF25TB24h

The tensile test measurement results of the reference materials summarized in Figure 37 resemble literature.[140, 163] The commercially available reference Pell demonstrates the highest UTS and EAB as well as the lowest stiffness, which is likely influenced by the significantly higher molecular weight compared to the synthesized TPU(U)s. Regarding the synthesized TPU(U)s, it can be observed, that the prevalence of a second CE like in 50TB generally leads to a decrease in stiffness (YM) and an increase in EAB compared to 100BH. Comparing 50HF32h and 50HF this trend is also visible as well as between 50TB and 25TB. Regarding the UTS, smaller amounts of a second CE seem to lead to an increase compared to 100BH, most notably for 25TB, though this reverses itself at higher amounts in the case of 50TB.

The tensile test results in Figure 38 show that TPU(U)s containing three different CEs in a single polymer (25HF25TB) similarly demonstrate a decreased YM and a higher EAB compared to 100BH with a single CE. The same trend is also visible between 25HF25TB TPU(U)s and TPU(U)s containing only two of the used CEs (50TB, 50HF32h). On the other hand, the UTS remains similar between 25HF25TB TPU(U)s and 100BH, despite the increase in different CE species, and sits in between the UTS of 50TB and 50HF32h. Comparing the individual 25HF25TB TPU(U)s, they do not vary significantly except for a minor decrease in UTS for 25HF25TB48h. Lastly, the polymer mixture 50HF32h+50TB shows a significant deviation from all other measured TPU(U)s with a particularly low EAB and a poor UTS. However, given the apparent narrow standard deviation between test specimens of a single film and a reproducibility of results using other polymer films of the same mixture, this observation is unlikely the product of a sampling error but could be related to the poor solubility of HBOF.

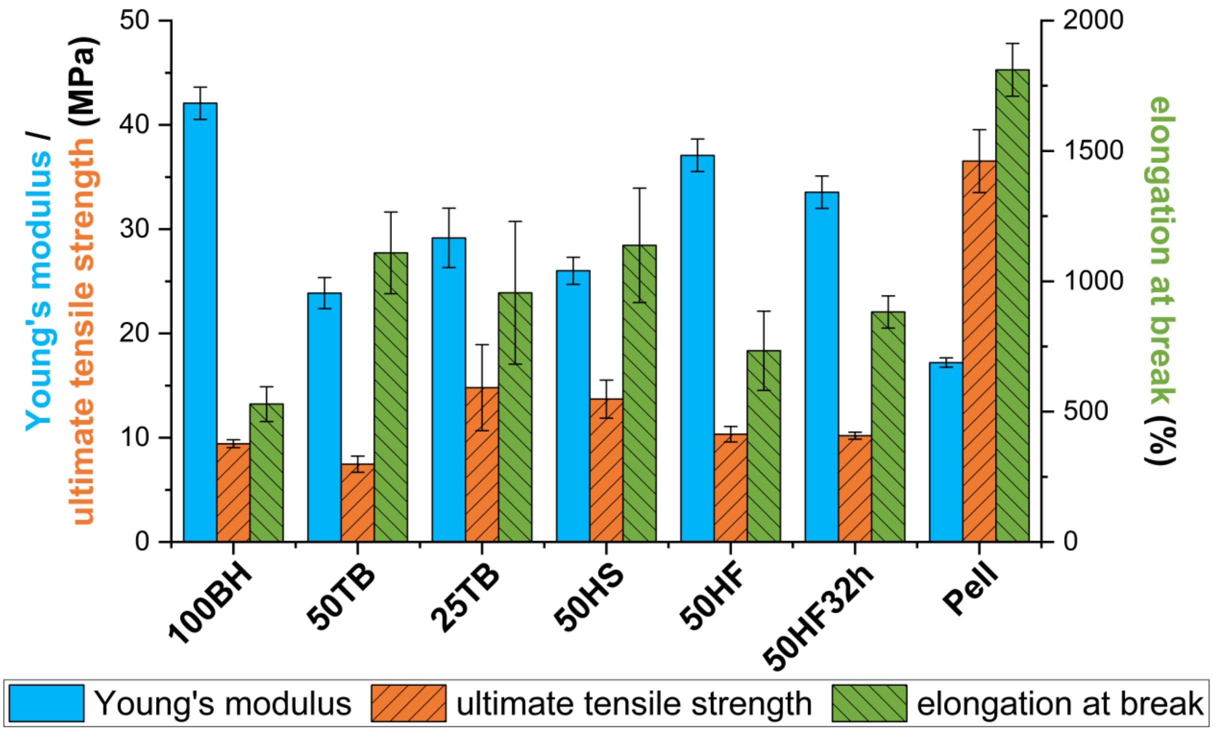

Figure 37: Tensile test results of the TPU(U)s 100BH, 50TB, 25TB, 50HS, 50HF, 50HF32h, and Pell regarding Young's modulus, ultimate tensile strength, and elongation at break.

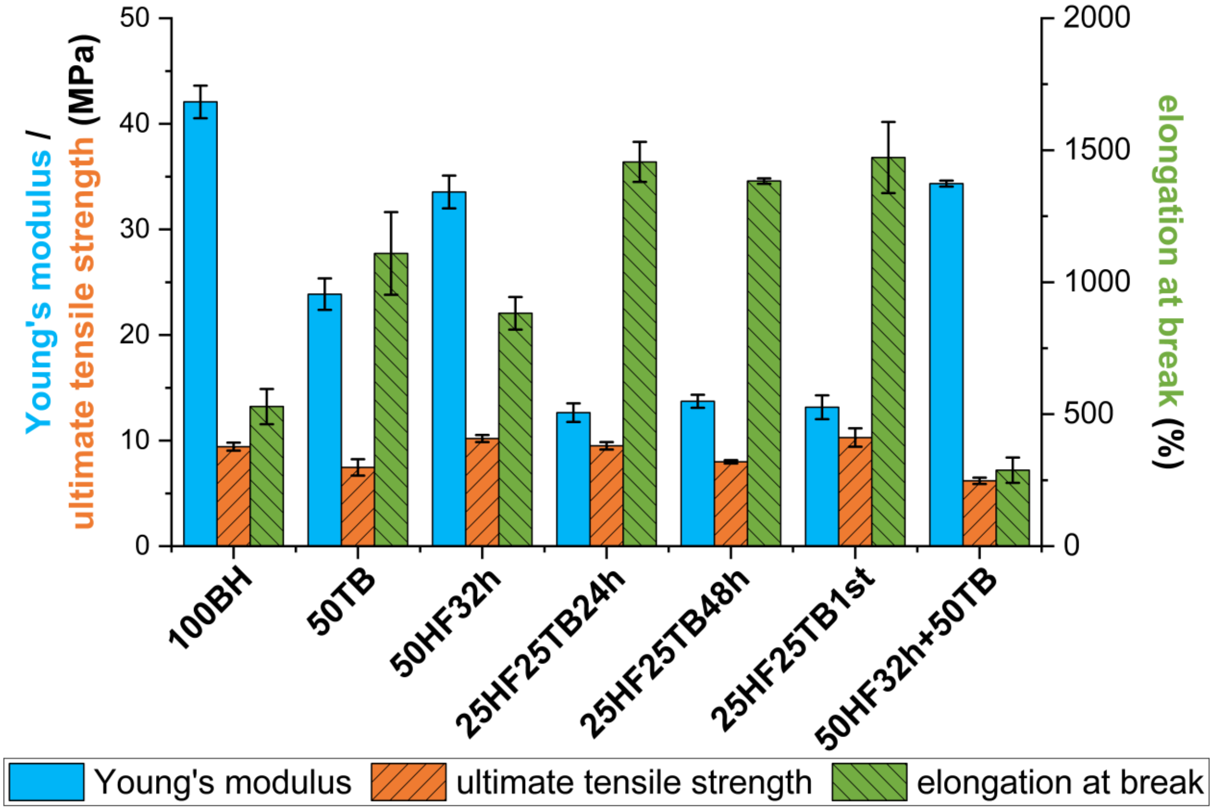

Figure 38: Tensile test results of the synthesized TPU(U)s 100BH, 50TB, 50HF32h, 25HF25TB24h, 25HF25TB48h, 25HF25TB1st, and the polymer mixture 50HF32h+50TB regarding Young's modulus, ultimate tensile strength, and elongation at break.

2. Self-reinforcement studies

The dynamic bonds of hindered-urea (**HUBs**) and oxime-urethane (**OUBs**) groups introduced by inclusion of the chain extenders TBEDA and HBOF into the polymer chain of thermoplastic poly(urethane(urea)) elastomers (**TPU(U)s**), enable a self-reinforcement effect (**SRE**) in hydrolytic environments (see Introduction chapter 5.3). To what extend this effect takes place can be determined through self-reinforcement studies: For a TPU(U) of interest, a polymer film is prepared as in chapter 1.4. and cut in half. One half is stored under dry conditions to minimize self-reinforcement, while the other half is submerged in deionized water and conditioned for a certain time period. After said time period, the conditioned film is removed from the water and dried, and both halves of the film are subsequently characterized *via* tensile tests similar to chapter 1.4.3. By comparing the results, the degree of self-reinforcement within the set time period can be determined. To observe the change in self-reinforcement over time, this procedure is repeated with additional films and different conditioning durations.

Self-reinforcement studies were performed on the commercial reference TPU(U) Pell, the synthesized reference TPU(U)s 100BH, 50TB, 25TB, and 50HF32h, the newly synthesized TPU(U)s containing three CEs 25HF25TB24h, 25HF25TB48h, and 25HF25TB1st, and the polymer mixture 50HF32h+50TB. For each of these polymers three conditioning durations of 1 day, 7 days and 21 days were chosen to determine the change in self-reinforcement over time. The relative change after self-reinforcement of the individual TPU(U)s is depicted in Figure 39 regarding different conditioning durations for Young's Modulus ($\boldsymbol{YM}$), ultimate tensile strength ($\boldsymbol{UTS}$), and elongation at break ($\boldsymbol{EAB}$). Comparisons between the tensile test results of unconditioned samples and samples conditioned for 21 days in deionized water are depicted Figure 40. The individual tensile test results of the test specimens of the different TPU(U)s for all duration periods are summarized in the appendix in Figure 69 regarding the unconditioned samples and Figure 70 regarding the conditioned samples.

As depicted in Figure 39, TPU(U)s containing the CE TBEDA show a significant SRE in line with literature due to the introduction of HUBs into the polymer chain.[23] In contrast, 50HF32h, showed no significant SRE, despite the known dynamic nature of the introduced OUBs.[140] However, this is likely due to the long dissolution time in HFIP during film preparation, which took multiple days and probably already led to conversion of the dynamic bonds before the self-reinforcement studies. Similarly, Pell and 100BH also showed no prominent SRE, but this was to be expected given the absence of dynamic bonds.

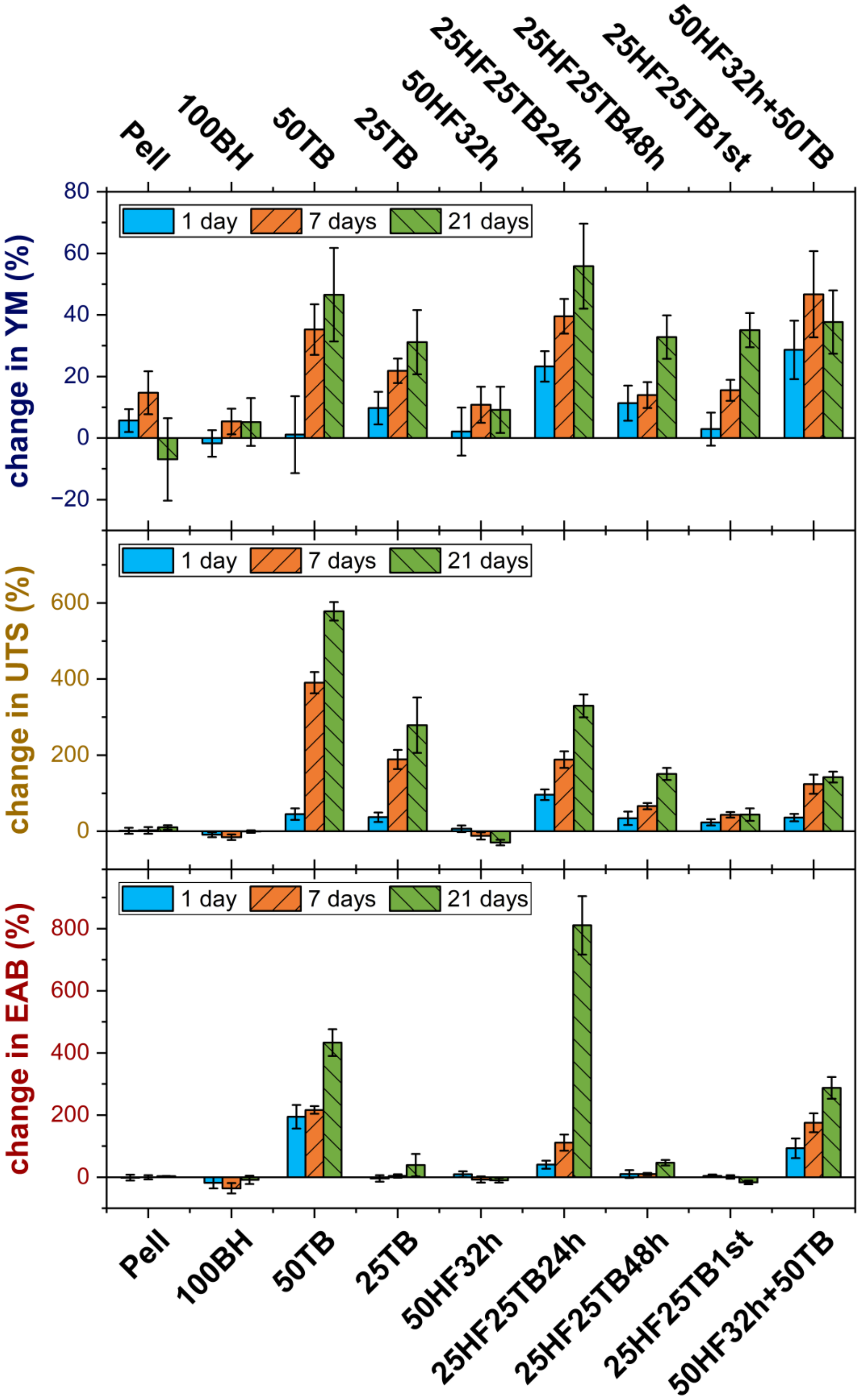

Figure 39: Change in Young's modulus (YM), ultimate tensile strength (UTS), and elongation at break (EAB) of the TPU(U)s Pell, 100BH, 50TB, 25TB, 50HF32h, 25HF25TB24h, 25HF25TB48h, and 25HF25TB1st, and the TPU(U) mixture 50HF32h+50TB between unconditioned and conditioned specimens in deionized water for 1, 7, and 21 days.

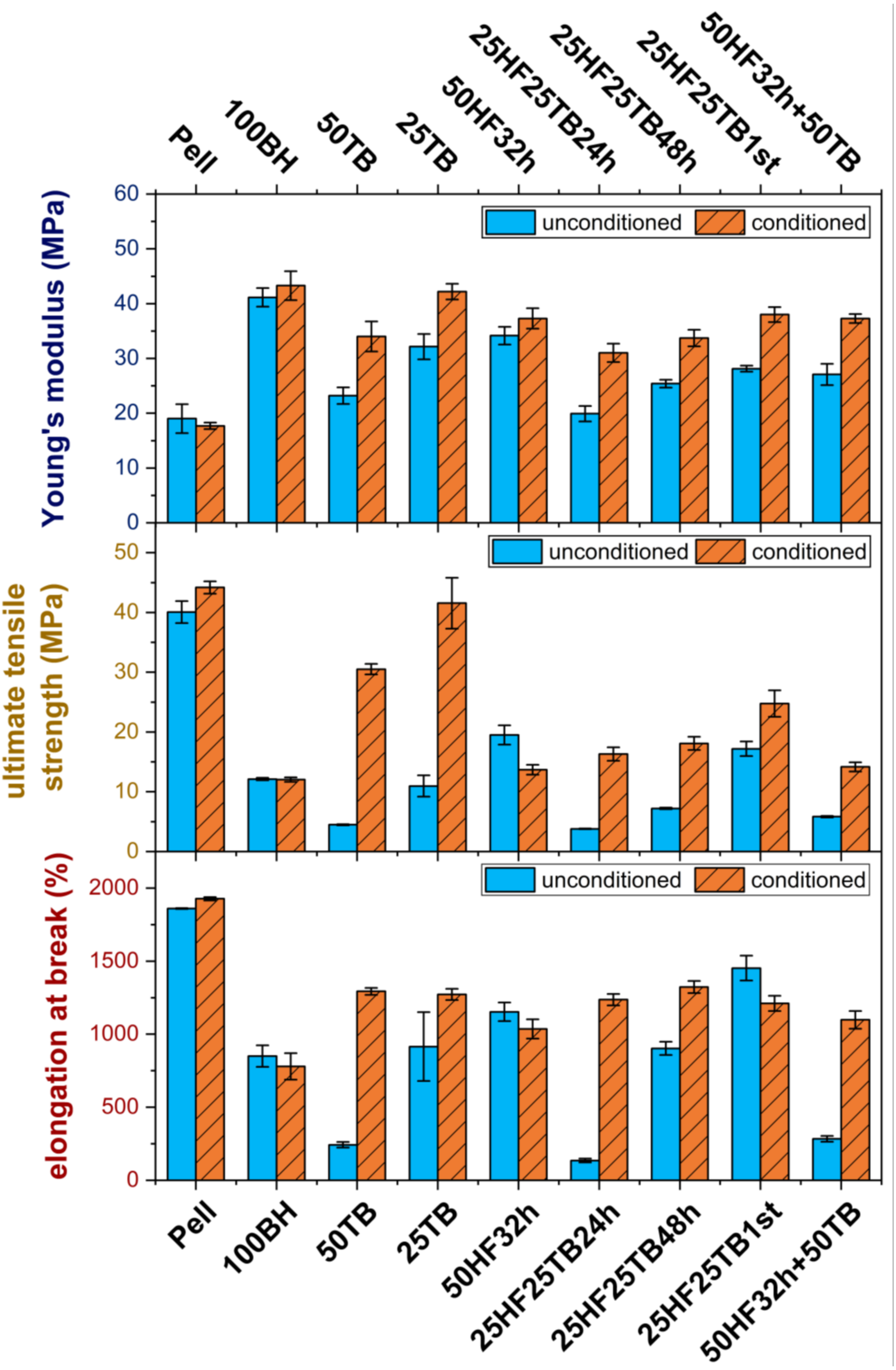

Figure 40: Comparison of Young's modulus, ultimate tensile strength, and elongation at break between unconditioned samples (unconditioned) and samples conditioned in deionized water for 21 days (conditioned) of the TPU(U)s Pell, 100BH, 50TB, 25TB, 50HF32h, 25HF25TB24h, 25HF25TB48h, and 25HF25TB1st, and the TPU(U) mixture 50HF32h+50TB.

Most prominently, SRE leads to an increase in UTS: This is best illustrated by the TPU(U) 50TB with the highest concentration of incorporated HUBs, where an increase in UTS by around 600 % can be observed after 21 days. Likewise, TPU(U) 25TB shows an increase of around 300 %, which coincides with the decrease in concentration of TBEDA by 50 %. However, it should be noted, that this degree of self-reinforcement is also partially influenced by a decrease in UTS of the unconditioned specimens over time from 15 MPa after 1 day to 10 MPa after 21 days (see Figure 69 in the appendix, page 132). Similarly, the 25HF25TB TPU(U)s and polymer mixture 50HF32h+50TB, which contain both dynamic CEs TBEDA and HBOF, show significant self-reinforcement of around 75 % to 300 % after 21 days. The highest self-reinforcement after 21 days among these TPU(U)s is achieved by 25HF25TB24h, which is the 25HF25TB TPU(U) with the highest HBOF concentration (see chapter 1.3.2). The polymer mixture 50HF32h+50TB demonstrates a similar self-reinforcement as 25HF25TB48h. 25HF25TB1st showed the lowest self-reinforcement amongst these TPU(U)s. However, regarding absolute values (see Figure 40), self-reinforced 25HF25TB1st specimens demonstrate a significantly higher UTS of around 25 MPa after 21 d compared to 25HF25TB24h, 25HF25TB48h, and 50HF32h+50TB, which average at around 20 MPa. Nonetheless, all these TPU(U)s show a significantly higher UTS than the reference 50HF32h, which only contains HBOF. The high UTS of self-reinforced 25TB and 50TB, which rivals almost Pell, however, could not be achieved with these TPU(U)s.

Regarding YM, significant increases can be observed for all TPU(U)s with dynamic CEs, although, in case of 50HF32h, this self-reinforcement is comparatively weak at around 10 %. The highest increase in YM was achieved by 50TB and 25HF25TB24h by around 50 % after 21 days. The increase in YM of the other TPU(U)s 25TB, 25HF25TB48h, 25HF25TB1st, and the polymer mixture 50HF32h+50TB sat at around 30 % after 21 days. The absolute values of self-reinforced TPU(U)s after 21 days are generally between 35 MPa and 40 MPa. The highest YM at around 45 MPa was achieved by 100BH, followed by 25TB at around 40 MPa. The 25HF25TB TPU(U)s and 50HF32h+50TB showed similar YM to 50TB and 50HF32h.

Concerning EAB, significant change was only observed for the TPU(U)s 50TB, 25HF25TB24h, and 50HF32h+50TB. These changes coincide with particularly low EAB of the unconditioned specimens after 21 days in dry storage (see Figure 69 in the appendix, page 132), which are significantly lower compared not only to the other TPU(U)s but in case of 50TB and 25HF25TB24h also lower than the EAB of the initial tensile tests performed in chapter 1.4.3: The unconditioned specimens of 25HF25TB24h, for example, demonstrate an EAB of 136 % after 21 days in dry storage compared to the EAB of 1456 % measured in chapter 1.4.3 within 48 h after film preparation.

Given that specimen fabrication and storage were done similar to the other TPU(U)s and the measured tensile test results show narrow variance, one likely explanation could be phase changes in the material over time due to thermal annealing.[177] As shown by the DSC measurements in chapter 1.4.1, especially 50TB but also 25HF25TB24h and 50HF32h+50TB show some degree of cold crystallization with onset temperatures starting at around 25 °C. A resulting increase in crystallinity would consequently result in reduction the EAB.

3. Electrospinning of materials

3.1. Setup

After synthesis and characterization of the prepared thermoplastic poly(urethane(urea)) elastomers (**TPU(U)s**) in bulk, it is also important to establish their viability for final processing and the properties of the final materials used for application. With regard to vascular grafts, final processing *via* electrospinning (**ES**) is of interest. As mentioned in Introduction chapter 3, ES is a fiber fabrication technique, which can be used to prepare nonwoven fabrics (**NWFs**) composed of filaments with diameters in the micrometer to nanometer range. As fiber precursors serve generally polymer solutions, which are introduced into a strong electric field, whereupon they are distorted into thin liquid jets and subsequently solidify through evaporation of the solvent. The setup of the ES device used in this work is depicted in Figure 41 and was custom-built by Simon Seisenbacher[178] as part of his ongoing diploma thesis.

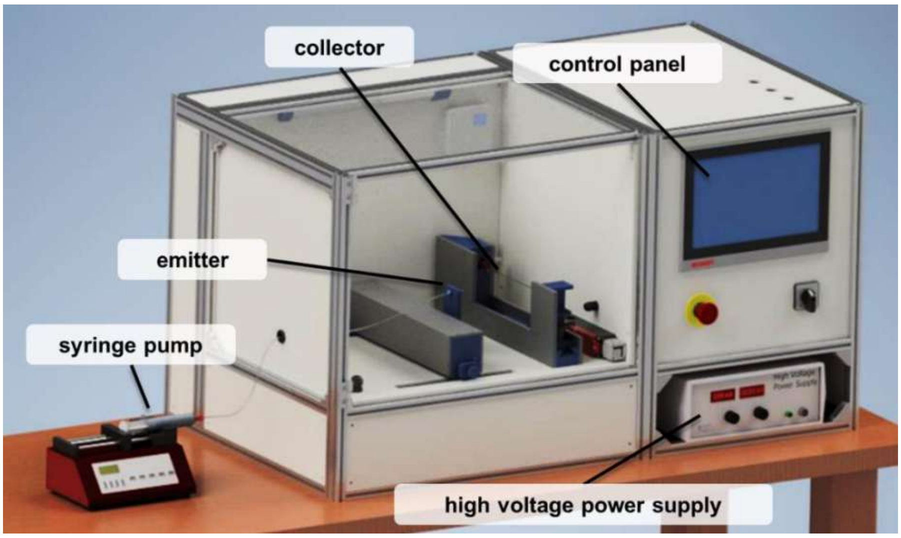

Figure 41: Digital rendering of the electrospinning setup by Simon Seisenbacher with description of the individual parts.[178]

The spinning chamber consists of an emitter electrode and a collector electrode surrounded by a Faraday cage. The emitter is a hollow steel needle and moveable in medial and lateral direction to set the emitter-collector distance and enable an even distribution of the electrospun fibers along the collector surface. The collector, meanwhile, is fixed in place and consists of a steel rod, which acts as a mandrel for the electrospun fabrics, and can be rotated around itself. The strong electric field between these two electrodes is generated by a high voltage power supply, which is connected to the emitter and creates a potential difference with the grounded collector. For temperature and humidity monitoring, the spinning chamber is further equipped with a corresponding sensor. To avoid charge and solvent build-up in the atmosphere of the spinning chamber over time, ionized air is blown in with a fan after every run.

To introduce the fiber precursor into the spinning chamber continuously and at a constant flow rate (i.e., feed rate), a syringe pump is used, which is placed outside the spinning chamber. Transfer of the fiber precursor from a clamped syringe into the spinning chamber is enabled by dielectric PTFE tubing, which connects the syringe with the emitter. An adjacent control panel can be used to set the desired ES parameters regarding emitter-collector distance, lateral position, movement and movement speed of the emitter, applied voltage and current, rotation speed of the mandrel and feed rate of the polymer solution.

To reduce the quantity of required material, fiber deposition can be focused onto the middle of the collector using thick PTFE tubes, which are placed on both ends of the collector and cover its surface there. In addition, to increase the tube diameter of the electrospun materials (**ESM**) or deposit electrospun fibers onto other substrates, the collector can be also covered with other materials like antistatic poly(ether)-poly(urethane) tubes or thinner PTFE tubes. The collector setup in such cases is depicted in Figure 42 using an antistatic poly(ether)-poly(urethane) tube.

Figure 42: Collector setup of the steel mandrel with PTFE tubes of an outer diameter of 6 mm on the collector edges and a black antistatic poly(ether)-poly(urethane) tube of an outer diameter of 4 mm in the collector middle as substrate material for fiber deposition

3.2. Procedure and parameters

3.2.1. General procedure

To perform ES, the fiber precursor must first be prepared. This is done by dissolving a weighed amount of desired polymer in the necessary amount of 1,1,1,3,3,3-hexafluoro-2-propanol (**HFIP**) to obtain a polymer solution with a concentration between 5 wt.% and 10 wt.%. After complete dissolution, the solution is drawn up into the syringe, which is then clamped into the syringe pump and connected to the emitter electrode. The device parameters are set to desired values, and the ES process is ultimately started. Once the process is finished, the tubular-shaped ESM is dried under reduced pressure and can then be removed from the mandrel for further characterization. To confirm fiber formation and the fibrous nature of the ESM, scanning electron microscopy (SEM) is performed for both inner and outer surface.

3.2.2. Emitter-collector distance

Successful ES requires the formation of solid fibers, which in turn depends on a multitude of different parameters: Some parameters are environmental like temperature and moisture, others depend on the chosen fiber precursor i.e., the used polymer, solvent and concentration of the solution, and still others are set by the ES device itself like the emitter-collector distance, the applied voltage, and the precursor feed rate. As a result, finding the right set of variable parameters for a general method is difficult. Additionally, depending on the used setup, only some of these parameters are controllable, while others have to be accepted. Consequently, reproducibility is a considerable issue and literature values, while useful as guidelines, generally cannot be adopted exactly.

For successful fiber formation, the formed jet of polymer solution must solidify. This happens through evaporation of the solvent, which is mainly dependent on the used solvent, temperature, humidity, solution feed rate, and travel time of the jet between the emitter and collector electrode (i.e., the emitter-collector distance): Given the poor solubility of TPU(U)s in most solvents, the choice for a universally applicable, non-flammable and volatile solvent is mainly restricted to HFIP. Given that the spinning chamber is neither thermally isolated nor hermetically sealed, also temperature and humidity of the environment must be accepted. Also, the used flow rate cannot be chosen freely and must be coordinated with the applied voltage to avoid either excessive build-up of polymer solution at the emitter electrode or breakup of the jet. Consequently, mainly the emitter-collector distance can be used to freely influence jet solidification.

Regarding the emitter-collector distance, two things need to be considered: First, as already mentioned, the distance should be large enough to ensure sufficient evaporation of the solvent, but, secondly, the distance also needs to be close enough for good deposition of the formed fibers onto the collector substrate. Therefore, it is important to keep the distance as long as necessary but as short as possible.

To find an appropriate distance between emitter and collector, four ES runs were performed at emitter-collector distances of 80 mm, 100 mm, 120 mm, and 150 mm using a 5 wt.% polymer solution of the TPU(U) 100BH in HFIP and a precursor feed rate of 3 mL/h. The initial distance of 80 mm, and a concentration of 5 wt.% were adopted from literature.[23] The feed rate was set in coordination with the applied voltage and was higher than the reference.

In all cases tubular materials were obtained: Thereby, the sample at a distance of 80 mm was optically transparent, while the prepared materials at distances of 100 mm, 120 mm, and 150 mm were white, non-transparent and slightly reflective (see Figure 43 for comparison). From all electrospun tubes, SEM images were taken of both the inner and outer surface. The images from the outer surface are depicted in Figure 44. The inner surfaces of all materials were relatively smooth and showed little microstructure, and their images are therefore omitted.

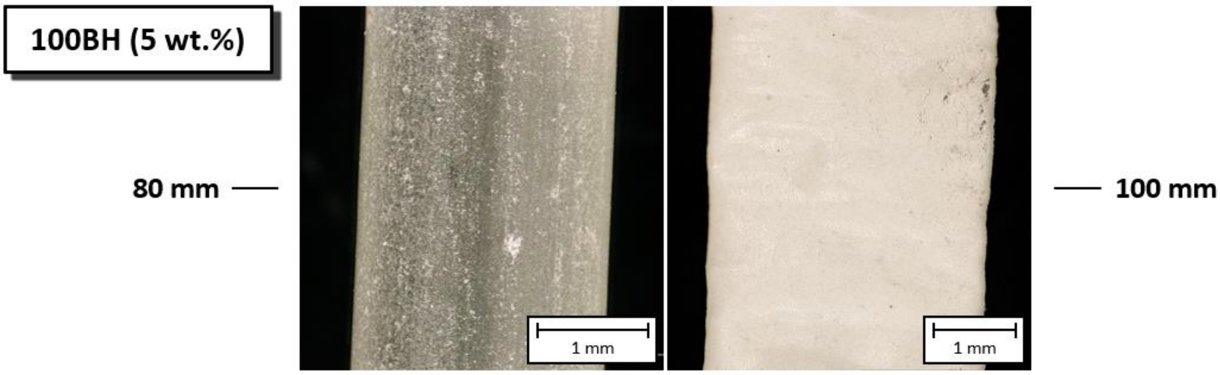

Figure 43: comparison of depth-resolved light microscopy images of the outer surface of electrospun samples prepared from a 5 wt.% 100BH solution in HFIP with emitter-collector distances of 80 mm (left), and 100 mm (right).

The recorded SEM images show that at emitter-collector distances of 80 mm and 100 mm, deposited material is fused together into a film. However, with an increase in distance, fusion decreases, which can be seen by an increase in surface roughness and appearance of clearly delimited bead-like structures, which stick together and make up the material. At distances of 120 mm and 150 mm, some fusion still occurs but only on a superficial level between beads, holding them together.

In all cases, proper fiber formation was not observed. This is likely due to insufficient entanglement of the macromolecules, which destabilizes the liquid jet during ES and leads to its disintegration into droplets as in the case of electrospraying.[82] To improve entanglement for a given precursor solution, either the molecular weight of the polymer needs to be increased, which would require synthesis of a new polymer batch, or the polymer concentration in solution needs to be raised.

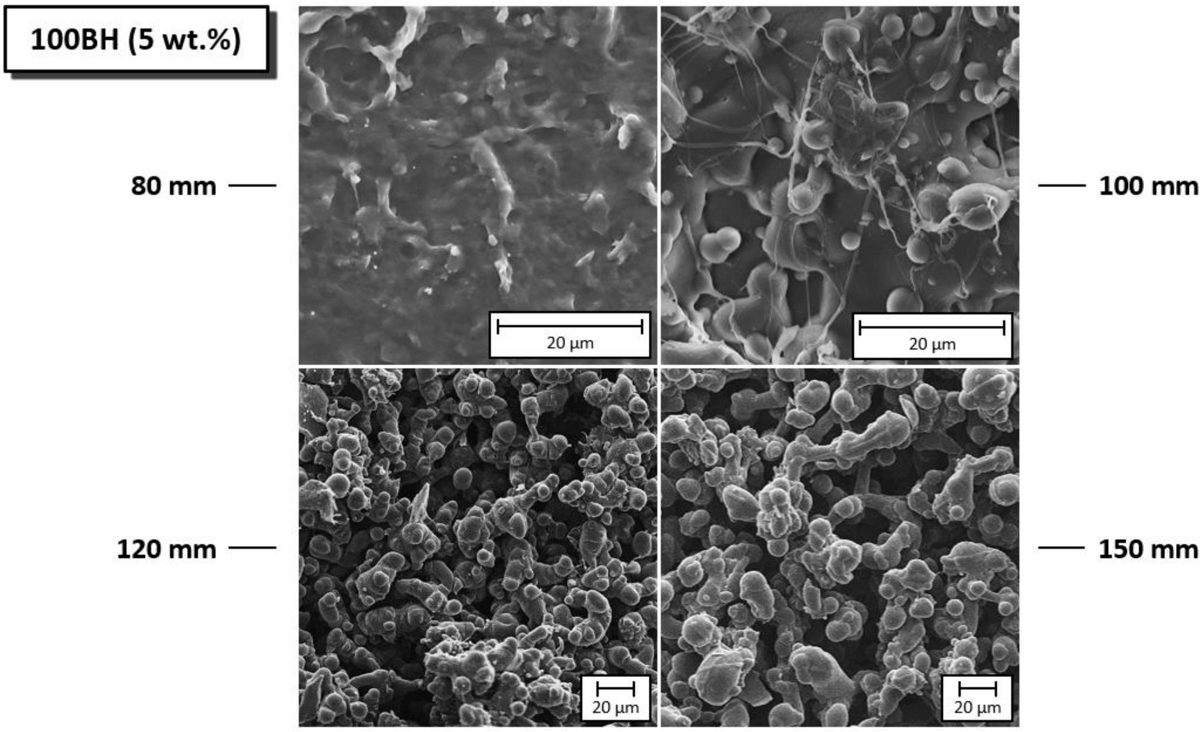

Figure 44: Scanning electron microscopy images of the outer surface of electrospun samples prepared from a 5 wt.% 100BH solution in HFIP with emitter-collector distances of 80 mm (top, left), 100 mm (top, right), 120 mm (bottom, left), and 150 mm (bottom, right), and a precursor feed rate of 3 mL/h.

3.2.3. Polymer concentration in solution

Apart from evaporation, also the polymer concentration in the fiber precursor solution is essential for fiber formation. While evaporation is needed for solidification of the liquid jet into fibers, the polymer concentration ensures the jet's stability during solidification and prevents the jet's disintegration on path to the collector. This is because in sufficient concentrations, dissolved polymers can entangle one another, increasing the viscosity of the solution and impeding atomization in a strong electric field.[179]

Next to the concentration, this entanglement depends also on the molecular weight of the given polymer and its disposition for intermolecular interactions.[180] These properties naturally vary between polymers and must be considered when adopting an existing ES method for a new substance. To confirm this, a 5 wt.% solution of the commercial TPU(U) Pell and a 10 wt.% solution of 100BH were electrospun over a emitter-collector distance of 150 mm similar to the 5 wt.% solution of 100BH in the previous chapter 3.2.2. A 10 wt.% solution of Pell was prepared as well but was ultimately too viscous for ES. Both the 10 wt.% solution of 100BH and the 5 wt.% solution of Pell were significantly more viscous compared to the 5 wt.% solution of 100BH. The obtained ESMs further appeared visibly more fibrous, and in case of Pell also showed a silky sheen, which differed from the previously prepared ESM of 100BH. Subsequent SEM confirmed these observations with the obtained images of the inner and outer surface of the ESMs being depicted in Figure 45.

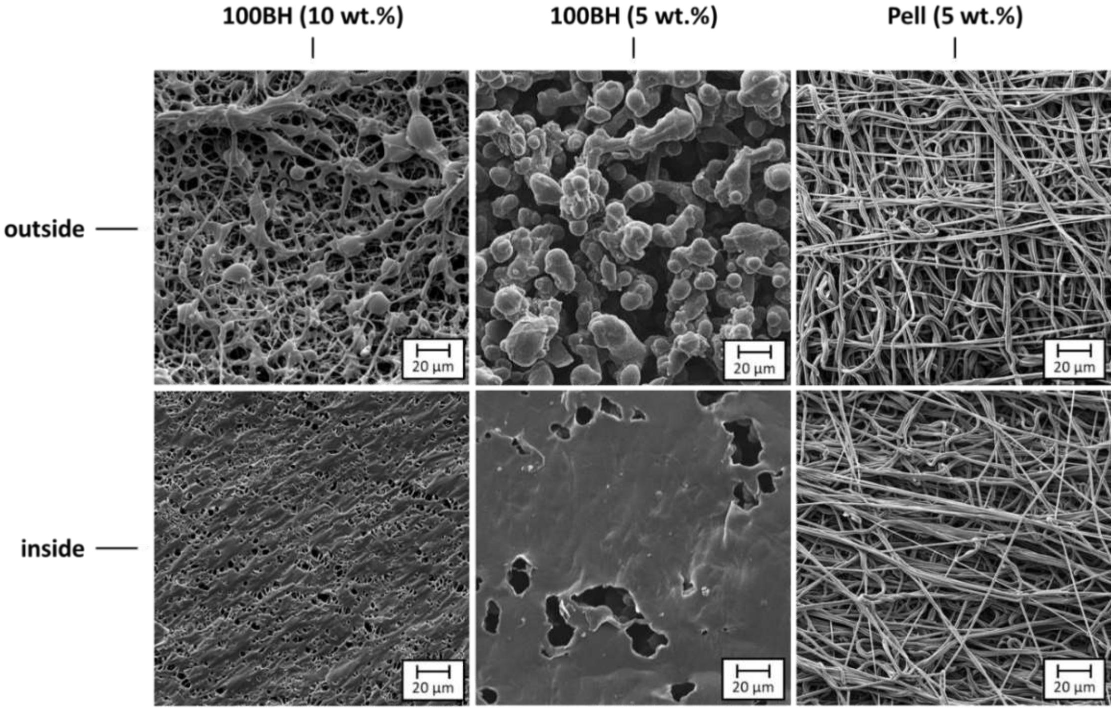

Figure 45: Scanning electron microscopy images of the outer (top) and inner (bottom) surface of electrospun materials spun from a 10 wt.% solution of 100BH (left), a 5 wt.% solution of 100BH (center), and a 5 wt.% solution of Pell (right) with HFIP at an emitter-collector distance of 150 mm.

The SEM images show, that for both the 10 wt.% solution of 100BH and the 5 wt.% solution of Pell a more fibrous material can be obtained compared to the previously prepared 5 wt.% solution of 100BH. This is especially the case of Pell, where a properly fibrous structure was successfully formed, likely due to the significantly higher molecular weight compared to 100BH (see chapter 1.2.4). Also, the material obtained from the 10 wt.% solution of 100BH shows fiber formation, but particularly the inner surface remains fused. A possible cause for this may be the steel of the collector that is used as deposition substrate. Ehrmann[23] observed that such conductive materials can facilitate fusion of ESM in direct contact with the surface. To circumvent this, other materials can be used for fiber deposition like dielectric PTFE.

3.2.4. Substrate material for fiber deposition

As demonstrated in the previous chapter 3.2.3, using conductive steel both as collector electrode and substrate for fiber deposition can coincide with fusion of the ESM on the inner surface facing the substrate. Depending on the application, this is generally not desired given the resulting structural inhomogeneity of the ESM and diminished microstructure on the inner surface. It also makes removal of the ESM from the deposition substrate more difficult due to a better adherence to the substrate surface. An alternative here is the use of less conductive substrate materials, which are placed in the electric field between emitter and collector electrode and catch passing fibers.[23]

For the used ES setup, such substrate materials can be simply put onto the rotating collector mandrel as tubes as mentioned in chapter 3.1. This was tried with an antistatic PU tube and a nonconductive PTFE tube, which were used in ES of both the 10 wt.% solution of 100BH and the 5 wt.% solution of Pell with otherwise similar spinning conditions as in the previous chapter. In both cases, deposition of ESM was observable for both TPU(U)s. However, deposition onto the antistatic PU tube was more evenly distributed across the tube surface, whereas deposition onto PTFE started at the edges of the substrate tube and moved from there towards the middle likely due to the insulating properties of PTFE. SEM images of the resulting ESM are depicted in Figure 46 for 100BH and Figure 47 for Pell.

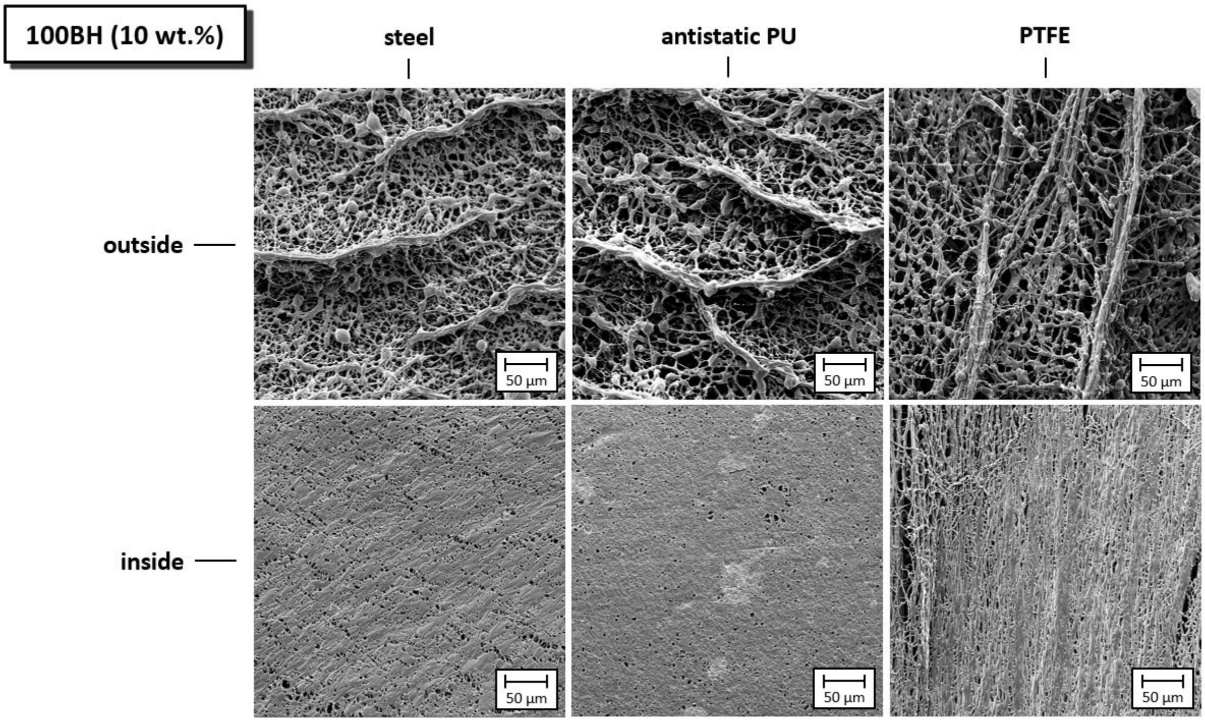

Figure 46: Scanning electron microscopy images of the outer (top) and inner (bottom) surface of electrospun material spun from a 10 wt.% solution of 100BH with HFIP at an emitter-collector distance of 150 mm onto steel (left), antistatic poly(urethane) (PU, center), and poly(1,1,2,2-tetrafluoroethylene, right).

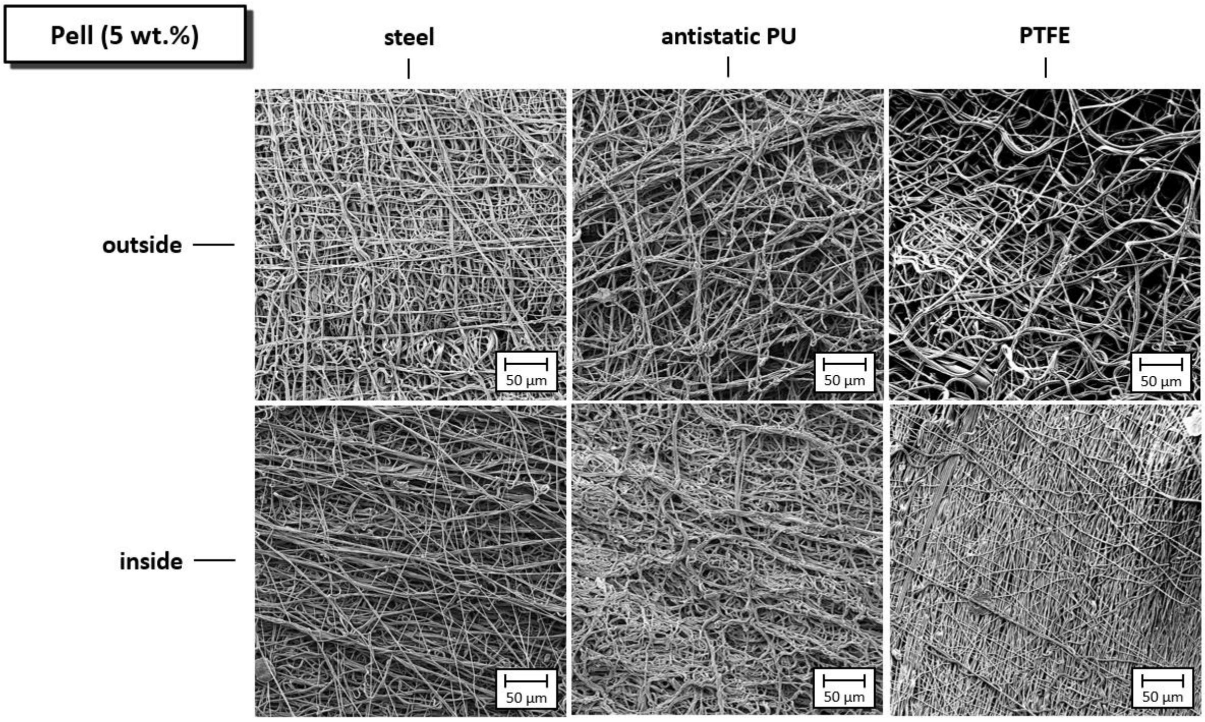

Figure 47: Scanning electron microscopy images of the outer (top) and inner (bottom) surface of electrospun material spun from a 5 wt.% solution of Pell with HFIP at an emitter-collector distance of 150 mm onto steel (left), antistatic poly(urethane) (PU, center), and poly(1,1,2,2-tetrafluoroethylene, right).

Regarding the SEM images in Figure 46, the ESMs of Pell demonstrate that proper fiber deposition is possible on all substrate materials regardless of electric conductivity. However, as can be seen in Figure 47, the use of nonconductive PTFE tubes leads to a more fibrous structure in case of 100BH on both the inner and outer surface of the ESM. ESM prepared on PTFE tubes is also easier to pull off from the substrate tube. Although, for both the antistatic PU tube and the PTFE tube, more amounts of fiber precursor are needed compared to steel. This is owed, for one, to the increased surface area of the substrate tubes compared to the steel collector on its own, which has a smaller diameter, but likely also the insulating properties of the tubes are contributing factors, since fiber deposition onto PTFE does not occur evenly during ES.

3.2.5. Electrospinning of the synthesized polymers

To compare the electrospinability of the TPU(U)s prepared in chapter 1, 10 wt.% solutions in HFIP of the synthesized TPU(U)s 100BH, 50TB, 25TB, and 25HF25TB24h were prepared, which yielded solutions with overall manageable viscosities. For Pell and 50HF32h, 5 wt.% solutions were prepared due to a too high viscosity. However, as seen in chapter 3.2.3, this concentration can lead to bead formation at least in case of 100BH and it was therefore not adopted for the other TPU(U)s.

Electrospinning was performed under similar conditions as in the previous chapter 3.2.4 with a PTFE tube as deposition substrate. The voltage was generally held at 7.5 kV except for 50TB, where a voltage of 11.5 kV was needed to achieve a stable Rayleigh jet. For all TPU(U) solutions, ES was successful and material deposition was observed with the exception of 50HF32h, where no stable jet formation was achieved and sputtering was observed. In this case an inhomogeneous ESM was produced showing irregular macroscopic structure and coloring, suggesting decomposition processes. The SEM images of the inner and outer surface of the prepared ESM are depicted in Figure 48.

The SEM images show fiber presence in the ESMs of all TPU(U)s on both the inner and outer surface. Although in case of 50HF32h, also embedded droplets are visible particularly on the outer surface. Furthermore, fibers present in the ESMs obtained from the 5 wt.% solutions of Pell and 50HF32h appear generally thicker than the fibers found in the ESMs prepared from the 10 wt.% solutions. This coincides with a higher viscosity of these otherwise diluted solutions, which may be the product of higher molecular weights as established in chapter 3.2.3 or different interactions of the polymers in solution.

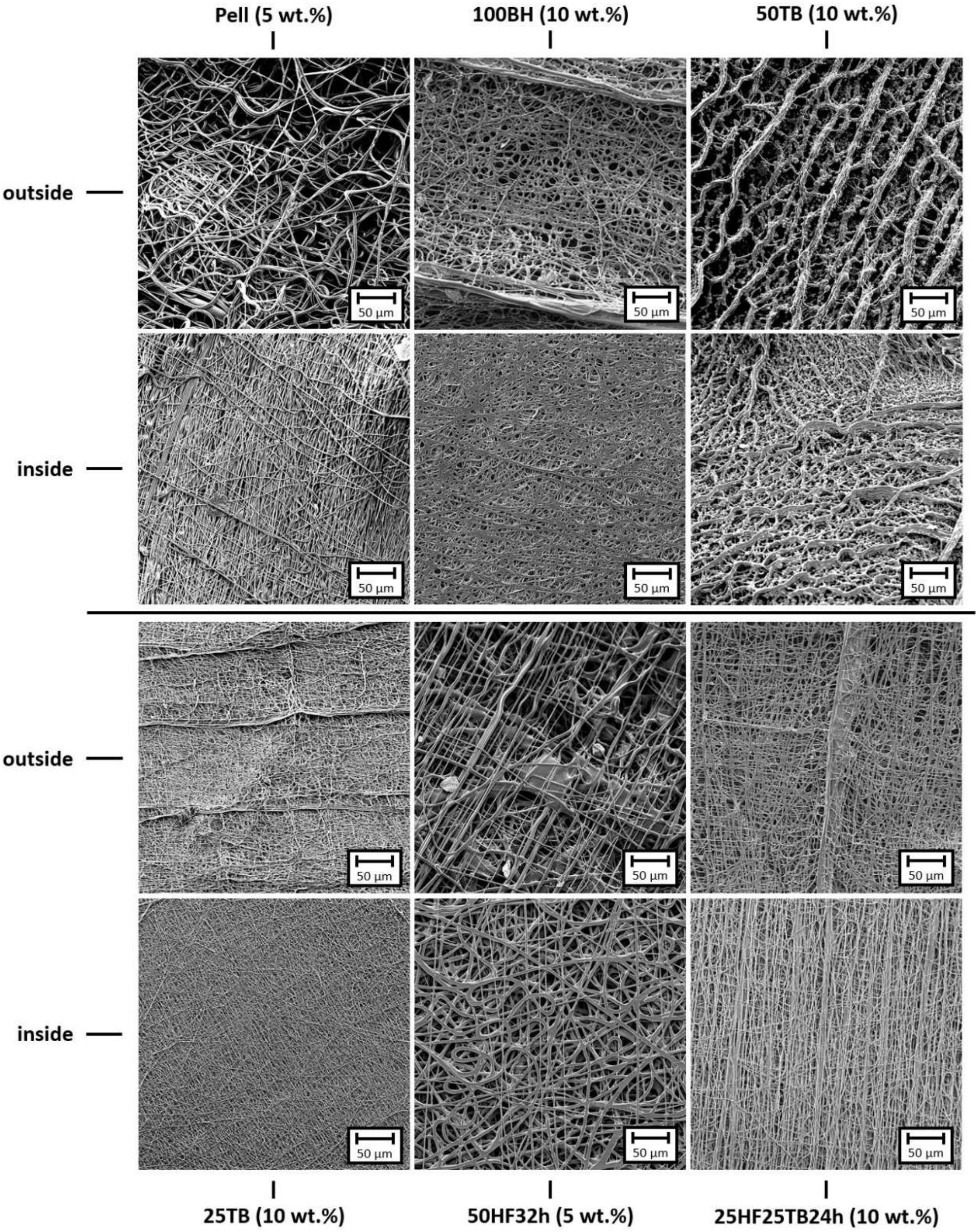

Figure 48: Scanning electron microscopy images of the outer (outside) and inner (inside) surface of electrospun material spun from a 5 wt.% solution of Pell and from 10 wt.% solutions of the TPU(U)s 100BH, 50TB, 25TB, 50HF32h, and 25HF25TB with HFIP as solvent at an emitter-collector distance of 150 mm onto a poly(1,1,2,2-tetrafluoroethylene) tube as deposition substrate and an applied voltage of 7.5 kV.

On first glance, the ESM of 50TB also shows fibers of increased diameter, however upon closer inspection, these structures are aggregates of multiple fibers wrapped around each other like in a thread and fused together (see Figure 49). Similarly, the fibers of the ESM of 100BH also appear to be somewhat fused together but to a lesser extent and without formation of significant aggregate structures. ESM of both 25TB and 25HF25TB show similar to Pell a dense network of fibers but with smaller fiber diameters.

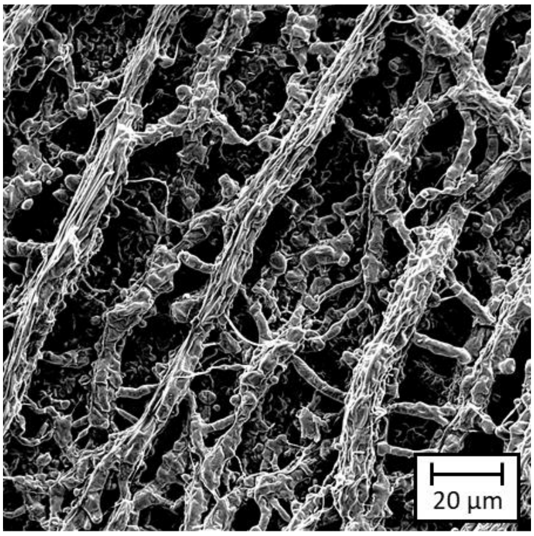

Figure 49: Scanning electron microscopy image of the fiber aggregate structures on the outer surface of the electrospun material spun from a 10 wt.% solution of 50TB with HFIP as solvent at an emitter-collector distance of 150 mm onto a poly(1,1,2,2-tetrafluoroethylene) tube as deposition substrate and an applied voltage of 7.5 kV.

3.3. Mechanical characterization of the electrospun material

3.3.1. General procedure

Due to the fibrous nature of ESMs, their mechanical properties significantly differ from those of bulk materials (see Introduction chapter 3). Furthermore, as potential vascular grafts, the most important properties are circumferential strength and burst pressure of the tubular structure regarding internal pressure, which cannot be sufficiently determined from the results of the tensile tests performed in chapter 1.4.3. Consequently, the ESMs need to be characterized on their own.[181]

However, mechanical characterization of tubular structures is not trivial particularly in ring direction and often requires special equipment.[182] In case of cardiovascular grafts, characterization procedures are specified in the standard ISO 7198:2016.[183] To determine the circumferential ring strength two methods are recommended: One involves filling the tubular test specimen with a liquid or gas at an appropriate pace, continuously increasing the internal pressure until the specimen burst. This way, stress is applied to the test specimen similar to physiological conditions and both ring strength and burst pressure can be directly determined. However, this method requires its own setup, which ensures precise pressure build-up and proper sealing of the tube ends to prevent leakage. The alternative, involves taking a ring sample of the tube, threading it onto two pins, and stretching the ESM by pulling apart the pins (see Figure 50) until failure occurs. This second method is less similar to the loading under physiological conditions, but requires less material compared to the first one, which is especially advantageous for electrospinning. Additionally, it can be performed with a conventional tensile testing setup, without the need for specialized equipment. Also the burst pressure, while not measurable directly, can be calculated with comparable results to the direct measurement according to *Laterreur et al.*[181] Because of these advantages and, admittedly, the absence of suitable equipment for the first method, mechanical characterization was done using this tensile test method.

Figure 50: Snapshot of the ring tensile test of an electrospun poly(urethane(urea)) ring specimen via pin displacement

To perform these ring tensile tests, rings of similar length are cut from the tubular ESM still resting on its deposition substrate and measured regarding their length. Afterwards, the cut ring specimens were removed from their substrate, measured regarding their ring thickness, and characterized *via* tensile testing to obtain burst pressure, elongation at break, and compliance of the ring specimens.

3.3.2. Sample preparation

Mechanical characterization was performed on ESMs prepared in chapter 3.2.5, with the exception of the ESM of 50HF32h, which was omitted due to its poor spinnability and heterogenous appearance. For the ring tensile tests, samples of similar length were cut from the obtained tubes. This was achieved using a custom 3D-printed cutting block (see Figure 51), where a given ESM, together with the PTFE tube onto which it was spun, was placed and cut to a desired length with a scalpel using the appropriate groove. Afterwards, the cut ring was taken up with a custom 3D-printed handling aid to minimize contact with the material surface, and the exact ring length was measured with a caliper. Lastly, the ESM was carefully peeled off the PTFE tube using tweezers before being stored under N_2 until further used. Upon removal, ESMs showed varying degrees of contraction, mainly in diameter, especially the ESM of Pell.

Figure 51: Equipment for removal of electrospun material. From left to right: 3D-printed cutting block with grooves at different lengths, scalpel, tweezers, collector tube with electrospun material, cut collector tube without electrospun material, removed electrospun material, and 3D-printed handling aid for tubes.

3.3.3. Tube thickness measurements

The mechanical properties of a tubular structure depend on its thickness. Therefore, developing a reliable method, which reproducibly yields meaningful and comparable results is important. In case of the prepared ESMs, this requires additional considerations: ESMs are thin (~ 100 µm) and comprised of fibers with average diameters around 1 µm. These fibers overlap randomly or form larger aggregate structures as seen in ESMs of 50TB and 100BH (see chapter 3.2.5), which create significant differences in the local thickness. Additionally, thickness gradients especially in longitudinal but also circumferential direction are formed during fabrication. Apart from the structure, the ESM is also flexible and elastically deforms easily upon application of a mechanical measuring force. Moreover, upon removal from its substrate, the ESMs contract particularly in diameter, which leads to a change in thickness between the ESM on and off the substrate. The most severe case in this regard was observed in the ESM of Pell (see Figure 52). However, the removed substrate in its loose state is subject to bending and buckling, which complicates optical measurements.

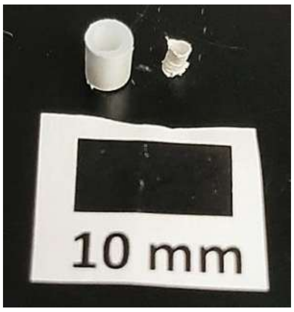

Figure 52: Electrospun material of Pell spun from a 5 wt.% solution on (left) and off (right) the PTFE deposition substrate.

Consequently, the average thickness needs to be determined for each individual specimen, which makes the procedures recommended by ISO 7198:2016,[183] involving cutting a ring sample into a sheet for measurement, not feasible. So, the thickness needs to be determined in a non-destructive way on the tubular structure. For this, either optical or mechanical measurements are possible.

Optical measurements would be ideal as they do not require direct contact with the specimen. This can be achieved using microscopy or specialized high-precision charge-coupled device (CCD) micrometers, which operate like photoelectric sensors.[181] However, these methods generally have to be performed with the ESM still on the substrate to obtain accurate results and avoid distortions due to bending or buckling of the loose ESM. Additionally, microscopy is time-consuming, as the focus has to be repeatedly adjusted and the evaluation needs to be done manually on multiple locations (see Figure 53). This quickly adds up when measuring multiple specimens of multiple ESMs. The manual evaluation can further decrease reproducibility. Meanwhile, optical micrometers with a sufficient precision are expensive, not available, and also require the ESM to remain on the substrate.

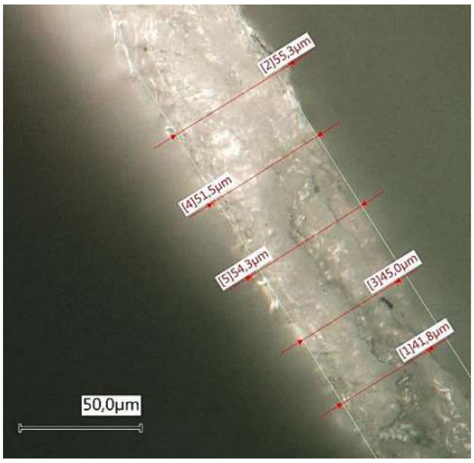

Figure 53: Depth-resolved light microscopy image of an edge segment of electrospun 100BH with digital measurements of the wall thickness

The alternative, mechanical measurement done with calipers, has the downside of requiring physical contact with the sample, which will inevitably affect the material. Additionally, the fibrous structure makes ESMs compressible, so the measured thickness is also influenced by the applied measuring force. To address both these issues, a caliper with a small, relatively constant measuring load and a broad measuring surface in contact with the sample is desired. Initially, this was tried using an available high-precision external digital caliper gauge (see Figure 54, left) with a measuring force between 0.8 N to 1.2 N on whose lower leg the electrospun tube was threaded. However, the measuring surface of the device proved too narrow for meaningful thickness measurements of the samples.

Figure 54: External digital caliper gauge (left) and setup for the thickness measurement of electrospun tubes (right)

Broadening the measuring surfaces on the other hand makes it impossible to thread the tube onto the lower leg, and only allows measurement of both tube walls pressed together. For rigid bulk materials, this would irreversibly deform the material making subsequent tensile tests less meaningful. But, in the case of the prepared ESMs, which are comprised of elastic TPU(U)s, this is less of an issue: After compressing an ESM between two plates and subsequently releasing it again, the sandwiched ESM quickly goes back into its initial shape with no visible marks from the procedure.

Following this observation, using the setup depicted on the right in Figure 54, a thickness of tubular ESMs could be determined, which matched the thickness of the same ESM measured according to ISO 7198:2016 (see Appendix chapter 3, page 135). The comparability between this mechanical thickness measurement and the optical thickness measurement performed *via* light microscopy was further confirmed using an ESM specimen of 100BH (see Appendix chapter 3, page 135). The measuring setup was inspired by a test device for the same purpose for voluminous nonwovens with a thickness below 20 mm depicted in ISO 9073-2:1996.[184]

Given that the determined thickness is not used for further calculations in the mechanical characterization of the ESM and serves primarily as a means for comparison, this method of determining a compressed thickness was deemed sufficient since the same force is applied to all specimens. The average thickness of the prepared ESM tubes, which were considered for mechanical characterization of the different TPU(U)s are summarized in Figure 55: The comparatively higher thicknesses of the tubular ESMs prepared from 100BH and 50TB are likely caused by the higher presence of aggregate structures (see Figure 49). The broad standard deviations are due to the aforementioned pronounced thickness gradient of the electrospun tubes in longitudinal direction, which is a byproduct of fabrication.

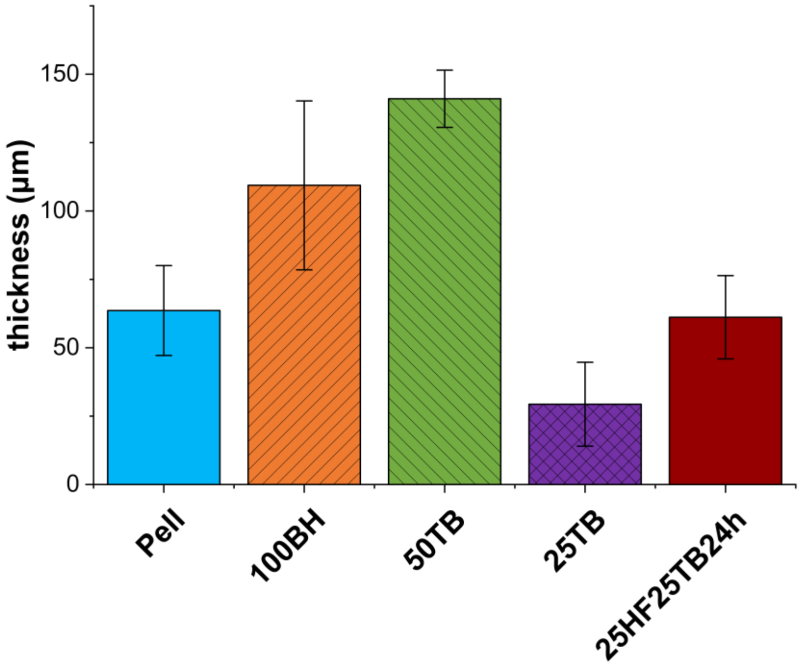

Figure 55: Average thickness of the electrospun tubes considered for mechanical characterization of the TPU(U)s Pell, 100BH, 50TB, 25TB and 25HF25TB24h.

3.3.4. Ring tensile tests

After determining their thickness in chapter 3.3.3, the prepared ring specimens were threaded onto pins for mechanical characterization following chapter 3.3.1. This was possible for all ring specimens except those prepared from Pell, which were too slim (see Figure 52) and did not fit onto the pins without getting damaged. Once the specimens were placed on the pins, the pins were pulled apart until specimen failure, and the measured force and pin displacement were recorded during the measurement.

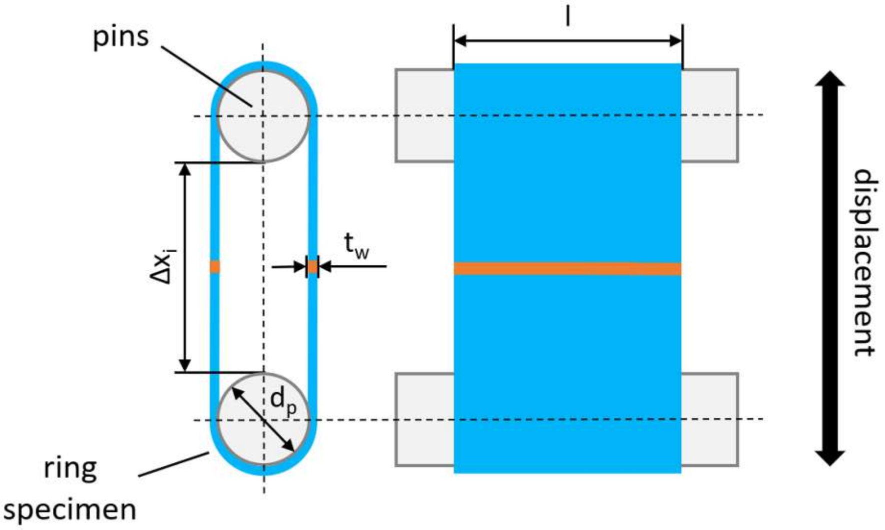

Figure 56: Schematic setup of ring tensile tests, where a ring specimen (blue) with a length l and wall thickness t_w is threaded onto two pins (grey) with a diameter d_p and pulled apart via displacement of the pins. Δx_i represents the distance between the pins at a given point in time. The orange line marks the longitudinal cross-section of the ring specimen.

Using Eq. 6 and Eq. 8 adopted from *Laterreur et al.*[181], the recorded pin displacement (Δx_i) and standard force (F) were then converted into the corresponding ring elongation (ε) and effective internal pressure (p_i): Ring elongation was determined from the change in ring circumference (u_i, see Eq. 5). p_i was determined using *Laplace's law*[185] for hollow-cylindrical objects. The effective stress acting on the ring specimen (σ_r) was determined *via* Eq. 7 using the surface of the longitudinal cross-section of the ring specimen. The unit of p_i was converted to mmHg in which blood pressure is normally specified. It is worth mentioning that the wall thickness of the ring specimen is no longer directly required for the calculation of the burst pressure *via* Eq. 7 as it is cut out of *Laplace's law* for hollow-cylindrical objects due to it being also a factor in σ_r.

The influence of pin strain (see Appendix chapter 4, page 137) was neglected in these calculations as it was deemed not significant in relation to pin displacement in the range of the measured forces considering the overall measurement uncertainty. Figure 57 compares the measuring curve regarding applied standard force and pin displacement of a ring specimen prepared from 25HF25TB24h with the subsequently calculated measuring curve of the effective internal pressure regarding ring elongation.

$$u_i = 2 \cdot \pi \cdot r_i = \pi \cdot d_p + 2 \cdot (d_p + \Delta x_i)$$ *Eq. 5*

$$\varepsilon = \frac{u_i - u_{i,0}}{u_{i,0}} \cdot 100\ \%$$ *Eq. 6*

$$\sigma_r = \frac{F}{2 \cdot l \cdot t_w}$$ *Eq. 7*

$$p_i = \frac{\sigma_r \cdot t_w}{r_i} = \frac{\pi \cdot F}{l \cdot u_i} \cdot 7500.6\ \frac{\text{mmHg}}{\text{N mm}^{-2}}$$ *Eq. 8*

r_i	… effective internal radius of ring specimen at a given pin displacement (mm)
d_p	… diameter of the sample holder pins (0.84 mm)
F	… measured standard force acting on the ring specimen at a particular elongation (N)
l	… length of the ring specimen (mm)
p_i	… internal pressure acting on the ring specimen (mmHg)
t_w	… wall thickness of the electrospun tube (mm)
u_i	… internal circumference of the ring specimen at a given pin displacement (mm)
$u_{i,0}$	… initial effective internal circumference of the ring specimen (mm)
Δx_i	… pin displacement at a given measuring point(mm)
ε	… ring elongation of the ring specimen (%)
σ_r	… effective stress acting on the ring specimen (N mm^{-2})

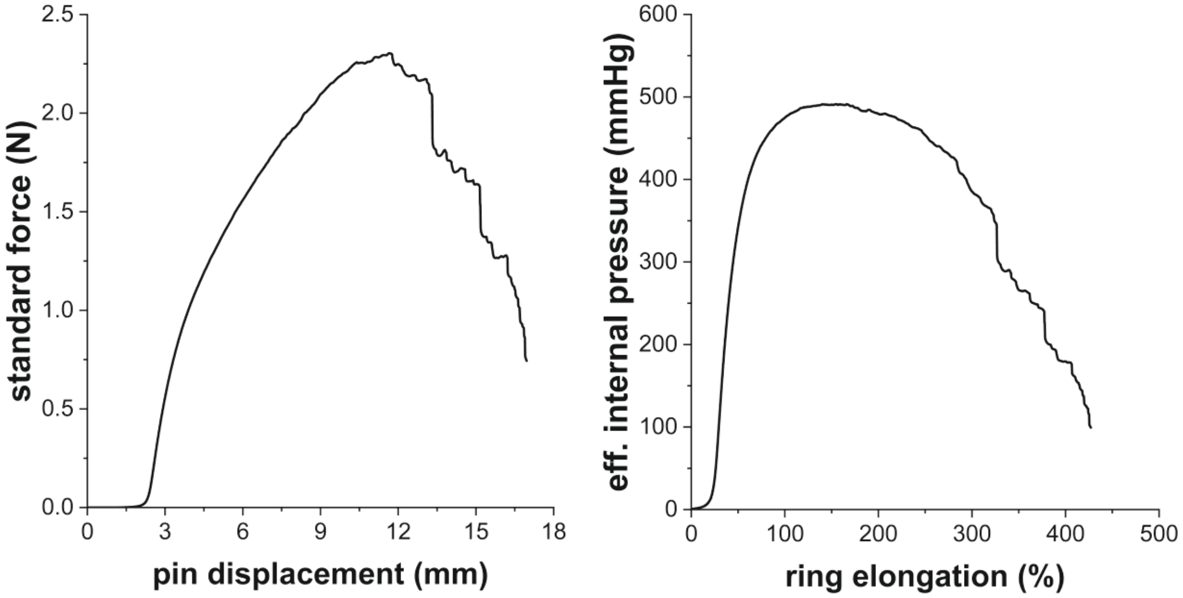

Figure 57: Measurement curves of the standard force regarding pin displacement (left) and the calculated effective internal pressure regarding ring elongation (right) for an electrospun ring specimen of 25HF25TB24h during ring tensile testing.

In general, all ring specimens showed considerable ductility during tearing, which is owed to their fibrous structure. The ring specimens were often only held together by a few threads before failure (see Figure 58), which were responsible for the prolonged necking. Conversion of the applied force and pin displacement into internal pressure and ring elongation showed a general shift of the pressure maximum (i.e., burst pressure) towards lower strains compared to the force maximum. This is because the change in pressure is not only influenced by the applied force but also the inner surface area of the ring, which depends on ring elongation.

Figure 58: Ring specimen prepared from 25TB held together by a few threads prior to failure

From the calculated internal pressure and ring strain values, the burst pressure (BP), ring strain at burst pressure ($RSBP$), and the ring strain at break (RSB) were determined. To estimate the relative change in inner graft radius under physiological conditions, the compliance (C) of the tube between 80 mmHg and 120 mmHg was calculated according to literature using Eq. 9.[129] The results are averaged across all ring specimens of a given tube and summarized in Figure 59.

$$C = \frac{u_{i,120mmHg} - u_{i,80mmHg}}{u_{i,80mmHg} \cdot (p_{i,120mmHg} - p_{i,80mmHg})} \cdot 100\ \% \qquad \text{Eq. 9}$$

C … compliance of ring specimen between 80 mmHg and 120 mmHg (% (100 mmHg)$^{-1}$)
$p_{i,j}$ … first effective internal pressure acting on ring specimen above j mmHg (mmHg)
ε_j … ring elongation of the ring specimen at $p_{i,j}$ (%)

Regarding C, the results can be divided into two groups with the ring specimens of the TPU(U)s 100BH and 50TB showing comparatively higher values between 0.2 % mmHg^{-1} and 0.3 % mmHg^{-1}. In contrast, the ring specimens prepared from 25TB and 25HF25TB24h demonstrated lower Cs at around 0.05 % mmHg^{-1}. In both cases, C similar to native tissue like in case of the saphenous vein at around 0.7 % (100 mmHg)$^{-1}$ - 2.6 % (100 mmHg)$^{-1}$ was not achieved. However, this is an issue of synthetic grafts in general and is the product of a steep increase in internal pressure as depicted on the right in Figure 57.[129]

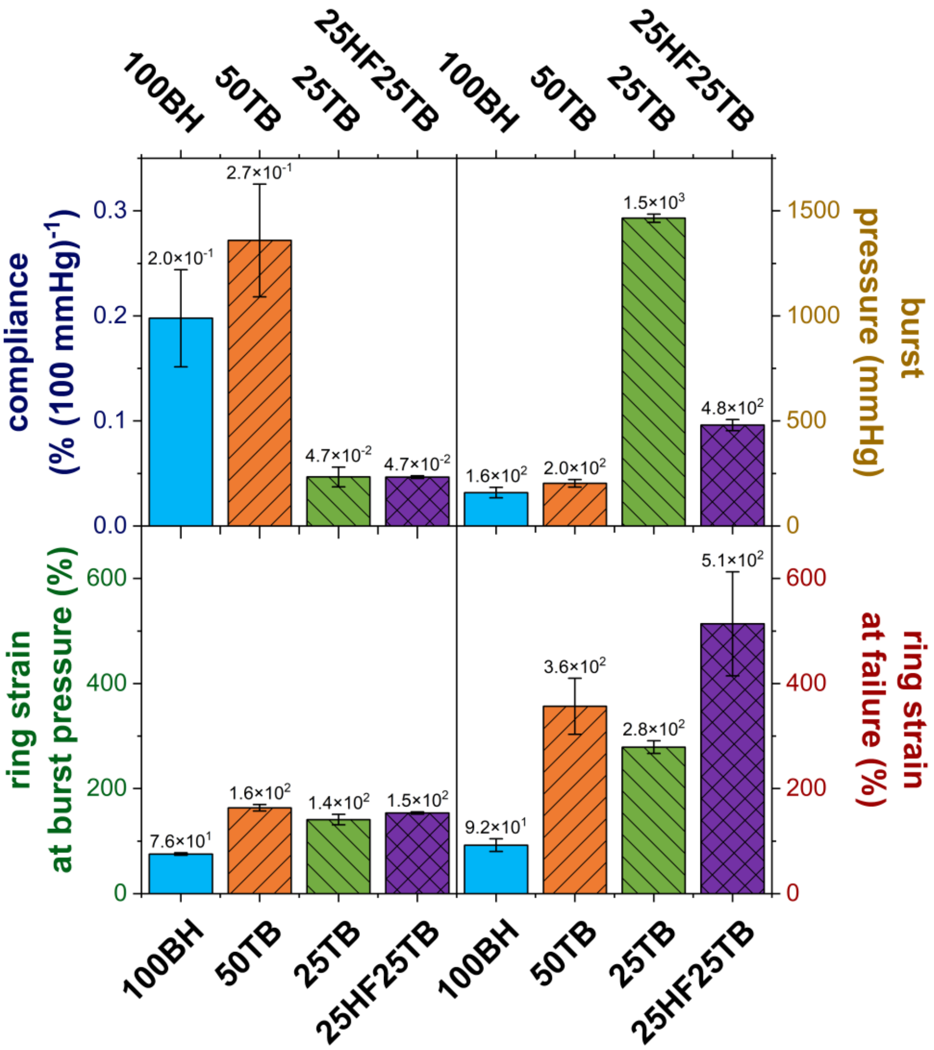

Figure 59: Summary of the compliance, burst pressure, ring strain at burst pressure, and ring strain at break of different electrospun tubes prepared by the TPU(U)s 100BH, 50TB, 25TB, 25HF25TB24h (25HF25TB) tested mechanically via ring tensile tests

The BP for all specimens was at or above 150 mmHg, and therefore higher than the worldwide age-standardized mean systolic blood pressure of men (127 mmHg) and women (122 mmHg)[186] and the onset of hypertension at 140 mmHg.[187] The highest BP of 1500 mmHg was achieved with ring specimens of electrospun 25TB, followed by those spun from 25HF25TB24h with 480 mmHg. The ring specimens of 100BH and 50TB, in contrast, showed significantly lower BPs at 150 mmHg and 200 mmHg respectively. However, since native blood vessels demonstrate burst pressures of 1600 mmHg – 2500 mmHg in case of the saphenous vein or even higher, further optimization will be necessary for all specimens.[129]

Regardless of BP, $RSBP$ was similar for all specimens at around 150 % ring strain except for the specimens electrospun from 100BH with around 75 % ring strain. RSB was highest in case of the ring specimens of 25HF25TB24h at around 500 % followed by those of 50TB and 25TB at around 300 % ring strain. The lowest RSB was found among specimens of 100BH at around 100 % ring strain.

Summary

Diseases related to the human cardiovascular system are some of the most fatal worldwide.[6] As typically noncommunicable diseases, which affect one of the largest and most vital systems in the body, they are difficult to address.[11] While preventative strategies can be taken to eliminate risk factors, treatment of such diseases often require surgical interventions. In case of atherosclerosis, which results in the occlusion of blood vessels, this can mean for example implantation of vascular bypasses.[12]

Ideally, such bypasses are themselves vascular tissue harvested from a donor or donor site of a patient. However, such transplants are often not available, which shifts the focus to synthetic vascular grafts.[128] While synthetic graft bypasses already find use for large-diameter blood vessels[15], an insufficient biocompatibility makes available materials so far unsuitable for small-diameter vascular grafts (< 6 mm).[16] To address this issue, ongoing research looks into new materials with one of the most promising being thermoplastic poly(urethane(urea)) elastomers (**TPU(U)s**), which demonstrate suitable biocompatibility, processibility, and mechanical properties.[130]

TPU(U)s are linear poly(urethane(urea))s, which form physically crosslinked networks through hydrogen bonding between urethane and urea groups. Stronger crosslinking and therefore stronger materials are formed through urea bonds, but come at the expense of poorer processibility.[104] This puts a limit on the effectively achievable mechanical properties of the final material, which is detrimental for applications with high mechanical demands such as vascular grafts. To alleviate this issue, starting with *Ehrmann*[23], our research group developed a macromolecular metamorphosis referred to as self-reinforcement, which allows the deliberate formation of urea bonds *in situ* after processing. This is achieved through incorporation of dynamic urethane and urea bonds into the polymer chain, which form hydrolysable isocyanate groups in the disassociated state (see Scheme 9). Through careful monomer design, these dynamic bonds can further be used to release small molecules during *in situ* urea formation, which also offers a pathway for targeted drug shuttling.

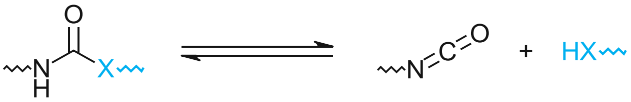

Scheme 9: General chemical structure and equilibrium of a dynamic urethane or urea bond between an isocyanate and a destabilizing functional group X with an active hydrogen

Dynamic urethane and urea bonds already studied in this regard are oxime urethane bonds (**OUBs**)[140], formed by addition of oximes and isocyanates, or hindered urea bonds (**HUBs**)[163] formed by addition of a sterically hindered amines with isocyanates. While HUBs demonstrate good self-reinforcement, the oximes released during self-reinforcement of OUBs are more interesting for potential pharmaceutical applications.[143] Aim of this thesis was therefore to look whether both HUBs and OUBs can be incorporated into the same polymer together, and what effects the combination of these two bonding motifs has on the material properties of the resulting TPU(U).

For this, multiple already established reference TPU(U)s were synthesized containing no dynamic bonds **(100BH)**[169], HUBs (**50TB, 25TB**)[163] or OUBs (**50HF, 50HS**)[140]. Synthesis followed a conventional prepolymer approach, where monomers are added stepwise to the reaction creating increasingly larger oligomers, which are ultimately linked together in a final step. The monomers typically used here were the macrodiol poly(tetrahydrofuran) (**pTHF**), the diisocyanate hexamethylene diisocyanate (**HMDI**), and the chain extender (**CE**) diol bis(2-hydroxyethyl) terephthalate (**BHET**) in substance amount ratio of 1:2:1. For formation of the HUBs, the sterically hindered diamine CE N,N′-di-tert-butylethylenediamine (**TBEDA**) was added instead of a given substance amount of BHET. Similarly, formation of OUBs was achieved by using one of the two dioxime CE bis(4-hydroxybenzaldehyde oxime)fumarate (**HBOF**) or bis(4-hydroxy-benzaldehyde oxime)succinate (**HBOS**). The chemical structures of all used monomers as well as the synthesized polymers are depicted in Figure 60. As a commercial reference served a batch of *Pellethane® 2636-80A 8* by *Lubrizol®* (**Pell**).

Syntheses of the TPU(U)s 100BH, 50TB, and 25TB were successful with yields above 70 % and desired chemical compositions regarding the ratio of incorporated monomers (BHET, TBEDA). Their number average molecular weights ($\overline{M_n}$) and weight average molecular weights ($\overline{M_w}$) determined *via* triple detection of multiple gel permeation chromatography (**GPC**) measurements were above 20 kDa and 30 kDa respectively. These values correspond to literature but are lower than for Pell, likely due to less optimized reaction conditions or higher residual moisture in the reaction environment.

Synthesis of oxime containing TPU(U)s 50HF and 50HS however proved challenging, yielding less than 40 % of solid polymer and containing only minor amounts of incorporated oxime monomer (HBOF, HBOS) based on ^{1}H-NMR. As *Ableidinger*[140] observed in the synthesis of a model oxime urethane compound, this may be the result of insufficient reaction times. Consequently, since 50HF demonstrated a better incorporation of the oxime monomer than 50HS, a second batch (50HF32h) was prepared with an extended reaction time of 32 h after addition of all monomers.

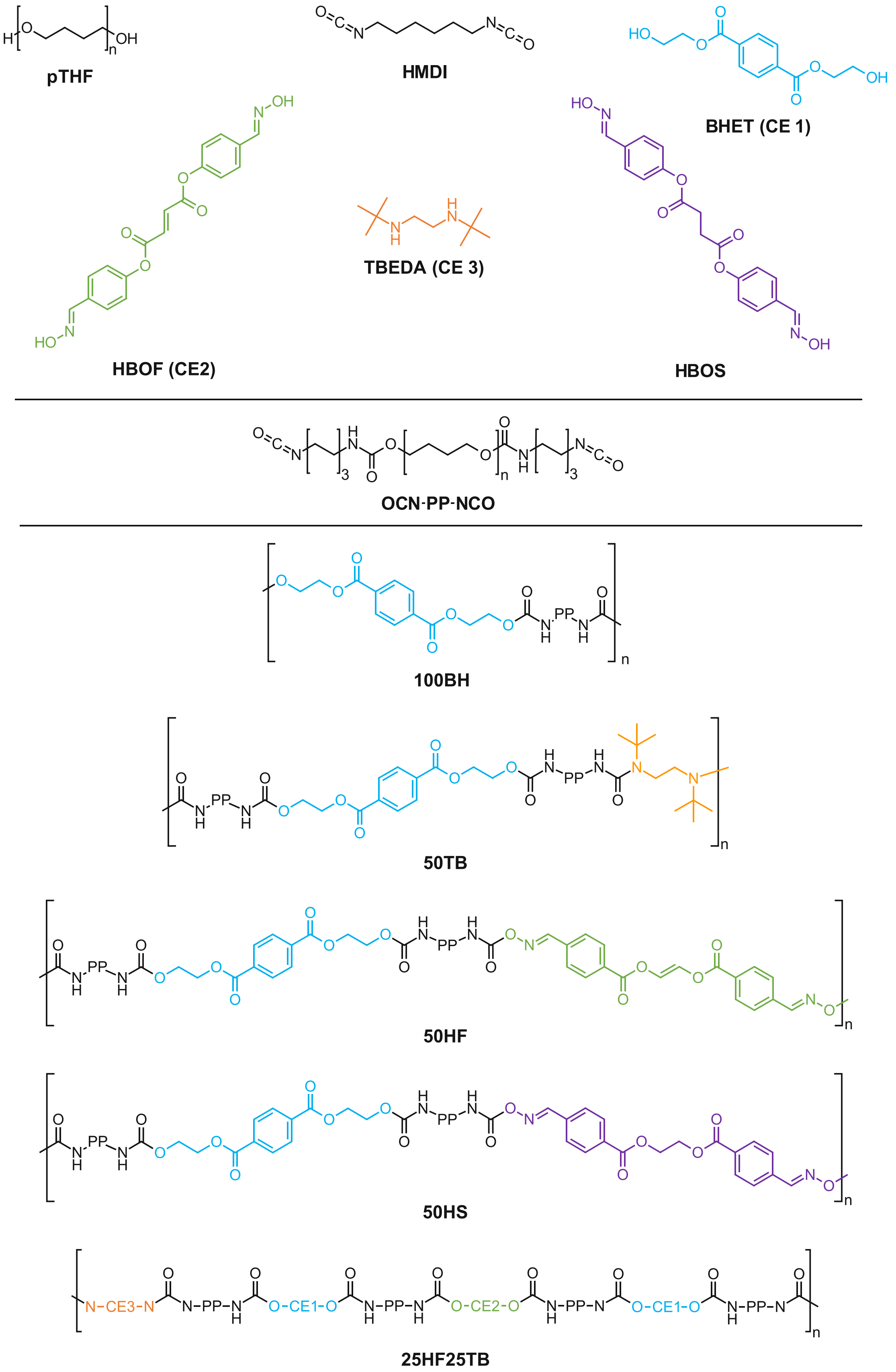

Figure 60: Chemical structures of the used monomers (poly(tetrahydrofuran) (pTHF), hexamethylene diisocyanate (HMDI), bis(2-hydroxyethyl) terephthalate (BHET, CE 1), N,N'-di-tert-butylethylenediamine (TBEDA, CE 2), bis(4-hydroxybenzaldehyde oxime)fumarate (HBOF, CE 3), and bis(4-hydroxybenzaldehyde oxime)succinate (HBOS)) and synthesized poly(urethane(urea))s (100BH, 50TB, 50HF, 50HS, and 25HF25TB).

This approach resulted in a higher yield of 62 % for 50HF32h and a more than threefold increase in the share of incorporated oxime monomer HBOF from 9 % in 50HF to 31 % in 50HF32h. The achieved $\overline{M_n}$ and $\overline{M_w}$ of 50HF32h are in the range and even slightly above those of the previously synthesized TPU(U)s with 53 kDa and 104 kDa respectively, which is likely owed to the extended reaction time.

Once the reference TPU(U)s were successfully synthesized, syntheses of TPU(U)s containing both HUBs and OUBs were performed with reaction times of 24 h (**25HF25TB24h**) and 48 h (**25HF25TB48h**) after the sequential addition of all CEs starting with BHET followed by HBOF and lastly TBEDA. Additionally, a batch, in which HBOF and TBEDA were added simultaneously rather than stepwise (**25HF25TB1st**), was also prepared. All these syntheses were successful with yields above 80 % and molecular weights corresponding to those of the synthesized reference TPU(U)s. Furthermore, also incorporation of all monomer species was achieved, though the amount of incorporated HBOF was in all cases below the target share of 25 %. Overview of all synthesized TPU(U)s, their yield, CE composition, and molecular weights are depicted in Table 5.

Table 5: Overview of the commercially obtained or synthesized thermoplastic poly(urethane(urea) elastomers (TPU(U)s), their yields, their number average ($\overline{M_n}$) and weight average ($\overline{M_w}$) molecular weights based on triple detection, as well as the ratio between their contained monomers bis(2-hydroxyethyl) terephthalate (BH), N,N'-di-tert-butyl ethylenediamine (TB), bis(4-hydroxy-benzaldehyde oxime)fumarate (HF) and bis(4 hydroxybenzaldehyde oxime)succinate (HS).

TPU(U)	**yield (%)**	**monomer ratio (%)**				**$\overline{M_n}$ (kDa)**	**$\overline{M_w}$ (kDa)**
		BH	**TB**	**HF**	**HS**		
Pell (commercial)	-	-	-	-	-	88	184
100BH[1]	85	100	-	-	-	24	34
50TB[2]	73	50	50	-	-	32	63
25TB	71	71	29	-	-	29	74
50HS	33	94	-	-	6	18	36
50HF	38	91	-	9	-	42	152
50HF32h	62	69	-	31	-	53	104
25HF25TB24h	87	52	32	16	-	20	63
25HF25TB48h	77	56	33	11	-	20	45
25HF25TB1st	82	51	41	9	-	30	80

[1]: batch 1 of three synthesized batches of 100BH
[2]: batch 1 of two synthesized batches of 50TB

After all desired TPU(U)s were obtained, their material properties were characterized using differential scanning calorimetry (**DSC**), thermogravimetric analysis (**TGA**), and tensile tests. These characterizations were performed on polymer films of the different TPU(U)s, which were solution cast using 1,1,1,3,3,3-hexafluoro-2-propanol (**HFIP**) as a solvent. A film of a polymer mixture of 50TB and 50HF32h in a ratio of 1:1 (**50HF32h+50TB**) was also prepared, to determine whether the incorporation of OUBs and HUBs into a single polymer result in different properties than a mixture of two polymers each containing only one of the two.

Regarding DSC, all synthesized TPU(U)s demonstrate broadly similar thermal properties with a glass transition temperature at around – 60 °C and an onset for melting at around 80 °C. However, while 100BH, 25TB and 50HS crystallize at around 70 °C during cooling, 50TB and 50HF32h do not and instead cold crystallization is observed during heating starting at around 30 °C. 25HF25TB24h, 25HF25TB48h, 25HF25TB1st and 50HF32h+50TB are somewhere in between with a diminished crystallization at around 50 °C and minor cold crystallization starting at around 25 °C. Pell shows a similar glass transition temperature to the other TPU(U)s but does not melt below 150 °C. Thermal degradation of the different TPU(U)s measured by TGA is also relatively similar with two main degradation stages at around 300 °C and 450 °C. Apart from 100BH and Pell, all TPU(U)s containing dynamic bonds also show minor mass losses at around 200 °C.

Tensile tests showed comparable values between reference TPU(U)s and literature. The highest stiffness was achieved by 100BH with a Young's modulus ($\boldsymbol{YM}$) of above 40 MPa. The use of additional CE species (TBEDA, HBOF, HBOS) leads to a decrease in stiffness with 25HF25TB TPU(U)s having the lowest YMs below 15 MPa, which is even slightly below Pell with around 17 MPa. Only the polymer mixture 50HF32h+50TB did not follow this trend with a YM of around 35 MPa. Conversely, elasticity increased with the incorporation of additional CE species, which resulted in elongations at break ($\boldsymbol{EAB}$) of around 1500 % for 25HF25TB TPU(U)s. The highest EAB was recorded for Pell at around 1800 %. 50HF32h+50TB and 100BH were the least elastic with around 300 % and 500 % respectively. Average ultimate tensile strengths ($\boldsymbol{UTS}$) of the synthesized TPU(U)s are at around 10 MPa with 25TB showing the highest strength with an average close to 15 MPa. The UTS of Pell is with around 35 MPa significantly higher in comparison, though this is mainly a consequence of its higher molecular weight.

Self-reinforcement of the obtained TPU(U)s was tested by cutting prepared polymer films in half with one half being stored in a dry desiccator while the other half is submerged in deionized water for conditioning. After 1 day, 7 days, or 21 days, the submerged film half was removed, dried and mechanical characterized by tensile testing together with its unconditioned counterpart. Regarding the results, conditioning led to a significant self-reinforcement of UTS (see Figure 61) particularly for 50TB with an increase of 600 % compared to unconditioned specimens after 21 days. Similarly, 25TB and 25HF25TB24h showed a self-reinforcement by around 300 %, and 25HF25TB48h and 50HF32h+50TB showed a self-reinforcement by around 100 % after 21 days. In absolute values, 25TB shows the highest UTS among the synthesized TPU(U)s with around 40 MPa after 21 days of conditioning, reaching similar values as Pell. 25HF25TB TPU(U)s show comparatively lower absolute UTS with around 20 MPa after 21 days of conditioning.

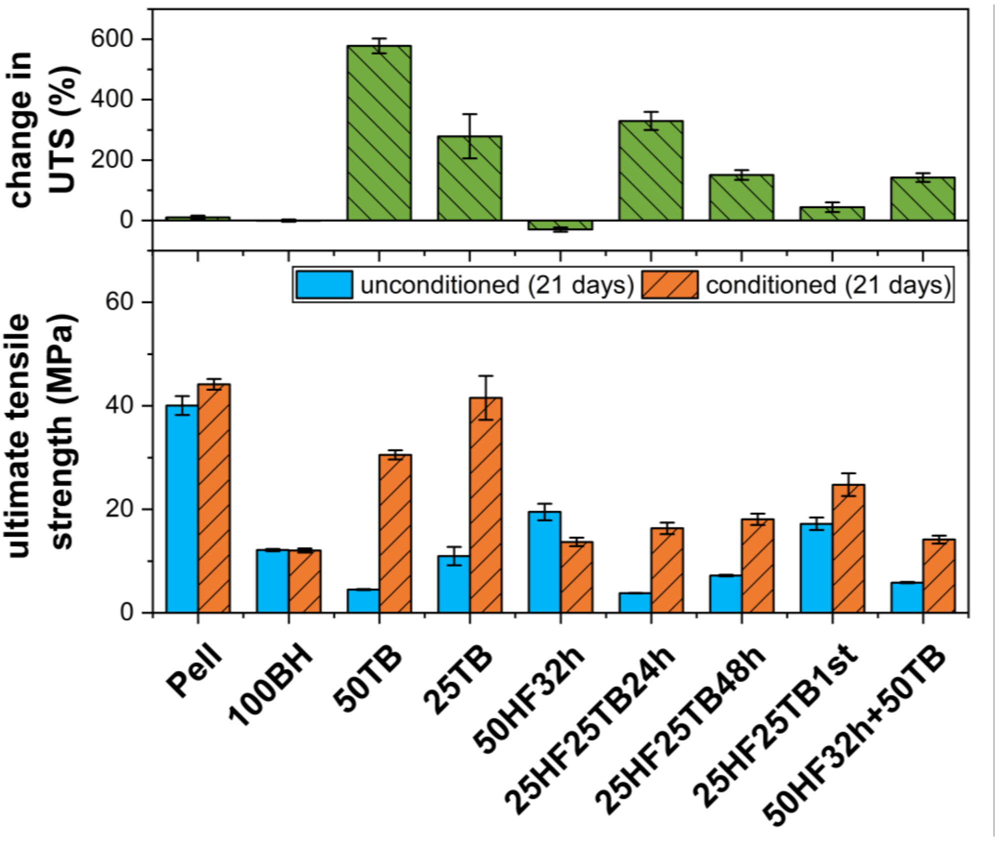

Figure 61: Summary of the results pertaining to the ultimate tensile strength (UTS) of the self-reinforcement study for various obtained thermoplastic poly(urethane(urea)) elastomers. The bottom chart summarizes the measured absolute UTS of the respective unconditioned (blue) and conditioned (orange) polymer specimens after 21 days of conditioning. The top chart depicts the resulting relative change in UTS of the conditioned specimens compared to the unconditioned ones.

YM also increased through conditioning for all TPU(U)s except Pell and 100BH, with 50TB and 25HF25TB24h showing the largest increase of around 50 % followed by 25TB, 25HF25TB48h, 25HF25TB1st, and 50HF32h+50TB with an increase of around 30 % after 21 days. *EAB* remained relatively stable for most TPU(U)s except for 50HF32h+50TB, 50TB, and 25HF25TB24h, which showed increases above 300 % after 21 days. This, however, is likely related to cold crystallization of the unconditioned specimens as seen during DSC measurements, which results in poorer elastic properties.

To further evaluate the suitability of the synthesized TPU(U)s for potential applications in vascular grafts, electrospinning (**ES**) was performed. ES is an electrohydrodynamic fiber formation technique, which uses a strong electric field to draw liquid fiber precursors launched from an emitter electrode into very thin jets that subsequently solidify into fibers with diameters in the micrometer to nanometer range. These fibers can then be collected into fibrous, nonwoven structures on an appropriate collector to produce various electrospun materials (**ESMs**).[68] In the context of this thesis, polymer solutions served as fiber precursors, which solidify through evaporation of the solvent. A steel mandrel was used as collector to produce tubular ESMs. All experiments were carried out on a custom-built electrospinning device built by *Seisenbacher*[178].

To establish a reliable working procedure for the electrospinning of the obtained TPU(U)s on this device, multiple parameters had to be fitted: Apart from setting the right voltage and current to produce an electric field strong enough to draw the polymer solution towards the collector, a corresponding flow rate of the solution into the electric field must be ensured to prevent snapping of the formed jet or trickling down of excess solution from the emitter. Furthermore, an appropriate emitter-collector distance, polymer concentration and substrate for fiber deposition have to be set. Given the good volatility, non-flammability and solubility of TPU(U)s, HFIP was chosen as solvent for the polymer solution. Ultimately, an ES method was chosen with a voltage of 7.5 kV, a current of 0.1 mA, a flow-rate of 0.5 mL h^{-1}, an emitter-collector distance of 150 mm, and a polymer concentration of 10 wt.% using a PTFE tube as deposition substrate. This method produced fibrous structures for all obtained TPU(U)s except Pell and 50HF32h, whose polymer solutions were too viscous for ES at that concentration. Instead, these two TPU(U)s were successfully electrospun from 5 wt.% solutions with otherwise identical set of ES parameters. The microstructures of all prepared ESMs were evaluated using scanning electron microscopy (**SEM**) like in Figure 62. Good results were achieved with ESMs of Pell, 25TB and 25HF25TB24h, while 100BH and 50TB showed partial condensation of fibers.

For mechanical characterization of the ESMs, ring specimens with a length of 0.5 mm were cut from the electrospun tubes and characterized regarding their thickness and tensile properties. For determination of the ring thickness, a mechanical measurement method was established, in which a cut ESM ring specimen is wedged between two microscopy cover glasses and measured using a caliper. Due to the elasticity of the material, the compression does not lead to irreversible deformation of the ring specimens, which adopt their initial shapes upon release. Consequently, this method can be performed quickly to produce reproducible and comparable results without destroying the test specimens during measurement. The average wall thickness of all ESM specimens could subsequently be determined ranging between around 25 µm in case of 25TB to around 140 µm in case of 50TB.

The tensile properties of the ring specimens were characterized following a method established by *Laterreur et al.*[181] where the prepared specimens are threaded onto two adjacent pins, which are then slowly moved apart. This allows determination of burst pressure and compliance using conventional tensile test setups without the need for specialized equipment. Results of this ring tensile tests showed the highest compliance in ESMs of 50TB and 100BH with around 0.27 % $(100\ \text{mmHg})^{-1}$ and 0.2 % $(100\ \text{mmHg})^{-1}$ respectively. Conversely, the highest burst pressure was achieved for ESMs of 25TB with close to 1500 mmHg followed by 25HF25TB24h with close to 500 mmHg. The ESMs of Pell could not be characterized due to a severe shrinkage in diameter of the material upon removal from the deposition substrate. Based on the findings, it can be hypothesized that compliance and burst pressure may be inversely correlated through fiber condensation.

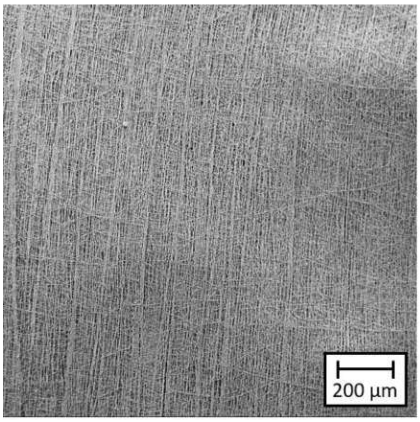

Figure 62: Scanning electron microscopy image of the outer surface of electrospun 25HF25TB24h from a 10 wt.% solution of 1,1,1,3,3,3-hexafluoro-2-propanol at 7.5 kV, 0.1 mA, 0.5 mL h^{-1}, 150 mm emitter-collector distance, collected on PTFE tube functioning as deposition substrate.

Based on all findings the following conclusions can be drawn:

- **synthesis of** thermoplastic **poly(urethane(urea))** elastomers **with up to three different chain extender** species is **possible.**
- **incorporation of both** dynamic **hindered urea and oxime urethane bonds** into poly(urethane(urea))s is **possible.**
- **thermal properties** of poly(urethane(urea))s with these two different dynamic bond motifs are **similar** to those with only one or none of those motifs. Minor differences relate only to crystallization.
- **mechanical properties** of poly(urethane(urea))s with these two different dynamic bond motifs show an **increase in elasticity and decrease in stiffness** compared to poly(urethane(urea))s with only one or none of those motifs. Ultimate tensile strength remains similar prior to self-reinforcement.
- **self-reinforcement of poly(urethane(urea))s** with these two different dynamic bond motifs can be **observed.**
- **electrospinning of** all obtained thermoplastic **poly(urethane(urea))** elastomers is **possible** and a **broadly applicable method** could be **established**, which allows electrospinning of most synthesized thermoplastic poly(urethane(urea)) elastomers under similar conditions for direct comparison with one another.
- a non-destructive, quick and reproducible **method to determine the thickness of tubular electrospun materials** could be **established.**
- a meaningful **method for mechanical characterization of tubular electrospun materials** through conventional ring tensile tests could be **established.**

As an outlook, further research should be done into varying the ratio of hindered urea bonds and oxime urethane bonds in thermoplastic poly(urethane(urea)) elastomers. As seen with 25TB in relation to 50TB and 100BH, the right amount of dynamic hindered urea bonds can lead to a significant improvement in ultimate tensile strength both prior and after self-reinforcement. Due to the low incorporation of available oxime-based chain extenders HBOS and HBOF as well as the low solubility of the resulting polymer in case of 50HF32h, it might also be useful to look for new oxime-based chain extenders, which are more reactive towards isocyanates and improve solubility of the formed poly(urethane(urea)).

In relation to electrospinning, improvements to the established procedure could be made. As seen by the significantly varying viscosities for example between a 10 wt.% solution of 100BH and Pell, using polymer concentrations based on weight percentage may not be ideal for obtaining solutions with similar properties. A potential alternative here could be concentrations based on weight average molecular weight of the individual polymer batches. Apart from concentration, the electrospinning procedure could also be further optimized towards using conductive PU deposition substrates instead of PTFE with the former being more conductive and therefore more attractive to fiber deposition.

Lastly, degradation studies for the newly synthesized TPU(U)s could be pursued. Also, self-reinforcement studies on the electrospun tubes should be conducted to determine whether the use of electrospinning has a discernable impact on the macromolecular metamorphosis of the material. Given the low thickness of the electrospun material in combination with potential degradation processes, a more viable procedure may even need to be established beforehand to enable such self-reinforcement studies on electrospun material.

Experimental

1. Polymer synthesis and characterization

1.1. Preparation of the reagents

1.1.2. Purification and water content of reagents

Recrystallization of the diol-based chain extender bis(2-hydroxyethyl) terephthalate (**BHET**) in deionized water followed common procedure[188] and crystals were isolated through suction filtration. Similarly, hexamethylene diisocyanate (**HMDI**) was distilled at 2 mbar and 85 – 90 °C head temperature and stored under N_2 atmosphere. The diamine-based chain extender *N,N′*-di-*tert*-butyl ethylenediamine (**TBEDA**) was distilled onto molecular sieves (3 Å) at 200 mbar and 170 -190 °C after 1 h of pre drying at 7 mbar and 90 °C heat bath temperature, and was subsequently stored under N_2 atmosphere until use.

For drying, poly(tetrahydrofuran) (**pTHF**), **BHET**, and the two oxime-based chain extenders bis(4-hydroxybenzaldehyde oxime) fumarate (**HBOF**), and bis(4-hydroxy-benzaldehyde oxime) succinate (**HBOS**) were dried at high vacuum and stored under N_2 atmosphere until further use.

Water content determination was done *via* coulometric Karl Fischer titration. Liquid substances were measured directly. To determine the moisture of solid substances, around 0.1 g were dissolved in around 1 mL (~ 0.94 g) of extra dry DMF, and the solution was titrated. The moisture of the solid substance was subsequently calculated *via* Eq. 10, using the concentration of the solution (c_S), as well as the water content of pure DMF ($w_{H_2O}^{DMF}$) and of the solution ($w_{H_2O}^{S}$).

$$w_{H_2O}^{A} = w_{H_2O}^{DMF} + \frac{1}{c_S}\left(w_{H_2O}^{S} - w_{H_2O}^{DMF}\right) \tag{Eq. 10}$$

c_S … concentration of used solution (g(sample) g(solvent)$^{-1}$)
m_A … mass of dissolved sample in used amount of solution for KFT (g)
m_{DMF} … mass of solvent in used solution (g)
m_S … mass of solution used for KFT (g)
$w_{H_2O}^{A}$ … water content of solid analyte in ppm (w/w)
$w_{H_2O}^{DMF}$ … water content of pure solvent *N,N*-dimethylformamide (DMF) in ppm (w/w)
$w_{H_2O}^{S}$ … water content of sample solution in ppm (w/w)

1.1.3. Molecular weight determination of poly(tetrahydrofuran)

1.1.3.1. Hydroxyl value

For titration a 0.5 N potassium hydroxide solution was prepared by dissolving 28.06 g potassium hydroxide with 1000 mL deionized water in a 1.5 L brown-glass bottle. Titrations were performed on a *Metrohm 848 Titrino Plus* and were automated using a pH electrode for detection of turnover points.

For titer determination, around 1 g of dry benzoic acid was dissolved in 100 mL of distilled methanol in a 30 mL beaker equipped with a magnetic stirring bar. After complete dissolution, the titration was started. During titration, 5 to 6 smaller turnover points and one big one, stemming from the benzoic acid, were detected, all of which could not be found in a blank measurement of pure methanol. In total, three measurements for benzoic acid were performed. Weigh-in, pH at the main turnover point, KOH consumption and calculated titer of each measurement are summarized in Table 6.

Table 6: Results of titer determination for methanolic 0.5 N potassium hydroxide titrant including the mass of used benzoic acid (m_{BA}), pH at turnover (pH_T), titrant consumption of benzoic acid (V_{BA}), and calculated titer (t) as well as their mean $\bar{t}$ and estimated standard deviation (STD).

Sample-#	m_{BA} **(mg)**	pH_T **(-)**	V_{BA} **(mL)**	t **(-)**
1	1.0075	10.8	17.4	0.947
2	0.9994	10.5	16.9	0.971
3	1.0301	10.6	17.2	0.979
			$\bar{t}$**:**	0.966
			***STD*:**	0.017

The acetic anhydride used for the hydroxyl value determination was distilled prior to use at 180 °C heat bath temperature after initial removal of existing acetic acid *via* distillation at 138 °C heat bath temperature. 3 mL distilled acetic anhydride were subsequently mixed with 9 mL dry pyridine for preparation of the acetylation agent used for hydroxyl value determination of pTHF. In case of the blank measurements, 2 mL of this agent was transferred into a dry crimp-top vial equipped with a stirring bar and was mixed with 5 mL dry pyridine. The vial was subsequently heated to 120 °C for 1.5 h. Then, 5 mL of deionized water were added to hydrolyze acetic anhydride, turning the liquid turbid, and the mixture was left for another 20 min at 120 °C. After cooling down to room temperature, titration was performed like for titer determination. In total, three blank mixtures were prepared and measured. Their pH at turnover and KOH consumption are summarized in Table 7.

The measurement of the pTHF samples occurred similar to the blanks, just that around 1.5 g of pTHF were added to the 2 mL acetylation agent and the 5 mL dry pyridine into the crimp-top vial. The hydroxyl value and number average molecular weight were subsequently determined *via* Eq. 11 and Eq. 12. using the weigh-in of pTHF and the KOH consumption of the sample, together with the mean blank value and titer.

Table 7: pH at turnover (pH_T) for the blank samples and blank consumption (V_B) of methanolic 0.5 N potassium hydroxide titrant as well as their mean $\overline{V_B}$ and estimated standard deviation (STD).

Blank-#	**pH_T (-)**	**V_B (mL)**
1	12.1	19.02
2	12.0	17.84
3	12.0	18.47
	$\overline{V_B}$:	18.45
	STD:	0.59

$$OHV = \frac{\overline{V_B} - V_S}{m_{pTHF}} \cdot c_{KOH} \cdot \bar{t} \cdot M_{KOH} \cdot f \qquad \text{Eq. 11}$$

$$\overline{M_n^{OHV}} = \frac{N_{OH} \cdot M_{KOH}}{OHV} \cdot f \qquad \text{Eq. 12}$$

OHV … hydroxyl value (mg KOH/g sample)
$\overline{V_B}$ … mean consumed methanolic 0.5 N KOH titrant for the blank (18.4482 mL)
V_S … consumed methanolic 0.5 N KOH titrant for the sample (mL)
m_{pTHF} … mass of used poly(tetrahydrofuran) (g)
c_{KOH} … concentration of methanolic KOH titrant ($0.5001 \cdot 10^{-4}$ mol mL^{-1})
$\bar{t}$ … titer of methanolic 0.5 N KOH titrant (0.963)
M_{KOH} … molecular weight of potassium hydroxide (56.1 g mol^{-1})
N_{OH} … number of hydroxy end groups per molecule pTHF (2)
f … correction factor (1000 mg g^{-1})
$\overline{M_n^{OHV}}$ … number average molecular weight of poly(tetrahydrofuran) determined *via* hydroxyl (g mol^{-1})

Calculated OHV and $\overline{M_n^{OHV}}$ for the three pTHF measurements are summarized in Table 8 together with their respective weigh-in, pH at turnover, and KOH consumption. The calculated means of $\overline{M_n^{OHV}}$ and OHV fit within the specified range given by the producer and correspond to the cited values.

Table 8: Results of molecular weight determination ($\overline{M_n^{OHV}}$) through the hydroxyl value (OHV) via back titration of acetic acid with methanolic 0.5 N potassium hydroxide titrant including the mass of used poly(tetrahydrofuran) (m_{pTHF}), pH at turnover (pH_T), titrant consumption (V_S), as well as the mean (mean) and estimated standard deviation (STD) of $\overline{M_n^{OHV}}$ and OHV.

Sample-#	**m_{pTHF} (mg)**	**pH_T (-)**	**V_S (mL)**	**OHV (mg g^{-1})**	**$\overline{M_n^{OHV}}$ (kDa)**
1	1.503	11.8	12.21	112.5	0.999
2	1.497	11.9	12.22	111.5	1.007
3	1.496	11.9	12.23	112.6	0.997
			$Mean$:	112.2	1.001
			STD:	0.6	0.005

1.1.3.2. Quantitative ^{31}P-NMR spectroscopy

To determine the molecular weight *via* quantitative ^{31}P-NMR spectroscopy, dry pTHF (31.86 g for experiment 1 and 37.72 g for experiment 2) were weighed into test vials and dissolved in 100 µL dry $CDCl_3$. Afterwards, 100 µL of dark red standard solution was added *via* piston pipette, containing 40.56 mg/mL cyclohexanol (M = 100.158 g mol^{-1}) as internal standard and 5.08 mg/mL chromium(III)acetylacetonate as relaxing agent[189] dissolved in pyridine for HCl scavenging. Separately, a solution of 100 µL of phosphorylation agent 2-chloro-4,4,5,5-tetramethyl-1,3,2-dioxaphospholane (TMDP) (yellow liquid) dissolved in 400 µL dry $CDCl_3$ was prepared in a second test tube and vortexed for homogenization. The solution containing TMDP was subsequently added to the sample solution using a syringe and the resulting mixture was vortexed again and transferred into an NMR tube. During addition, heat release and vapor formation could be observed. ^{31}P-NMR measurement was conducted around 10 minutes after addition of TMDP on a 600 MHz NMR spectrometer by *Bruker* using method *N-P31IG-MC2*.

The spectra were evaluated *via MestreNova*. Phase and baseline correction were done manually. The signal of dimerized TMDP was set to 132.20 ppm for reference and the peak integral of the phosphorylated standard at 145.0 ppm was normalized to 1.00. The signal at 147.1 ppm was attributed to the phosphorylated pTHF. After spectrum evaluation (see Figure 67 and Figure 68 in the appendix.), the number average molecular weight of pTHF was determined *via* Eq. 13.

$$\overline{M_n^{31P}} = N_{OH} \cdot \frac{I_{St}}{I_{EG}} \cdot \frac{M_{St}}{c_{St} \cdot V_{St}} \cdot m_{pTHF} \qquad \textit{Eq. 13}$$

c_{St} … concentration of the standard solution (for experiment 1 and 2: 40.56 mg mL^{-1}, for experiment 3: 63.89 mg mL^{-1})
V_{St} … used volume of internal standard solution (0.100 mL)
M_{St} … molecular weight of cyclohexanol (100.16 g mol^{-1})
I_{St} … integral over the phosphorylated cyclohexanol signal at 145.0 ppm (1.00)
I_{EG} … integral over the diphosphorylated pTHF signal at 147.1 ppm (-)
N_{OH} … number of hydroxy end groups per molecule (2)
m_{pTHF} … mass of used poly(tetrahydrofuran) (mg)
$\overline{M_n^{31P}}$ … number average molecular weight of poly(tetrahydrofuran) determined *via* quantitative ^{31}P-NMR spectroscopy (g mol^{-1})

The experiment was performed thrice. m_{pTHF}, I_{EG}, and $\overline{M_n^{31P}}$ of the individual measurements are summarized in Table 9. The calculated $\overline{M_n^{31P}}$ fit within the specification range given by the producer and are close to the stated analysis results.

Table 9: Results of the quantitative ^{31}P-NMR spectroscopy measurements including mass of used poly(tetrahydrofuran) (m_{pTHF}), integral over the diphosphorylated pTHF signals (I_{EG}), and number average molar mass of poly(tetrahydrofuran) ($\overline{M_n^{31P}}$) as well as the mean ($mean$) and estimated standard deviation (STD) of $\overline{M_n^{31P}}$

Experiment-#	m_{pTHF} **(mg)**	I_{EG} **(-)**	$\overline{M_n^{31P}}$ **(kDa)**
1	31.86	1.57	1.00
2	37.72	1.83	1.02
3	34.1	1.07	1.00
		$\boldsymbol{Mean}$**:**	1.01
		$\boldsymbol{STD}$**:**	0.01

1.2. Synthesis of reference polymers

1.2.1. General procedure

TPU(U) synthesis follows a general procedure adopted from literature[23, 169], which was adapted to fit the individual systems of chain extenders. Prior to synthesis, all reagents and solvents are prepared and characterized according to chapter1.1. For the approach, weigh-ins of the diisocyanate HMDI and the different chain extenders (CE) are adjusted to the amount of weighed macrodiol pTHF with an assumed molecular weight of 1000 g/mol, which was determined based on the results of chapter 1.1.3. The reaction is performed in a 100 mL dry three-necked round-bottom flask equipped with stirring bar, stop-cock, and two glass plugs under N_2 atmosphere. To avoid moisture from the environment during transfers, conventional Schlenk techniques are employed. Prior to addition, all added substance except for pTHF and the catalyst $Sn(Oct)_2$ were each dissolved in either 10 mL of dry DMF in the case of HMDI or 5 mL of dry DMF in case of the individual CEs in a dry crimp top vial.

For synthesis, the reaction vessel is assembled hot, charged with 1 eq. of dry pTHF, and further dried for 1 h *in vacuo* at 90 °C. After cooling back down to room temperature, the prepared DMF solution of 2 eq. HMDI, and 3 drops of catalyst $Sn(Oct)_2$ are added to pTHF *via* syringe in N_2 counter flow. To ensure a quantitative transfer, the vial of the HMDI solution is subsequently rinsed twice with a total volume of 5 mL dry DMF. Then, the reaction is heated to 60 °C and stirred for 3 h. Afterwards, a total of 1 eq. CE is added to the reaction in a similar procedure to HMDI. If multiple CEs are part of the formulation, they are added sequentially in their respective equivalents: After addition of the first CE, the reaction is stirred for 3 h at a set temperature before the second CE is added. A third CE is added the following day after the reaction was stirred over night at set temperature. Set temperature is 60 °C for the diol BHET and room temperature as soon as the dynamic chain extenders TBEDA, HBOS, or HBOF are present. After all chain extenders are added, the reaction is stirred overnight at set temperature.

For work-up, the reaction mixture was filled into a dropping funnel and added dropwise into a beaker of 1 L dry Et_2O under stirring at room temperature, leading to white precipitation. To ensure a complete transfer of the polymer, the reaction vessel and dropping funnel were subsequently rinsed with a total of 10 mL dry DMF. Afterwards, the precipitate was isolated using a suction filter, washed with additional dry Et_2O and residual solvent was removed *in vacuo*. For characterization, ^{1}H-NMR, ATR-FTIR, and GPC were performed to determine chemical composition and molecular weight.

1.2.2. Synthesized polymers and yields

1.2.2.1. 100BH

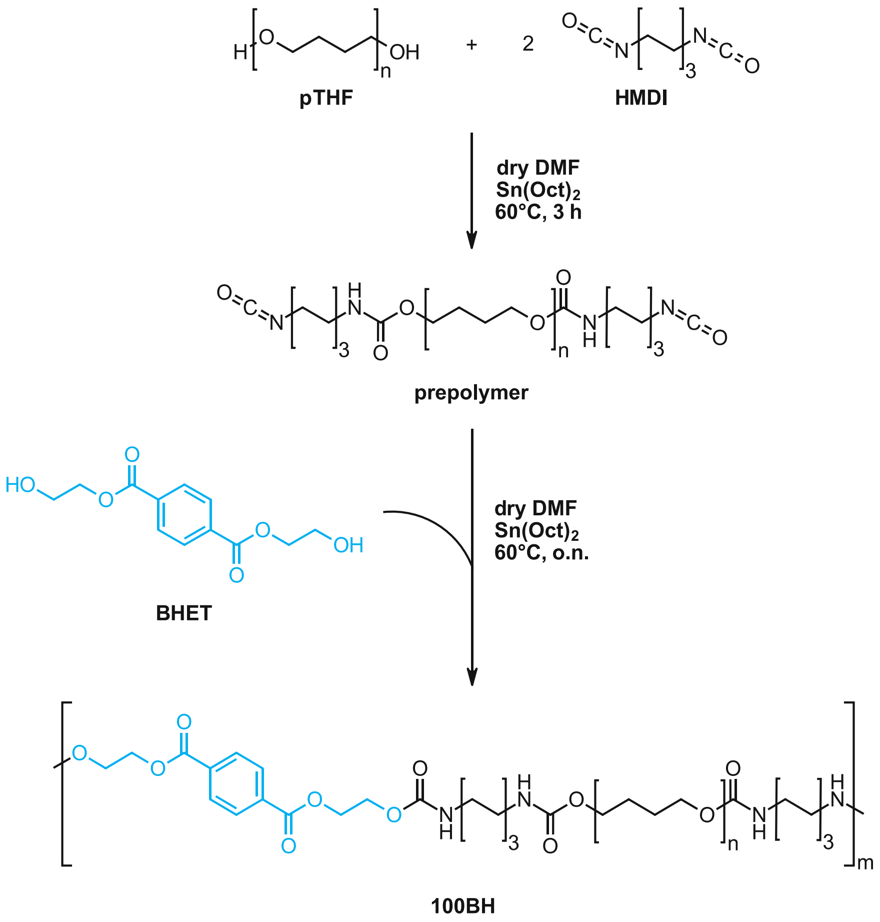

Scheme 10: Reaction scheme for the synthesis of 100BH

Table 10: Used molecular weights (M), equivalences (eq.), amount of substance (n), mass (m), and volume (V) of reagents, catalyst, solvent, and precipitation agent for the synthesis of 100BH

Reactant	*M* (g/mol)	*eq.* (-)	*n* (mmol)	*m* (g)	*V* (ml)
pTHF	1000.0	1.00	5.01	5.0105	-
HMDI	168.2	2.00	10.03	1.6864	-
BHET	254.2	1.00	5.01	1.2744	-
Cat.:	**Sn(Oct)$_2$**				3 drops
Solvent:	**DMF (dry)**				10+5+5+5
Prec. agent:	**Et$_2$O (dry)**				1500

Synthesis and work-up of 100BH followed general procedure established in chapter 1.2.1, but with a single chain extender BHET, which was added at once. The reaction scheme is depicted in Scheme 1. The reaction was kept at 60 °C over the entire time, and was stirred overnight prior to work-up.

Yield: 6.53 g (81.9 %, white granules)

^{1}H NMR (400 MHz, CDCl$_3$, ppm) δ = 8.14 – 8.05 (m, 4H, BHET- CH^{ar}), 4.91 (s, 2H, urethane-NH), 4.74 (s, 2H, urethane-NH), 4.50 (s, 4H, BHET-OCH$_2$), 4.40 (s, 4H, BHET-OCH$_2$), 4.04 (s, 4H, pTHF-(C=O)O-CH$_2$), 3.47 – 3.34 (m, 60H, pTHF-ROCH$_2$), 3.21 – 3.09 (m, 9H, HMDI-NCH$_2$), 1.70 – 1.54 (m, 65H, pTHF-CH$_2$), 1.52 – 1.41 (m, 9H, HMDI- CH$_2$), 1.36 – 1.27 (m, 9H, HMDI- CH$_2$).

IR (ATR, cm^{-1}) 3319.17 ($\upsilon_{N\text{-}H,urethane}$), 2938.64 ($\upsilon_{C\text{-}CH}$), 2858.42 ($\upsilon_{O\text{-}CH}$), 2800.65 ($\upsilon_{N\text{-}CH}$), 1715.11 ($\upsilon_{C=O}$), 1683.03 ($\upsilon_{C=O}$), 1535.26 ($\upsilon_{C=C}$) 1261.06 ($\upsilon_{C\text{-}O\text{-}C,urethane}$), 1103.55 ($\upsilon_{C\text{-}O\text{-}C,ether}$)

GPC (conventional calibration): M_n = 20 kDa, M_w = 33 kDa, PDI = 1.9

GPC (triple detection, dn/dc = 0.078): M_n = 32 kDa, M_w =56 kDa, PDI = 2.2

1.2.2.2. 50TB

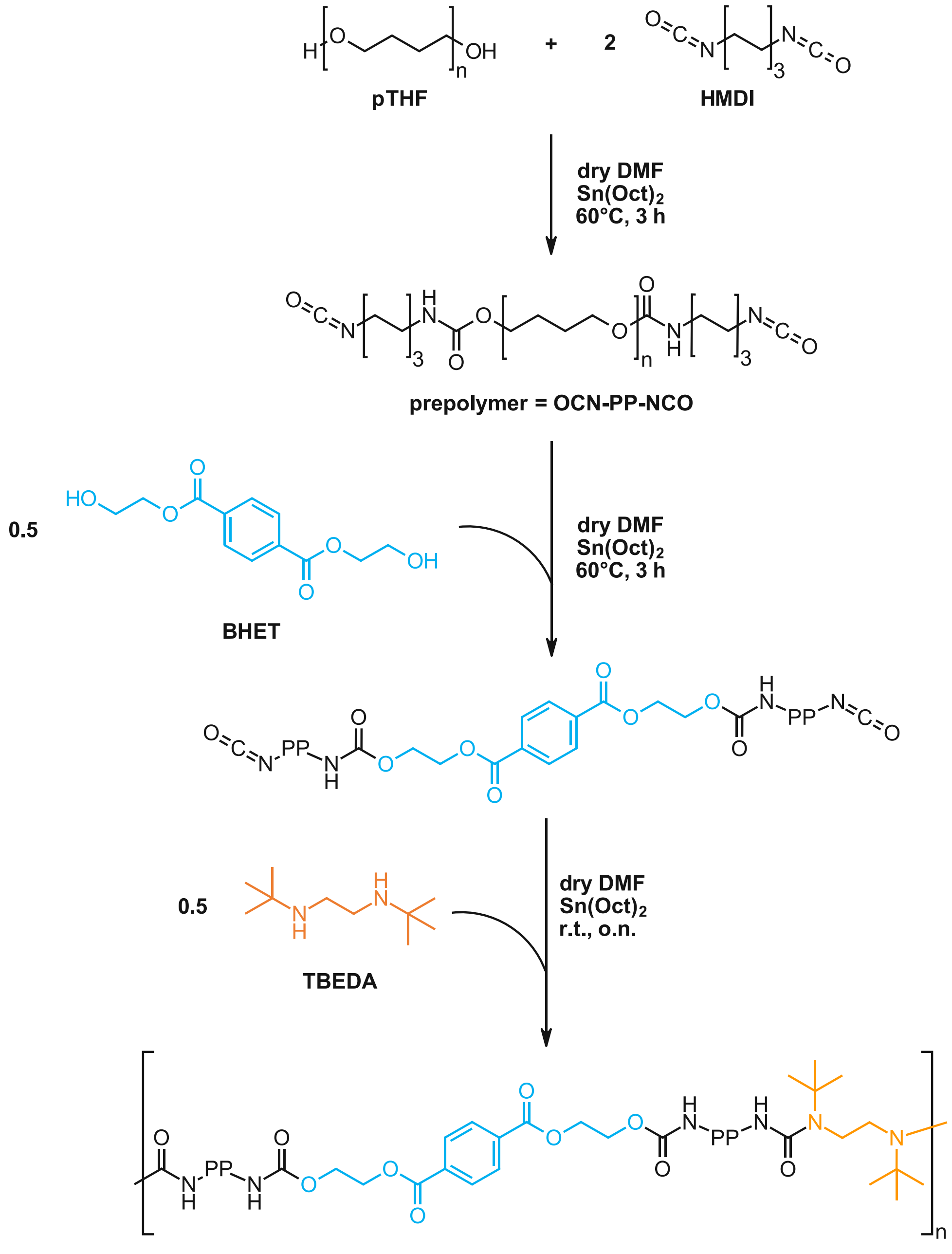

Scheme 11: Reaction scheme for the synthesis of 50TB

Table 11: Used molecular weights (M), equivalences (eq.), amount of substance (n), mass (m), and volume (V) of reagents, catalyst, solvent, and precipitation agent for the synthesis of 50TB.

Reactant	M (g/mol)	$eq.$ (-)	n (mmol)	m (g)	V (ml)
pTHF	1000.0	1.00	5.10	5.1024	-
HMDI	168.2	2.00	10.21	1.7174	-
BHET	254.2	0.50	2.55	0.6490	-
TBEDA	172.3	0.50	2.55	0.4398	-
Cat.:	**Sn(Oct)$_2$**				3 drops
Solvent:	**DMF (dry)**				10+5+5+5+5+5
Prec. agent:	**Et$_2$O (dry)**				1500

Synthesis and work-up of 50TB followed general procedure established in chapter 1.2.1 but with two chain extenders BHET and TBEDA in a ratio of 1:1. The reaction scheme is depicted in Scheme 11. The reaction was kept at 60 °C until addition of TBEDA and then at room temperature. BHET was added first and after an additional 3 h of stirring at 60 °C, TBEDA was added at room temperature. Afterwards, the reaction was left stirring overnight and work-up was performed the following day.

Yield: 5.77 g (73.0 %, white granules)

^{1}H NMR (400 MHz, CDCl$_3$, ppm) δ = 8.13 – 8.06 (m, 4H, BHET- CH^{ar}), 5.95 (s, 2H, urea-NH), 4.92 (s, 2H, urethane-NH), 4.83 (s, 1H, urea-NH), 4.73 (s, 3H, urethane-NH), 4.50 (s, 4H, BHET_OCH$_2$), 4.40 (s, 4H, BHET-OCH$_2$), 4.05 (s, 9H, pTHF-ROCH$_2$), 3.68 – 3.30 (m, 119H), 3.25 (s, 4H, TBEDA-NCH$_2$), 3.21 – 3.09 (m, 18H, HMDI-NCH$_2$), 1.70 – 1.54 (m, 129H, pTHF-CH$_2$), 1.54 – 1.04 (m, 57H, HMDI-CH$_2$ and TBEDA-CH$_3$).

IR (ATR, cm^{-1}) 3320.89 ($\upsilon_{\text{N-H,urethane}}$), 2937.18 ($\upsilon_{\text{C-CH}}$), 2854.43 ($\upsilon_{\text{O-CH}}$), 2796.62 ($\upsilon_{\text{N-CH}}$), 1717.59 ($\upsilon_{\text{C=O}}$), 1684.38 ($\upsilon_{\text{C=O}}$), 1534.54 ($\upsilon_{\text{C=C}}$) 1250.04 ($\upsilon_{\text{C-O-C,urethane}}$), 1103.83 ($\upsilon_{\text{C-O-C,ether}}$)

GPC (conventional calibration): M_n = 39 kDa, M_w = 77 kDa, PDI = 2.0

GPC (triple detection, dn/dc = 0.064): M_n =32 kDa, M_w = 63 kDa, PDI = 2.0

1.2.2.3. 25TB

Table 12: Used molecular weights (M), equivalences (eq.), amount of substance (n), mass (m), and volume (V) of reagents, catalyst, solvent, and precipitation agent for the synthesis of 25TB.

Reactant	M (g/mol)	$eq.$ (-)	n (mmol)	m (g)	V (ml)
pTHF	1000	1.00	5.18	5.1765	-
HMDI	168	2.00	10.36	1.7423	-
BHET	254	0.75	3.88	0.9876	-
TBEDA	172	0.25	1.29	0.2231	-
Cat.:	**Sn(Oct)$_2$**				3 drops
Solvent:	**DMF (dry)**				15+10+10
Prec. agent:	**Et$_2$O (dry)**				1500

Synthesis and work-up of 25TB followed general procedure established in chapter 1.2.1 but with two chain extenders BHET and TBEDA in a ratio of 3:1. As such, the synthesis follows the same scheme as 50TB (see Scheme 11) but with different stoichiometric ratios of 0.75 eq. BHET and 0.25 eq. TBEDA instead of 0.5 eq. for both BHET and TBEDA.

Yield: 5.78 g (71.1 %, white flakes)

^{1}H NMR (400 MHz, CDCl$_3$, ppm) δ = 8.09 (d, J = 4.6 Hz, 4H, BHET ar-CH), 5.95 (t, J = 21.4 Hz, 1H, NH-urea), 5.10 – 4.66 (m, 5H, NH-urethane/urea), 4.51 (s, 4H, BHET-OCH$_2$), 4.40 (s, 4H, BHET-OCH$_2$), 4.05 (s, 6H, pTHF urethane-OCH$_2$), 3.42 – 3.38 (m, 78H, pTHF-ROCH$_2$), 3.28 – 2.84 (m, 14H, HMDI/TBEDA NCH$_2$), 1.71 – 1.54 (m, 86H, pTHF CCH$_2$), 1.52 – 1.04 (m, 32H, HMDI/TBEDA CCH$_2$).

IR (ATR, cm^{-1}) ν = 3320.61 ($\upsilon_{N\text{-}H,urethane}$), 2939.17 ($\upsilon_{C\text{-}CH}$), 2858.21 ($\upsilon_{N\text{-}CH}$), 2801.6 ($\upsilon_{C=O}$), 1718.54 ($\upsilon_{C=O}$), 1686.18 ($\upsilon_{C=C}$), 1249.73 ($\upsilon_{C\text{-}O\text{-}C,urethane}$), 1104.12 ($\upsilon_{C\text{-}O\text{-}C,ether}$)

GPC (conventional calibration): M_n = 42 kDa, M_w = 93 kDa, PDI = 2.2

GPC (triple detection, dn/dc = 0.062): M_n = 29 kDa, M_w = 74 kDa, PDI = 2.6

1.2.2.1. 50HS

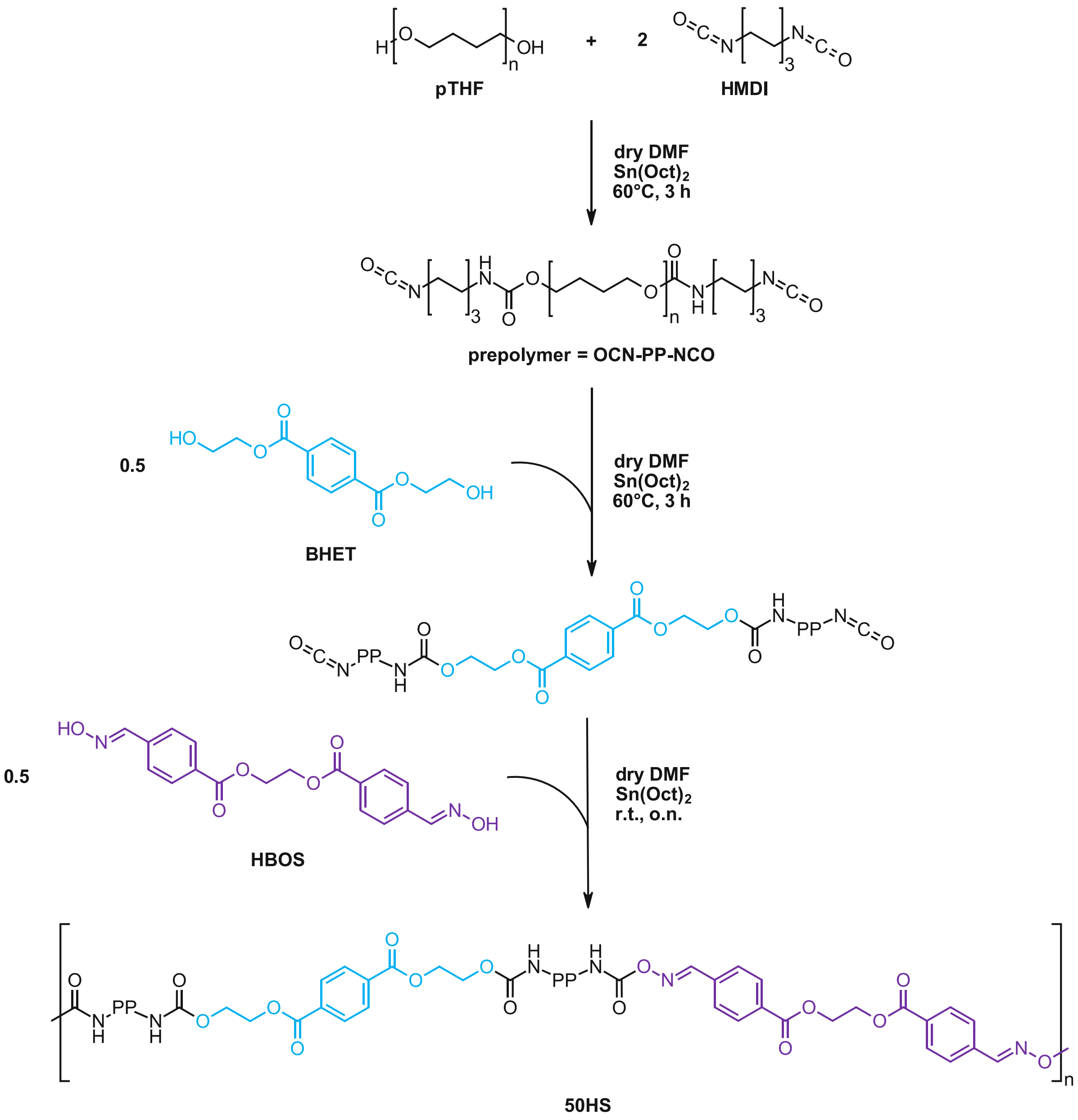

Scheme 12: Reaction scheme for the synthesis of 50HS

Table 13: Used molecular weights (M), equivalences (eq.), amount of substance (n), mass (m), and volume (V) of reagents, catalyst, solvent, and precipitation agent for the synthesis of 50HS.

Reactant	***M*** **(g/mol)**	***eq.*** **(-)**	***n*** **(mmol)**	***m*** **(g)**	***V*** **(ml)**
pTHF	1000	1.0	5.13	5.1267	-
HMDI	168	2.0	10.26	1.7255	-
BHET	254	0.5	2.56	0.6521	-
HBOS	356	0.5	2.56	0.9139	-
Cat.:	**$Sn(Oct)_2$**				3 drops
Solvent:	**DMF (dry)**				15+10+10
Prec. agent:	**Et_2O (dry)**				1500

Synthesis and work-up of 50HS followed general procedure established in chapter 1.2.1 but with two chain extenders BHET and HBOS in a ratio of 1:1. The reaction scheme is depicted in Scheme 12. The reaction was kept at 60 °C until addition of HBOS and then at room temperature. BHET was added first and after an additional 3 h of stirring at 60 °C, HBOS was added at room temperature. Afterwards, the reaction was left stirring overnight and work-up was performed the following day.

Yield: 2.79 g (33.1 %, white chunks)

^{1}H NMR (400 MHz, $CDCl_3$, ppm) δ = 8.31 (s, 2H, HBOS oxime-CH), 8.10 (d, *J* = 4.4 Hz, 60H, BHET ar-CH), 7.75 – 7.65 (m, 3H, HBOS ar-CH), 7.23 – 7.07 (m, 5H, HBOS ar-CH), 6.50 – 6.17 (m, 2H, urea-NH), 4.91 (s, 28H, urethane-NH), 4.73 (s, 44H, urethane-NH), 4.51 (s, 62H, BHET CH_2), 4.40 (s, 62H, BHET CH_2), 4.28 – 3.82 (m, 96H, pTHF urethane-OCH_2), 3.63 – 3.33 (m, 1112H, pTHF $COCH_2$), 3.33 – 2.87 (m, 202H, HMDI NCH_2), 1.82 – 1.54 (m, 1222H, pTHF CCH_2), 1 1.53 – 1.20 (m, 376H, HMDI CH_2).

IR (ATR, cm^{-1}) ν = 3315.64 ($\upsilon_{N\text{-}H,urethane}$), 2938.91 ($\upsilon_{C\text{-}CH}$), 2859.19 ($\upsilon_{N\text{-}CH}$), 2802.54 ($\upsilon_{C=O}$), 1714.25 ($\upsilon_{C=O}$), 1683.1 ($\upsilon_{C=C}$), 1251.07 ($\upsilon_{C\text{-}O\text{-}C,urethane}$), 1104.14 ($\upsilon_{C\text{-}O\text{-}C,ether}$)

GPC (conventional calibration): M_n = 26 kDa, M_w = 49 kDa, PDI = 1.9

GPC (triple detection, dn/dc = 0.062): M_n = 18 kDa, M_w = 36 kDa, PDI = 2

1.2.2.2. 50HF

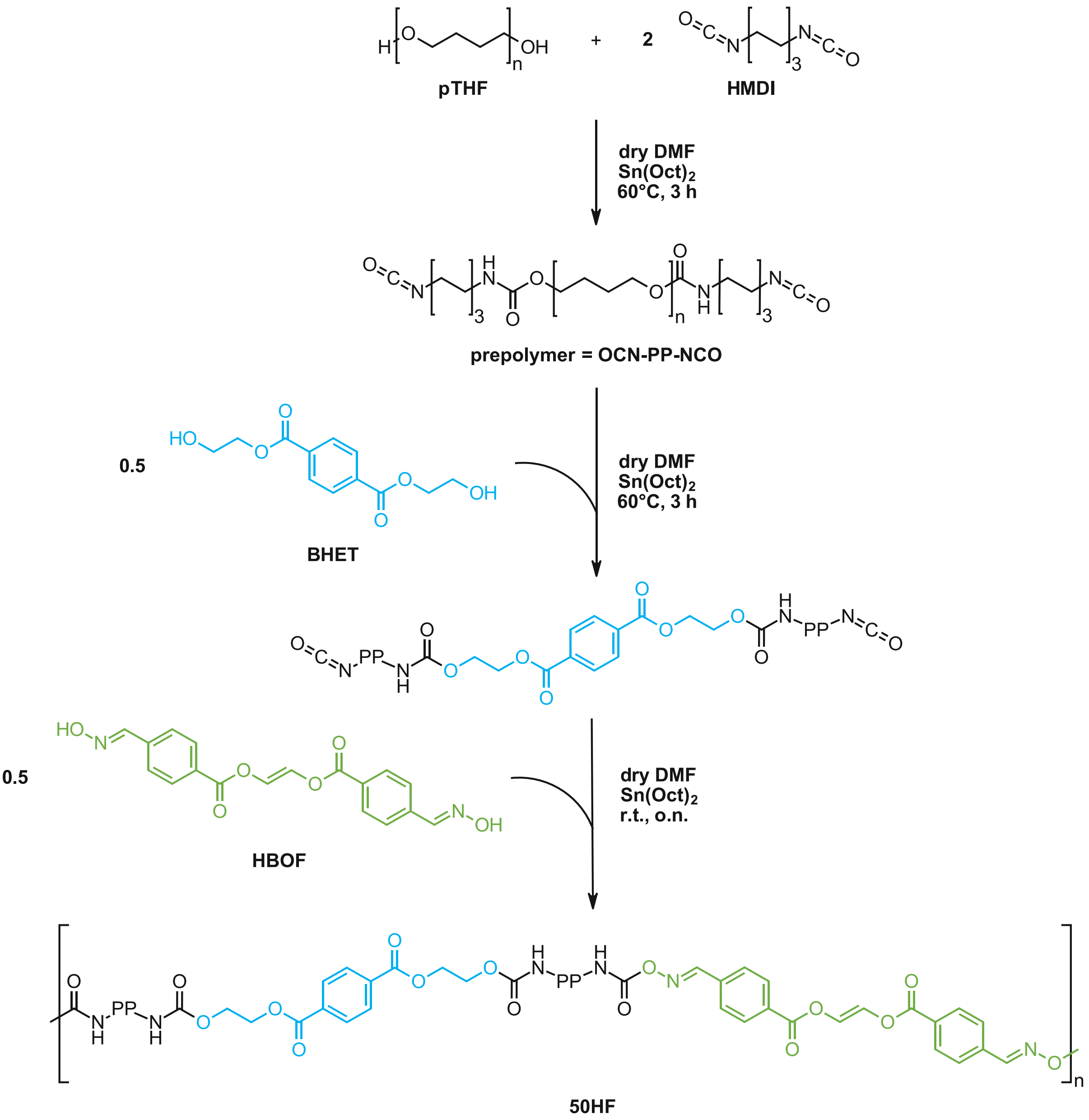

Scheme 13: Reaction scheme for synthesis of 50HF

Table 14: Used molecular weights (M), equivalences (eq.), amount of substance (n), mass (m), and volume (V) of reagents, catalyst, solvent, and precipitation agent for the synthesis of 50HF.

Reactant	M (g/mol)	$eq.$ (-)	n (mmol)	m (g)	V (ml)
pTHF	1000	1.0	5.08	5.0814	-
HMDI	168	2.0	10.17	1.7103	-
BHET	254	0.5	2.54	0.6463	-
HBOF	354	0.5	2.54	0.9007	-
Cat.:	**Sn(Oct)$_2$**				3 drops
Solvent:	**DMF (dry)**				15+10+10
Prec. agent:	**Et$_2$O (dry)**				1500

Synthesis and work-up of 50HF followed general procedure established in chapter 1.2.1 but with two chain extenders BHET and HBOF in a ratio of 1:1. The reaction scheme is depicted in Scheme 13. The reaction was kept at 60 °C until addition of HBOF and then at room temperature. BHET was added first and after an additional 3 h of stirring at 60 °C, HBOF was added at room temperature. Afterwards, the reaction was left stirring overnight and work-up was performed the following day.

Yield: 3.17 g (38.0 %, yellow chunks)

^{1}H NMR (400 MHz, CDCl$_3$, ppm) δ = 8.33 (s, 2H, HBOS oxime-CH), 8.09 (d, J = 4.5 Hz, 40H, BHET ar-CH), 7.78 – 7.71 (m, 4H, HBOS ar-CH), 7.25 – 7.22 (m, 4H. HBOS ar-CH), 7.20 – 7.16 (m, 2H, HBOS C=CH), 6.53 – 6.18 (m, 1H, urea-NH), 4.92 (s, 15H, urethane-NH), 4.74 (s, 30H, urethane-NH), 4.51 (s, 40H, BHET CH$_2$), 4.40 (s, 40H, BHET CH$_2$), 4.04 (s, 65H, pTHF urethane-OCH$_2$), 3.64 – 3.21 (m, 828H, pTHF OCH$_2$), 3.20 – 2.86 (m, 120H, HMDI, NCH$_2$), 1.86 – 1.53 (m, 904H, pTHF CCH$_2$), 1.52 – 1.28 (m, 248H, HMDI CCH$_2$).

IR (ATR, cm^{-1}) ν = 3317.75 ($\upsilon_{\text{N-H,urethane}}$), 2938.44 ($\upsilon_{\text{C-CH}}$), 2856.88 ($\upsilon_{\text{N-CH}}$), 2799.91 ($\upsilon_{\text{C=O}}$), 1714.38 ($\upsilon_{\text{C=O}}$), 1683.15 ($\upsilon_{\text{C=C}}$), 1250.33 ($\upsilon_{\text{C-O-C,urethane}}$), 1103.85 ($\upsilon_{\text{C-O-C,ether}}$)

GPC (conventional calibration): M_n = 42 kDa, M_w = 148 kDa, PDI = 3.6

GPC (triple detection, dn/dc = 0.055): M_n = 42 kDa, M_w = 152 kDa, PDI = 3.6

1.2.3. Chemical composition

For determination of the chemical composition of the polymer chains, the integral ratios of the individual CEs relative to their corresponding number of hydrogens were compared in the ^{1}H-NMR spectrum. For the diol BHET, the signal of its four aromatic hydrogens at 8.10 ppm was used and for the dioximes HBOF and HBOS, the signal of the two hydrogens at the aldehyde oxime carbons at around 8.3 ppm were chosen. Since the signals of TBEDA partially overlap with those of HMDI, their integrals were calculated out of the combined areas of HMDI and TBEDA signals for more representative results: At around 3.1 ppm, signals of multiples of 4 HMDI and 4 TBEDA hydrogens connected to carbon atoms next to nitrogen overlap. Their individual contributions to the combined integral (I_{NCH_2}) correspond to their overall amount incorporated into the polymer relative to each other (k_T, k_H) following Eq. 14. Similarly, the signals at around 1.4 ppm of multiples of 8 HMDI and 18 TBEDA hydrogen atoms connected to carbon atoms next to carbon also contribute differently to the combined integral (I_{CCH_2}) depending on their relative prevalence in the polymer chain compared to one another following Eq. 15. Using these two equations, the contributed integral of TBEDA ($I^T_{NCH_2}$) to the combined integral I_{NCH_2} can be determined *via* Eq. 16.

$$I_{NCH_2} = k_T \cdot 4 + k_H \cdot 4 \qquad \text{Eq. 14}$$

$$I_{CCH_2} = k_T \cdot 18 + k_H \cdot 8 \qquad \text{Eq. 15}$$

$$I^T_{NCH_2} = k_T \cdot 4 = \frac{2 \cdot I_{CCH_2} - 4 \cdot I_{NCH_2}}{5} \qquad \text{Eq. 16}$$

k_T … share of TBEDA in relation to HMDI in the combined integral (-)
k_H … share of HMDI in relation to TBEDA in the combined integral (-)
I_{NCH_2} … combined hydrogen integrals of HMDI and TBEDA on carbon atoms next to nitrogen at around 3.1 ppm (-)
I_{CCH_2} … combined hydrogen integrals of HMDI and TBEDA on carbon atoms next to carbon at around 1.4 ppm (-)
$I^T_{NCH_2}$ … hydrogen integral of TBEDA on carbon atoms next to nitrogen at around 3.1 ppm (-)

1.2.4. Molecular weight

For gel permeation chromatography (GPC), polymer samples were prepared by dissolving 4 mg to 8 mg polymer in 2 mL tetrahydrofuran (THF) spiked with 0.5 mg mL^{-1} butylhydroxytoluol (BHT) as flow rate marker to yield solutions between 2 mg mL^{-1} and 4 mg mL^{-1}. The prepared solutions were subsequently filtered into 1.5 mL crimp neck vials through a 0.2 µm PTFE syringe filter by *Pall Corporation*. Due to poor solubility of the TPU(U) 50HF in pure THF, it was necessary to dissolve the weighed amount of 50HF initially in 0.2 mL of 1,1,1,3,3,3-hexafluoro-2-propanol (HFIP) overnight prior to complete dissolution in at least 2 mL THF.

1.3. Synthesis of oxime-containing polymers

1.3.1. Synthesized polymers and yields

1.3.1.1. 50HF32h

Table 15: Used molecular weights (M), equivalences (eq.), amount of substance (n), mass (m), and volume (V) of reagents, catalyst, solvent, and precipitation agent for the synthesis of 50HF48h.

Reactant	M (g/mol)	$eq.$ (-)	n (mmol)	m (g)	V (ml)
pTHF	1000	1.0	5.07	5.0674	-
HMDI	168	2.0	10.13	1.7047	-
BHET	254	0.5	2.53	0.6442	-
HBOF	354	0.5	2.53	0.8977	-

Cat.:	**Sn(Oct)$_2$**	3 drops
Solvent:	**DMF (dry)**	15+10+10
Prec. agent:	**Et$_2$O (dry)**	1000

Synthesis and work-up of 50HF32h was done similar to 50HF (see chapter 1.2.2.2) and followed general procedure established in chapter 1.2.1. However, this time, the reaction was left stirring for32 h after the addition of HBOF rather than overnight.

Yield: 5.15 g (62 %, off-white chunks)

^{1}H NMR (400 MHz, CDCl$_3$, ppm) δ = 8.34 (s, 2H, HBOF oxime-CH), 8.10 (d, J = 4.6 Hz, 22H, BHET ar-CH), 7.79 – 7.46 (m, 8H, HBOF ar-CH), 6.97 – 6.81 (m, 2H, HBOF C=CH), 6.57 – 6.16 (m, 1H, urethane-NH), 4.93 (s, 9H, urethane-NH), 4.75 (s, 15H, urethane-NH), 4.51 (s, 18H, BHET CH$_2$), 4.41 (s, 18H, BHET CH$_2$), 4.05 (s, 31H, pTHF urethane-OCH$_2$), 3.60 – 3.28 (m, 395H, pTHF OCH$_2$), 3.20 - 3.09 (m, 60H, HMDI NCH$_2$), 1.61 (s, 425H, pTHF CCH$_2$), 1.51 – 1.21 (m, 136H, HMDI CCH$_2$).

IR (ATR, cm^{-1}) ν = 3320 ($\upsilon_{\text{N-H,urethane}}$), 2937 ($\upsilon_{\text{C-CH}}$), 2854 ($\upsilon_{\text{N-CH}}$), 2796 ($\upsilon_{\text{C=O}}$), 1715 ($\upsilon_{\text{C=O}}$), 1682 ($\upsilon_{\text{C=C}}$), 1250.33 ($\upsilon_{\text{C-O-C,urethane}}$), 1103 ($\upsilon_{\text{C-O-C,ether}}$)

GPC (conventional calibration): M_n = 23 kDa, M_w = 58 kDa, PDI = 2.9

GPC (triple detection, dn/dc = 0.070): M_n = 53 kDa, M_w = 104 kDa, PDI = 2.0

1.3.1.2. 25HF25TB24h

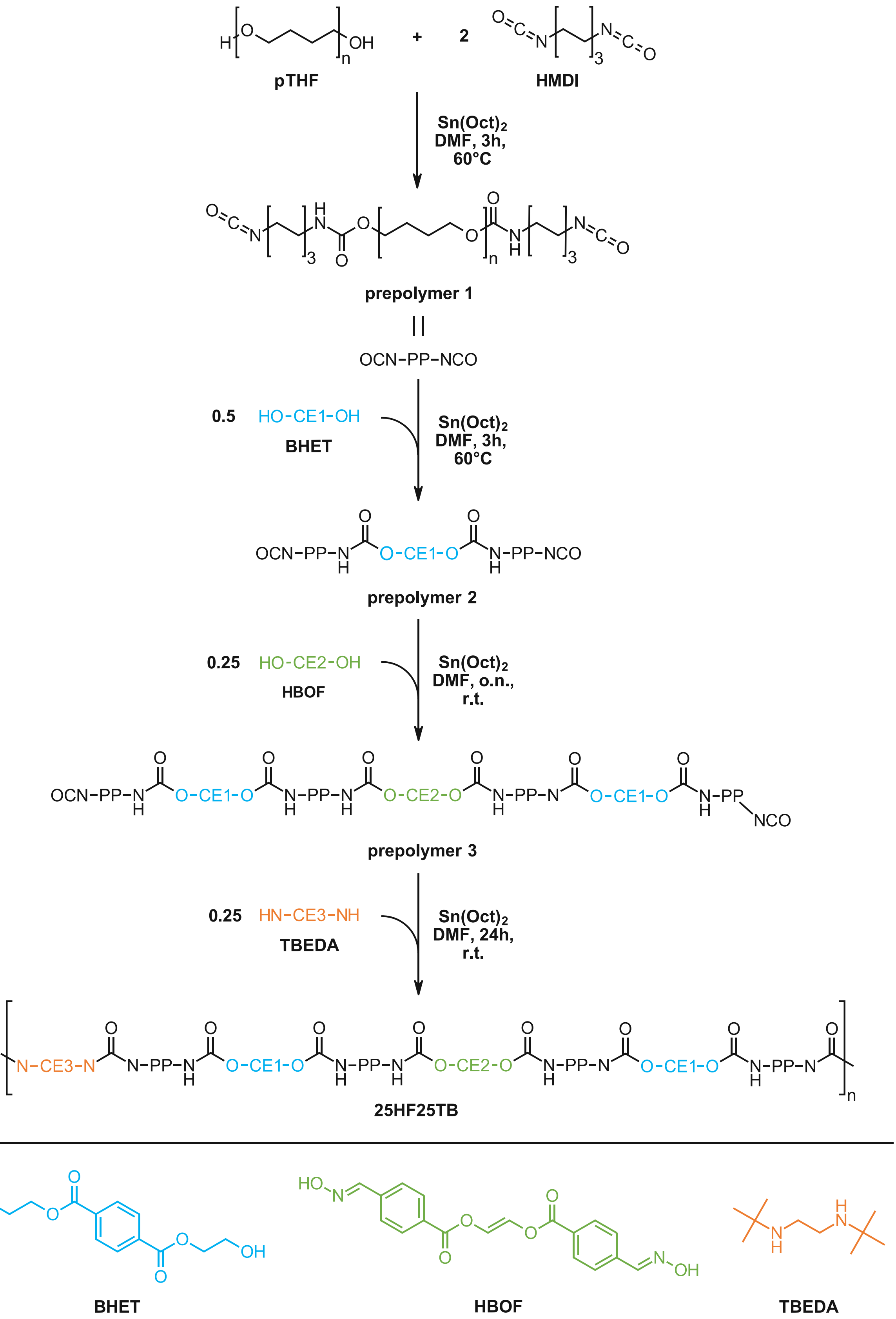

Scheme 14: Reaction scheme for synthesis of 25HF25TB24h

Table 16: Used molecular weights (M), equivalences (eq.), amount of substance (n), mass (m), and volume (V) of reagents, catalyst, solvent, and precipitation agent for the synthesis of 25HF25TB24h.

Reactant	M (g/mol)	$eq.$ (-)	n (mmol)	m (g)	V (ml)
pTHF	1000	1.0	5.039	5.0363	-
HMDI	168	2.0	10.078	1.6951	-
BHET	254	0.5	2.519	0.6406	-
HBOF	172	0.25	1.260	0.4463	
TBEDA	354	0.25	1.260	0.2171	-
Cat.:	**$Sn(Oct)_2$**				3 drops
Solvent:	**DMF (dry)**				15+5+5+10
Prec. agent:	**Et_2O (dry)**				1000

Synthesis and work-up of 25HF25TB24h followed general procedure established in chapter 1.2.1 but with three chain extenders BHET, HBOF, and TBEDA in a ratio of 2:1:1. The reaction scheme is depicted in Scheme 14. The reaction was kept at 60 °C until addition of HBOF, and then at room temperature. BHET was added first and after an additional 3 h of stirring at 60 °C, HBOF was added at room temperature. Afterwards, the reaction was left stirring overnight at room temperature. The following day, TBEDA was added and stirring at room temperature continued for additional 24 h, followed by reaction and work-up.

Yield: 7.02 g (87 %, off-white flakes)

^{1}H NMR (400 MHz, $CDCl_3$, ppm) δ = 8.37 – 8.12 (m, 2H, HBOF oxime-CH), 8.11 – 8.08 (m, 13H, BHET ar-CH), 7.83 – 7.48 (m, 4H, HBOF ar-CH), 7.41 – 7.28 (m, 2H, HBOF ar-CH), 7.25 – 7.17 (m, 2H, HBOF ar-CH), 7.01 – 6.86 (m, 2H, HBOF C=CH), 6.34 – 5.82 (m, 6H, urethane/urea-NH), 4.92 – 4.81 (m, 9H, urethane/urea-NH), 4.73 (s, 11H, urethane/urea-NH), 4.51 (s, 13H, BHET CH_2), 4.41 (s, 13H, BHET CH_2), 4.05 (s, 29H, pTHF OCH_2), 3.48 – 3.34 (m, 353H, pTHF OCH_2), 3.29 – 3.05 (m, 62H, HMDI/TBEDA NCH_2), 1.83 – 1.55 (m, 390H, pTHF CCH_2), 1.55 – 1.26 (m, 150H, HMDI-CH_2 and TBEDA CCH_3).

IR (ATR, cm^{-1}) ν = 3320 ($\upsilon_{\text{N-H,urethane}}$), 2938 ($\upsilon_{\text{C-CH}}$), 2855 ($\upsilon_{\text{N-CH}}$), 2797 ($\upsilon_{\text{C=O}}$), 1716 ($\upsilon_{\text{C=O}}$), 1259 ($\upsilon_{\text{C-O-C,urethane}}$), 1103 ($\upsilon_{\text{C-O-C,ether}}$)

GPC (conventional calibration): M_n = 31 kDa, M_w = 76 kDa, PDI = 2.5

GPC (triple detection, dn/dc = 0.075): M_n = 20 kDa, M_w = 63 kDa, PDI = 3.2

1.3.1.3. 25HF25TB48h

Table 17: Used molecular weights (M), equivalences (eq.), amount of substance (n), mass (m), and volume (V) of reagents, catalyst, solvent, and precipitation agent for the synthesis of 25HF25TB48h.

Reactant	***M*** **(g/mol)**	***eq.*** **(-)**	***n*** **(mmol)**	***m*** **(g)**	***V*** **(ml)**
pTHF	1000	1.0	5.367	5.3637	-
HMDI	168	2.0	10.733	1.8053	-
BHET	254	0.5	2.683	0.6822	-
HBOF	172	0.25	1.342	0.4754	
TBEDA	354	0.25	1.342	0.2312	-
Cat.:	**Sn(Oct)$_2$**				3 drops
Solvent:	**DMF (dry)**				15+5+5+10
Prec. agent:	**Et$_2$O (dry)**				1000

Synthesis and work-up of 25HF25TB48h was done similar to 25HF25TB24h (see 1.3.1.2) and followed general procedure established in chapter 1.2.1 The reaction scheme resembles the one in Scheme 14. However, here, the reaction was left stirring for 48 h after the addition of HBOF rather than just for 24 h prior to work-up.

Yield: 6.59 g (77 %, off-white flakes)

^{1}H NMR (400 MHz, CDCl$_3$, ppm) δ = 8.62 – 8.17 (m, 2H, HBOF oxime-CH), 8.14 – 7.99 (m, 20H, BHET ar-CH), 7.96 – 7.38 (m, 4H, HBOF ar-CH), 7.36 – 7.30 (m, 1H, HBOF ar-CH), 7.23 – 7.06 (m, 3H, HBOF ar-CH), 7.07 – 6.76 (m, 2H, HBOF C=CH), 6.43 – 5.67 (m, 5H, urethane/urea-NH), 5.40 – 4.81 (m, 17H, urethane/urea-NH), 4.75 (s, 15H, urethane/urea-NH), 4.50 (s, 20H, BHET CH$_2$), 4.40 (s, 20H, BHET CH$_2$), 4.04 (m, 44H, pTHF OCH$_2$), 3.66 – 3.30 (m, 553H, pTHF OCH$_2$), 3.29 – 3.00 (m, 94H, HMDI/TBEDA NCH$_2$), 2.09 – 1.53 (m, 600H, pTHF CCH$_2$), 1.49 – 1.24 (m, 218H, HMDI/TBEDA CCH$_2$)

IR (ATR, cm^{-1}) ν = 3322 ($\upsilon_{\text{N-H,urethane}}$), 2938 ($\upsilon_{\text{C-CH}}$), 2856 ($\upsilon_{\text{N-CH}}$), 2799 ($\upsilon_{\text{C=O}}$), 1720 ($\upsilon_{\text{C=O}}$), 1250 ($\upsilon_{\text{C-O-C,urethane}}$), 1103 ($\upsilon_{\text{C-O-C,ether}}$)

GPC (conventional calibration): M_n = 28 kDa, M_w = 58 kDa, PDI = 2.1

GPC (triple detection, dn/dc = 0.067): M_n = 20 kDa, M_w = 45 kDa, PDI = 2.2

1.3.1.4. 25HF25TB1st

Table 18: Used molecular weights (M), equivalences (eq.), amount of substance (n), mass (m), and volume (V) of reagents, catalyst, solvent, and precipitation agent for the synthesis of 25HF25TB1st.

Reactant	M (g/mol)	$eq.$ (-)	n (mmol)	m (g)	V (ml)
pTHF	1000	1.0	5.445	5.4418	-
HMDI	168	2.0	10.889	1.8316	-
BHET	254	0.5	2.722	0.6921	-
HBOF	172	0.25	1.361	0.4823	
TBEDA	354	0.25	1.361	0.2345	-

Cat.:	**Sn(Oct)$_2$**	3 drops
Solvent:	**DMF (dry)**	15+5+5+10
Prec. agent:	**Et$_2$O (dry)**	1000

Synthesis and work-up of 25HF25TB1st was done similar to 25HF25TB24h (see 1.3.1.2) and followed general procedure established in chapter 1.2.1 The reaction scheme resembles the one depicted in Scheme 14. However, here, HBOF and TBEDA were added simultaneously, which lead to an orange discoloration of the reaction solution. The reaction was subsequently left stirring for 48 h prior to work-up.

Yield: 7.1 g (82 %, off-white orange flakes)

^{1}H NMR (400 MHz, CDCl$_3$, ppm) δ = 8.50 – 8.17 (m, 2H, HBOF oxime-CH), 8.14 – 8.01 (m, 23H, BHET ar-CH), 7.92 – 7.42 (m, 4H, HBOF ar-CH), 7.34 – 7.27 (m, 1H, HBOF ar-CH), 7.23 – 7.11 (m, 3H, HBOF ar-CH), 7.02 – 6.81 (m, 2H, HBOF C=CH), 6.36 – 5.80 (m, 5H, urethane/urea-NH), 5.44 – 4.83 (m, 17H, urethane/urea-NH), 4.75 (s, 20H, urethane/urea-NH), 4.64 – 4.45 (m, 23H, BHET CH$_2$), 4.45 – 4.24 (m, 23H, BHET CH$_2$), 4.21 – 3.84 (m, 53H, pTHF OCH$_2$), 3.46 – 3.32 (m, 653H, pTHF OCH$_2$), 3.29 – 3.01 (m, 114H, HMDI/TBEDA NCH$_2$), 1.74 – 1.54 (m, 702H, pTHF CCH$_2$), 1.54 – 1.18 (m, 274H, HMDI/TBEDA CCH$_2$).

IR (ATR, cm^{-1}) ν = 3322 ($\upsilon_{\text{N-H,urethane}}$), 2940 ($\upsilon_{\text{C-CH}}$), 2859 ($\upsilon_{\text{N-CH}}$), 2803 ($\upsilon_{\text{C=O}}$), 1719 ($\upsilon_{\text{C=O}}$), 1250 ($\upsilon_{\text{C-O-C,urethane}}$), 1104 ($\upsilon_{\text{C-O-C,ether}}$)

GPC (conventional calibration): M_n = 35 kDa, M_w = 69 kDa, PDI = 2

GPC (triple detection, dn/dc = 0.051): M_n = 30 kDa, M_w = 80 kDa, PDI = 2.7

1.3.2. Chemical composition

The chemical composition of the synthesized polymers regarding the ratios between chain extenders was determined similar to chapter 1.2.3. 50HF32h showed poor solubility in any deuterated solvent, and required three days and repeated heating by a heat gun to fully dissolve in $CDCl_3$.

1.3.3. Molecular weight

Determination of the molecular weight using both conventional calibration and triple detection was done similar to chapter 1.2.4. 50HF32h showed particularly poor solubility in THF, and had to be dissolved in solvent mixture containing 10 wt.% HFIP over three days at room temperature.

1.4. Material characterization

For material characterization, polymer films of the synthesized materials from chapter 1.2 and 1.3 were prepared, as well as the commercial TPU(U) *Pellethane® 2636-80A* (Pell), and a polymer mixture containing 50HF and 50TB in a ratio of 1:1 for reference. This was done *via* solution casting of 5 mL of a 0.1 g mL^{-1} 1,1,1,3,3,3-hexafluoropropan-2-ol solution into a designated PTFE mold (see Material and Methods).

Pieces of the prepared film were subsequently cut off and used for differential scanning calorimetry, and thermogravimetric analysis, or punched out and prepared for tensile tests following the procedures described in Material and Methods.

2. Self-reinforcement studies

For the self-reinforcement studies, three polymer films were prepared as in chapter 1.4 of the commercial reference TPU(U) Pell, the synthesized reference TPU(U)s 100BH, 50TB, 25TB, and 50HF32h, the newly synthesized TPU(U)s containing three CEs 25HF25TB24h, 25HF25TB48h, and 25HF25TB1st, as well as the polymer mixture 50HF32h+50TB. Each of the films were subsequently cut in half along their width, with one half being stored under dry conditions in a desiccator, while the other half was conditioned in deionized water according to Material and Methods for either 1 day, 7 days or 21 days. The dry and conditioned film halves were then characterized through tensile testing according to Material and Methods. The degree of self-reinforcement was subsequently determined by calculating the relative change in a given property between the unconditioned and conditioned test specimens following Eq. 17. The respective experimental standard deviation was approximated using Gauss' propagation of uncertainty according to Eq. 18.

$$\bar{x}_{SR} = \frac{\bar{x}_{cond} - \bar{x}_{uncond}}{\bar{x}_{uncond}} \cdot 100 \qquad \text{Eq. 17}$$

$$s_{SR} = \sqrt{\left(-\frac{100 \cdot \bar{x}_{cond}}{\bar{x}_{uncond}^2}\right)^2 \cdot s_{uncond}^2 + \left(\frac{100}{\bar{x}_{uncond}}\right)^2 \cdot s_{cond}^2} \qquad \text{Eq. 18}$$

$\bar{x}_{cond}$ … mean property measured on a conditioned specimen (-)
$\bar{x}_{SR}$ … mean degree of change of a given property between conditioned and unconditioned specimens (%)
$\bar{x}_{uncond}$ … mean property measured on unconditioned specimen (-)
s_{cond} … experimental standard deviation of property measured on a conditioned specimen (-)
s_{SR} … experimental standard deviation of a given property between conditioned and unconditioned specimens (%)
s_{uncond} … experimental standard deviation of property measured on a unconditioned specimen (-)

3. Electrospinning of materials

3.2. Procedure and parameters

3.2.2. Emitter-collector distance

Electrospinning (**ES**), light microscopy and scanning electron microscopy (**SEM**) were performed according to Material and Methods: For each ES run, 0.10 g of the TPU(U) 100BH were dissolved in 1.2 mL 1,1,1,3,3,3-hexafluoro-2-propanol (**HFIP**) to obtain a 5 wt.% fiber precursor solution. All runs were performed with a precursor feed rate of 3 mL h^{-1} and the naked steel mandrel as collector and substrate for deposition of the electrospun material (**ESM**). An applied voltage between 7 kV to 8 kV was used. Between runs, the emitter-collector distance was varied between 80 mm, 100 mm, 120 mm, and 150 mm. The ESMs were carefully pulled off of the mandrel, dried under reduced pressure, analyzed *via* light microscopy and smaller pieces were subsequently cut off for characterization *via* SEM.

3.2.3. Polymer concentration in solution

ES and characterization of the obtained materials was done similar to chapter 3.2.2. For ES of the 5 wt.% solution of Pell, 0.10 g Pell was dissolved in 1.2 mL HFIP. The 10 wt.% solution of 100BH was obtained by dissolution of 0.21 g of 100BH in 1.2 mL HFIP. For both runs, a precursor feed rate of 0.5 mL h^{-1} and an emitter-collector distance of 150 mm was set. As deposition substrate, the naked steel mandrel was used. The applied voltage for ES of the 5 wt.% solution of Pell was set to 9 kV and for the 10 wt.% solution of 100BH to 7 kV.

3.2.4. Substrate material for fiber deposition

Solution preparation, ES and characterization of the obtained ESM was done similar to chapter 3.2.3. However, instead of the steel collector on its own, 3.5 cm long tubes of antistatic PU and PTFE tubes were put onto the collector for fiber deposition.

3.2.5. Electrospinning of the synthesized polymers

Electrospinning and subsequent characterization of the TPU(U)s Pell, 100BH, 50TB, 25TB, 50HF32h, and 25HF25TB24h under comparable conditions were done similar to chapter 3.2.4 at a emitter-collector distance of 150 mm, a flow rate of 0.5 mL h^{-1}, and an applied voltage of 7.5 kV onto a PTFE tube acting as deposition substrate. Only exception was 50TB, which was spun at 11.5 kV to achieve stable jet formation. For Pell and 50HF32h, 5 wt.% solutions with HFIP were prepared due to viscosity issues at higher concentrations. For 100BH, 50TB, 25TB, and 25HF25TB24h, 10 wt.% solutions were used.

3.3. Mechanical characterization

3.3.2. Sample preparation

Preparation of the ring samples from the ESMs prepared in chapter 3.2.5 was achieved by cutting the PTFE tube substrate with the deposited ESM to the length of 5 mm using a scalpel and a custom 3D-printed cutting block with grooves of 0.7 µm at specified lengths, which were just wide enough for the scalpel to fit in between. The cut ring was subsequently taken up with a custom 3D-printed handling aid and the length of the ring was determined with a caliper, while the ESM still remained on the PTFE tubes. Lastly, the ESM was carefully removed from the collector tube using tweezers and stored under N_2 atmosphere until further use.

3.3.3. Tube thickness determination

Determination of the thickness of the ring specimens prepared in the previous chapter 3.3.2 was ultimately done by wedging the ESM between two microscopy cover glasses and measuring the thickness of the resulting composite using the external digital caliper gauge *209-943* by *Mitutoyo*. A picture of the measurement setup is depicted in Figure 54. The cover glasses had a surface roughness beneath the measuring range of the device and showed a similar thickness across their entire surface. The thickness of the electrospun tube was subsequently determined using Eq. 19. The procedure was repeated thrice at different positions along the tubes central axis to determine its average thickness.

$$t_w = \frac{t_C - t_G}{2}$$ Eq. 19

t_C … combined thickness of the tube electrospun tube and the cover glasses (mm)
t_w … wall thickness of the electrospun tube (mm)
t_G … combined thickness of the cover glasses (0.300 mm)

3.3.4. Ring tensile tests

Mechanical characterization of the ring specimens prepared in chapter 3.3.2 were done after determination of their thickness (see chapter 3.3.3). The measurement setup was similar to the setup for the tensile tests of the bulk material (see Material and Methods). However, rather than clamping the ring specimens directly into the measuring clamps of the device, they were threaded onto two adjacent pins (Ø = 0.84 mm) held by these clamps (see Figure 50). The pins used for this purpose were custom-made by Thomas Koch from the *Institute of Materials Science and Technology* by bending of conventional paper clips into the shape depicted in Figure 63 .

Figure 63: Sample holder prepared from a paper clip for the mechanical characterization of the electrospun tubes via ring tensile tests. The depicted tiles have a side length of 1 cm.

For measurement, one of these pins is then slowly moved away from the other at a rate of 2 mm s^{-1}, leading first to deformation and subsequently tearing of the ring specimen. No pre-load and a force cut-off threshold of 95 % was set. During measurement, dislocation of the pins and the applied stress on the ring specimens were recorded. For calculation of the resulting ring strain (see Eq. 6), the first effective internal circumference of the ring at an applied standard force above 0.001 N was chosen as the initial effective internal circumference ($d_{i,0}$) for all measured ring specimens. For each electrospun tube, 4 ring specimens were mechanically characterized.

Material and Methods

Reagents and solvents for synthesis, characterization and processing were obtained in appropriate purity, unless stated otherwise. Purification steps followed conventional procedures.[188] Organic reactants were analyzed through ^{1}H-NMR prior to use. All commercially obtained substances are summarized in Table 19.

Table 19: Commercially obtained polymers, reagents and solvents with their abbreviations, supplier, purification procedure, and CAS number

substance name (abbreviation)	supplier	purification	CAS
1,1,1,3,3,3-hexafluoro-2-propanol (HFIP)	Fluorochem	-	920-66-1
2-chloro-4,4,5,5-tetramethyl-1,3,2 dioxaphospholane (TMDP)	Sigma-Aldrich	-	14812-59-0
acetic anhydride (Ac_2O)	unknown	distilled	108-24-7
benzoic acid (BA)	unknown	dried	65-85-0
bis(2-hydroxyethyl) terephthalate (BHET)	Sigma-Aldrich	recrystallized	959-26-2
chloroform-d ($CDCl_3$)	Eurisotop	-	865-49-6
chromium(III)acetylacetonate	Fluka	-	21679-31-2
cyclohexanol	Sigma-Aldrich	-	108-24-7
dimethylsulfoxide-d$_6$	Eurisotop	-	2206-27-1
hexamethylene diisocyanate (HMDI)	TCI	distilled	822-06-0
methanol (MeOH)	unknown	-	67-56-1
N,N′-di-*tert*-butyl ethylenediamine (TBEDA)	Sigma Aldrich	distilled	4062-60-6
N,N-dimethylformamide 99.8 %, Extra Dry over Molecular Sieve, AcroSeal® (DMF)	Acros Organics	-	68-12-2
Pellethane® 2636-80A	Lubrizol	-	-
poly(tetrahydrofuran) average M_n ~1,000 g mol^{-1} (pTHF)	Sigma Aldrich	-	25190-06-1
potassium hydroxide (KOH)	Carl Roth	-	1310-58-3
pyridine ACS reagent, ≥ 99.0 % (PY)	Sigma Aldrich	-	110-86-1
tin(II) 2-ethylhexanoate ($Sn(Oct)_2$)	Sigma Aldrich	-	301-10-0

Attenuated total reflection Fourier-transform infrared (ATR-FTIR) spectroscopy measurements were performed on a *Perkin Elmer Spectrum 65* FTIR spectrometer using a heatable *MKII Golden Gate*^{TM} single reflection ATR System by *Specac*. A working range of 4000 cm^{-1} to 600 cm^{-1} was set for all measurements with a number of 8 scans and a resolution of 2 cm^{-1}. Measurements were done at 25 °C using a *Eurotherm 2216E* temperature controller and the results were evaluated with the software *PerkinElmer Spectrum* version 10.03.07.0112.

Coulometric Karl Fischer titrations (KFT) was performed on an *Enviortech CA-21* moisture meter to check the residual moisture in reagents for TPU(U) synthesis. As anode solution served *Aquamicron AX* by *Mitsubishi Chemicals*. For the cathode solution *Aquamicron CXU* by *Mitsubishi Chemicals* was used. For measurement, around 0.1 mL of liquid sample were weighed into a syringe with 0.01 mg accuracy, and injected into the device through a septum. The mass of the injected volume was determined by weighing the difference, and was put into the device prior to measurement start. A stirrer speed of 5 was kept for all measurements. The residual moisture was returned in ppm (w/w).

Data visualization for the various figures was performed using *OriginPro 2023b* (64-bit) *SR1* version 10.0.5.157 by *OriginLab* corporation.

Differential scanning calorimetry (DSC) was performed on a *DSC 2500* by *TA Instruments* together with Thomas Koch from the *Institute of Materials Science and Technology* at the Institute of Materials Science and Technology. For sample preparation, an aluminum pan and its lid, both produced by *Netzsch*, are tared and charged with 3 mg to 5 mg of polymer sample. Afterwards, the lid is placed onto the filled pan and both are compressed using a custom hand press by *Netzsch* to seal the sample material. The prepared vessel is then put into an autosampler and the measurement commences under N_2 atmosphere following the heating program in Table 20 adopted from Markus Fitzka[163].

Table 20: Heating program for dynamic scanning calorimetry of TPU(U)s

step	query
1	equilibrate at -90 °C and hold for 5 min
2	ramp to 150 °C at 10 °C/min and hold for 2 min
3	cooling to -90 °C at 10 °C/min and hold for 5 min
5	ramp to 150 °C at 10 °C/min and hold for 2 min

Electrospinning (ES) was performed on the custom-built electrospinning device *PL-30kV* by Simon Seisenbacher. The setup is depicted in Results and Discussion chapter 3.1. For sample preparation, between 0.10 g and 0.21 g of a dry TPU(U) are weighed into a 4 mL shell vial and dissolved in 1.2 mL HFIP (ρ = 1.60 g mL^{-1}) to obtain a solution with a concentration between 5 wt.% to 15 wt.%. 1 mL of this solution was then taken up with a 5 mL syringe (inner diameter: 10 mm). The syringe is then clamped into the syringe pump *NE-1000* by *New Era Pump Systems* and connected *via* PTFE tubing to a hollow flat-tipped steel needle (length: 25 cm; outer width: 20gauge (0.812 mm)) serving as emitter electrode. Feed-rate and emitter-collector distance were set to desired values. Rotation speed of the collector was generally set at 200 rpm. Lateral location of the emitter was left at 0 mm. Amplitude of the lateral movement of the emitter were set to 10 mm and lateral movement speed to 20 mm s^{-1}. For the electric field, a current of 0.1 A and 6 kV to 12 kV was set using a *LNC 30000-2 pos* high-voltage power supply by *Heinzinger*. As collector served a steel rod with 2 mm diameter over a length of up to 180 cm (total length: 250 cm). The mandrel is rotated at 200 rpm during the run and is used on its own as well as in combination with antistatic poly(ether)-poly(urethane) tubes (⌀ = 4 mm x 2.5 mm) by *Landefeld Druckluft und Hydraulik*, or *Rotilabo*® PTFE tubes (⌀ = 3 mm x 2 mm) by *Carl Roth* as substrate for fiber deposition. To focus fiber deposition on the middle of the collector mandrel, 6 cm long *Rotilabo*® PTFE tubes (⌀ = 6 mm x 4 mm) by *Carl Roth* were put on both ends of the mandrel. Temperature in the chamber varied from 22 °C to 28 °C and moisture from 55 % to 35 % during runs depending on ambient conditions and run time.

Film conditioning for self-reinforcement studies was done by fully immersing a piece of cast film into a bowl filled with deionized water for a certain period of time (1 d, 7 d, or 21 d). To counteract evaporation and keep the film continuously immersed, deionized water was regularly refilled. A septum was used as weight to hold down the film (see Figure 64). After the period of time had passed, the film was removed from the bowl, dapped dry, and further dried under reduced pressure in a desiccator overnight.

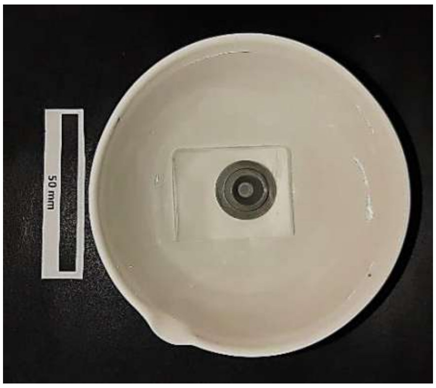

Figure 64: Top-down film conditioning setup: Cast film piece is placed in a bowl filled with deionized water and weighed down with a septum to ensure continuous submersion.

Gel permeation chromatography (GPC) was performed on a *Malvern Viscotek TDA* system in combination with a *Malvern Viscotek GPCmax* autosampler and pump system. Separation occurs in three successively linked *PSS SDV* columns (porosity of 100 Å, 1000 Å, and 100000 Å respectively). For detection, a *Malvern Viscotek SEC-MALS 9* multi-angle light scattering detector, a *Malvern Viscotek TDA 305-021* refractive index (RI) and on-line viscosity detector, as well as a *Azura UVD 2.1S* UV detector by *Knauer* were used. Measurements were done at a precursor feed rate of 0.8 mL min^{-1} over a duration of 70 min with THF as eluent. For conventional calibration, a calibration of external polystyrene standards between 479 kDa and 44 kDa was used. In case of triple detection, the molecular weight of the polymer sample was determined over a dn/dc calibration by injecting the sample solution with five different volumes between 80 µL and 120 µL. Evaluation of the results was performed on the software *OmniSEC* version 5.12.461 by *Malvern*.

Light microscopy was performed on a *Keyence VHX* digital microscope by *Keyence International* at the Institute of Chemical Technologies and Analytics in consultation with Katharina Rauchenwald usually under ring light illumination and at different magnifications. All recorded images are depth-resolved.

NMR-spectroscopy: ^{1}H and ^{13}C-NMR spectra were recorded on a *Bruker Advance* spectrometer at 400 MHz and 101 MHz respectively. ^{31}P-NMR spectra for determination of the molecular weight of pTHF were measured on a *Bruker Advance* spectrometer with 600 MHz. The measured spectra were interpreted using *MestReNova v14.3.3-33362* by *Mestrelab Research S.L.* The chemical shifts are given in ppm. After phase and baseline correction, all signals of the ^{1}H and ^{13}C-NMR spectra were referenced to characteristic signals of the used deuterated solvents (^{1}H: $CDCl_3$ = 7.26 ppm, DMSO-d^6 = 2.50 ppm; ^{13}C: $CDCl_3$ = 77.16 ppm, DMSO-d^6 = 39.52 ppm). The signals of the fine structures were grouped into singlets (s), duplets (d), triplets (t) or multiplets (m), and the integrals normed onto an appropriate signal with a known number of corresponding hydrogens or carbons per molecule.

Potentiometric KOH titrations were performed on an *Metrohm 848 Titrino Plus system* in combination with a *Metrohm 801 Stirrer* using a 0.5 N methanolic KOH solution to determine the hydroxyl value of pTHF. Equivalence point detection was done *via* pH electrode. For titer determination benzoic acid was used as primary titer substance.

Scanning electron microscopy (SEM) was performed on a *Zeiss EVO 10* by Thomas Koch from the *Institute of Materials Science and Technology* at the Institute of Materials Science and Technology. Material samples were prepared by placing them onto 8 mm wide conductive double sided carbon tape by *Nisshin EM* attached to a metal sample holder with the side of interest facing upwards (see Figure 65). Afterwards, the samples were sputtered with gold for 30 s at a 10 mA current under 0.1 mbar using an automatic sputter coater by *Agar scientific*, to facilitate sample discharge during measurement.

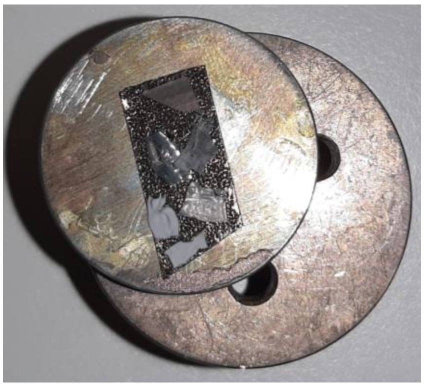

Figure 65: Sample holder for scanning electron microscopy with attached conductive double sided carbon tape upon which multiple polymer samples (white to transparent pieces) are placed.

Solution casting was done by dissolving 0.5 g of dry polymer in 5 mL 1,1,1,3,3,3-hexafluoro-2-propanol in a screw-cap vial under stirring at room temperature. After complete dissolution, the solution was cast into PTFE molds (60 mm x 40 mm x 2 mm) within a fume hut. Formed bubbles were burst using a syringe canula or pushed towards the edges to ensure homogeneity. After casting, the solution was left to dry and to solidify into a film overnight. To avoid the introduction of dust from the environment, a reversed funnel was placed over the mold after casting. The solid film was carefully removed from the mold by prying of the edges from the mold using a spatula and further dried in a desiccator under reduced pressure for 1 h.

Tensile tests were performed on a *Zwick Z050* by *Zwick* under supervision of Thomas Koch from the *Institute of Materials Science and Technology* at the Institute of Materials Science and Technology. In the case of **polymer films**, test specimens were punched out of the prepared polymer films using a punching iron of the shape 5B following *ISO 527-1* (see Figure 66). Punching was performed, using a hammer. The produced specimens were subsequently wrapped in adhesive tape at the end points to improve handling during sample clamping and measured on their thickness using a digital *Filetta* micrometer with a spherical anvil by *SGM.* These thickness measurements were done in triplicates for individual samples at different positions on the bridge. For length and width of the bridge,12 mm and 2 mm were assumed respectively. For tensile testing, the prepared test specimens were clamped into the measuring position, so that its bridge was parallel to the applied forces. The measurement was performed with a cross-head speed of 50 mm/min, owed to the general elasticity of TPU(U)s, under a maximum load of 20 N and in a resolution of 1 mN. For each polymer batch three test specimens were measured. Ultimate tensile strength (UTS), Young's modulus (YM), and the elongation at break (EAB) were calculated *via* software.

Figure 66: Punching equipment from left to right: Punching iron, tweezers, polymer film with punched holes and punched out polymer test specimen ready for tensile tests. Sides of the grid squares have a length of 1 cm.

Tensile tests of electrospun tubes are specified in experimental part chapter 3.3.4.

Thermogravimetric analysis (TGA) was performed on a *TGA Q500* by *TA Instruments* together with Thomas Koch from the *Institute of Materials Science and Technology*. For measurement, around 10 mg of polymer were cut from the prepared films, chopped into small pieces using a razor blade, and weighed into a tared, baked-out crucible with a Pt handle. After sample loading, the measurement commenced under N_2 atmosphere following a heating program adopted from Markus Fitzka[163] depicted in Table 21.

Table 21: Heating program for thermogravimetric analysis of thermoplastic poly(urethane(urea) elastomers)

step	**query**
1	ramp to 150 °C at 10 °C/min
2	hold for 1 min
3	ramp to 300 °C at 10 °C/min
4	hold for 2 min
5	ramp to 500 °C at 10 °C/min

Thickness measurement of electrospun tubes was done using the external digital caliper gauge *209-943* by *Mitutoyo* with a measuring range of 0 - 10 mm, a resolution of 0.005 mm and a measuring force of 0.8 - 1.2 N.

Abbreviations

100BH	TPU containing pTHF, HMDI and BHET in a ratio of 1:2:1
25TB	TPU(U) containing pTHF, HMDI, BHET and TBEDA in a ratio around 1:2:0.75:0.25
25HF25TB	TPU(U)s containing pTHF, HMDI, BHET, TBEDA and HBOF in a theoretical ratio of 1:2:0.5:0.25:0.25
25HF25TB24h	TPU(U) containing pTHF, HMDI, BHET, TBEDA and HBOF in a theoretical ratio of 1:2:0.5:0.25:0.25, with work-up after synthesis being performed 24 h after addition
25HF25TB48h	TPU(U) containing pTHF, HMDI, BHET, TBEDA and HBOF in a theoretical ratio of 1:2:0.5:0.25:0.25, with work-up after synthesis being performed 48 h after addition
25HF25TB1st	TPU(U) containing pTHF, HMDI, BHET, TBEDA and HBOF in a theoretical ratio of 1:2:0.5:0.25:0.25, with TBEDA and HBOF being added simultaneously
50HF	TPU(U) containing pTHF, HMDI, BHET and HBOF in a ratio around 1:2:0.5:0.5
50HF48h	TPU(U) containing pTHF, HMDI, BHET and HBOF in a ratio around 1:2:0.5:0.5, with work-up after synthesis being performed 48 h after addition
50HS	TPU(U) containing pTHF, HMDI, BHET and HBOS in a ratio around 1:2:0.5:0.5
50TB	TPU(U) containing pTHF, HMDI, BHET and TBEDA in a ratio around 1:2:0.5:0.5
Ac_2O	acetic anhydride
BA	benzoic acid
BHET	bis(2-hydroxyethyl) terephthalate
DSC	differential scanning calorimetry
Et_2O	diethyl ether
ES	electrospinning
Eq.	equation
ESM	electrospun material
HBOF	bis(4-hydroxybenzaldehyde oxime)fumarate
HBOS	bis(4-hydroxybenzaldehyde oxime)succinate
HFIP	1,1,1,3,3,3-hexafluoropropan-2-ol
HMDI	hexamethylene diisocyanate
KOH	potassium hydroxide
KFT	Karl Fischer titration
NWFs	nonwoven fabrics
pTHF	poly(tetrahydrofuran)
$Sn(Oct)_2$	tin(II) 2-ethylhexanoate
SRE	self-reinforcement effect
TBEDA	N,N′-di-tert-butylethylene-diamine
TGA	thermogravimetric analysis
TMDP	2-chloro-4,4,5,5-tetramethyl-1,3,2-dioxaphospholane
TPU	thermoplastic poly(urethane)
TPU(U)	thermoplastic poly(urethane(urea))
TS	tensile tests
C	compliance of ring specimen between 80 mmHg and 120 mmHg (% $(100\ \text{mmHg})^{-1}$)
c_S	concentration of used solution (g(sample) g(solvent)^{-1})
c_{St}	concentration of the standard solution (mg mL^{-1})
c_{KOH}	concentration of methanolic potassium hydroxide titrant (mol mL^{-1})
d_i	effective internal diameter of ring specimen (mm)

d_p … diameter of the sample holder pins (mm)

EAB … elongation at break (%)

EAB_r … highest strain on ring specimen before failure (-)

F_{max} … highest measured force acting on the ring specimen at a particular strain (N)

f … correction factor (1000 mg g^{-1})

I_{CCH_2} … combined hydrogen integrals of HMDI and TBEDA on carbon atoms next to carbon at around 1.4 ppm (-)

I_{EG} … integral over the diphosphorylated pTHF signal at 147.1 ppm (-)

I_{NCH_2} … combined hydrogen integrals of HMDI and TBEDA on carbon atoms next to nitrogen at around 3.1 ppm (-)

$I^T_{NCH_2}$ … hydrogen integral of TBEDA on carbon atoms next to nitrogen at around 3.1 ppm (-)

I_{St} … integral over the phosphorylated cyclohexanol signal at 145.0 ppm (-)

k_T … share of TBEDA in relation to HMDI in the combined integral (-)

k_H … share of HMDI in relation to TBEDA in the combined integral (-)

l … length of the specimen (mm)

M_i … molecular weight of molecules of size I (g mol^{-1})

$\overline{M_n}$ … number average molecular weight (g mol^{-1})

$\overline{M_n^{31P}}$ … number average molecular weight of poly(tetrahydrofuran) determined *via* quantitative ^{31}P-NMR spectroscopy (g mol^{-1})

$\overline{M_n^{OHV}}$ … number average molecular weight of poly(tetrahydrofuran) determined *via* hydroxyl (g mol^{-1})

$\overline{M_n^{GPC,c}}$ … number average molecular weight determined *via* gel permeation chromatography and conventional calibration (g mol^{-1})

$\overline{M_n^{GPC,t}}$ … number average molecular weight determined *via* gel permeation chromatography and triple detection (g mol^{-1})

M_{KOH} … molecular weight of cyclohexanol (g mol^{-1})

M_{St} … molecular weight of internal standard cyclohexanol (g mol^{-1})

$\overline{M_w}$ … weight average molecular weight (g mol^{-1})

$\overline{M_w^{GPC,c}}$ … weight average molecular weight determined *via* gel permeation chromatography and conventional calibration (g mol^{-1})

$\overline{M_w^{GPC,t}}$ … weight average molecular weight determined *via* gel permeation chromatography and triple detection (g mol^{-1})

m_{pTHF} … mass of used poly(tetrahydrofuran) (mg)

m_A … mass of dissolved sample in used amount of solution for KFT (g)

m_{DMF} … mass of solvent in used solution (g)

m_S … mass of solution used for KFT (g)

N_i … number of molecules of size I (-)

N_{OH} … number of hydroxy end groups per molecule (-)

OHV … hydroxyl value (mg KOH/g sample)

PDI … polydispersity (-)

p … reaction conversion

p_i … internal pressure acting on the ring specimen (mmHg)

$p_{i,j}$ … first effective internal pressure acting on ring specimen above j mmHg (mmHg)

$p_{i,max}$ … highest internal pressure acting on the ring specimen i.e., burst pressure (MPa)

q	… ratio between the number of reacting functional groups (-)
r_i	… effective internal radius of ring specimen at a given pin displacement (mm)
s_{cond}	… experimental standard deviation of property measured on a conditioned specimen (-)
s_{SR}	… experimental standard deviation of a given property between conditioned and unconditioned specimens (%)
s_{uncond}	… experimental standard deviation of property measured on a unconditioned specimen (-)
T_{cc}	… cold crystallization temperature (°C)
T_g	… glass transition temperature (°C)
$T_{m,i}$	… onset melting temperature (°C)
$T_{m,i}$	… end temperature of the melting interval (°C)
t	… titer of methanolic 0.5 N KOH titrant (-)
t_C	… combined thickness of the tube electrospun tube and the cover glasses (µm)
t_w	… wall thickness of the electrospun tube (µm)
t_G	… combined thickness of the cover glasses (µm)
UTS	… ultimate tensile strength (MPa)
u_i	… effective internal circumference of ring specimen (mm)
$u_{i,0}$	… initial effective internal circumference of ring specimen (mm)
$u_{i,max}$	… highest effective internal circumference of ring specimen before failure (mm)
V_{St}	… used volume of internal standard solution (mL)
V_B	… consumed methanolic 0.5 N KOH titrant for the blank (mL)
V_S	… consumed methanolic 0.5 N KOH titrant for the sample (mL)
$w_{H_2O}^{A}$	… water content of solid analyte in ppm (w/w)
$w_{H_2O}^{DMF}$	… water content of pure solvent *N,N*-dimethylformamide (DMF) in ppm (w/w)
$w_{H_2O}^{S}$	… water content of sample solution in ppm (w/w)
$\overline{X_n}$	… mean degree of polymerization
$\bar{x}_{cond}$	… mean property measured on a conditioned specimen (-)
$\bar{x}_{SR}$	… mean degree of change of a given property between conditioned and unconditioned specimens (%)
$\bar{x}_{uncond}$	… mean property measured on unconditioned specimen (-)
YM	… Young's modulus (MPa)
Δx_i	… pin displacement (mm)
ε	… ring elongation of the ring specimen (%)
ε_j	… ring elongation of the ring specimen at $p_{i,j}$ (%)
ρ	… density
σ_r	… effective stress acting on the ring specimen (N mm^{-2})

References

(1) Bell, D. R. Overview of the cardiovascular system and hemodynamics. In *Medical Physiology: Principles for Clinical Medicine*, LWW, 2013; pp 207-220.

(2) *Introduction to the Cardiovascular System*. U.S. Department of Health and Human Services, National Institutes of Health, National Cancer Institute, 2024. https://training.seer.cancer.gov/anatomy/cardiovascular/ (accessed 08/08/2024).

(3) Athanasiou, L. S.; Fotiadis, D. I.; Michalis, L. K. Introduction. In *Atherosclerotic Plaque Characterization Methods Based on Coronary Imaging*, 2017; pp 1-21.

(4) Hoehn, E. N. M. K. The Cardiovascular System: Blood Vessels. In *Human Anatomy and Physiology*, Pearson 2021.

(5) *Causes of death statistics*. European Statistical Office, 2024. https://ec.europa.eu/eurostat/statistics-explained/index.php?title=Causes_of_death_statistics (accessed 20/08/2024).

(6) *Cardiovascular diseases (CVDs)*. World Health Organizaiton, 2021. https://www.who.int/en/news-room/fact-sheets/detail/cardiovascular-diseases-(cvds) (accessed 08/08/2024).

(7) *The top 10 causes of death*. World Health Organizaiton, 2024. https://www.who.int/news-room/fact-sheets/detail/the-top-10-causes-of-death (accessed 20/08/2024).

(8) *Renal Artery Stenosis*. National Institute of Diabetes and Digestive and Kidney Diseases (NIDDK), 2014. https://www.niddk.nih.gov/health-information/kidney-disease/renal-artery-stenosis (accessed 20/08/2024).

(9) Johnston, K. W.; Rutherford, R. B.; Tilson, M. D.; Shah, D. M.; Hollier, L.; Stanley, J. C. Suggested standards for reporting on arterial aneurysms. *J Vasc Surg* **1991**, *13* (3), 452-458. DOI: https://doi.org/10.1067/mva.1991.26737 From NLM Medline.

(10) Strobel, H. A.; Qendro, E. I.; Alsberg, E.; Rolle, M. W. Targeted Delivery of Bioactive Molecules for Vascular Intervention and Tissue Engineering. *Front Pharmacol* **2018**, *9*, 1329. DOI: https://doi.org/10.3389/fphar.2018.01329 From NLM PubMed-not-MEDLINE.

(11) *Noncommunicable diseases*. World Health Organizaiton, 2024. https://www.who.int/news-room/fact-sheets/detail/noncommunicable-diseases (accessed 20/08/2024).

(12) Zemaitis, M. R.; Boll, J. M.; Dreyer, M. A. *Peripheral Arterial Disease*; National Library of Medicine (NIH), Treasure Island (FL), United States of America, 2023. https://www.ncbi.nlm.nih.gov/books/NBK430745/ (accessed 28.09.2024).

(13) Shahjehan, R. D.; S., B. B. *Coronary Artery Disease*; National Library of Medicine (NIH), Treasure Island (FL), United States of America, 2023. https://www.ncbi.nlm.nih.gov/books/NBK564304/.

(14) Yu, L.; Newton, E. R.; Gillis, D. C.; Sun, K.; Cooley, B. C.; Keith, A. N.; Sheiko, S. S.; Tsihlis, N. D.; Kibbe, M. R. Coating small-diameter ePTFE vascular grafts with tunable poly(diol-co-citrate-co-ascorbate) elastomers to reduce neointimal hyperplasia. *Biomaterials Science* **2021**, *9* (15), 5160-5174, 10.1039/D1BM00101A. DOI: https://doi.org/10.1039/D1BM00101A.

(15) Shahriari-Khalaji, M.; Shafiq, M.; Cui, H.; Cao, R.; Zhu, M. Advancements in the fabrication technologies and biomaterials for small diameter vascular grafts: A fine-tuning of physicochemical and biological properties. *Applied Materials Today* **2023**, *31*, 101778. DOI: https://doi.org/10.1016/j.apmt.2023.101778.

(16) Ma, H.; Hu, J.; Ma, P. X. Polymer Scaffolds for Small-Diameter Vascular Tissue Engineering. *Advanced Functional Materials* **2010**, *20* (17), 2833-2841. DOI: https://doi.org/10.1002/adfm.201000922.

(17) Eldeeb, A. E.; Salah, S.; Elkasabgy, N. A. Biomaterials for Tissue Engineering Applications and Current Updates in the Field: A Comprehensive Review. *AAPS PharmSciTech* **2022**, *23* (7), 267. DOI: https://doi.org/10.1208/s12249-022-02419-1 From NLM Medline.

(18) Vacanti, J. P.; Langer, R. Tissue engineering: the design and fabrication of living replacement devices for surgical reconstruction and transplantation. *The Lancet* **1999**, *354*, S32-S34. DOI: https://doi.org/10.1016/S0140-6736(99)90247-7.

(19) Viola, J.; Lal, B.; Grad, O. *The Emergence of Tissue Engineering as a Research Field: 3.0 Emergence and Evolution of a Shared Concept*; National Science Foundation, Arlington, Virginia, USA, 2003. https://www.nsf.gov/pubs/2004/nsf0450/emergence.htm (accessed 26.06.2024).

(20) Chardack, W. M.; Bruseske, D. A.; Santomauro, A. P.; Fazekas, G. Experimental Studies on Synthetic Substitutes for Skin and Their Use in the Treatment of Burns. *Annals of Surgery* **1962**, *155* (1), 127-139.

(21) Berthiaume, F.; Maguire, T. J.; Yarmush, M. L. Tissue engineering and regenerative medicine: history, progress, and challenges. *Annu Rev Chem Biomol Eng* **2011**, *2*, 403-430. DOI: https://doi.org/10.1146/annurev-chembioeng-061010-114257 From NLM Medline.

(22) Hasan, A. *Tissue Engineering for Artificial Organs: Regenerative Medicine, Smart Diagnostics and Personalized Medicine*; Wiley, 2017.

(23) Ehrmann, K. Development of Thermoplastic Elastomers for Cardiovascular Tissue Regeneration. Technische Universität Wien, Vienna, 2020.

(24) Fu, L.; Li, P.; Li, H.; Gao, C.; Yang, Z.; Zhao, T.; Chen, W.; Liao, Z.; Peng, Y.; Cao, F.; et al. The Application of Bioreactors for Cartilage Tissue Engineering: Advances, Limitations, and Future Perspectives. *Stem Cells Int* **2021**, *2021*, 6621806. DOI: https://doi.org/10.1155/2021/6621806 From NLM PubMed-not-MEDLINE.

(25) Adel, I. M.; ElMeligy, M. F.; Elkasabgy, N. A. Conventional and Recent Trends of Scaffolds Fabrication: A Superior Mode for Tissue Engineering. *Pharmaceutics* **2022**, *14* (2). DOI: https://doi.org/10.3390/pharmaceutics14020306 From NLM.

(26) Gaharwar, A. K.; Singh, I.; Khademhosseini, A. Engineered biomaterials for in situ tissue regeneration. *Nature Reviews Materials* **2020**, *5* (9), 686-705. DOI: https://doi.org/10.1038/s41578-020-0209-x.

(27) *Glossary of Terms*. National Institute of Biomedical Imaging and Bioengineering, 2024. https://www.nibib.nih.gov/science-education/glossary/b (accessed 30.09.2024).

(28) Zhao, X. 1 - Introduction to bioactive materials in medicine. In *Bioactive Materials in Medicine*, Zhao, X., Courtney, J. M., Qian, H. Eds.; Woodhead Publishing, 2011; pp 1-13.

(29) Prasad, K.; Bazaka, O.; Chua, M.; Rochford, M.; Fedrick, L.; Spoor, J.; Symes, R.; Tieppo, M.; Collins, C.; Cao, A.; et al. Metallic Biomaterials: Current Challenges and Opportunities. *Materials (Basel)* **2017**, *10* (8). DOI: https://doi.org/10.3390/ma10080884 From NLM.

(30) Baranwal, J.; Barse, B.; Fais, A.; Delogu, G. L.; Kumar, A. Biopolymer: A Sustainable Material for Food and Medical Applications. *Polymers (Basel)* **2022**, *14* (5). DOI: https://doi.org/10.3390/polym14050983 From NLM.

(31) Benrashed, M. A.; Alyousef, N. I.; AlQahtani, N. H.; AlMaimouni, Y. K.; Khan, M.; Khan, A. S. 7 - Conventional to advanced endodontics: Use of bioactive materials. In *Biomaterials in Endodontics*, Khurshid, Z., Zafar, M. S., Najeeb, S. Eds.; Woodhead Publishing, 2022; pp 169-194.

(32) III - Biomaterial types. In *Definitions of Biomaterials for the Twenty-First Century*, Williams, D., Zhang, X. Eds.; Elsevier, 2019; pp 25-54.

(33) Williams, D. F. On the mechanisms of biocompatibility. *Biomaterials* **2008**, *29* (20), 2941-2953. DOI: https://doi.org/10.1016/j.biomaterials.2008.04.023.

(34) Jurak, M.; Wiącek, A. E.; Ładniak, A.; Przykaza, K.; Szafran, K. What affects the biocompatibility of polymers? *Advances in Colloid and Interface Science* **2021**, *294*, 102451. DOI: https://doi.org/10.1016/j.cis.2021.102451.

(35) Abdulghani, S.; Mitchell, G. R. Biomaterials for In Situ Tissue Regeneration: A Review. *Biomolecules* **2019**, *9* (11), 750. DOI: https://doi.org/10.3390/biom9110750.

(36) Khan, M. U. A.; Aslam, M. A.; Bin Abdullah, M. F.; Hasan, A.; Shah, S. A.; Stojanović, G. M. Recent perspective of polymeric biomaterial in tissue engineering– a review. *Materials Today Chemistry* **2023**, *34*, 101818. DOI: https://doi.org/10.1016/j.mtchem.2023.101818.

(37) Almouemen, N.; Kelly, H. M.; O'Leary, C. Tissue Engineering: Understanding the Role of Biomaterials and Biophysical Forces on Cell Functionality Through Computational and Structural Biotechnology Analytical Methods. *Computational and Structural Biotechnology Journal* **2019**, *17*, 591-598. DOI: https://doi.org/10.1016/j.csbj.2019.04.008.

(38) Derakhshani, A.; Hasani, S.; Navaei, T. 5 - Hemocompatible polymers for medical applications. In *Handbook of Polymers in Medicine*, Mozafari, M., Singh Chauhan, N. P. Eds.; Woodhead Publishing, 2023; pp 143-175.

(39) He, W.; Hu, Z.; Xu, A.; Liu, R.; Yin, H.; Wang, J.; Wang, S. The Preparation and Performance of a New Polyurethane Vascular Prosthesis. *Cell Biochemistry and Biophysics* **2013**, *66* (3), 855-866. DOI: https://doi.org/10.1007/s12013-013-9528-5.

(40) Cui, M.; Chai, Z.; Lu, Y.; Zhu, J.; Chen, J. Developments of polyurethane in biomedical applications: A review. *Resources Chemicals and Materials* **2023**, *2* (4), 262-276. DOI: https://doi.org/10.1016/j.recm.2023.07.004.

(41) Mooney, D. J.; Baldwin, D. F.; Suh, N. P.; Vacanti, J. P.; Langer, R. Novel approach to fabricate porous sponges of poly(d,l-lactic-co-glycolic acid) without the use of organic solvents. *Biomaterials* **1996**, *17* (14), 1417-1422. DOI: https://doi.org/10.1016/0142-9612(96)87284-X.

(42) Sola, A.; Bertacchini, J.; D'Avella, D.; Anselmi, L.; Maraldi, T.; Marmiroli, S.; Messori, M. Development of solvent-casting particulate leaching (SCPL) polymer scaffolds as improved three-dimensional supports to mimic the bone marrow niche. *Materials Science and Engineering: C* **2019**, *96*, 153-165. DOI: https://doi.org/10.1016/j.msec.2018.10.086.

(43) Mapossa, A. B.; Tewo, R. K.; Ray, S. S.; Mhike, W.; Sundararaj, U. A review on thermally induced phase separation technology in the fabrication of microporous polymer membrane devices for sustained-repellent delivery: Crystallization and morphological studies. *Journal of Polymer Science* **2024**, *n/a* (n/a). DOI: https://doi.org/10.1002/pol.20240232.

(44) Gorth, D.; J Webster, T. 10 - Matrices for tissue engineering and regenerative medicine. In *Biomaterials for Artificial Organs*, Lysaght, M., Webster, T. J. Eds.; Woodhead Publishing, 2011; pp 270-286.

(45) Rabionet, M.; Guerra, A. J.; Puig, T.; Ciurana, J. 3D-printed Tubular Scaffolds for Vascular Tissue Engineering. *Procedia CIRP* **2018**, *68*, 352-357. DOI: https://doi.org/10.1016/j.procir.2017.12.094.

(46) Lee, S. J.; Yoo, J. J.; Lim, G. J.; Atala, A.; Stitzel, J. In vitro evaluation of electrospun nanofiber scaffolds for vascular graft application. *Journal of Biomedical Materials Research Part A* **2007**, *83A* (4), 999-1008. DOI: https://doi.org/10.1002/jbm.a.31287.

(47) Bakare, A.; Mohanadas, H. P.; Tucker, N.; Ahmed, W.; Manikandan, A.; Faudzi, A. A. M.; Mohamaddan, S.; Jaganathan, S. K. Advancements in textile techniques for cardiovascular tissue replacement and repair. *APL Bioeng* **2024**, *8* (4), 041503. DOI: https://doi.org/10.1063/5.0231856 From NLM.

(48) Gandhi, K. L.; Sondhelm, W. S. 4 - Technical fabric structures – 1. Woven fabrics. In *Handbook of Technical Textiles (Second Edition)*, Horrocks, A. R., Anand, S. C. Eds.; Woodhead Publishing, 2016; pp 63-106.

(49) Anand, S. C. 5 - Technical fabric structures – 2. Knitted fabrics. In *Handbook of Technical Textiles (Second Edition)*, Horrocks, A. R., Anand, S. C. Eds.; Woodhead Publishing, 2016; pp 107-162.

(50) Wilson, A. 1 - Development of the nonwovens industry. In *Handbook of Nonwovens*, Russell, S. J. Ed.; Woodhead Publishing, 2007; pp 1-15.

(51) Yilmaz, K. B.; Sabuncuoglu, B.; Yildirim, B.; Silberschmidt, V. V. A brief review on the mechanical behavior of nonwoven fabrics. *Journal of Engineered Fibers and Fabrics* **2020**, *15*, 1558925020970197. DOI: https://doi.org/10.1177/1558925020970197.

(52) Russell, S. J.; Smith, P. A. 6 - Technical fabric structures – 3. Nonwoven fabrics. In *Handbook of Technical Textiles (Second Edition)*, Horrocks, A. R., Anand, S. C. Eds.; Woodhead Publishing, 2016; pp 163-188.

(53) Misnon, M. I.; Islam, M. M.; Epaarachchi, J. A.; Lau, K.-t. Potentiality of utilising natural textile materials for engineering composites applications. *Materials & Design* **2014**, *59*, 359-368. DOI: https://doi.org/10.1016/j.matdes.2014.03.022.

(54) Wysokińska, Z.; Czajkowski, T.; Grabowska, K. Nonwovens: Global Trends in World Economy, European Foreign Trade, and Selected Case Studies from Poland and Asian Brics Countries. *Autex Research Journal* **2020**, *20* (4), 382-414. DOI: https://doi.org/10.2478/aut-2020-0028 (acccessed 2024-12-10).

(55) Cuartero, F. C. *Global Nonwoven Markets Report 2023-2028*. European Disposables and Nonwovens Association, 2024. https://www.edana.org/about-us/news/edana-and-inda-release-the-global-nonwoven-markets-report-2023-2028 (accessed 10.12.2024).

(56) Trevisol, T. C.; Langbehn, R. K.; Battiston, S.; Immich, A. P. S. Nonwoven membranes for tissue engineering: an overview of cartilage, epithelium, and bone regeneration. *Journal of Biomaterials Science, Polymer Edition* **2019**, *30* (12), 1026-1049. DOI: https://doi.org/10.1080/09205063.2019.1620592.

(57) Mao, N.; Russell, S. J.; Pourdeyhimi, B. 9 - Characterisation, testing and modelling of nonwoven fabrics. In *Handbook of Nonwovens*, Russell, S. J. Ed.; Woodhead Publishing, 2007; pp 401-514.

(58) Bunsell, A. R. 1 - Introduction to fibre tensile properties and failure. In *Handbook of Tensile Properties of Textile and Technical Fibres*, Bunsell, A. R. Ed.; Woodhead Publishing, 2009; pp 1-17.

(59) Elias, H.-G. Fasern, Fäden und Gewebe. In *Makromoleküle*, WILEY-VCH Verlag GmbH, 2002; pp 154-243.

(60) Long, A. C.; Boisse, P.; Robitaille, F. 2 - Mechanical analysis of textiles. In *Design and Manufacture of Textile Composites*, Long, A. C. Ed.; Woodhead Publishing, 2005; pp 62-109.

(61) Saville, B. P. 5 - Strength and elongation tests. In *Physical Testing of Textiles*, Saville, B. P. Ed.; Woodhead Publishing, 1999; pp 115-167.

(62) Silberstein, M. N.; Pai, C.-L.; Rutledge, G. C.; Boyce, M. C. Elastic–plastic behavior of non-woven fibrous mats. *Journal of the Mechanics and Physics of Solids* **2012**, *60* (2), 295-318. DOI: https://doi.org/10.1016/j.jmps.2011.10.007.

(63) Brydon, A. G.; Pourmohammadi, A. 2 - Dry-laid web formation. In *Handbook of Nonwovens*, Russell, S. J. Ed.; Woodhead Publishing, 2007; pp 16-111.

(64) White, C. 3 - Wet-laid web formation. In *Handbook of Nonwovens*, Russell, S. J. Ed.; Woodhead Publishing, 2007; pp 112-142.

(65) Bhat, G. S.; Malkan, S. R. 4 - Polymer-laid web formation. In *Handbook of Nonwovens*, Russell, S. J. Ed.; Woodhead Publishing, 2007; pp 143-200.

(66) Formhals, A. Process and apparatus for preparing artificial threads. United States of America 1934.

(67) Greiner, A.; Wendorff, J. H. Electrospinning: A Fascinating Method for the Preparation of Ultrathin Fibers. *Angewandte Chemie International Edition* **2007**, *46* (30), 5670-5703. DOI: https://doi.org/10.1002/anie.200604646.

(68) Iranshahi, K.; Defraeye, T.; Rossi, R. M.; Müller, U. C. Electrohydrodynamics and its applications: Recent advances and future perspectives. *International Journal of Heat and Mass Transfer* **2024**, *232*, 125895. DOI: https://doi.org/10.1016/j.ijheatmasstransfer.2024.125895.

(69) Xue, J.; Wu, T.; Dai, Y.; Xia, Y. Electrospinning and Electrospun Nanofibers: Methods, Materials, and Applications. *Chemical Reviews* **2019**, *119* (8), 5298-5415. DOI: https://doi.org/10.1021/acs.chemrev.8b00593.

(70) Duft, D.; Achtzehn, T.; Müller, R.; Huber, B. A.; Leisner, T. Rayleigh jets from levitated microdroplets. *Nature* **2003**, *421* (6919), 128-128. DOI: https://doi.org/10.1038/421128a.

(71) Huang, S.; Mansouri, J.; Le-Clech, P.; Leslie, G.; Tang, C. Y.; Fane, A. G. A comprehensive review of electrospray technique for membrane development: Current status, challenges, and opportunities. *Journal of Membrane Science* **2022**, *646*, 120248. DOI: https://doi.org/10.1016/j.memsci.2021.120248.

(72) Mkhize, N.; Bhaskaran, H. Electrohydrodynamic Jet Printing: Introductory Concepts and Considerations. *Small Science* **2022**, *2* (2), 2100073. DOI: https://doi.org/10.1002/smsc.202100073.

(73) Brown, T. D.; Dalton, P. D.; Hutmacher, D. W. Melt electrospinning today: An opportune time for an emerging polymer process. *Progress in Polymer Science* **2016**, *56*, 116-166. DOI: https://doi.org/10.1016/j.progpolymsci.2016.01.001.

(74) Nayak, R.; Padhye, R.; Arnold, L. 2 - Melt-electrospinning of nanofibers. In *Electrospun Nanofibers*, Afshari, M. Ed.; Woodhead Publishing, 2017; pp 11-40.

(75) Salas, C. 4 - Solution electrospinning of nanofibers. In *Electrospun Nanofibers*, Afshari, M. Ed.; Woodhead Publishing, 2017; pp 73-108.

(76) Yucheng, Y.; Glubay, S.; Stirling, R.; Ma, Q.; McKenzie, J. Improved fiber control through ohmic/convective flow behavior. *Journal of Materials Science* **2022**, *57* (22), 10457-10469. DOI: https://doi.org/10.1007/s10853-022-07304-7.

(77) Gatford, J. *A diagram of the electrospinning process showing the onset of instability*. The New Zealand Institute for Plant and Food Research Ltd, https://upload.wikimedia.org/wikipedia/commons/c/ca/Electrospinning_Diagram.jpg (accessed 29.09.2024).

(78) Reneker, D. H.; Yarin, A. L. Electrospinning jets and polymer nanofibers. *Polymer* **2008**, *49* (10), 2387-2425. DOI: https://doi.org/10.1016/j.polymer.2008.02.002.

(79) Shenoy, S. L.; Bates, W. D.; Frisch, H. L.; Wnek, G. E. Role of chain entanglements on fiber formation during electrospinning of polymer solutions: good solvent, non-specific polymer–polymer interaction limit. *Polymer* **2005**, *46* (10), 3372-3384. DOI: https://doi.org/10.1016/j.polymer.2005.03.011.

(80) Reneker, D.; Yarin, A.; Fong, H.; Koombhongse, S. Bending Instability of Electrically Charged Liquid Jets of Polymer Solutions in Electrospinning. *Journal of Applied Physics* **2000**, *87*, 4531-4547. DOI: https://doi.org/10.1063/1.373532.

(81) Rahmati, M.; Mills, D. K.; Urbanska, A. M.; Saeb, M. R.; Venugopal, J. R.; Ramakrishna, S.; Mozafari, M. Electrospinning for tissue engineering applications. *Progress in Materials Science* **2021**, *117*, 100721. DOI: https://doi.org/10.1016/j.pmatsci.2020.100721.

(82) Haider, A.; Haider, S. *Electrospinning and Electrospraying : Techniques and Applications*; [Place of publication not identified] : : IntechOpen, 2019. DOI: http://doi.org/10.5772/intechopen.77414.

(83) Casper, C. L.; Stephens, J. S.; Tassi, N. G.; Chase, D. B.; Rabolt, J. F. Controlling surface morphology of electrospun polystyrene fibers: Effect of humidity and molecular weight in the electrospinning process. *Macromolecules* **2004**, *37* (2), 573-578, Article. DOI: https://doi.org/10.1021/ma0351975 Scopus.

(84) Yao, T.; Chen, H.; Samal, P.; Giselbrecht, S.; Baker, M. B.; Moroni, L. Self-assembly of electrospun nanofibers into gradient honeycomb structures. *Materials & Design* **2019**, *168*, 107614. DOI: https://doi.org/10.1016/j.matdes.2019.107614.

(85) Jiang, L.; Zhao, Y.; Zhai, J. A Lotus-Leaf-like Superhydrophobic Surface: A Porous Microsphere/Nanofiber Composite Film Prepared by Electrohydrodynamics. *Angewandte Chemie International Edition* **2004**, *43* (33), 4338-4341. DOI: https://doi.org/10.1002/anie.200460333.

(86) Blume, C.; Kraus, X.; Heene, S.; Loewner, S.; Stanislawski, N.; Cholewa, F.; Blume, H. Vascular implants - new aspects for in situ tissue engineering. *Eng Life Sci* **2022**, *22* (3-4), 344-360. DOI: https://doi.org/10.1002/elsc.202100100 From NLM.

(87) Huang, J.; Fu, P.; Li, W.; Xiao, L.; Chen, J.; Nie, X. Influence of crosslinking density on the mechanical and thermal properties of plant oil-based epoxy resin. *RSC Advances* **2022**, *12* (36), 23048-23056, 10.1039/D2RA04206A. DOI: https://doi.org/10.1039/d2ra04206a.

(88) Pal, K.; Panwar, V.; Bahadur, J. 10 - Rubber blend nanocomposites. In *Progress in Rubber Nanocomposites*, Thomas, S., Maria, H. J. Eds.; Woodhead Publishing, 2017; pp 319-348.

(89) Spontak, R. J.; Patel, N. P. Thermoplastic elastomers: fundamentals and applications. *Current Opinion in Colloid & Interface Science* **2000**, *5* (5), 333-340. DOI: https://doi.org/10.1016/S1359-0294(00)00070-4.

(90) Kear, K. E. *Developments in Thermoplastic Elastomers*; Rapra Technology, 2003.

(91) Drobny, J. G. 2 - Brief History of Thermoplastic Elastomers. In *Handbook of Thermoplastic Elastomers (Second Edition)*, Drobny, J. G. Ed.; William Andrew Publishing, 2014; pp 13-15.

(92) Çoban, M.; Konuklar, F. A. S. A computational study on the mechanism and the kinetics of urethane formation. *Computational and Theoretical Chemistry* **2011**, *963* (1), 168-175. DOI: https://doi.org/10.1016/j.comptc.2010.10.017.

(93) Polloni, A.; Valério, A.; Oliveira, D.; Hermes de Araujo, P. H.; Sayer, C. Ultrasound assisted miniemulsion polymerization to prepare poly(urea-urethane) nanoparticles. *Polímeros* **2018**, *28*. DOI: https://doi.org/10.1590/0104-1428.02517.

(94) Prisacariu, C. *Polyurethane Elastomers: From Morphology to Mechanical Aspects*; Springer-Verlag, 2011. DOI: https://doi.org/10.1007/978-3-7091-0514-6_1.

(95) Versteegen, R. M.; Sijbesma, R. P.; Meijer, E. W. Synthesis and Characterization of Segmented Copoly(ether urea)s with Uniform Hard Segments. *Macromolecules* **2005**, *38* (8), 3176-3184. DOI: https://doi.org/10.1021/ma0478207.

(96) Schollenberger, C. S. Simulated vulcanizates of polyurethane elastomers. United States of America 1955.

(97) He, Y.; Xie, D.; Zhang, X. The structure, microphase-separated morphology, and property of polyurethanes and polyureas. *Journal of Materials Science* **2014**, *49* (21), 7339-7352. DOI: http://dx.doi.org/10.1007/s10853-014-8458-y.

(98) Buckley, C. P.; Prisacariu, C.; Martin, C. Elasticity and inelasticity of thermoplastic polyurethane elastomers: Sensitivity to chemical and physical structure. *Polymer* **2010**, *51* (14), 3213-3224. DOI: https://doi.org/10.1016/j.polymer.2010.04.069.

(99) Touchet, T. J.; Cosgriff-Hernandez, E. M. Hierarchal structure–property relationships of segmented polyurethanes. In *Advances in Polyurethane Biomaterials*, Stuart L. Cooper, J. G. Ed.; Elsevier Ltd. , 2016; pp 3-22.

(100) Baudis, S.; Ligon, S. C.; Seidler, K.; Weigel, G.; Grasl, C.; Bergmeister, H.; Schima, H.; Liska, R. Hard-block degradable thermoplastic urethane-elastomers for electrospun vascular prostheses. *Journal of Polymer Science Part A: Polymer Chemistry* **2011**, *50* (7), 1272-1280. DOI: https://doi.org/10.1002/pola.25887.

(101) Ehrmann, K.; Potzmann, P.; Dworak, C.; Bergmeister, H.; Eilenberg, M.; Grasl, C.; Koch, T.; Schima, H.; Liska, R.; Baudis, S. Hard Block Degradable Polycarbonate Urethanes: Promising Biomaterials for Electrospun Vascular Prostheses. *Biomacromolecules* **2020**, *21* (2), 376-387. DOI: https://doi.org/10.1021/acs.biomac.9b01255 From NLM Medline.

(102) Drobny, J. G. 9 - Thermoplastic Polyurethane Elastomers. In *Handbook of Thermoplastic Elastomers (Second Edition)*, Drobny, J. G. Ed.; William Andrew Publishing, 2014; pp 233-253.

(103) Elias, H.-G. Polykondensationen und Polyadditionen. In *Makromoleküle*, WILEY-VCH Verlag GmbH, 1999; pp 417-486.

(104) Delebecq, E.; Pascault, J.-P.; Boutevin, B.; Ganachaud, F. On the Versatility of Urethane/Urea Bonds: Reversibility, Blocked Isocyanate, and Non-isocyanate Polyurethane. *Chemical Reviews* **2013**, *113* (1), 80-118. DOI: https://doi.org/10.1021/cr300195n.

(105) Zhang, M. Q. Dynamic bonds in polymers. *Journal of Polymer Science* **2024**, *62* (5), 785-786. DOI: https://doi.org/10.1002/pol.20240044.

(106) Fortman, D. J.; Brutman, J. P.; Cramer, C. J.; Hillmyer, M. A.; Dichtel, W. R. Mechanically Activated, Catalyst-Free Polyhydroxyurethane Vitrimers. *Journal of the American Chemical Society* **2015**, *137* (44), 14019-14022. DOI: 10.1021/jacs.5b08084.

(107) Yan, P.; Zhao, W.; Fu, X.; Liu, Z.; Kong, W.; Zhou, C.; Lei, J. Multifunctional polyurethane-vitrimers completely based on transcarbamoylation of carbamates: thermally-induced dual-shape memory effect and self-welding. *RSC Advances* **2017**, *7* (43), 26858-26866, 10.1039/C7RA01711A. DOI: https://doi.org/10.1039/C7RA01711A.

(108) Li, L.; Chen, X.; Torkelson, J. M. Reprocessable Polymer Networks via Thiourethane Dynamic Chemistry: Recovery of Cross-link Density after Recycling and Proof-of-Principle Solvolysis Leading to Monomer Recovery. *Macromolecules* **2019**, *52* (21), 8207-8216. DOI: https://doi.org/10.1021/acs.macromol.9b01359.

(109) Zhang, Q.; Wang, S.; Rao, B.; Chen, X.; Ma, L.; Cui, C.; Zhong, Q.; Li, Z.; Cheng, Y.; Zhang, Y. Hindered urea bonds for dynamic polymers: An overview. *Reactive and Functional Polymers* **2021**, *159*, 104807. DOI: https://doi.org/10.1016/j.reactfunctpolym.2020.104807.

(110) Ying, H.; Zhang, Y.; Cheng, J. Dynamic urea bond for the design of reversible and self-healing polymers. *Nature Communications* **2014**, *5* (1), 3218. DOI: https://doi.org/10.1038/ncomms4218.

(111) Liu, W.-X.; Zhang, C.; Zhang, H.; Zhao, N.; Yu, Z.-X.; Xu, J. Oxime-Based and Catalyst-Free Dynamic Covalent Polyurethanes. *Journal of the American Chemical Society* **2017**, *139* (25), 8678-8684. DOI: https://doi.org/10.1021/jacs.7b03967.

(112) Huang, R.; Yang, A.; Liu, Z.; Liu, F.; Fang, T.; He, F.; Li, Y.; Jiang, Z.; Lan, H.; Zhang, K.; et al. Poly(ethylene glycol)-based polyurethanes based on dynamic oxime-urethane bonds for sustainable thermal energy storage. *Colloids and Surfaces A: Physicochemical and Engineering Aspects* **2024**, *698*, 134544. DOI: https://doi.org/10.1016/j.colsurfa.2024.134544.

(113) Wen, Z.; Han, X.; Fairbanks, B. D.; Yang, K.; Bowman, C. N. Development of thiourethanes as robust, reprocessable networks. *Polymer* **2020**, *202*, 122715. DOI: https://doi.org/10.1016/j.polymer.2020.122715.

(114) Zhang, Z. P.; Rong, M. Z.; Zhang, M. Q. Mechanically Robust, Self-Healable, and Highly Stretchable “Living” Crosslinked Polyurethane Based on a Reversible C□C Bond. *Advanced Functional Materials* **2018**, *28* (11), 1706050. DOI: https://doi.org/10.1002/adfm.201706050 (acccessed 2025/02/10).

(115) Chen, J.-H.; Hu, D.-D.; Li, Y.-D.; Meng, F.; Zhu, J.; Zeng, J.-B. Castor oil derived poly(urethane urea) networks with reprocessibility and enhanced mechanical properties. *Polymer* **2018**, *143*, 79-86. DOI: https://doi.org/10.1016/j.polymer.2018.04.013.

(116) Wojtecki, R. J.; Meador, M. A.; Rowan, S. J. Using the dynamic bond to access macroscopically responsive structurally dynamic polymers. *Nature Materials* **2011**, *10* (1), 14-27. DOI: https://doi.org/10.1038/nmat2891.

(117) Sun, H.; Kabb, C. P.; Dai, Y.; Hill, M. R.; Ghiviriga, I.; Bapat, A. P.; Sumerlin, B. S. Macromolecular metamorphosis via stimulus-induced transformations of polymer architecture. *Nature Chemistry* **2017**, *9* (8), 817-823. DOI: https://doi.org/10.1038/nchem.2730.

(118) Kloxin, C. J.; Scott, T. F.; Adzima, B. J.; Bowman, C. N. Covalent Adaptable Networks (CANs): A Unique Paradigm in Cross-Linked Polymers. *Macromolecules* **2010**, *43* (6), 2643-2653. DOI: https://doi.org/10.1021/ma902596s.

(119) Webber, M. J.; Tibbitt, M. W. Dynamic and reconfigurable materials from reversible network interactions. *Nature Reviews Materials* **2022**, *7* (7), 541-556. DOI: https://doi.org/10.1038/s41578-021-00412-x.

(120) Nande, A.; Kalyani, N. T.; Tiwari, A.; Dhoble, S. J. 1 - Exploring the world of functional materials. In *Functional Materials from Carbon, Inorganic, and Organic Sources*, Dhoble, S. J., Nande, A., Kalyani, N. T., Tiwari, A., Arof, A. K. Eds.; Woodhead Publishing, 2023; pp 1-19.

(121) Cahn, R. W. Chapter 7 - Functional Materials. In *Pergamon Materials Series*, Vol. 5; Pergamon, 2001; pp 253-304.

(122) Vasiliev, V. V.; Morozov, E. V. Chapter 1 - Introduction. In *Advanced Mechanics of Composite Materials (Third Edition)*, Vasiliev, V. V., Morozov, E. V. Eds.; Elsevier, 2013; pp 1-27.

(123) Schwarzl, P.; Koch, T.; Liska, R.; Baudis, S. Macromolecular metamorphosis of thermoplastic poly(thio)urethanes containing boronic acid esters. *Journal of Applied Polymer Science* **2025**, *142* (5), e56429. DOI: https://doi.org/10.1002/app.56429.

(124) Theodosis-Nobelos, P.; Charalambous, D.; Triantis, C.; Rikkou-Kalourkoti, M. Drug Conjugates Using Different Dynamic Covalent Bonds and their Application in Cancer Therapy. *Curr Drug Deliv* **2020**, *17* (7), 542-557. DOI: https://doi.org/10.2174/1567201817999200508092141 From NLM.

(125) Lorenzatti, A. J.; Retzlaff, B. M. Unmet needs in the management of atherosclerotic cardiovascular disease: Is there a role for emerging anti-inflammatory interventions? *International Journal of Cardiology* **2016**, *221*, 581-586. DOI: https://doi.org/10.1016/j.ijcard.2016.07.061.

(126) Chhabra, L.; Zain, M. A.; Siddiqui, W. J. Coronary Stents. In *StatPearls*, StatPearls Publishing

Copyright © 2025, StatPearls Publishing LLC., 2025.

(127) Serruys, P. W.; Unger, F.; Sousa, J. E.; Jatene, A.; Bonnier, H. J.; Schönberger, J. P.; Buller, N.; Bonser, R.; van den Brand, M. J.; van Herwerden, L. A.; et al. Comparison of coronary-artery bypass surgery and stenting for the treatment of multivessel disease. *N Engl J Med* **2001**, *344* (15), 1117-1124. DOI: https://doi.org/10.1056/nejm200104123441502 From NLM.

(128) Ravi, S.; Chaikof, E. L. Biomaterials for vascular tissue engineering. *Regen Med* **2010**, *5* (1), 107-120. DOI: https://doi.org/10.2217/rme.09.77 From NLM.

(129) Kumar, V. A.; Brewster, L. P.; Caves, J. M.; Chaikof, E. L. Tissue Engineering of Blood Vessels: Functional Requirements, Progress, and Future Challenges. *Cardiovasc Eng Technol* **2011**, *2* (3), 137-148. DOI: https://doi.org/10.1007/s13239-011-0049-3 From NLM.

(130) Yavuz, M.; Aydınoğlu, A.; Güner, M. B.; Yoruç Hazar, A. B. 8 - Polyurethane as biomaterials for biomedical applications. In *Handbook of Polymers in Medicine*, Mozafari, M., Singh Chauhan, N. P. Eds.; Woodhead Publishing, 2023; pp 243-262.

(131) Drobny, J. G. 15 - Applications of Thermoplastic Elastomers. In *Handbook of Thermoplastic Elastomers (Second Edition)*, Drobny, J. G. Ed.; William Andrew Publishing, 2014; pp 301-337.

(132) Asensio, M.; Costa, V.; Nohales, A.; Bianchi, O.; Gómez, C. M. Tunable Structure and Properties of Segmented Thermoplastic Polyurethanes as a Function of Flexible Segment. *Polymers* **2019**, *11* (12), 1910. DOI: https://doi.org/10.3390/polym11121910.

(133) Schoental, R. Carcinogenic and Chronic Effects of 4,4′-Diaminodiphenylmethane, an Epoxyresin Hardener. *Nature* **1968**, *219* (5159), 1162-1163. DOI: https://doi.org/10.1038/2191162a0.

(134) Cardy, R. H. Carcinogenicity and chronic toxicity of 2,4-toluenediamine in F344 rats. *J Natl Cancer Inst* **1979**, *62* (4), 1107-1116. DOI: https://pubmed.ncbi.nlm.nih.gov/285285/ From NLM.

(135) Wu, H.; Liu, X.; Sheng, D.; Zhou, Y.; Xu, S.; Xie, H.; Tian, X.; Sun, Y.; Shi, B.; Yang, Y. High performance and near body temperature induced self-healing thermoplastic polyurethane based on dynamic disulfide and hydrogen bonds. *Polymer* **2021**, *214*, 123261. DOI: https://doi.org/10.1016/j.polymer.2020.123261.

(136) Kim, S.-M.; Jeon, H.; Shin, S.-H.; Park, S.-A.; Jegal, J.; Hwang, S. Y.; Oh, D. X.; Park, J. Superior Toughness and Fast Self-Healing at Room Temperature Engineered by Transparent Elastomers. *Advanced Materials* **2018**, *30* (1), 1705145. DOI: https://doi.org/10.1002/adma.201705145.

(137) Lai, Y.; Kuang, X.; Yang, W.-H.; Wang, Y.; Zhu, P.; Li, J.-P.; Dong, X.; Wang, D.-J. Dynamic Bonds Mediate π-π Interaction via Phase Locking Effect for Enhanced Heat Resistant Thermoplastic Polyurethane. *Chinese Journal of Polymer Science* **2021**, *39* (2), 154-163. DOI: https://doi.org/10.1007/s10118-020-2494-7.

(138) Park, K. H.; Tani, T.; Kakimoto, M.-a.; Imai, Y. Synthesis and characterization of new soluble aromatic poly(ureaimide)s from N,N′-dimethyl-N,N′-bis(aminophenyl)ureas and aromatic tetracarboxylic dianhydrides. *Macromolecular Chemistry and Physics* **1998**, *199* (3), 457-461. DOI: https://doi.org/10.1002/(SICI)1521-3935(19980301)199:3<457::AID-MACP457>3.0.CO;2-W.

(139) Tahir, M.; Heinrich, G.; Mahmood, N.; Boldt, R.; Wießner, S.; Stöckelhuber, K. W. Blending In Situ Polyurethane-Urea with Different Kinds of Rubber: Performance and Compatibility Aspects. *Materials* **2018**, *11* (11), 2175. DOI: https://doi.org/10.3390/ma11112175.

(140) Ableidinger, K. Self-reinforcing elastomers based on dynamic polyurethanes. Technische Universität Wien, Vienna, 2021.

(141) Xianyu, B.; Xu, H. Dynamic covalent bond-based materials: From construction to biomedical applications. *Supramolecular Materials* **2024**, *3*, 100070. DOI: https://doi.org/10.1016/j.supmat.2024.100070.

(142) Wilson, B. W. Cholinesterase Inhibition. In *Encyclopedia of Toxicology (Second Edition)*, Wexler, P. Ed.; Elsevier, 2005; pp 588-599.

(143) Dhuguru, J.; Zviagin, E.; Skouta, R. FDA-Approved Oximes and Their Significance in Medicinal Chemistry. *Pharmaceuticals* **2022**, *15* (1), 66.

(144) Fathi-Karkan, S.; Banimohamad-Shotorbani, B.; Saghati, S.; Rahbarghazi, R.; Davaran, S. A critical review of fibrous polyurethane-based vascular tissue engineering scaffolds. *Journal of Biological Engineering* **2022**, *16* (1), 6. DOI: https://doi.org/10.1186/s13036-022-00286-9.

(145) Karkan, S. F.; Rahbarghazi, R.; Davaran, S.; Kaleybar, L. S.; Khoshfetrat, A. B.; Heidarzadeh, M.; Zolali, E.; Akbarzadeh, A. Electrospun polyurethane/poly (ε-caprolactone) nanofibers promoted the attachment and growth of human endothelial cells in static and dynamic culture conditions. *Microvascular Research* **2021**, *133*, 104073. DOI: https://doi.org/10.1016/j.mvr.2020.104073.

(146) Ma, W.; Liu, Z.; Zhu, T.; Wang, L.; Du, J.; Wang, K.; Xu, C. Fabric-Enhanced Vascular Graft with Hierarchical Structure for Promoting the Regeneration of Vascular Tissue. *Adv Healthc Mater* **2024**, *13* (16), e2302676. DOI: https://doi.org/10.1002/adhm.202302676 From NLM.

(147) Mostofizadeh, M.; Pitcher, M. L.; Sheikhi, A. Chapter 5 - Coaxial electrospinning. In *Electrospun and Nanofibrous Membranes*, Kargari, A., Matsuura, T., Shirazi, M. M. A. Eds.; Elsevier, 2023; pp 105-126.

(148) Kouhi, M.; Mobasheri, M.; Valipouri, A. Chapter 7 - Needleless electrospinning. In *Electrospun and Nanofibrous Membranes*, Kargari, A., Matsuura, T., Shirazi, M. M. A. Eds.; Elsevier, 2023; pp 145-171.

(149) Wu, R.; Sui, C.; Chen, T.-H.; Zhou, Z.; Li, Q.; Yan, G.; Han, Y.; Liang, J.; Hung, P.-J.; Luo, E.; et al. Spectrally engineered textile for radiative cooling against urban heat islands. *Science* **2024**, *384* (6701), 1203-1212. DOI: https://doi.org/10.1126/science.adl0653.

(150) Wang, C.; Wu, S.; Jian, M.; Xie, J.; Xu, L.; Yang, X.; Zheng, Q.; Zhang, Y. Silk nanofibers as high efficient and lightweight air filter. *Nano Research* **2016**, *9* (9), 2590-2597. DOI: https://doi.org/10.1007/s12274-016-1145-3.

(151) Boaretti, C.; Pasquini, L.; Sood, R.; Giancola, S.; Donnadio, A.; Roso, M.; Modesti, M.; Cavaliere, S. Mechanically stable nanofibrous sPEEK/Aquivion® composite membranes for fuel cell applications. *Journal of Membrane Science* **2018**, *545*, 66-74. DOI: https://doi.org/10.1016/j.memsci.2017.09.055.

(152) Senthamizhan, A.; Balusamy, B.; Uyar, T. Glucose sensors based on electrospun nanofibers: a review. *Analytical and Bioanalytical Chemistry* **2016**, *408* (5), 1285-1306. DOI: https://doi.org/10.1007/s00216-015-9152-x.

(153) Apsite, I.; Stoychev, G.; Zhang, W.; Jehnichen, D.; Xie, J.; Ionov, L. Porous Stimuli-Responsive Self-Folding Electrospun Mats for 4D Biofabrication. *Biomacromolecules* **2017**, *18* (10), 3178-3184. DOI: https://doi.org/10.1021/acs.biomac.7b00829.

(154) George, G.; Senthil, T.; Luo, Z.; Anandhan, S. 22 - Sol-gel electrospinning of diverse ceramic nanofibers and their potential applications. In *Electrospun Polymers and Composites*, Dong, Y., Baji, A., Ramakrishna, S. Eds.; Woodhead Publishing, 2021; pp 689-764.

(155) Wang, Y.; Huang, H.; Gao, J.; Lu, G.; Zhao, Y.; Xu, Y.; Jiang, L. TiO2–SiO2 composite fibers with tunable interconnected porous hierarchy fabricated by single-spinneret electrospinning toward enhanced photocatalytic activity. *Journal of Materials Chemistry A* **2014**, *2* (31), 12442-12448, 10.1039/C4TA01208A. DOI: https://doi.org/10.1039/C4TA01208A.

(156) Bauer, A.; Lee, K.; Song, C.; Xie, Y.; Zhang, J.; Hui, R. Pt nanoparticles deposited on TiO2 based nanofibers: Electrochemical stability and oxygen reduction activity. *Journal of Power Sources* **2010**, *195* (10), 3105-3110. DOI: https://doi.org/10.1016/j.jpowsour.2009.11.107.

(157) Miao, X.; Chen, Z.; Wang, N.; Nuli, Y.; Wang, J.; Yang, J.; Hirano, S.-i. Electrospun V2MoO8 as a cathode material for rechargeable batteries with Mg metal anode. *Nano Energy* **2017**, *34*, 26-35. DOI: https://doi.org/10.1016/j.nanoen.2017.02.014.

(158) Sill, T. J.; von Recum, H. A. Electrospinning: Applications in drug delivery and tissue engineering. *Biomaterials* **2008**, *29* (13), 1989-2006. DOI: https://doi.org/10.1016/j.biomaterials.2008.01.011.

(159) Zhou, J.; Cao, C.; Ma, X.; Lin, J. Electrospinning of silk fibroin and collagen for vascular tissue engineering. *International Journal of Biological Macromolecules* **2010**, *47* (4), 514-519. DOI: https://doi.org/10.1016/j.ijbiomac.2010.07.010.

(160) Bergmeister, H.; Grasl, C.; Walter, I.; Plasenzotti, R.; Stoiber, M.; Schreiber, C.; Losert, U.; Weigel, G.; Schima, H. Electrospun Small-Diameter Polyurethane Vascular Grafts: Ingrowth and Differentiation of Vascular-Specific Host Cells. *Artificial Organs* **2012**, *36* (1), 54-61. DOI: https://doi.org/10.1111/j.1525-1594.2011.01297.x.

(161) Grasl, C.; Stoiber, M.; Röhrich, M.; Moscato, F.; Bergmeister, H.; Schima, H. Electrospinning of small diameter vascular grafts with preferential fiber directions and comparison of their mechanical behavior with native rat aortas. *Materials Science and Engineering: C* **2021**, *124*, 112085. DOI: https://doi.org/10.1016/j.msec.2021.112085.

(162) Rohringer, S.; Grasl, C.; Ehrmann, K.; Hager, P.; Hahn, C.; Specht, S. J.; Walter, I.; Schneider, K. H.; Zopf, L. M.; Baudis, S.; et al. Biodegradable, Self-Reinforcing Vascular Grafts for In Situ Tissue Engineering Approaches. *Advanced Healthcare Materials* **2023**, *12* (23), 2300520. DOI: https://doi.org/10.1002/adhm.202300520.

(163) Fitzka, M. A systematic study on self-reinforcing thermoplastic urethane/urea elastomers. Technische Universität Wien, Vienna, 2021.

(164) McKeen, L. W. Chapter 1 - Introduction to plastics, polymers, and their properties. In *The Effect of Temperature and Other Factors on Plastics and Elastomers (Fourth Edition)*, McKeen, L. W. Ed.; William Andrew Publishing, 2023; pp 1-45.

(165) Shrivastava, A. 2 - Polymerization. In *Introduction to Plastics Engineering*, Shrivastava, A. Ed.; William Andrew Publishing, 2018; pp 17-48.

(166) V., D. I. f. N. e. *DIN-53240-1: Bestimmung der Hydroxylzahl*

Berlin, 2013.

(167) Pu, Y.; Cao, S.; Ragauskas, A. J. Application of quantitative 31P NMR in biomass lignin and biofuel precursors characterization. *Energy & Environmental Science* **2011**, *4* (9). DOI: https://doi.org/10.1039/C1EE01201K.

(168) Granata, A.; Argyropoulos, D. S. 2-Chloro-4,4,5,5-tetramethyl-1,3,2-dioxaphospholane, a Reagent for the Accurate Determination of the Uncondensed and Condensed Phenolic Moieties in Lignins. *Journal of Agricultural and Food Chemistry* **2002**, *43* (6), 1538-1544. DOI: https://doi.org/10.1021/jf00054a023.

(169) Baudis, S. Development and Processing of Materials for Vascular Tissue Regeneration. TU Wien, Vienna, 2010. http://hdl.handle.net/20.500.12708/10290.

(170) Elias, H.-G. Makrokonformationen. In *Makromoleküle*, WILEY-VCH Verlag GmbH, 2000; pp 66-137.

(171) Elias, H.-G. Mikrokonformationen. In *Makromoleküle*, WILEY-VCH Verlag GmbH, 2000; pp 40-65.

(172) Elias, H.-G. Thermische Eigenschaften. In *Makromoleküle*, WILEY-VCH Verlag GmbH, 2000; pp 426-469.

(173) Elias, H.-G. Prüfung. In *Makromoleküle*, WILEY-VCH Verlag GmbH, 2002; pp 130-153.

(174) Ishino, K.; Shingai, H.; Hikita, Y.; Yoshikawa, I.; Houjou, H.; Iwase, K. Cold Crystallization and the Molecular Structure of Imidazolium-Based Ionic Liquid Crystals with a p-Nitroazobenzene Moiety. *ACS Omega* **2021**, *6* (48), 32869-32878. DOI: https://doi.org/10.1021/acsomega.1c04866 From NLM.

(175) Merck. *N,N'-Di-tert-butylethylenediamine*. Merck, 2024. https://www.sigmaaldrich.com/AT/en/product/aldrich/447005?srsltid=AfmBOoqgFI9KEjzTpExR6qY2yofKKBVhC3xIXCBnrjQ_r4DOa_8SInYg (accessed 17.11.2024).

(176) Elias, H.-G. Elastizität. In *Makromoleküle*, WILEY-VCH Verlag GmbH, 2000; pp 517-567.

(177) Yu, W.; Wang, X.; Yin, X.; Ferraris, E.; Zhang, J. The effects of thermal annealing on the performance of material extrusion 3D printed polymer parts. *Materials & Design* **2023**, *226*, 111687. DOI: https://doi.org/10.1016/j.matdes.2023.111687.

(178) Seisenbacher, S. Benutzerhandbuch: Elektrospinnmaschine PL-30kV. In *Institut für Angewandte Synthesechemie (IAS)*, Technische Universität Wien: Vienna, 2023.

(179) Elias, H.-G. Viskosität verdünnter Lösungen. In *Makromoleküle*, WILEY-VCH Verlag GmbH, 2000; pp 395-425.

(180) Elias, H.-G. Thermodynamik von Polymerlösungen. In *Makromoleküle*, WILEY-VCH Verlag GmbH, 2000; pp 292-362.

(181) Laterreur, V.; Ruel, J.; Auger, F. A.; Vallières, K.; Tremblay, C.; Lacroix, D.; Tondreau, M.; Bourget, J.-M.; Germain, L. Comparison of the direct burst pressure and the ring tensile test methods for mechanical characterization of tissue-engineered vascular substitutes. *Journal of the Mechanical Behavior of Biomedical Materials* **2014**, *34*, 253-263. DOI: https://doi.org/10.1016/j.jmbbm.2014.02.017.

(182) Calaf-Chica, J.; Martínez-Peña, J.; Bravo Díez, P. M.; Preciado Calzada, M. Ring Hoop Tension Test for yield strength estimation: Numerical analysis for a novel correlation method and applicability for mechanical testing of tubes and pipes. *Mechanics of Materials* **2022**, *169*, 104295. DOI: https://doi.org/10.1016/j.mechmat.2022.104295.

(183) *ISO-7198:2016: Cardiovascular implants and extracorporeal systems - Vascular prostheses - Tubular vascular grafts and vascular patches*; 2016.

(184) *ISO 9073-2: 1995: Textiles - Test methods for nonwovens - Part 2: Determination of thickness*; Geneva, 1996.

(185) Valentinuzzi, M. E.; Kohen, A. J. Laplaces law: What it is about, where it comes from, and how it is often applied in physiology [retrospectroscope]. *IEEE Pulse* **2011**, *2* (4), 74-81+84, Article. DOI: http://dx.doi.org/10.1109/MPUL.2011.942054 Scopus.

(186) Worldwide trends in blood pressure from 1975 to 2015: a pooled analysis of 1479 population-based measurement studies with 19·1 million participants. *Lancet* **2017**, *389* (10064), 37-55. DOI: https://doi.org/10.1016/S0140-6736(16)31919-5 From NLM.

(187) Worldwide trends in hypertension prevalence and progress in treatment and control from 1990 to 2019: a pooled analysis of 1201 population-representative studies with 104 million participants. *Lancet* **2021**, *398* (10304), 957-980. DOI: https://doi.org/10.1016/s0140-6736(21)01330-1 From NLM.

(188) Armarego, W. L. F. Chapter 1 - Common Physical Techniques Used in Purification. In *Purification of Laboratory Chemicals (Eighth Edition)*, Armarego, W. L. F. Ed.; Butterworth-Heinemann, 2017; pp 1-70.

(189) Cookson, D. J.; Smith, B. E. Optimal conditions for obtaining quantitative 13C NMR, data. *Journal of Magnetic Resonance (1969)* **1984**, *57* (3), 355-368. DOI: https://doi.org/10.1016/0022-2364(84)90253-1.

Appendix

1. ^{31}P-NMR spectra of phosphorylated poly(tetrahydrofuran)

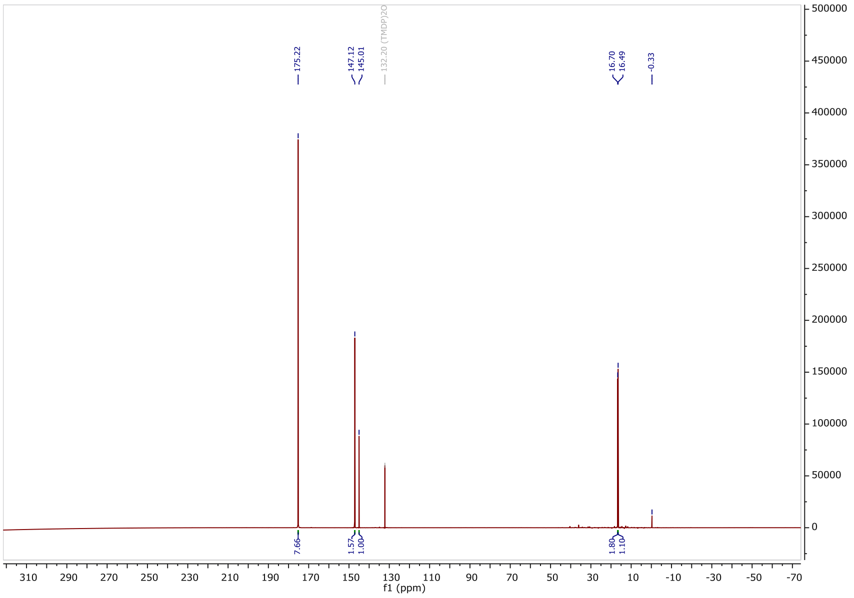

Figure 67: 600 MHz ^{31}P-NMR spectrum of reaction mixture from experiment 1 after phosphorylation for determination of the number average molecular weight of pTHF

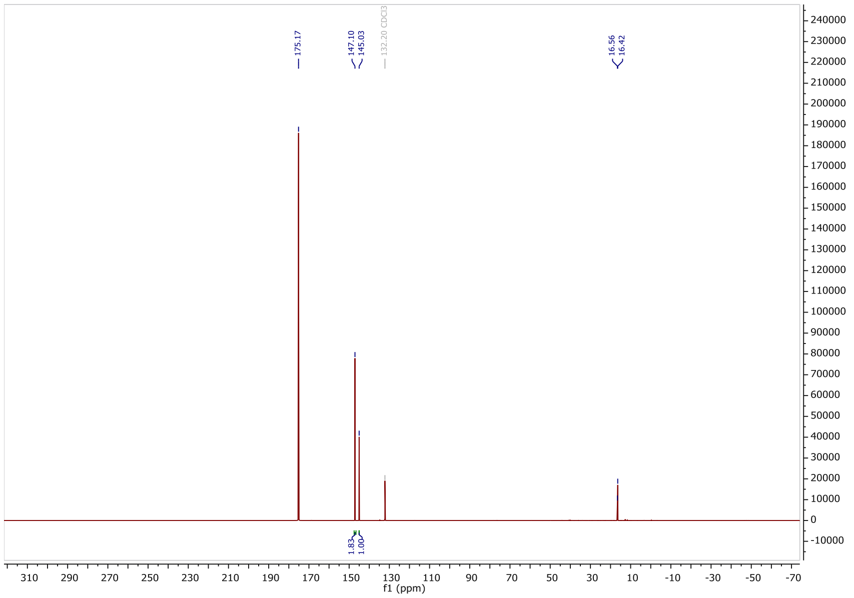

Figure 68: 600 MHz ^{31}P-NMR spectrum of reaction mixture from experiment 2 after phosphorylation for determination of the number average molecular weight of pTHF

2. Tensile test results for self-reinforcement study

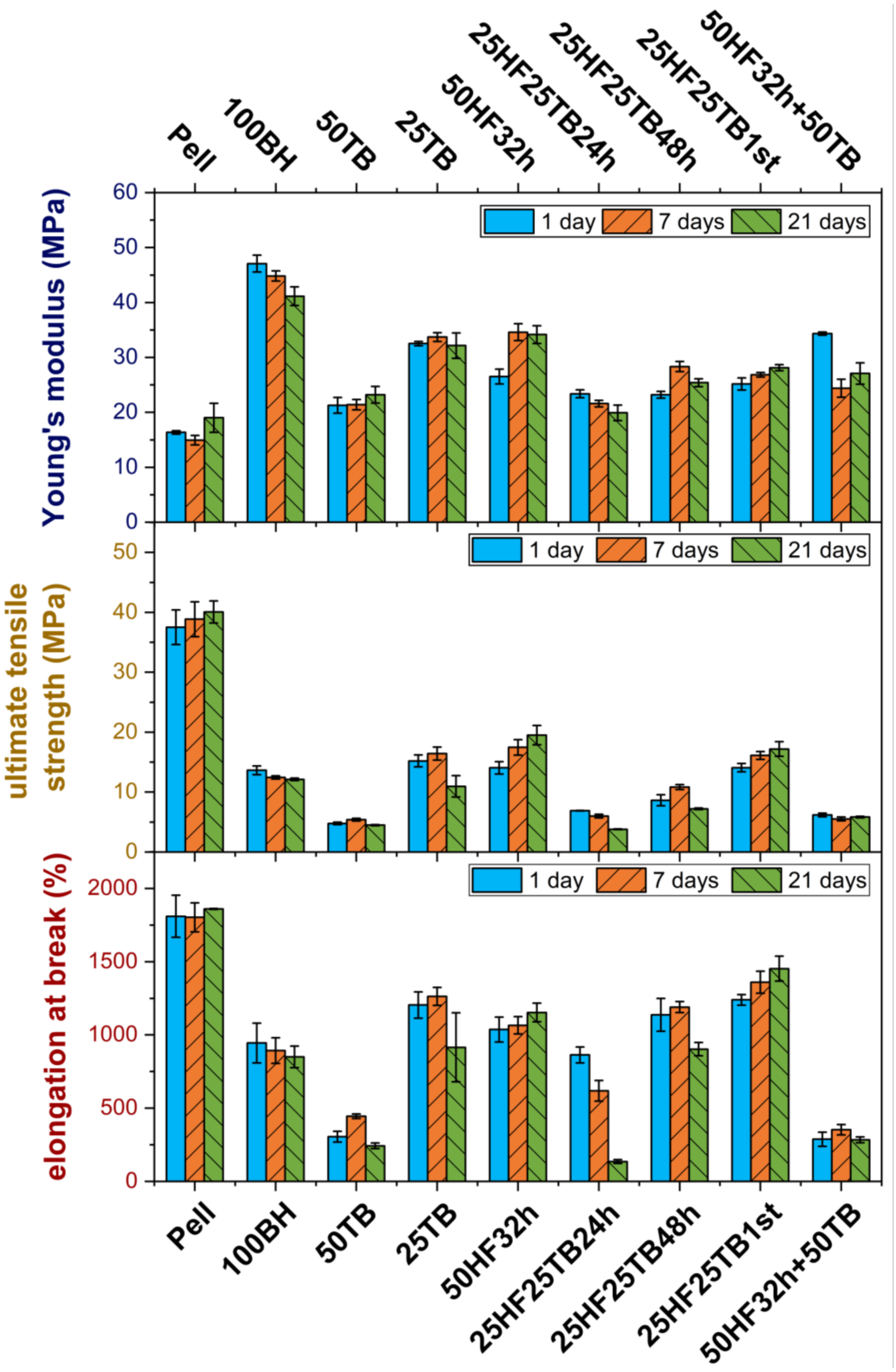

Figure 69: Tensile test results regarding Young's modulus, ultimate tensile strength, and elongation at break of the unconditioned TPU(U) specimens of Pell, 100BH, 50TB, 25TB, 50HF32h, 25HF25TB24h, 25HF25TB48h, and 25HF25TB1st, and the TPU(U) mixture 50HF32h+50TB after 1, 7, and 21 day of dry storages

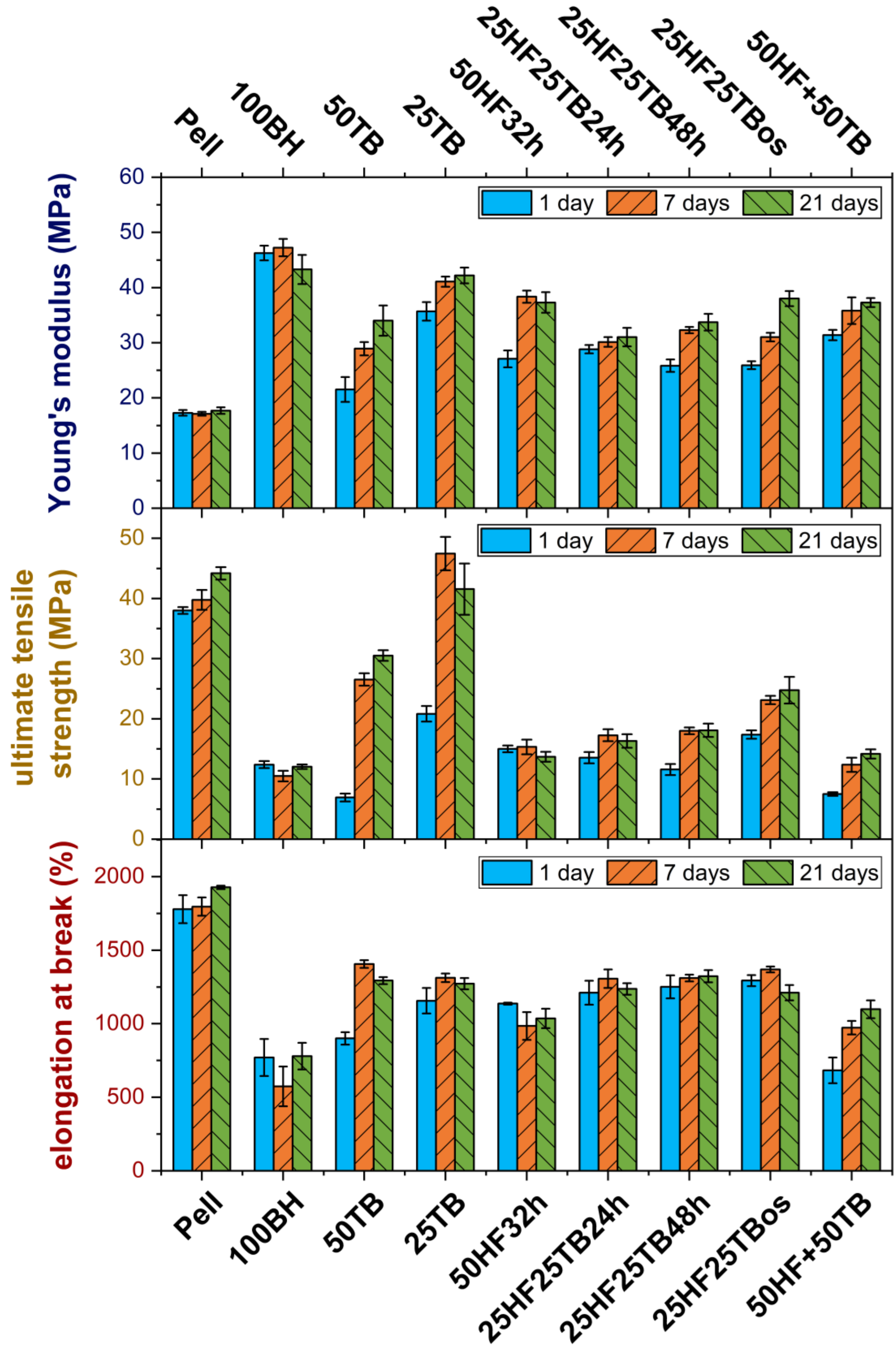
Pell
100BH
50TB
25TB
50HF32h
25HF25TB24h
25HF25TB48h
25HF25TBos
50HF+50TB
Young's modulus (MPa)
0
10
20
30
40
50
60
ultimate tensile strength (MPa)
0
10
20
30
40
50
elongation at break (%)
0
500
1000
1500
2000
1 day
7 days
21 days

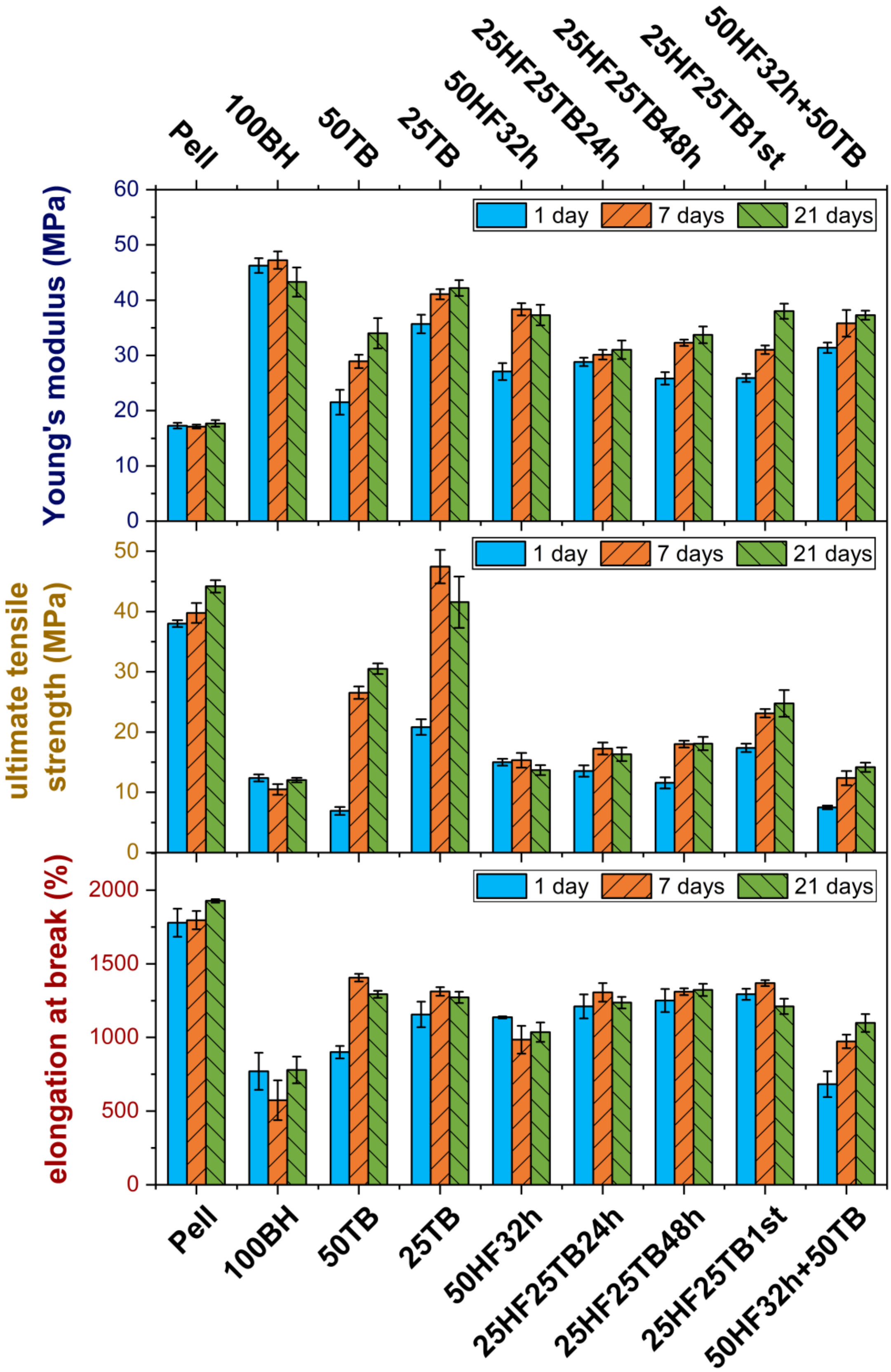

Figure 70: Tensile test results regarding Young's modulus, ultimate tensile strength, and elongation at break of the conditioned TPU(U) specimens of Pell, 100BH, 50TB, 25TB, 50HF32h, 25HF25TB24h, 25HF25TB48h, and 25HF25TB1st, and the TPU(U) mixture 50HF32h+50TB after conditioning in deionized water for 1, 7, and 21 days

3. Method evaluation for thickness determination

To confirm, whether the method of thickness determination established in Results and Discussion chapter 3.3.3 yields similar results as the thickness measurement of the same material on a single sheet. A tube of ESM prepared from each TPU(U) Pell, 100BH, 50TB, 25TB, and 25HF25TB was first measured with the new method by wedging the tube between two microscopy cover glasses, and determining the thickness as specified in Experimental chapter 3.3.3. Then, the tube was cut open into a single sheet as suggested by ISO 7198:2016, which was subsequently also wedged between the two microscopy cover glasses and measured regarding its thickness. For both methods, the thickness was measured at 6 different locations each. Their averages and standard deviations are summarized in Figure 71 and show comparable values for each TPU(U).

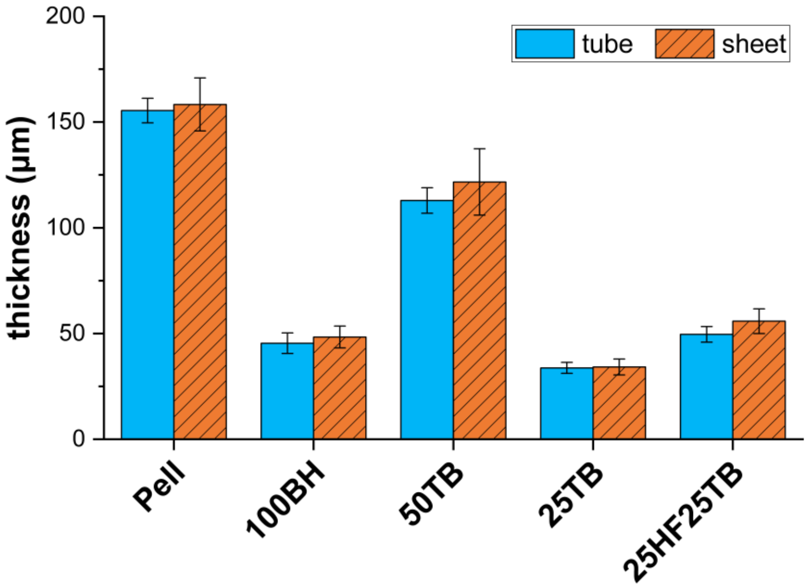

Figure 71: Results of mechanical thickness measurements via compression of an electrospun tube (tube) and of a single sheet of the same electrospun tube cut open (sheet) between two microscopy cover glasses.

Apart from these mechanical thickness measurements, the used tubular ESM of 100BH was also, previously, characterized optically *via* microscopy. The comparison between the mechanical thickness measurement and the optical measurement of the tubular ESM is shown in Figure 72 and also shows comparable values. The higher standard deviation of the optical method is thereby the product of thickness differences in circumferential direction due to the rough surface of the material.

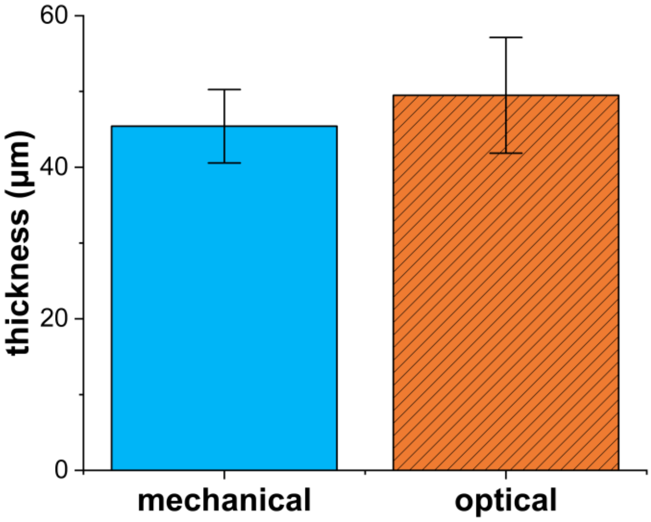

Figure 72: Thickness of a tubular electrospun material of 100BH determined mechanically with a caliper (blue) and optically via microscopy (orange).

4. Elongation of the sample holder for mechanical characterization of electrospun tubes

To determine the actual elongation of the tubular test specimens during their mechanical characterization (see Results and Discussion chapter 3.3.4), the elongation of the sample holders under the applied load need to be considered as well. For this, an aluminum ring with an outer diameter of 6.01 ± 0.01 mm, a length of 4.40 ± 0.08 mm, and a ring thickness of 0.56 ± 0.02 mm was threaded onto the sample holders (see Figure 73) and stretched with the same method as the tubular test specimens until the standard force passed 5 N.

Figure 73: Image of the measuring setup with the aluminum ring

Assuming a negligent elongation of the more rigid aluminum ring, the corresponding strain measured by the device could then be attributed to the deformation of the sample holders. This experiment was repeated 4 times. The results of these experiments regarding the elongation in relation to the force applied to the system are summarized in Figure 74. It can be seen, that elongation depending on the applied force occurs similarly between runs with an elongation of around 0.15 mm at 1 N, 0.2 mm at 2 N and 0.3 mm at 5 N. The increase in elongation after 1.5 mm corresponds to the compliance of the measuring system.

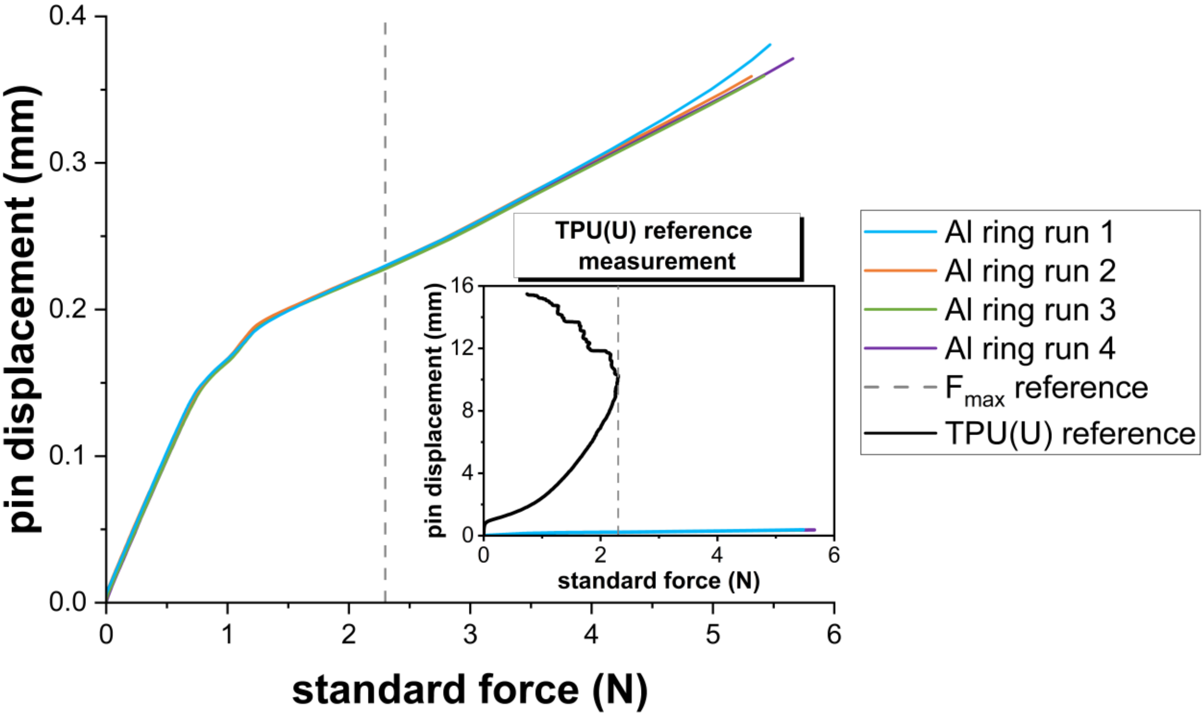

Figure 74: Pin displacement on the sample holders in relation to an applied standard force of up to 5 N for mechanical characterization of tubular specimens over four different runs (1 – 4). For reference, the smaller plot depicts these runs in comparison to the stress-strain behavior of an electrospun ring specimen of 25HF25TB24h during a ring tensile test. The grey stripped line in both plots marks the maximal force maintained by the electrospun ring specimen.